Lehrstuhl E23 für Technische Physik
Walther-Meissner-Institut für Tieftemperaturforschung
der Bayerischen Akademie der Wissenschaften

Raman Scattering Study of Electronic Correlations in Cuprates: Observation of an Unconventional Metal-Insulator Transition

Francesca Venturini

Vollständiger Abdruck der von der Fakultät für Physik der Technischen Universität München zur Erlangung des akademischen eines

Doktors der Naturwissenschaften

genehmigten Dissertation.

Vorsitzender		Prof. Dr. M. Kleber
Prüfer der Dissertation	1.	Prof. Dr. R. Gross
	2.	Prof. Dr. H. Kinder

Die Dissertation wurde am 18.12.2002 bei der Technischen Universität München eingereicht und durch dir Fakultät für Physik am 16.04.2003 angenommen

Contents

Chapter 1

Introduction

Copper-oxide superconductors [1] are among the most intensively studied compounds in condensed matter physics. This was originally - and partly still is - due to the fascination of the high superconducting transition temperature T_c of the order of 100 K, and to the consequent promise of technological applications. In addition, cuprates raise fundamental questions about the collective quantum properties of strongly interacting electrons in a lattice.

Despite unprecedented research activity, a many-body theory of the solid state of these materials is still missing. This is related to the strong electronic correlations which, depending on temperature, stoichiometry and pressure, lead to an extremely rich phase diagram [2]. At half filling cuprates are Mott-Hubbard insulators in which a large on-site Coulomb repulsion suppresses charge fluctuations and prevents metallic behaviour. Upon doping with electrons or holes long-range antiferromagnetism disappears; eventually, the materials become superconducting. The transition temperature increases with increasing carrier concentration until it reaches a maximum at a concentration which is referred to as optimum doping. For further increasing concentrations, T_c decreases again. At high temperatures cuprates are in an unconventional metallic state with properties which seem to be determined by fluctuations and various ordering phenomena including lattice instabilities. Above a certain doping level superconductivity disappears and the normal state becomes more and more conventional.

Due to the strong correlations, to the vicinity of the relevant energy scales, and to the surprisingly high transition temperatures, the question arises of whether the traditional theoretical concept of Landau Fermi liquids with well defined quasiparticles is an appropriate starting point for a microscopic understanding [3].

Quantum phase transitions, which occur as a result of competing ground states [4, 5], have been recently proposed as a possible scenario to describe the rich phe-

nomenology observed. Such transitions, which are accessed at zero temperature by the variation of a non-thermal control parameter, can influence the behaviour of the system over a wide range of the phase diagram. However, this description does not specify the underlying microscopic interaction and is therefore not unanimously accepted [1], and further experimental investigations are necessary.

Since the discovery of cuprates in 1986 [1], the full spectrum of solid-state investigation tools has been applied and a huge number of experiments unveiled several aspects of their electronic properties. Experimental observations which are interpreted as an indication of the existence of a quantum critical point include, for example, NMR measurements in $YBa_2Cu_3O_{6+x}$ (YBCO) [7] and transport in $La_{2-x}Sr_xCuO_4$ (LSCO) in high magnetic fields [8] (for a review see [4, 9] and references therein). However, the comparison between different spectroscopies does not lead to a consistent picture and seems, instead, to pose new questions.

Raman spectroscopy is a useful tool to investigate cuprates because, in addition to good energy resolution common to other experimental techniques, it possesses also momentum resolution. By adjusting the polarization states of the incoming and scattered photons it is in fact possible to selectively probe excitations with momentum in different regions of the first Brillouin zone. Momentum resolution is particularly important in these compounds because of their highly anisotropic properties. Due to the long penetration depth of the laser light in cuprates, Raman spectroscopy has the advantage of being a bulk probe, and is therefore not particularly sensitive to surface effects. In addition, since the scattered intensity is related to a two-particle correlation function the many-body effects, which are believed to be particularly important in these strongly-correlated systems, can be effectively probed. Finally, the improved sample quality achieved in the last years allows now a clear distinction between intrinsic properties defect-induced effects overcoming the difficulties which initially hampered progress.

In this thesis various cuprate materials are investigated by Raman scattering. The evolution of the electronic properties with temperature and doping is extensively studied with the purpose of achieving a consistent picture of different spectroscopic observations.

The thesis is organized as follows: after a brief introduction to the most important characteristics of cuprates (Chapter 2), the theoretical background of the Raman effect is introduced (Chapter 3). Then the details on the sample preparation and characterization, and the experimental setup are described (Chapter 4). By

[1] "The first fad of the 21^{st} century is the Quantum Critical Point" P.W. Anderson [6].

comparing single-particle and two-particle properties, many-body effects are studied in the normal state (Chapter 5). The evolution with doping of the Raman spectra shows the existence of a transition in the dynamics of the carriers (Chapter 6). The superconducting state properties are then investigated (Chapter 7) and, although an anomalous evolution with doping is observed, no direct evidence of the normal-state crossover is found below the critical temperature. To investigate the origin of such a transition, the role of antiferromagnetic correlations is finally studied both theoretically and experimentally (Chapter 8).

Chapter 2

The cuprates

The study of cuprate superconductors started in 1986 when G. Bednorz and A. Müller [1] discovered that the oxide $La_{1.85}Ba_{0.15}CuO_4$ became superconducting at a transition temperature of $T_c \simeq 30$ K. Soon after, new ceramic compounds were discovered with transition temperatures as high as 93 K (YBCO) [10] or 125 K ($Tl_2Ba_2Ca_2Cu_3O_{10}$) [11]. This new class of materials, often referred to as high-temperature superconductors, attracted a lot of interest because they opened the way to applications which required nitrogen (liquid below 77 K) rather than helium for cooling. From a more fundamental point of view, the question which they posed was which mechanism is responsible for superconductivity and whether the superconducting state is the same Cooper-paired state described by the Bardeen-Cooper-Schrieffer (BCS) theory [12].

In this chapter the properties of cuprate superconductors will be reviewed with the focus placed on those issues relevant for this work.

2.1 Introduction

Although the chemical composition varies, there are a number of common physical and structural properties for the different cuprates. The most relevant ones are summarized here.

- Cuprates are quasi-two-dimensional doped insulators. In fact, by adding carriers to the antiferromagnetic insulating compound, a metal or a superconductor can be obtained.
- The unit cell is strongly anisotropic and has a layered structure.
- The critical temperature for the superconducting transition is of the order of 100 K.

- The superconducting coherence length ξ is very short, ~ 1 Å, comparable with the size of the unit cell, and is different for different crystallographic directions.
- The magnetic penetration depth λ is typically of the order of 1000 Å. The short ξ and large λ imply that cuprates are type-II superconductors, with $\kappa = \lambda/\xi \gg 1$, and a very large upper critical field, which is estimated to be as high as 260 T for the compound $Bi_2Sr_2CaCu_2O_{8+\delta}$ (BSCCO) [13].

2.2 Structural and electronic properties

The unit cell of all high-temperature superconductors is composed of a sequence of conducting and insulating layers, as shown schematically in Fig. 2.1. The conducting planes, parallel to the $a-b$ crystallographic axes, are composed of oxygen and copper atoms, while the adjacent insulating layers act as charge reservoirs: altering their composition modifies the number of mobile carriers in the CuO_2 planes.

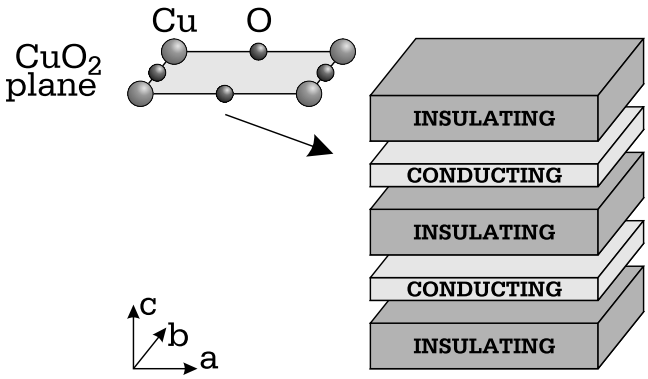

Figure 2.1: *Schematic structure of the unit cell of cuprate superconductors.*

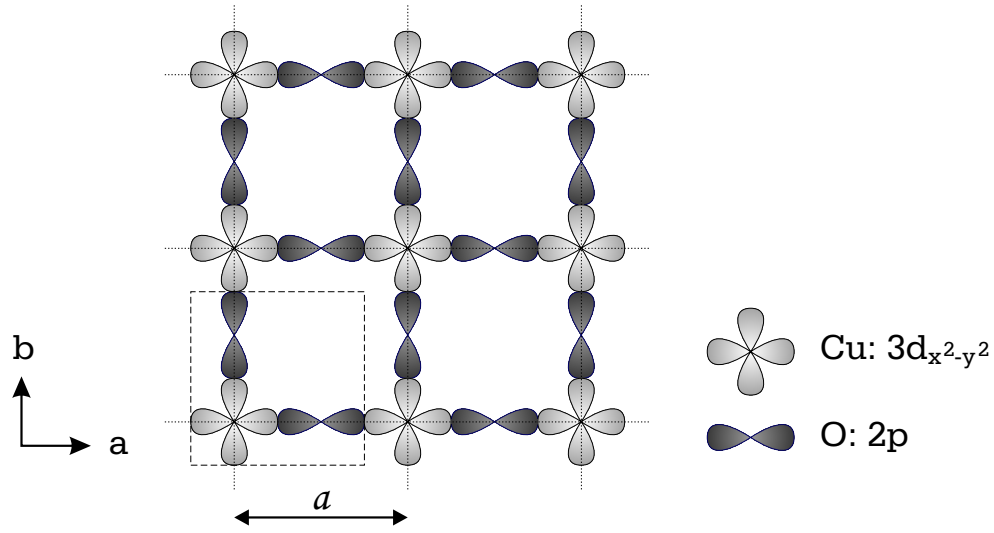

Figure 2.2: *Schematic view of the relevant orbitals of a CuO_2 layer. The dashed line marks a CuO_2 unit cell; a is the lattice constant.*

Since the mobile carriers are located in these quasi-2D CuO_2 planes, they are believed to be responsible for the majority of the properties observed in these materials including superconductivity.

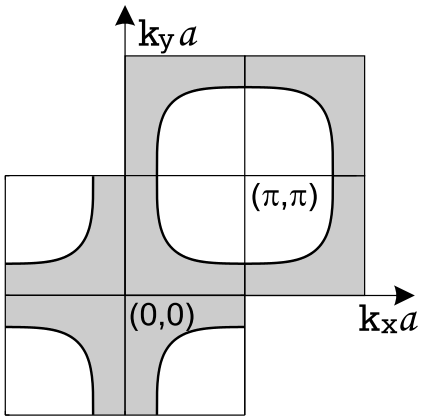

Figure 2.3: *Typical Fermi surface in cuprates.*

Outside the conducting layers, the electrons are in tightly bound localized states on the ions, far away from the Fermi surface: they play little role in the electron dynamics except as dopants.

According to electronic band structure calculations, the occupied orbitals with the highest energy are those whose lobes lie in the $a-b$ plane: $3d_{x^2-y^2}$ for copper, strongly hybridized with the oxygen $2p_x$ and $2p_y$ orbitals (Fig. 2.2).

Due to the little overlap between the CuO_2 planes, where the electron density is strongly concentrated, the carriers move almost entirely in the $a-b$ plane, leading to a nearly cylindrical Fermi surface. Angle-resolved photoemission spectroscopy (ARPES) has been successfully employed to study its shape [14] revealing a barrel-like structure centred at the (π, π) point of the Brillouin zone with only a small doping dependence [15]. A typical Fermi surface is shown schematically in Fig. 2.3, where the shaded areas correspond to the occupied states.

2.3 Phase diagram

As a function of carrier concentration all cuprates have surprisingly similar phase diagrams. Depending on whether the doping is achieved by electrons or holes the material is said to be electron-doped or hole-doped. In this work only the hole-doped side of the phase diagram (Fig. 2.4) will be studied.

The "parent" compounds with one hole per unit cell in the CuO_2 planes are antiferromagnetic insulators (AFI) with a Néel temperature, T_N, of several hundred Kelvin. As the hole concentration is increased the Néel temperature decreases and long-range antiferromagnetism disappears; eventually the material becomes superconducting (SC). The temperature below which superconductivity exists, T_c, also increases with increasing carrier concentrations until the maximum T_c^{max}, which appears when $\simeq 0.16$ holes per CuO_2 planes are added to the "parent" compound. This hole concentration is referred to as optimum doping; for increasing concentrations T_c decreases again. The regions corresponding to concentrations lower and higher

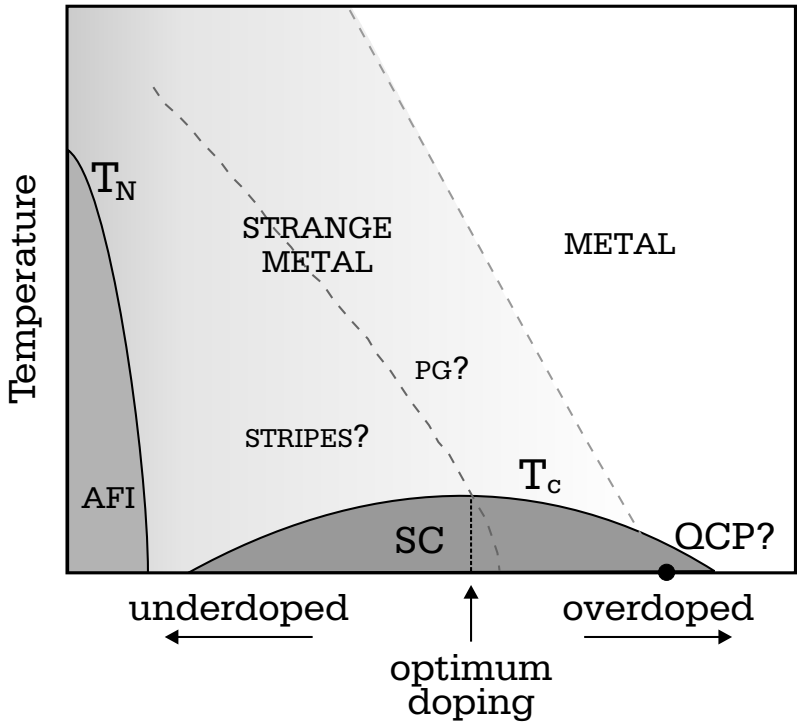

Figure 2.4: *Schematic phase diagram for hole-doped cuprates. The solid lines mark the phase transitions, the dashed lines possible crossovers. AFI and SC are the antiferromagnetic and the superconducting phases, respectively. PG indicates the region where a pseudogap is believed to open. T_N and T_c are the Néel and superconducting transition temperatures.*

than the optimum one are said to be underdoped and overdoped, respectively.

Also the high-temperature properties are strongly doping dependent: in the overdoped region the normal state shows metallic behaviour (METAL), and the concept of Landau quasiparticles can be applied; when the concentration is reduced the opening of a momentum-dependent partial gap or pseudogap (PG) is observed [16], together with a spin and charge modulation, interpreted as formation of STRIPES [17, 18]. The nature of the metallic state at these concentrations (STRANGE METAL) is believed to be characterized by a highly resistive hopping conduction, typical of localized electronic states.

The existence of crossovers (dashed in Fig. 2.4) in the electronic properties has been recently ascribed to the existence of a quantum critical point (QCP), located in the overdoped region of the phase diagram [9]. The corresponding phase transition occurs at zero temperature and therefore is driven by quantum fluctuations rather than thermal fluctuations. At present, however, there is no agreement on either the very existence or the location of the QCP.

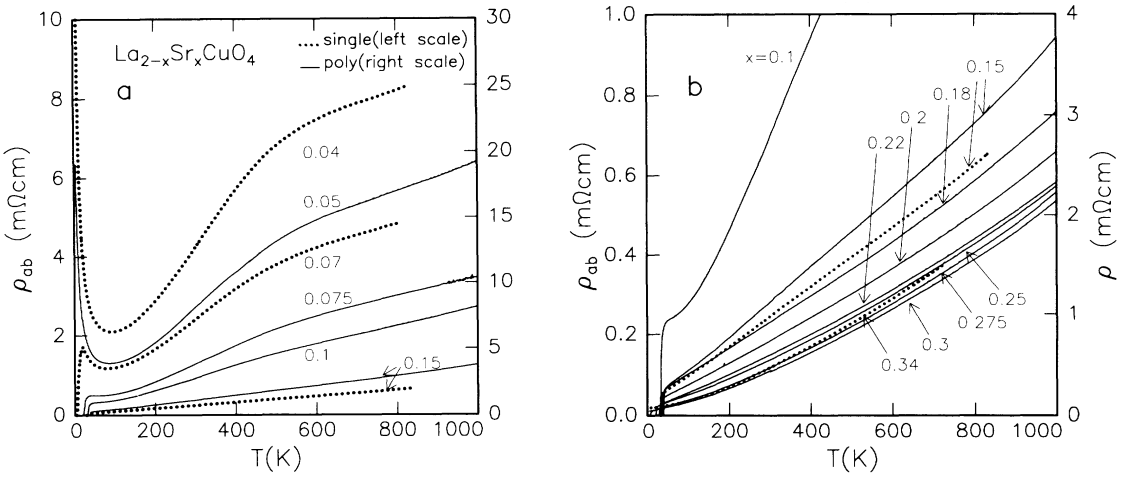

Figure 2.5: *Temperature dependence of the resistivity of $La_{2-x}Sr_xCuO_4$ for different carrier concentrations from Ref. [19]: a) $0 < x \leq 0.15$, b) $0.1 \leq x < 0.35$. The dotted lines mark the in-plane resistivity ρ_{ab} of single-crystal films; solid lines mark the resistivity ρ of polycrystalline samples.*

2.4 Electronic scattering rates in the normal state

The investigations about the properties of the cuprates in the normal state (at $T > T_c$) have revealed anomalous behaviours. In fact, although these materials have mainly metallic properties, the detailed behaviour is strongly dependent on the carrier concentration (see Fig. 2.4). In addition, the general picture is complicated by strong anisotropies mainly caused by the two-dimensional nature of the CuO_2 planes, and by the existence of magnetic phases close to the superconducting region.

The evolution with temperature of the scattering rate of the carriers, measured for example by transport through the in-plane resistivity ρ_{ab}, has revealed that at least at optimal doping the behaviour is distinctively non-Fermi-liquid like. In fact, in contrast to what would be expected in the case of a Fermi liquid, the electron-electron scattering rate in cuprates varies linearly with temperature or frequency over a wide range.

This can clearly be seen from measurements of the resistivity of $La_{2-x}Sr_xCuO_4$ for different Sr concentrations x shown in Fig. 2.5 from Ref. [19]. At optimum doping ($x = 0.15$), the linear behaviour extends up to approximately 1000 K and extrapolates to zero resistance at zero temperature. In the overdoped regime ($x > 0.15$) the resistivity no longer extrapolates to zero and a more Fermi-liquid behaviour is qualitatively recovered, while for low carrier concentrations ($x < 0.15$) a drop in the resistivity appears below a temperature T^* which increases with decreasing x. This reduced scattering has been attributed to the opening of the pseudogap [16].

The distribution in momentum space of the electron-electron scattering rate has been extensively studied by photoemission spectroscopy, and one of the earlier results is shown in Fig. 2.6 Ref. [20]. The spectra of an underdoped (A) and an

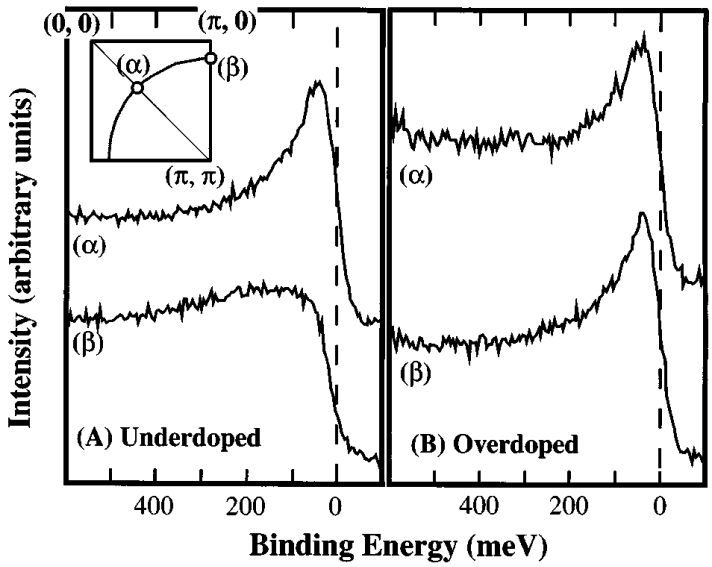

Figure 2.6: *ARPES spectra from an underdoped (A) and an overdoped (B) BSCCO sample measured at 100K in two points on the Fermi surface, as shown in the inset. The figure is taken from Ref. [20].*

overdoped (B) BSCCO sample, with $T_c \simeq 84$ K and $T_c \simeq 80$ K, measured at 100 K and at two positions on the Fermi surface are compared. α denotes a point on the Fermi surface along the Brillouin zone diagonal, close to $(\pi/2, \pi/2)$, and β a point on the axis, close to $(\pi, 0)$. Upon doping from the underdoped (A) to the overdoped (B) superconductor, the quasiparticle peak at the **k**-point β moves toward the Fermi energy, becomes sharper, and increases in intensity. In contrast, doping has relatively little effect on the peak at the α point.

Since the intensity measured by ARPES reflects the single-particle spectral function (see Chapter 5), these observations seem to point in the direction of an anisotropic scattering rate which is strongest along the axis of the Brillouin zone (β) and which is doping dependent. In Chapter 5 raw photoemission data on an overdoped BSCCO are analyzed and compared with Raman results in the same material. The evolution of the relaxation rates determined by Raman with the carrier concentration is the focus of Chapter 6.

2.5 Energy gaps in the superconducting state

Among the key questions concerning the superconducting state are the symmetry and the magnitude of the superconducting gap. It is now well established that in the conventional low-T_c superconductors (like Pb, Al, Nb) the phonon-mediated electron-electron interaction leads to a pairing which is constant in the Brillouin zone; the resulting energy gap possess therefore s-wave symmetry (Fig. 2.7 (a)).

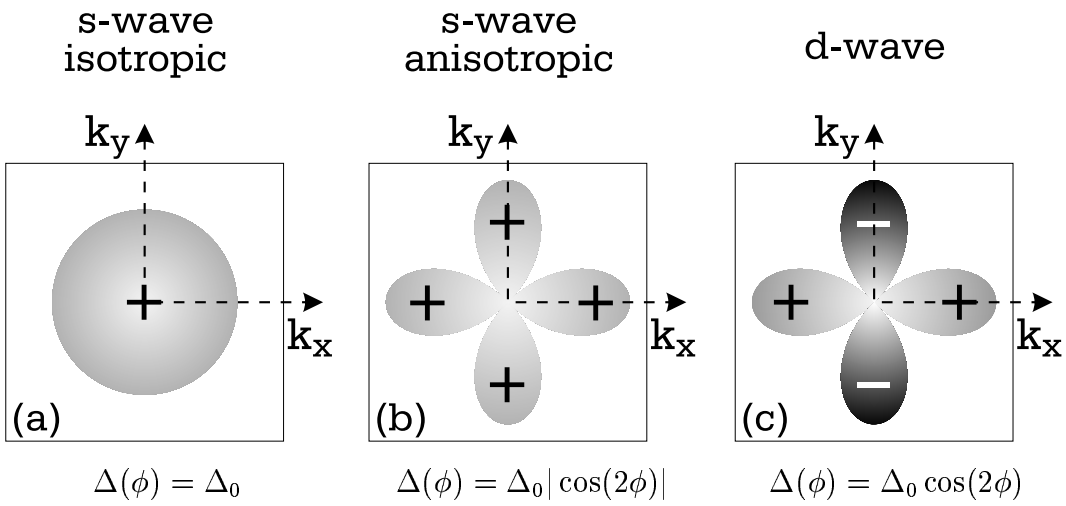

Figure 2.7: *Different symmetries of the gap function in momentum space: (a) isotropic s-wave, (b) anisotropic s-wave, (c) d-wave. ϕ is the angle around the Fermi surface.*

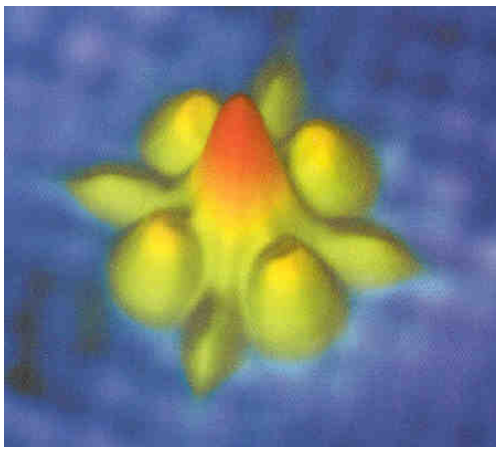

Figure 2.8: *Scanning-tunneling-microscope image showing the disturbance brought in a high-temperature superconductor by a single zinc impurity [21].*

In the cuprates, although it is now clear that the electronic charges are paired [22], the nature of the pairing mechanism remains a subject of strong debate. Since the pairing between electrons reflects itself directly in what is called the order parameter Δ in the superconducting state, the question of the symmetry of the order parameter (which coincides with the energy gap in BCS theory [12]) has attracted strong attention since the discovery of these materials.

Non-phase-sensitive experiments such as Raman scattering, penetration depth, specific heat, and thermal conductivity

measurements provide evidence for a highly anisotropic order parameter with nodes along the diagonal directions of the Brillouin zone (Fig. 2.7 (b)). The phase-sensitive probes such as flux quantization measurements have shown that $\Delta(\phi)$ changes sign in the Brillouin zone Fig. 2.7 (c). For a review on experimental results on $\Delta(\phi)$ see [23]. The symmetry of the gap is called d-wave, or more precisely $d_{x^2-y^2}$. Additional support has recently come from tunneling experiments on BSCCO doped with Zn impurities [24]. The spatial distribution of the measured density of states has in fact a four-fold symmetry (Fig. 2.8 [21]), which reflects the underlying d-wave symmetry of the pairing.

The answer to the problem of what is the maximum value of the superconducting energy gap does not seem to have a straightforward answer. In fact, different experimental techniques lead to different values of the gap, which have a distinctively different evolution with the carrier concentration. In Fig. 2.9 data from various kinds of experiments and for a number of cuprates are collected from Ref. [25].

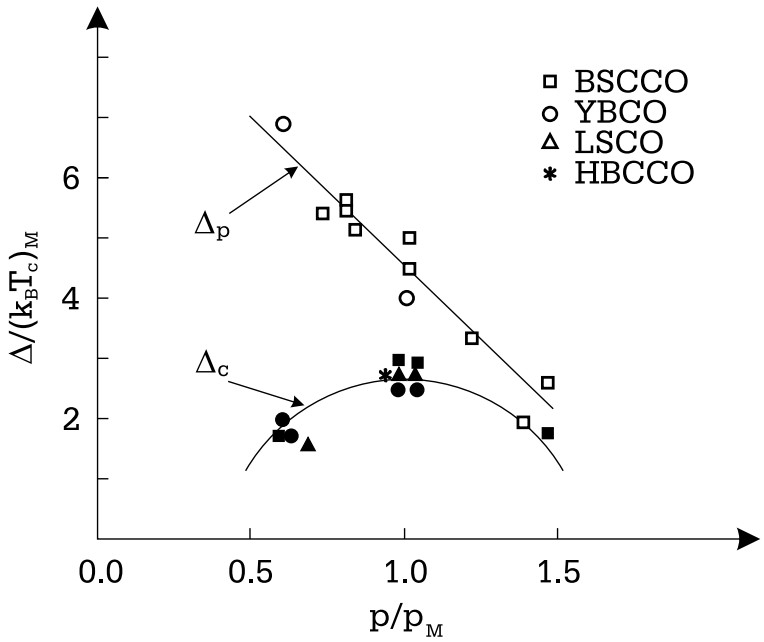

Figure 2.9: *The pairing energy, Δ_p, and the coherence energy, Δ_c, for several cuprates. The results are shown as a function of the normalized doping level (p/p_M) with p_M the doping at the maximum value of T_c; the gap values are normalized by the maximum values of k_BT_c in the respective material classes. Δ_p values are from tunneling and photoemission data (open symbols); Δ_c values are from Andreev, penetration depth and Raman B_{2g} data (filled symbols). The figure is taken from Ref. [25].*

From this analysis two distinct energy scales emerge, called by Ref. [25] pairing energy, Δ_p, and coherence energy, Δ_c. These two gaps can be understood as the

energy required to split the paired carriers and the energy range of coherence in the superconducting state, respectively. Even if the interpretation of these observations is controversial, an important experimental result is that both energy scales appear to merge in the overdoped region.

In Chapter 7 the superconducting state is investigated in detail and an estimation of the energy gap is given from measurements in different scattering geometries and at several carrier concentrations.

2.6 Antiferromagnetic correlations in cuprates

Due to its proximity to the antiferromagnetic insulating phase the superconducting state is affected by magnetic correlations, which become shorter in range with increasing carrier concentration. Such correlations are believed to play an important role in both the superconducting and the normal state properties.

Nuclear magnetic resonance measurements have revealed that the dynamical spin susceptibility $\chi_s(\mathbf{q},\omega)$ strongly peaks at wave vectors close to $\mathbf{q} = (\pi,\pi) \equiv \mathbf{Q}$ [26]. As a consequence, it has been proposed [27, 28] that the electronic spectral density at the Fermi surface and the electron-spin interaction are strongly anisotropic, leading to a qualitatively different behaviour for those quasiparticles which are located at the $\mathbf{k}$-points such that $\varepsilon_{\mathbf{k}} \approx \varepsilon_{\mathbf{k}+\mathbf{Q}}$ (with $\varepsilon_{\mathbf{k}}$ the band dispersion), called "hot" quasiparticles, and those far away from this condition, named "cold" quasiparticles.

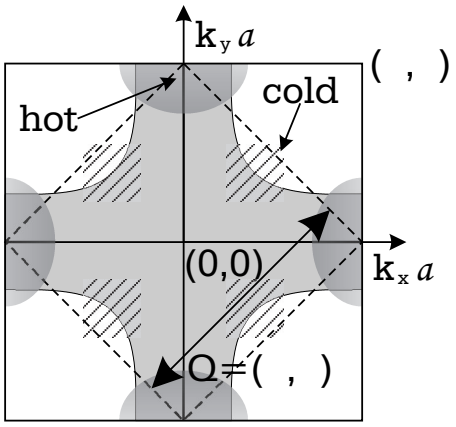

Figure 2.10: *Typical Fermi surface in the first Brillouin zone (solid line) and the magnetic Brillouin zone boundary (dashed line). The hot spots are those regions of the Fermi surface which can be connected by the wave vector* $\mathbf{Q} = (\pi,\pi)$. *With this Fermi surface the cold quasiparticles are located along the Brillouin zone diagonals.*

In fact, being located close to the momentum points on the Fermi surface which can be connected by $\mathbf{Q}$, the hot quasiparticles feel the effect of the antiferromagnetic interaction and are strongly scattered. The cold quasiparticles, on the other hand, feel only a weak effect of antiferromagnetic interaction and have a reduced scattering.

In Fig. 2.10 are shown the hot and cold regions of the Fermi surface, which are located along the axis at $(\pi, 0)$ and along diagonals at $(\pi/2, \pi/2)$ respectively.

The existence of spots on the Fermi surface with anomalous scattering leads to very anisotropic electron lifetimes. Among the experimental methods to investigate this anisotropy transport does not play a key role, since the resistivity is dominated by the lifetime in the points of the Fermi surface away from the hot spots (cold spots) [29]. On the contrary, Raman scattering as a $\mathbf{k}$-sensitive probe can independently follow the evolution of the scattering rate of hot and cold quasiparticles throughout the entire phase diagram, as is discussed in Chapter 6. The role of antiferromagnetic fluctuations is investigated in detail in Chapter 8 both theoretically and experimentally. As a result magnetic correlations are found to play a key role both in the normal and in the superconducting states.

Chapter 3

Raman scattering

The contribution of Raman scattering to the understanding of cuprate superconductors is related to its ability to probe excitation dynamics on different regions of the Brillouin zone rather than being restricted to measure averages over the Fermi surface. Due to this, Raman spectroscopy has proved to be a useful tool to study these materials, to analyze the scattering rate of the electrons in certain regions of the **k**-space above T_c [30], and to investigate the magnitude and the symmetry of the energy gap in the superconducting state [31, 32].

In this chapter the essentials of the theory of Raman scattering in metals are summarized. In particular, the formalism to calculate the Raman response both in the normal and in the superconducting state is introduced and is used later in this thesis to interpret the experimental observations.

3.1 The Raman effect

Raman scattering is an inelastic two-photon process in which one photon with frequency ω_I and momentum $\mathbf{k}_I$ is absorbed and one photon with frequency ω_S and momentum $\mathbf{k}_S$ is emitted, while the material makes a transition from the initial state $|i\rangle$ to the final state $|f\rangle$, as shown schematically in Fig. 3.1. The conservation of energy and momentum in the process can be written as

$$\begin{aligned} \hbar\omega &= \hbar\omega_I - \hbar\omega_S \quad && \textit{Raman shift} \\ \mathbf{q} &= \mathbf{k}_I - \mathbf{k}_S && \textit{momentum transferred to the system} \end{aligned} \tag{3.1}$$

If the scattered photon has a lower energy than the incident one ($\omega > 0$), the process is called Stokes, otherwise ($\omega < 0$) anti-Stokes.

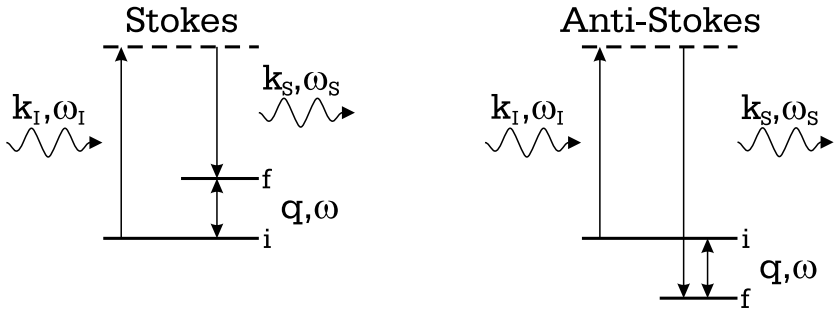

Figure 3.1: *Schematic representation of the Raman effect. If $\omega > 0$ the process is called Stokes, if $\omega < 0$ anti-Stokes.*

3.2 Electronic Raman scattering

The intensity of inelastically scattered light is proportional to the differential photon scattering cross section [33]

$$\frac{\partial^2\sigma}{\partial\omega\partial\Omega} = \frac{\omega_S}{\omega_I}\, r_0^2\, S_{\gamma\gamma}(\mathbf{q},\omega) \tag{3.2}$$

where Ω is the solid angle for the scattered light, $r_0 = e^2/mc^2$ is the Thompson radius, with e and m the charge and bare mass of the electron and c the speed of light, ω_I and ω_S are the frequencies of the incoming and scattered photons respectively. $S_{\gamma\gamma}$ is the generalized structure function, which is related to the imaginary part of the Raman response function $\chi_{\gamma\gamma}$ through the fluctuation-dissipation theorem [34],

$$S_{\gamma\gamma}(\mathbf{q},\omega) = -\frac{\hbar}{\pi}\,[1+n(\omega)]\,\mathrm{Im}\;\chi_{\gamma\gamma}(\mathbf{q},\omega) \tag{3.3}$$

with $n(\omega)$ the Bose-Einstein distribution. The Raman response $\chi_{\gamma\gamma}$ measures "effective electronic density" fluctuations, and at finite temperature is given by

$$\chi_{\gamma\gamma}(\mathbf{q},i\omega) = \int_0^\beta d\tau\, e^{-i\omega\tau}\langle T_\tau[\tilde{\rho}_{\mathbf{q}}(\tau)\tilde{\rho}_{-\mathbf{q}}(0)]\rangle, \tag{3.4}$$

with $\beta = (k_B T)^{-1}$, T the temperature, T_τ the time-ordering operator and $\langle ...\rangle$ denoting a thermal average. The effective charge density operator $\tilde{\rho}_{\mathbf{q}}$ is an average over the Brillouin zone weighted by the $\mathbf{k}$-dependent Raman scattering amplitude $\gamma_{\mathbf{k},\mathbf{q}}(\omega_I,\omega_S)$ [31]

$$\tilde{\rho}_{\mathbf{q}} = \sum_{\mathbf{k},\sigma} \gamma_{\mathbf{k},\mathbf{q}}(\omega_I,\omega_S)\, c^\dagger_{\mathbf{k}+\mathbf{q},\sigma} c_{\mathbf{k},\sigma} \tag{3.5}$$

where σ is the spin index, $c^\dagger_{\mathbf{k},\sigma}$, $c_{\mathbf{k},\sigma}$ are the creation and annihilation operators of an electron with momentum $\mathbf{k}$ and spin σ, respectively. In the following the approximation of a weak dependence of the Raman scattering amplitude (or vertex

function) $\gamma_{\mathbf{k},\mathbf{q}}$ on $\mathbf{q}$ is used [31]. This is justified since $\mathbf{q} \approx 0$ for the large optical penetration depth in cuprates ($\lambda \sim 1000$ Å, Sect. 2.1).

The scattering amplitude can be determined starting from the Hamiltonian for electrons interacting with an external electromagnetic field [34]

$$H_{int} = -\frac{e}{m}\sum_j \mathbf{A}(\mathbf{r}_j)\cdot\mathbf{p}_j + \frac{e^2}{2m}\sum_j \mathbf{A}(\mathbf{r}_j)\cdot\mathbf{A}(\mathbf{r}_j) \tag{3.6}$$

where $\mathbf{A}(\mathbf{r}_j)$ is the vector potential, $\mathbf{r}_j$ and $\mathbf{p}_j$ are the position and momentum position of the j^{th} electron. The contributions up to the second perturbative order in $\mathbf{A}$ are considered, since the process involves two photons. Assuming that the initial and final state differ only by excitations of electrons within a given band and that the intermediate state differs from the initial and final states only by a single particle excitation [33], the Raman vertex for vanishing $\mathbf{q}$ is given by

$$\begin{aligned}\gamma_{\mathbf{k}}(\omega_I,\omega_S) &= \mathbf{e}^I\cdot\mathbf{e}^S + \frac{1}{\hbar m}\sum_\nu \\ &\times\left[\frac{\langle n,\mathbf{k}|\mathbf{e}^S\cdot\mathbf{p}|\nu,\mathbf{k}\rangle\langle\nu,\mathbf{k}|\mathbf{e}^I\cdot\mathbf{p}|n,\mathbf{k}\rangle}{\varepsilon(\mathbf{k})-\varepsilon_\nu(\mathbf{k})+\hbar\omega_I} + \frac{\langle n,\mathbf{k}|\mathbf{e}^I\cdot\mathbf{p}|\nu,\mathbf{k}\rangle\langle\nu,\mathbf{k}|\mathbf{e}^S\cdot\mathbf{p}|n,\mathbf{k}\rangle}{\varepsilon(\mathbf{k})-\varepsilon_\nu(\mathbf{k})-\hbar\omega_S}\right]\end{aligned} \tag{3.7}$$

where $\mathbf{e}^I, \mathbf{e}^S$ are the incident and scattered polarization vectors, $\mathbf{p} = -i\hbar\nabla$, $\varepsilon(\mathbf{k}) \equiv \varepsilon_{\mathbf{k}}$ and $\varepsilon_\nu(\mathbf{k})$ are the Bloch conduction and an intermediate state energies respectively [35].

In general, as evident from Eq. (3.7), the Raman vertex depends nontrivially on both the incident and the scattered photon frequencies. However, it was shown [35] that, in the limit of vanishingly small light frequencies and for a single band near the Fermi level, $\gamma_{\mathbf{k}}$ can be related to the curvature of the conduction band and to the incident and scattered photon polarization vectors $\mathbf{e}^{I,S}$ as

$$\lim_{\omega_I,\omega_S\to 0}\gamma_{\mathbf{k}}(\omega_I,\omega_S) = \sum_{\mu,\nu} e^I_\mu \frac{\partial^2\varepsilon_{\mathbf{k}}}{\partial k_\mu \partial k_\nu} e^S_\nu, \tag{3.8}$$

where terms of the order of $1-\omega_S/\omega_I$ are dropped, and $\mu,\nu = x,y$. This approximation, which is valid if the incoming laser light cannot excite direct band-band transitions, is called "effective-mass approximation". It has, however, a questionable region of validity for cuprates, since the incoming photons have an energy of the order of 2 eV, comparable to the bandwidth and the inter-band excitations according to local density calculations [36].

An alternative approach [31] is based on the experimental observation that the electronic continuum in the metallic normal state depends only weakly on the incoming frequency for a wide range of cuprate materials. Then the Raman vertex

can be expanded in a complete set of orthonormal functions $\Phi_L(\mathbf{k})$ defined on the Fermi surface or in the Brillouin zone

$$\gamma_{\mathbf{k}}(\omega_I, \omega_S) = \sum_L \gamma_L(\omega_I, \omega_S)\Phi_L(\mathbf{k}), \tag{3.9}$$

In general the functions $\Phi_L(\mathbf{k})$ can be chosen to be Brillouin zone or Fermi surface harmonics [37]. In this work, when this approach is used (Chapter 5, Chapter 6, and Chapter 8) the prefactors $\gamma_L(\omega_I, \omega_S)$ are approximated to be constants, since they represent the magnitude but not the $\mathbf{k}$-dependence of scattering, and used as parameters to fit the intensities measured experimentally. The role of the vertex modeling and the dependence of the response on its details will be discussed later in this work (Chapter 8).

3.3 Raman response function

The main process contributing to the Raman response is represented diagrammatically in Fig. 3.2, where the dashed and solid lines correspond to photonic and fermionic propagators, respectively. The shaded areas (γ) represent the $\mathbf{k}$-dependent Raman vertex, which contains the detail of photon-electron interaction.

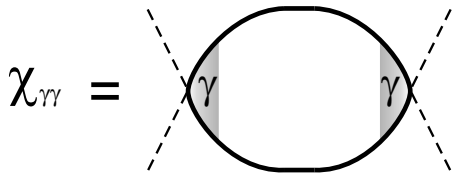

Figure 3.2: *Feynman diagram for the Raman response. Dashed and solid lines represent photonic and fermionic propagators, respectively.*

The general expression for the Raman scattering would include also the effect of vertex corrections. For the issues investigated in this work such effects have been shown to produce only minor changes in the spectra [32] and are therefore neglected. Vertex correction become however important for the evaluation of the transport coefficients [38]: they account for the fact that back scattering is an effective means of degrading a current while forward scattering is not [39].

The Raman response function $\chi_{\gamma\gamma}$ is therefore given by

$$\chi_{\gamma\gamma}(\mathbf{q}, i\omega) = \frac{1}{\beta}\sum_{\mathbf{k}, i\omega'} \gamma_{\mathbf{k}} G(\mathbf{k}, i\omega')\gamma_{\mathbf{k}} G(\mathbf{k}-\mathbf{q}, i\omega' - i\omega) \tag{3.10}$$

where the convention $\hbar = 1, k_B = 1$ is used. $G(\mathbf{k}, i\omega')$ is the fermionic propagator, $\beta = T^{-1}$, $i\omega$ and $i\omega'$ are bosonic and fermionic Matsubara frequencies [40], respectively.

In general, the electronic propagator is renormalized due, for example, to impurities or to phonon mediated electron-electron interactions. The renormalized Green function is then expressed through the Dyson equation,

$$G(\mathbf{k}, i\omega)^{-1} = G^{(0)}(\mathbf{k}, i\omega)^{-1} - \Sigma(\mathbf{k}, i\omega) \ , \tag{3.11}$$

which is graphically represented in Fig. 3.3. $G^{(0)}$ is the bare propagator and Σ is the

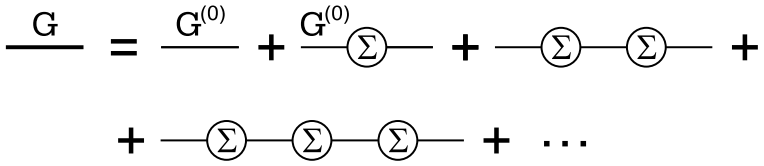

Figure 3.3: *Schematic representation of the Dyson equation: the thick and thin lines are renormalized and bare propagators respectively; the bubble represents the self energy.*

self energy, generally complex, $\Sigma(\mathbf{k}, \omega) = \Sigma'(\mathbf{k}, \omega) + i\Sigma''(\mathbf{k}, \omega)$. The imaginary part Σ'' can be interpreted as causing the damping of the particle motion, and is related to the mean free path of the excitation; the real part Σ' represents an energy shift of the excitation, which may change its dynamical motion.

Finally, the total Raman response has to be calculated in that gauge-invariant form which results from taking into account the long wavelength fluctuations of the order parameter to guarantee local charge conservation [32]. The total Raman susceptibility thus follows as

$$\chi(i\omega) = \chi_{\gamma\gamma}(i\omega) - \frac{\chi_{\gamma 1}^2(i\omega)}{\chi_{11}(i\omega)} \tag{3.12}$$

where $\chi_{\gamma 1}$ and χ_{11} are obtained by the replacement $\gamma(\mathbf{k}) \to 1$ in one or both bare Raman vertices in Eq. (3.10). The response in this form is sometimes referred to as "screened". Since the scattering cross section is proportional to the imaginary part of the response function (Eq. (3.2) and Eq. (3.3)), the imaginary part of Eq. (3.12) must be taken after the analytic continuation to real frequencies, $i\omega \to \omega + i0^+$.

In the next two sections the explicit expression for the Raman response will be derived in both the normal and the superconducting state.

3.3.1 Normal state

In the normal state, the bare electronic propagator is $G^{(0)}(\mathbf{k}, i\omega)^{-1} = i\omega - \xi_{\mathbf{k}}$ and therefore the renormalized one from Eq. (3.11) is

$$G(\mathbf{k}, i\omega) = \frac{1}{i\omega - \xi_{\mathbf{k}} - \Sigma(\mathbf{k}, i\omega)} \tag{3.13}$$

$\xi_{\mathbf{k}} = \varepsilon_{\mathbf{k}} - \mu$ is the band dispersion and μ the chemical potential. The form and the consequences of the band structure will be discussed in more detail in Sect. 3.5. To analytically evaluate Eq. (3.10) it is convenient to use the Lehman or spectral representation [40] for $G(\mathbf{k}, i\omega)$

$$G(\mathbf{k}, i\omega) = -\int_{-\infty}^{\infty} \frac{dy}{\pi} \frac{G''(\mathbf{k}, y)}{i\omega - y} \tag{3.14}$$

where $G''(y, \mathbf{k})$ is the imaginary part of the electronic propagator $G(y, \mathbf{k}) = G'(y, \mathbf{k}) + iG''(y, \mathbf{k})$; after performing the sum over the fermionic Matsubara frequencies $i\omega'$ [40] in Eq. (3.10) the resulting Raman response is

$$\begin{aligned} \chi_{\gamma\gamma}(\mathbf{q}, i\omega) &= \sum_{\mathbf{k}} \gamma_{\mathbf{k}}^2 \int_{-\infty}^{\infty} \frac{dy_1}{\pi} \int_{-\infty}^{\infty} \frac{dy_2}{\pi} G''(y_1, \mathbf{k}) G''(y_2, \mathbf{k} - \mathbf{q}) \\ &\quad \frac{n_F(y_2) - n_F(y_1)}{y_2 - y_1 + i\omega} \end{aligned} \tag{3.15}$$

with $n_F(y)$ the Fermi-Dirac distribution.

Taking the imaginary part of the expression obtained performing the analytical continuation $i\omega \to \omega + i0^+$ Eq. (3.15) gives

$$\chi''_{\gamma\gamma}(\mathbf{q}, \omega) = \sum_{\mathbf{k}} \gamma_{\mathbf{k}}^2 \int_{-\infty}^{\infty} \frac{dy}{\pi} G''(y, \mathbf{k}) G''(y - \omega, \mathbf{k} - \mathbf{q}) \left[n_F(y) - n_F(y - \omega) \right] \tag{3.16}$$

The final expression can be further simplified taking the limit $\mathbf{q} \to 0$, because of the large optical penetration depth in cuprates.

Note that, if the self energy is $\Sigma \equiv 0$, for phase space restrictions $\chi''(\omega)$ is identically zero. This, which can be shown by substituting the imaginary part of the electronic propagator of Eq. (3.13) in Eq. (3.16), implies that a finite Σ is required to evaluate the normal state Raman response.

At present there is not a widely accepted model describing the self energy although the frequency, doping, temperature and momentum dependence of the single-particle scattering rate are the subject of a wealth of investigations. In fact, since Σ includes the effects of many-body interactions, its determination is a crucial problem in the understanding of the physics in cuprates.

Indirect measurements of the self energy can be made by different experimental probes, since Σ is related to the quasiparticle lifetime. For example, transport indicates that for optimally doped compounds the inverse lifetime at the Fermi level is linear with temperature over a wide temperature range [41, 19] (see Sect. 2.4). Furthermore, infrared studies indicate that the scattering rate is linear in both temperature and frequency [42].

Raman spectroscopy, being **k**-sensitive, can be expected to reflect variations of Σ in the **k**-space in the symmetry-dependent scattering rates. The best technique to extract the details of the self energy is, however, angle-resolved photoemission spectroscopy, which is a truly single-particle, **k**-resolved probe. In Chapter 5 the detailed energy, momentum and temperature dependence of the self energy extracted from photoemission data is used to interpret the Raman results.

3.3.2 Superconducting state

In the superconducting state the Nambu-Gor'kov formalism must be introduced to preserve the Feynman-Dyson perturbation description [43]. The electronic propagator, in the case of singlet pairing and in the BCS approximation, must be written as a matrix and is

$$\hat{G}(\mathbf{k}, i\omega) = \frac{i\omega\hat{\tau}_0 + \xi_{\mathbf{k}}\hat{\tau}_3 + \Delta(\mathbf{k})\hat{\tau}_1}{(i\omega)^2 - E(\mathbf{k})^2} \tag{3.17}$$

where $\hat{\tau}_i$ with $i = 1, 2, 3$ are the 2×2 Pauli matrices and $\hat{\tau}_0 = \hat{1}$; $E(\mathbf{k})$ is the dispersion of the quasiparticles $E(\mathbf{k})^2 = \Delta(\mathbf{k})^2 + \xi_{\mathbf{k}}^2$, with $\Delta(\mathbf{k})$ the superconducting energy gap. In this case Eq. (3.10) is written as

$$\chi_{\gamma\gamma}(\mathbf{q}, i\omega) = \frac{1}{\beta}\mathrm{Tr}\sum_{\mathbf{k},\mathrm{i}\omega'} \hat{\gamma}(\mathbf{k})\hat{\mathrm{G}}(\mathbf{k}, \mathrm{i}\omega')\ \hat{\gamma}(\mathbf{k})\ \hat{\mathrm{G}}(\mathbf{k}-\mathbf{q}, \mathrm{i}\omega' - \mathrm{i}\omega) \tag{3.18}$$

where $i\omega'$ are fermionic Matsubara frequencies, and $\hat{\gamma}(\mathbf{k}) = \hat{\tau}_3\gamma_{\mathbf{k}}$ is the bare Raman vertex. Tr denotes the trace operator.

After performing the Matsubara frequency summation over $i\omega'$ and taking the trace of the resulting expression, in the limit $\mathbf{q} \to 0$, the Raman response is

$$\chi_{\gamma\gamma}(i\omega) = \sum_{\mathbf{k}} \gamma_{\mathbf{k}}^2 \lambda(\mathbf{k}, i\omega) \tag{3.19}$$

where $\lambda(\mathbf{k}, i\omega)$, called Tsuneto function, is

$$\lambda(\mathbf{k}, i\omega) = \frac{\Delta(\mathbf{k})^2}{E(\mathbf{k})^2}\tanh\left(\frac{E(\mathbf{k})}{2T}\right)\left[\frac{1}{2E(\mathbf{k}) + i\omega} + \frac{1}{2E(\mathbf{k}) - i\omega}\right] \tag{3.20}$$

Again, the imaginary part must be taken after the analytical continuation.

While Eqs. (3.19) and (3.20) describe the main contribution to the Raman response, processes of higher order may play a non negligible role in cuprates. In particular, antiferromagnetic correlations are observed in the superconducting phase of several families of high-temperature superconductors [44, 45, 46]. For this reason, this calculation is extended in Sect. 8.2 to include the scattering of quasiparticles from magnetic excitations.

3.4 Memory-function approach

A quantitative analysis of the dynamics of the carriers can be performed from the experimentally measured imaginary part of the Raman response $\chi''(\omega, T)$ through a recently developed memory-function approach [30]. The method consists in writing the Raman susceptibility $\chi(\omega, T)$ in terms of a memory-function $M(\omega, T)$ [47] as

$$\chi(\omega, T) = \frac{M(\omega, T)}{\omega + M(\omega, T)} \tag{3.21}$$

where

$$M(\omega, T) = i\Gamma(\omega, T) + \omega\lambda(\omega, T) \ . \tag{3.22}$$

$\Gamma(\omega, T)$ corresponds to the dynamical relaxation rate of the carriers and $1+\lambda(\omega, T) = m^*(\omega, T)/m$ to the mass renormalization factor. From Eq. (3.21) and Eq. (3.22) the imaginary part of the response function can be written as

$$\chi''(\omega, T) = \frac{\omega\Gamma(\omega, T)}{\omega^2(1 + \lambda(\omega, T))^2 + \Gamma^2(\omega, T)} \ . \tag{3.23}$$

In order to extract $\Gamma(\omega, T)$ and $1 + \lambda(\omega, T)$ from the measured $\chi''(\omega, T)$, it is convenient to define two functions $I(\omega, T)$ and $K(\omega, T)$ as

$$\begin{aligned} I(\omega, T) &= \frac{\chi''(\omega, T)}{\omega} \\ K(\omega, T) &= -\frac{2}{\pi}\,\mathcal{P}\int_0^\infty \frac{I(\xi, T)}{\xi^2 - \omega^2} d\xi \end{aligned} \tag{3.24}$$

where $\mathcal{P}$ stands for principal value of the integral. Γ and $1+\lambda$ can now be rewritten as [30]

$$\begin{aligned} \Gamma(\omega, T) &= R\,\frac{I(\omega, T)}{I^2(\omega, T) + \omega^2 K^2(\omega, T)} \\ 1 + \lambda(\omega, T) &= R\,\frac{K(\omega, T)}{I^2(\omega, T) + \omega^2 K^2(\omega, T)} \end{aligned} \tag{3.25}$$

where the constant R can be determined by the sum rule

$$R = \frac{2}{\pi}\int_0^\infty \frac{\chi''(\omega, T)}{\omega} d\omega \ . \tag{3.26}$$

Following this approach the Raman relaxation rates are studied in Chapter 6 as a function of frequency, temperature and doping.

3.5 Band structure effects

The knowledge of the band structure in cuprates is essential to determine the electronic properties: the shape and size of the Fermi surface, for example, determine the type and number of charge carriers in the material as well as the charge and spin dynamics.

Even if the determination of the band structure and therefore the Fermi surface is not trivial since these materials exhibit broad ill-defined electronic excitations due to the strong correlations [48], some key features are clarified by now especially due to extensive ARPES measurements [14, 15]. In this section a more quantitative description of the band structure is added to the general considerations of Sect. 2.2.

Since the electronic conduction in these materials takes place predominantly in the CuO_2 planes, where copper and oxygen form an approximately square planar arrangement, these layers are frequently modeled as a two-dimensional square lattice, as shown in Fig. 3.4; a and b represent the crystal axes, a the lattice constant. The hopping of an electron to the nearest neighbor or to the next-nearest neighbor site is characterized by the hopping integrals t and t', respectively. In a tight-binding picture, the band $\xi_{\mathbf{k}}$ can be easily calculated and is

$$\xi_{\mathbf{k}} = -2t[\cos(k_x a) + \cos(k_y a)] + 4t' \cos(k_x a)\cos(k_y a) - \mu \tag{3.27}$$

The parameters t, t' can either be taken from local density approximation (LDA) calculations or determined by fitting the Fermi surface measured by ARPES. The first approach is based on the observation that the 8-band Hamiltonian describing the copper-oxygen planes in cuprates can be down-folded into a 3-band Hamiltonian of which Eq. (3.27) is the antibonding band [49]. The second approach is explicitly applied in Chapter 5, where the Fermi surface is directly determined from ARPES measurements in an overdoped BSCCO sample.

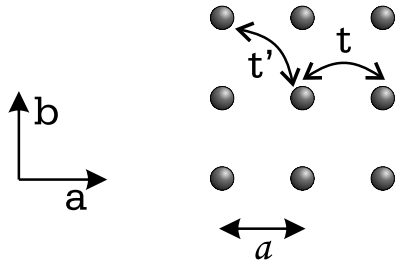

Figure 3.4: *Schematic model for the CuO_2 plane.*

The band structure resulting from Eq. (3.27) is shown in Fig. 3.5; the parameters used for the plot are $t'/t = 0.45$ and $\mu/t = -1.373$, which are typical values for optimally doped samples. In this picture a variation of the doping is modeled by changes of the chemical potential, which has the effect of rigidly shifting the band; for example, a reduction of carrier concentration corresponds to a shift of the band to higher energy values.

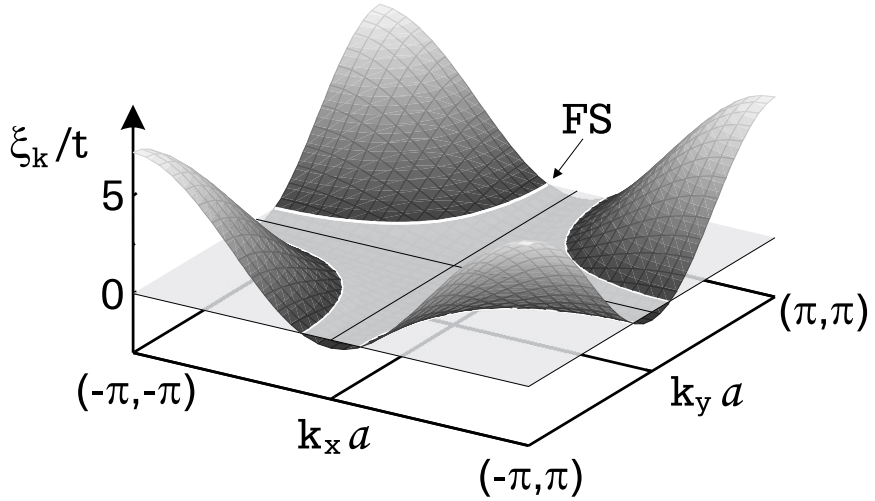

Figure 3.5: *Band structure and Fermi surface (FS) in the tight-binding model of Eq. (3.27). The parameters used for the plot are $t'/t = 0.45$ and $\mu/t = -1.373$ which correspond to a filling characteristic of optimal doping.*

3.6 Symmetry properties of the Raman response

The importance of Raman scattering studies in the investigation of cuprates is due to the fact that the polarization selection rules on the incident and scattered light make Raman scattering a **k**-sensitive probe. In this section the symmetry properties of the Raman vertex and the selection rules will be described.

3.6.1 Raman vertex

The symmetry properties of the Raman vertex are conveniently studied in terms of Brillouin zone harmonics in the expansion of Eq. (3.9) which allows the separation of energy (ω_I, ω_S) and momentum $(\mathbf{k})$ dependences in the function $\gamma_{\mathbf{k}}$. Since the Brillouin zone or Fermi surface harmonics transform according to point group transformations of the crystal, the vertex is conveniently expanded as

$$\gamma_{\mathbf{k}}(\omega_I, \omega_S) = \sum_{L,\mu} \gamma_L^{\mu}(\omega_I, \omega_S)\Phi_L^{\mu}(\mathbf{k}), \tag{3.28}$$

where L marks the Lth-order contribution to the vertex which transforms according to the μth irreducible representation of the point group symmetry of the crystal.

In a tetragonal D_{4h} crystal structure, which applies to most of the cuprates, the lowest order contributions in the relevant symmetries are

$$\begin{aligned} \Phi_{A_{1g}}(\mathbf{k}) &= \text{constant} + \cos(k_x a) + \cos(k_y a) + \ldots \\ \Phi_{B_{1g}}(\mathbf{k}) &= \cos(k_x a) - \cos(k_y a) + \ldots \\ \Phi_{B_{2g}}(\mathbf{k}) &= \sin(k_x a)\sin(k_y a) + \ldots \end{aligned} \tag{3.29}$$

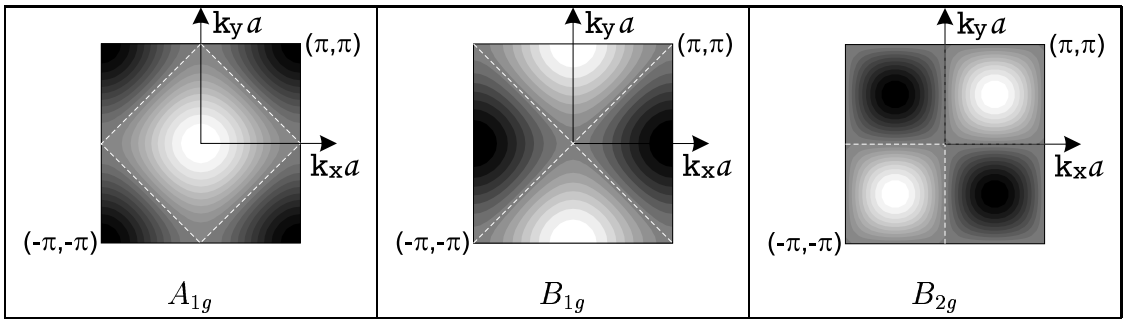

Figure 3.6: *Momentum dependence of the basis functions in the first Brillouin zone: white and black mark maximum positive and negative values respectively; the dashed lines are the points where the scattering amplitude vanishes.*

The **k**-dependence of the basis functions in the first Brillouin zone is best clarified by the contour plots explicitly shown in Fig. 3.6. The positive and negative values are represented by white and black respectively, and the dashed lines mark the points where the scattering amplitude vanishes. From that it is clear that the B_{1g} spectra probes light scattering events along the k_x or k_y axes, B_{2g} probes the diagonals, while A_{1g} is a weighted average over the entire Brillouin zone. By comparison with Fig. 2.10, B_{1g} mainly probes the "hot" electrons on the Fermi surface, while the B_{2g} the "cold" ones. In this manner information about the momentum dependence of the quasiparticle scattering rate can be obtained.

Since the superconducting gap has a strong **k**-dependence (see Sect. 2.5), differences are expected between the various symmetry channels. The B_{1g} channel, possessing the same symmetry of a d-wave gap, is an effective probe of the gap amplitude. The B_{2g}, on the other hand, being most sensitive in the directions where the d-wave gap vanishes, probes the low-lying quasiparticle excitations. The dependence on doping and temperature of the response in the two symmetries is discussed in detail in Chapter 7.

3.6.2 Selection Rules

The Raman vertex symmetry components can be directly projected out by a selection of the polarization orientations of the incident and scattered light [34]. In this work, the reference for the polarization vectors are the copper-oxygen bonds of the CuO_2 planes, being $\hat{x}$ and $\hat{y}$ parallel to the bonds, and $\hat{x}'$ and $\hat{y}'$ at 45°. The connection between linear polarizations and symmetries is shown in Fig. 3.7 for linearly polarized light.

As is clear from Fig. 3.7, the measured intensity is always the sum of two con-

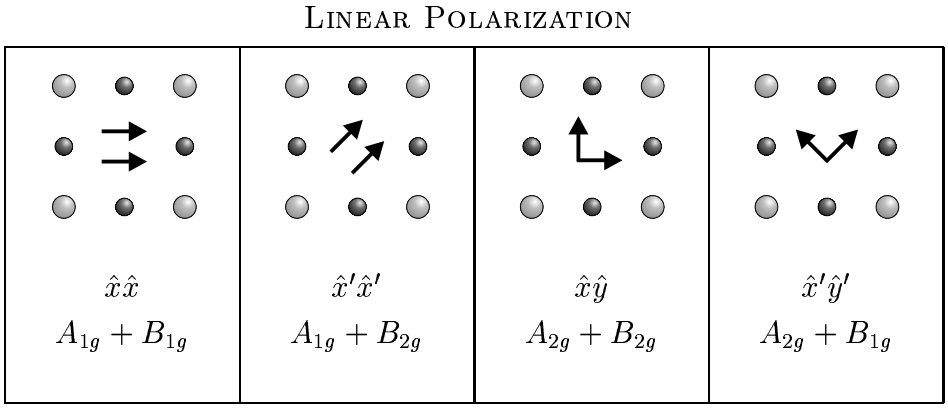

Figure 3.7: *Symmetries which are projected out with different linear polarizations. The arrows represent the polarization vectors of the incident and scattered light.*

tributions, independent of the choice of the polarization configuration. From this set of measurements alone, it is not possible to extract the pure symmetries. The problem has been solved up to now by assuming the A_{2g} component to be negligible and the B_{1g} and B_{2g} symmetries to be projected out with the polarization vectors $\hat{x}'\hat{y}'$ and $\hat{x}\hat{y}$, respectively. This is, however, not generally true and will be discussed in Sect. 8.3. In this work, circular polarization configurations were measured in addition to the linear ones. The combinations of spectra obtained with linearly (Fig. 3.7) and circularly (Fig. 3.8) polarized light allows the extraction of all pure symmetries.

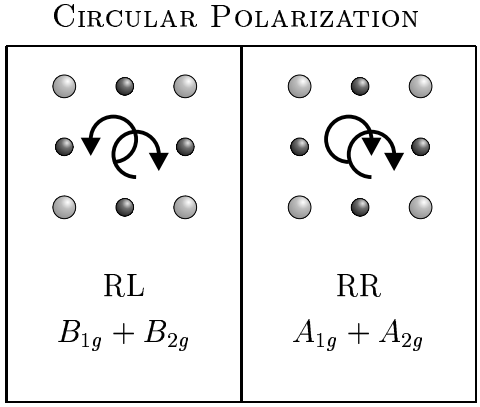

Figure 3.8: *Symmetries which are projected out with different circular polarizations for the incident and scattered light.*

Chapter 4

Samples and experimental details

In this chapter the properties of the compounds analyzed and the details of the experimental apparatus are described. Particular attention is paid to new facilities which were built during this work to anneal and characterize the samples before the Raman measurement. For the Raman apparatus, a new method to adjust appropriately the polarization states of the incident and scattered light was developed. This method allows a precise polarization analysis and the exact determination of all symmetry components of the Raman response.

4.1 Sample preparation and characterization

The availability of high quality single crystals, especially with a variety of doping levels, is a difficult but necessary condition to perform experiments probing intrinsic features. In cuprates, where in most of the cases the highest T_c is achieved at non-stoichiometric compositions, imperfections such as inhomogeneities or impurities strongly modify the observed properties. This motivated the establishment of a method which is practical, simple to use and sensitive enough to check routinely every sample before starting Raman measurements. The knowledge of the quality of the samples is in fact fundamental to interpret correctly the spectroscopic behaviour observed.

The samples studied in this work belong to three different material classes of the hole-doped cuprates: LSCO, YBCO, and BSCCO. In each class, single crystals with different doping levels are analyzed to investigate the dynamics of the carriers in the entire phase diagram. The comparison of the results for different compounds allows a separation of those features common to all cuprate from those specific to a material class.

4.1.1 $La_{2-x}Sr_xCuO_4$

$La_{2-x}Sr_xCuO_4$ (LSCO) is characterized by a body centered tetragonal structure, called the T-structure and shown in Fig. 4.1. The CuO_2 planes, roughly 6.6 Å apart, are separated by two LaO planes which form the charge reservoir. In the crystal the oxygen is in a O^{2-} state, the lanthanum in La^{3+} and, to conserve the charge neutrality, the copper is in a Cu^{2+} state, with a net spin of 1/2. Each copper atom in the conducting planes has an oxygen above and below in the *c*-direction, called apical oxygens. Therefore, in this compound the copper atoms are surrounded by octahedra of oxygens (shown in Fig. 4.1). The dominant bonds are those in the planes, since the Cu-O distance in the c-direction ($\simeq$ 2.4 Å) is larger than in the plane ($\simeq$ 1.9 Å).

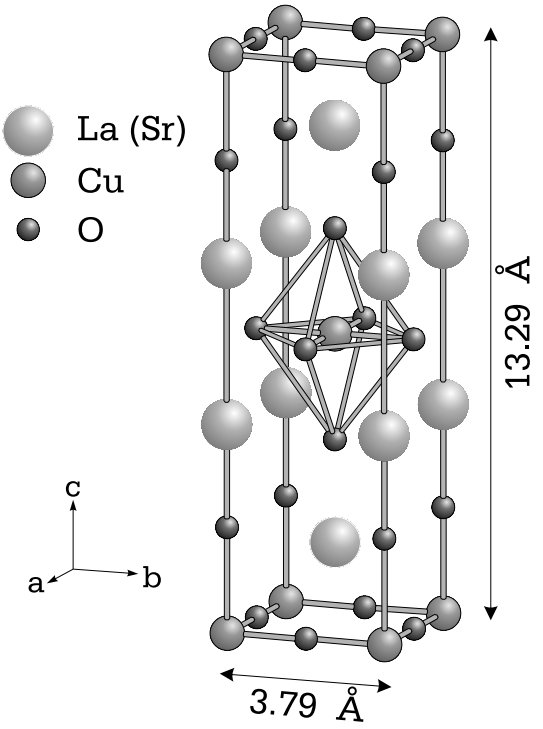

Figure 4.1: *Crystal structure of $La_{2-x}Sr_xCuO_4$.*

The doping is achieved by substituting La^{3+} by Sr^{2+} which results in removing electrons from the CuO_2 planes. For Sr-concentrations between $x \simeq 0.05$ and $x \simeq 0.30$ the material is superconducting [50]; the maximum transition temperature is $T_c \simeq 40$ K found at a doping level $x \simeq 0.15$.

The material undergoes several structural phase transitions. In fact, below a temperature which depends on doping and is approximately 190 K at optimal doping, the copper atoms and the surrounding oxygen atoms move out of their positions and form an orthorhombic structure [51].

In this work three single crystals have been studied: an underdoped (UD), an optimally doped (Opt) and a strongly overdoped non-superconducting (OD) one. All the samples have been prepared and characterized by N. Kikugawa and T. Fujita at Hiroshima University, Japan. The crystals were grown by the traveling-solvent-floating-zone (TSFZ) technique and the Sr content was determined by energy-dispersive X-ray spectroscopy. After polishing, the UD and Opt samples were reannealed in flowing oxygen for 50 hours at 920°C, cooled down to 500°C in 50 hours, and kept for another 50 hours at this temperature. Finally they were cooled

LSCO	T_c	ΔT_c	p	Label
$La_{1.9}Sr_{0.10}CuO_4$	28 K	1 K	0.10	UD
$La_{1.85}Sr_{0.15}CuO_4$	38 K	1 K	0.15	Opt
$La_{1.74}Sr_{0.26}CuO_4$	not SC	-	0.26	OD

Table 4.1: *$La_{2-x}Sr_xCuO_4$ samples studied, with the corresponding transition temperature T_c, transition width ΔT_c, doping level p, and label used in the text.*

down to ambient temperature in 50 hours. This procedure ensured that the crystal surface was strain free. The characteristics of the samples studied are summarized in Tab. 4.1. The transition temperature T_c was determined from the $ab-$resistivity ρ_{ab}, which is shown in Fig. 4.2 for all samples. The transition width ΔT_c corresponds to 10-90% width of the resistivity jump. The doping level p corresponds to the Sr concentration ($p = x$).

4.1.2 $YBa_2Cu_3O_{6+x}$

$YBa_2Cu_3O_{6+x}$ (YBCO) belongs to the class of bilayer materials, since its crystal structure is characterized by two copper-oxygen planes per unit cell, separated by yttrium ions as shown in Fig. 4.3. The intra-bilayer distance ($\simeq$ 3.2 Å) is much smaller than the inter-bilayer one ($\simeq$ 8.2 Å).

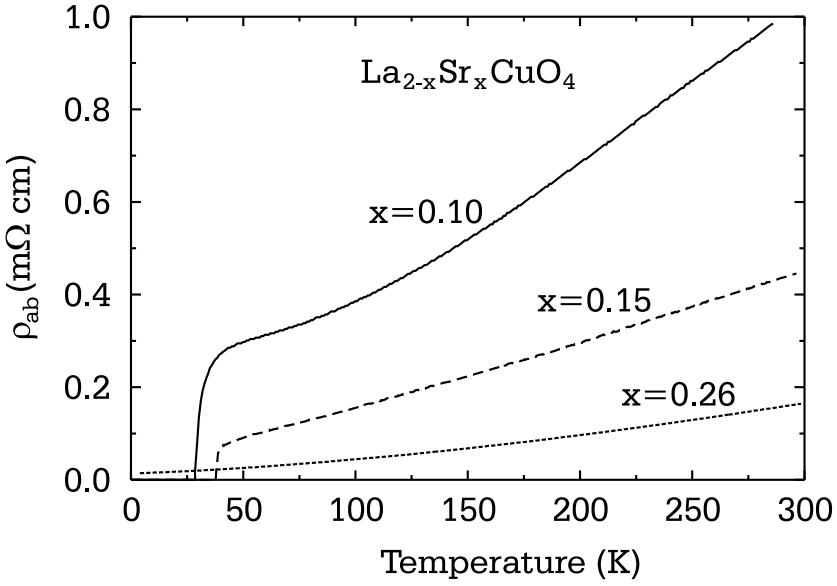

Figure 4.2: *In-plane resistivity ρ_{ab} of the $La_{2-x}Sr_xCuO_4$ samples studied, between 4.2 and 300 K.*

The planar oxygen ions are shifted toward the interior of the bilayer giving rise to a buckling of the CuO_2 planes [52]. The conducting CuO_2 planes are themselves separated by layers of atoms containing barium, oxygen and copper, which act as "charge reservoir".

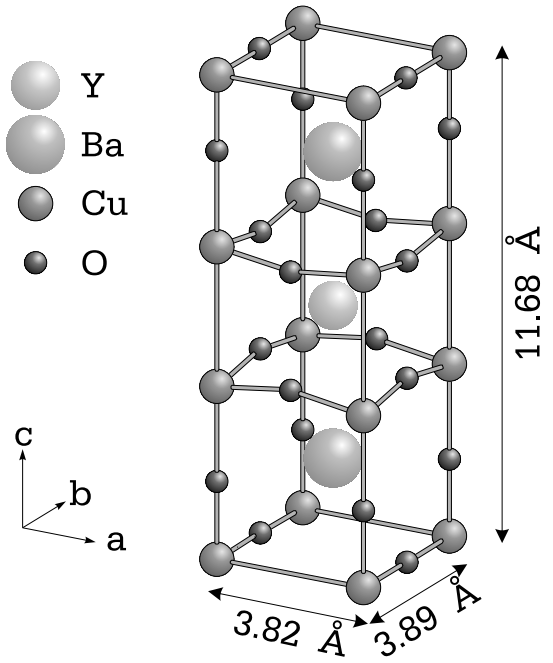

Figure 4.3: *Crystal structure of* $YBa_2Cu_3O_7$.

The number of carriers depends on the oxygen content and can be quantified by the formula $YBa_2Cu_3O_{6+x}$. In the case $x = 1$, the oxygen atoms outside the CuO_2 planes form one dimensional structures along the b direction which are called the "Cu-O chains", as shown in Fig. 4.3. At the minimum oxygen concentration ($x = 0$), no Cu-O chains exist. Then the oxidation states are Y^{3+} for yttrium, Ba^{2+} for barium, Cu^{2+} and Cu^{1+} for copper in the planes and chains respectively, and O^{2-} for oxygen [53].

The concentration of the carriers in the conducting planes is modified by altering the oxygen content in the Cu-O chains: the new oxygen becomes O^{2-} by trapping two electrons from the Cu^{1+} of the chains. Since copper can give only one electron to oxygen, holes are formed in the chains, which are partially filled by electrons of the CuO_2 planes.

For x close to 0 an antiferromagnetic phase is observed. Above $x \simeq 0.4$ ($p \simeq 0.035$) a magnetic transition into a short range antiferromagnetically correlated spin-glass-like state is observed [54]. Above $x \simeq 0.4 - 0.5$ ($p \simeq 0.05$) the superconducting phase develops [55]. The spin glass regime extends into the superconducting state up to $x \simeq 0.6$ ($p \simeq 0.10$). The "optimal" composition, corresponding to the maximal T_c, is close to $x \simeq 0.93$. Near $x \simeq 0.4$ also a structural phase transition occurs, from a tetragonal at lower doping levels, to an orthorhombic phase at higher concentrations [56], similar to what is found in $La_{2-x}Sr_xCuO_4$. In this structural transition the conduction planes CuO_2 are almost unaffected.

The YBCO single crystals measured in this work were prepared and characterized by A. Erb at the DPMC, University of Geneve, Switzerland. They were grown in the inert crucible material, $BaZrO_3$, technique which enables one to reach the highest purity [57]. The samples studied and their properties are summarized in Tab. 4.2.

YBCO	T_c	p	Label
$YBa_2Cu_3O_6$	-	0	AF
$YBa_2Cu_3O_{6.93}$	93.5 K	0.16	Opt

Table 4.2: *$YBa_2Cu_3O_{6+x}$ samples studied with the corresponding transition temperature T_c, doping level p, and label used in the text.*

The doping level p is determined from the measured T_c using the empirical formula [58]

$$T_c = T_c^{max}[1 - 82.6(p - 0.16)^2] \tag{4.1}$$

where T_c^{max} the highest T_c obtainable in the material.

4.1.3 $Bi_2Sr_2Ca_{1-x}Y_xCu_2O_{8+\delta}$

BSCCO belongs to the family of bismuth-based cuprates, whose general formula is $Bi_2Sr_2Ca_{n-1}Cu_nO_{2n+4+\delta}$, where $n = 1, 2$ or 3 corresponds to one, two or three CuO_2 planes sandwiched between Bi-O insulating bilayers. In this work the compound with $n = 2$ has been studied.

The crystal structure is shown in Fig. 4.4 in a simplified form, since the long range modulation in the b direction is neglected. Note that the Cu-O bonds are not parallel to the crystal axes, but rotated by an angle of $\sim 45°$. As a consequence of the complex structure, BSCCO has the strongest anisotropy in transport properties between in-plane and out-of-plane behaviour. The Bi-O double layers play a similar role as the Cu-O chains in YBCO, in that they act as a charge reservoir. Because of the rich structure, the doping adjustment, which is achieved by changing the oxygen content δ, is more critical. To access the underdoped region of the phase diagram the calcium atoms (Ca^{2+}) between the CuO_2 planes can be substituted by yttrium (Y^{3+}).

As-grown $Bi_2Sr_2CaCu_2O_{8+\delta}$ samples are typically close to the optimum doping, and oxygen-annealing can be used to vary the oxygen content and therefore the carrier concentration. The excess oxygen atoms are incorporated in the BiO plane, resulting in remarkable superstructure modulations.

In contrast to the previous classes BSCCO can easily be cleaved to obtain fresh surfaces because the bonds between the Bi-O layers are weak.

The single crystals studied in this work cover a wide doping range and are listed in Tab. 4.3. p was determined from the measured T_c as described for the YBCO samples.

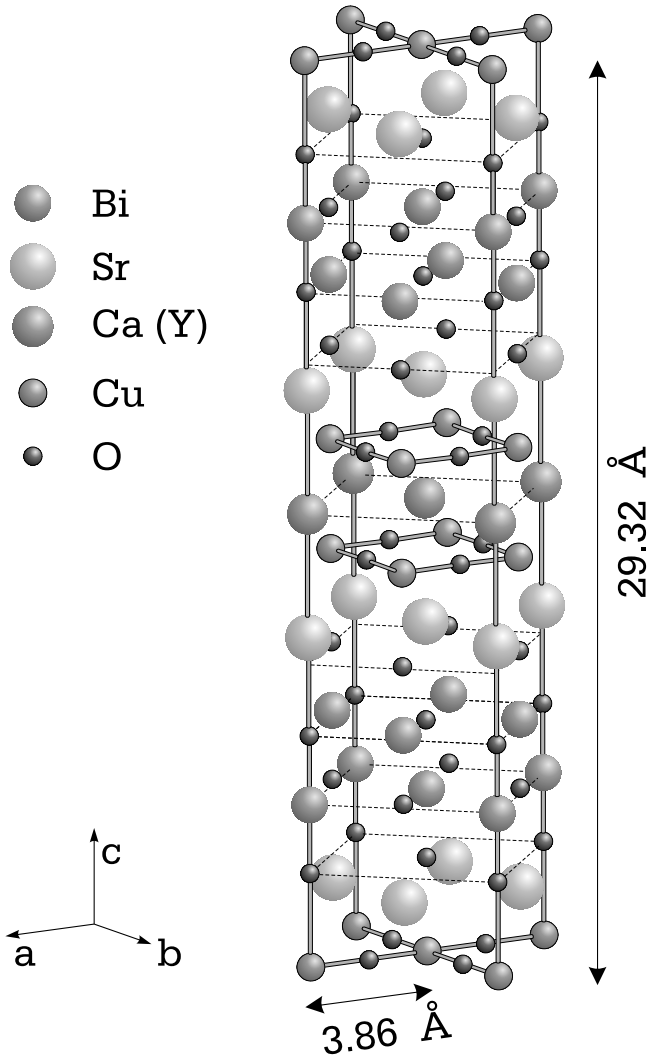

Figure 4.4: *Crystal structure of* $Bi_2Sr_2Ca_{1-x}Y_xCu_2O_{8+\delta}$.

The antiferromagnetic sample (AF) was grown with a flux method in a ZrO_2 crucible by H. Berger at the EPFL in Lausanne, Switzerland. The optimally doped sample (Opt95) was grown by Y. Ando, at the CRIEPI, Tokyo, Japan, with the TSFZ method. The as-grown material had a superconducting transition of $T_c = 86$ K, but showed superconductivity up to 112 K, possibly indicating an admixture of a trilayer phase. The sample was annealed in this work as described in Sect. 4.1.4, and a $T_c = 95$ K was achieved.

The optimally doped Opt92 and the overdoped OD78 were grown by the same method and characterized by B. Revaz, at the DPMC, University of Geneva, Switzerland. OD78 is a particularly homogeneous sample with a $T_c = 77.8$ K and a transition width of only 0.2 K. From this sample two pieces were cut and annealed for seven days at 350°C in oxygen pressures of 260 bar and 1400 bar, respectively. As

BSCCO	T_c	p	Label
$Bi_2Sr_2YCu_2O_{8+\delta}$	-	0	AF
$Bi_2Sr_2CaCu_2O_{8+\delta}$	95 K	0.16	Opt95
$Bi_2Sr_2CaCu_2O_{8+\delta}$	92 K	0.16	Opt92
$Bi_2Sr_2CaCu_2O_{8+\delta}$	77.8 K	0.20	OD78
$Bi_2Sr_2CaCu_2O_{8+\delta}$	65 K	0.22	OD65
$Bi_2Sr_2CaCu_2O_{8+\delta}$	62 K	0.22	OD62
$Bi_2Sr_2CaCu_2O_{8+\delta}$	56 K	0.23	OD56

Table 4.3: *$Bi_2Sr_2Ca_{1-x}Y_xCu_2O_{8+\delta}$ samples studied with the corresponding transition temperature T_c, doping level p, and label used in the text.*

a result, two more strongly overdoped samples were obtained, OD62 and OD56, with $T_c \simeq 62$ K and $T_c \simeq 56$ K, respectively. The overdoped OD65 sample was obtained from an as-grown sample prepared with the TSFZ method by B. Revaz, also annealed for four days at 350° C in an oxygen pressure of 1400 bar. The heat treatment conditions for the samples annealed during this work are summarized in Tab. 4.4.

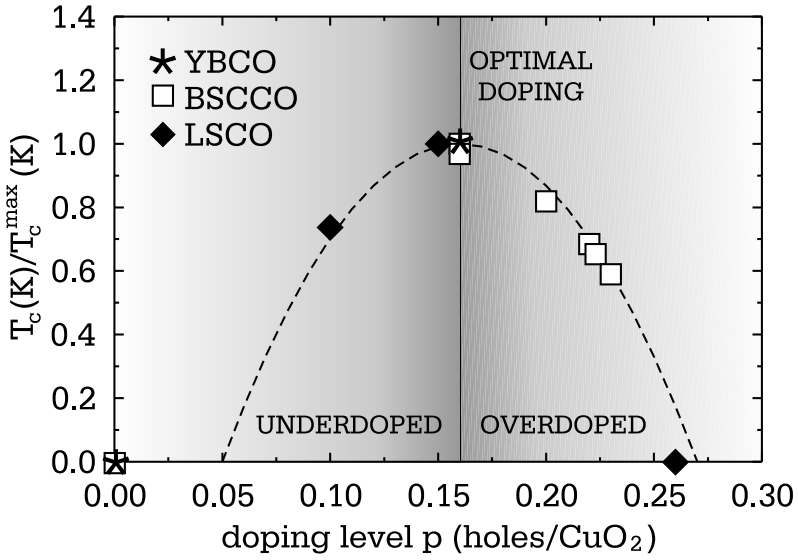

Figure 4.5: *Doping levels and corresponding critical temperatures scaled by the maximal value of each material class for all the studied samples. The dashed line represents the empirical law of Eq. (4.1).*

In Fig. 4.5 are shown the characteristics of all the samples studied. The T_c divided by T_c^{max} of each material class is plotted as a function of the doping level p. The dashed line represents the empirical law of Eq. (4.1).

4.1.4 Annealing of the crystals

In this work many BSCCO single crystals were studied since a wide range of the phase diagram is accessible. By varying the conditions of the sample preparation like annealing temperature, oxygen partial pressure, and cooling procedure different doping levels are obtained.

The "as-grown" samples have normally critical temperatures which are below the maximal value and sometimes show inhomogeneous phases; to reach the highest T_c, which corresponds to optimal doping, the samples must be annealed for a few days in air at high temperatures. Different hole concentrations can be obtained by annealing the samples in oxygen atmosphere under appropriate conditions. A detailed analysis of the properties of BSCCO pellets after different annealing procedures was performed in Ref. [59] and is shown in Fig. 4.6. The lines represent iso-T_c lines. Full and open squares mark individual samples; the grey areas represent regions where the crystal structure is not stable.

For single crystals a similar study is not existing, partly because the interplay of oxygen concentration and cation composition is not yet completely clarified. It is in

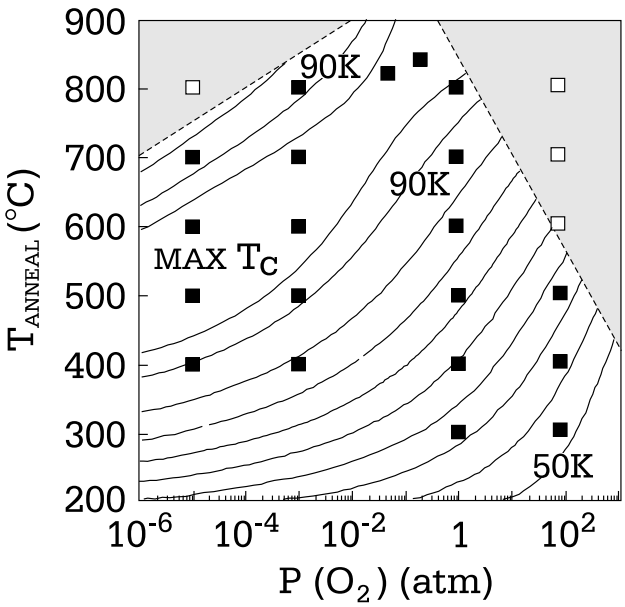

Figure 4.6: *Investigation of the properties of BSCCO pellets for different oxygen pressures and quenching temperatures from Ref. [59]. The lines represent iso-T_c lines and are spaced 5 K from 50 K to 90 K and 2.5 K above 90 K. Full and open squares mark samples which resulted superconducting and non superconducting, respectively; the grey areas indicate regions where the superconducting phase is not stable.*

Sample	Time	Temperature	O_2 pressure
Opt95	3 days	850°C	in air
OD65	4 days	350°C	1450 bar of O_2
OD62	7 days	350°C	260 bar of O_2
OD56	7 days	350°C	1400 bar of O_2

Table 4.4: *Heat treatment for the annealing of the various sample studied, indicating the sample label, the time of annealing, temperature maintained and the estimated pressure inside the annealing cell.*

fact observed that sometimes the annealing process modifies the samples irreversibly, especially in the underdoped range. In particular, samples annealed in oxygen or argon to reach underdoping result often damaged, probably because the oxygen is taken out of the CuO_2 planes rather then out of the charge-reservoir. For this reason underdoping is mainly achieved by Y substitution [60].

The annealing at high oxygen pressure was performed in a cell made of SWAGELOK® components. The cell with the samples inside was plunged into liquid oxygen, filled with O_2, closed and tightened in the liquid. By warming the cell, the oxygen becomes gaseous and the sample is in oxygen atmosphere. The estimated pressure at 350°C inside the cell is approximately 1800 bar. The annealing pressure is more accurately determined by measuring the volume of the gas contained in the cell when reopening it at room temperature after the heat treatment. Typical oxygen pressures inside the cell at 350°C are roughly 1400 bar. In one case, when the cell was made of used components, part of the oxygen gas was lost upon warming the cell; in this case a pressure of only 260 bar was obtained. The heat treatment conditions for the annealing of the various sample are summarized in Tab. 4.4.

To investigate the results of the annealing procedure and characterize the samples it is necessary to have a fast, easily operated and quite sensitive method for the measurement of the critical temperature. In the next section the method and the apparatus built during this work will be described.

4.2 T_c measurement

For the analysis of sample properties before and after the annealing process a new experimental setup has been built during this work. The method used was introduced originally to measure the critical current density J_c and the transition

temperature T_c in high-transition temperature oxides [61]. Its main advantage for our purposes is to be contactless, so it leaves the surface to be later measured by light scattering unaffected. This method is preferable to the simple susceptibility measurement, because its higher sensitivity allows the measurement of a signal at the superconducting transition also in samples of sub-millimeter dimensions. In addition, it allows a probing of sample inhomogeneities which could arise, for example, from a too short annealing process.

The method consists in measuring the third harmonic component of the *ac*-susceptibility of the sample when immersed in a sinusoidal electromagnetic field. The non linear components of the *ac*-susceptibility are a measure of the losses induced by flux motion in a type-II superconductor. Above T_c, the nonlinear response is vanishingly small; well below T_c the critical current J_c is greater than the current induced by the ac magnetic field in the sample. In this regime, the dissipation is small and the third harmonic is again too small to give a detectable contribution. Close to T_c however, J_c drops to zero and a hysteresis occurs in presence of an alternating magnetic field. The surface losses due to hysteresis generate then an anharmonic signal.

4.2.1 Methodology

The existence of anharmonic components of the *ac*-susceptibility can be understood in terms of the Bean model [62] for type-II superconductors which is based on the assumption that there exists a limiting constant macroscopic superconducting current density J_c: any electromotive force due to an applied magnetic field, however small, will induce this full current to flow locally.

The flux density profiles in a slab of thickness d when a small alternating field H_{ac} is applied parallel to the surface are shown in Fig. 4.7. In the state marked by (1) no magnetic field is applied and no current flows in the material. When a small field is applied, a current density flows in a surface layer so that the internal local field is reduced to zero (2). At this stage vortices are created due to the applied magnetic field. A further increase of the field to its maximum value H_3 (3) will produce a bigger region of penetrating field in the sample. When the field is reduced, the direction of the current density is reversed at the surface. At the time the field reaches the zero value again (4), the trapped field inside the vortices causes the current density to be different from zero. The existence of a hysteresis, and of the associated irreversibility, generates the higher harmonics, including therefore the third, in the *ac*-susceptibility.

The derivation of the harmonic components is not straightforward and depends

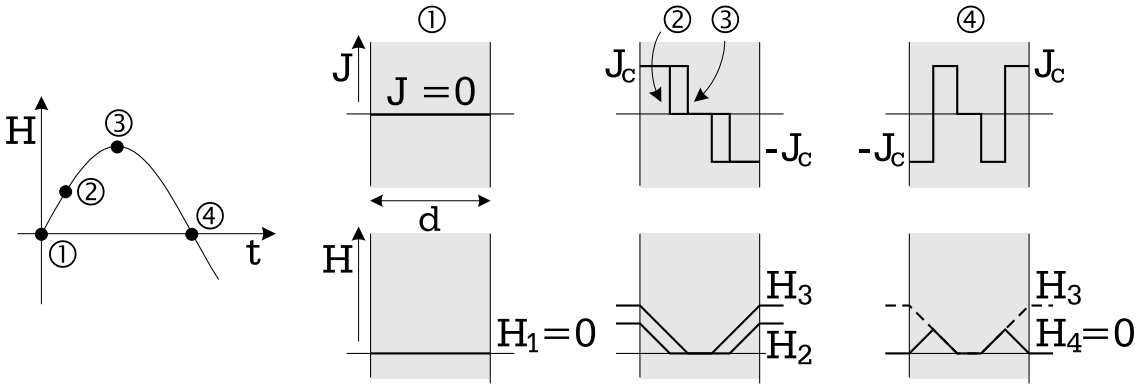

Figure 4.7: *Current density and local field in a slab when a small alternating field H_{ac} is applied parallel to the surface.*

on the model for the pinning forces in the sample. Here the derivation of Shatz *et al.* [63] is considered, where the effect of a small external *ac*-field H_{ac} on a type-II superconductor immersed in a *dc*-field H_{dc} is derived. The magnitude of the third harmonic χ_3 of the *ac*-susceptibility is

$$|\chi_3| \propto \delta(H^*)\ \theta(1-\delta(H^*)) + \frac{1}{\delta(H^*)}\sqrt{\frac{20}{\delta^2(H^*)} - \frac{44}{\delta(H^*)} + 25}\ \theta(\delta(H^*)-1) \qquad (4.2)$$

where $\theta(x)$ is the Heavside function, and $\delta(H^*)$ is a parameter which measures the extent of penetration of the field into the material. It therefore depends on H^*, the local field inside the sample, which is given by $H^* = 4\pi a J_c/c$ with J_c the critical current density, $2a$ the width of the slab and c the speed of light. The analytical expression of $\delta(H^*)$ depends on how the pinning forces are modelled; the simplest form is the one given by the Bean model, $\delta(H^*) = H_{ac}/H^*$.

From Eq. (4.2) it is clear that $|\chi_3|$ is the sum of two components, one proportional to δ and therefore inversely proportional to the internal field H^* for low values of the applied field H_{ac}, and one inversely proportional to δ and therefore linear in H^* for values of the applied field greater than H^*.

For the specific measurements performed in this work, it is of interest to understand the temperature dependence of $|\chi_3|$. The temperature dependence of J_c can be approximated in a two fluid picture [64] as

$$J_c(T) = \left[1 - \left(\frac{T}{T_c}\right)^2\right]\left[1 - \left(\frac{T}{T_c}\right)^4\right]^{1/2}. \qquad (4.3)$$

In Fig. 4.8 the dependence of the third harmonic component for various $H^*(T = 0)/H_{ac}$ on the normalized temperature T/T_c is plotted using Eq. (4.2) and Eq. (4.3).

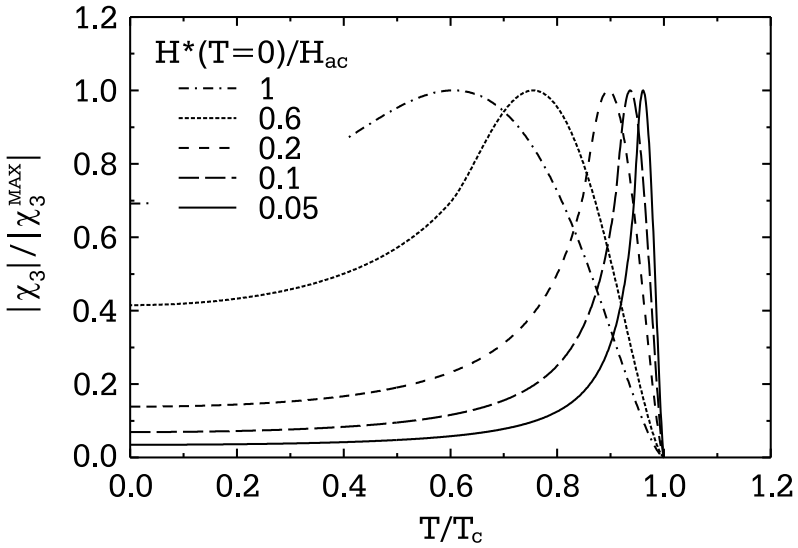

Figure 4.8: *Temperature dependence of $|\chi_3|$ for various values of the applied ac field within the Bean model.*

From Fig. 4.8 it is clear that for any $H^*(T = 0)/H_{ac}$ the critical temperature is marked by the onset of the anharmonic signal. This will be used as the criterium for the determination of T_c in all the samples characterized.

The physical origin of the peak may be understood by considering the ratio between the amplitude of the alternating field H_{ac} and the difference between the local fields in the middle and at the surface of the sample. When this ratio is small, the alternating field does not penetrate much into the sample; the whole signal is small and so are its harmonics. Any increase of this ratio will result in a larger signal. However, beyond a certain point the alternating field penetrates the whole sample and the signal reaches its maximum possible value. Any further increase of the ratio will not change the signal, but the resulting normalized harmonics (relative to H_{ac}) will be smaller. In the framework of the Bean-model we can understand this feature as follows. For $H_{ac} < H^*$ at $T < T_c$ J_c is large. As the temperature increases, the amplitude of the third harmonic χ_3, being proportional to the inverse of J_c, should increase since J_c decreases with increasing temperature. But as the temperature approaches T_c, the critical current becomes very small causing H^* to become much smaller than H_{ac}, so that the nth component χ_n becomes proportional to H^*. As a result, χ_n should decrease with $J_c(T)$ near T_c, and we should expect a peak somewhere near the transition temperature.

4.2.2 Experimental setup

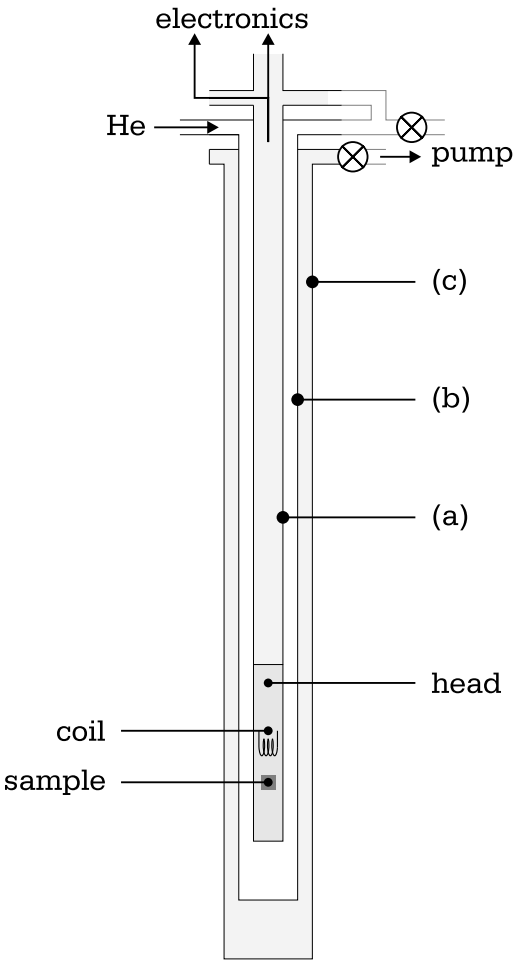

Figure 4.9: *Schema of the cryogenic apparatus used for the measurements of the critical temperature. (a), (b), (c) are three stainless steel tubes.*

When planning the setup, its applicability in an ultra-high vacuum (UHV) environment was considered. In fact, in later development, the setup with only minor modifications can be used for in-situ characterization of samples in an already existing UHV chamber for Raman measurements. For this reason, among different possible configurations a "self-inductance" geometry with only one coil placed in proximity to the samples, was selected.

The schema of the experimental setup is shown in Fig. 4.9. The dip stick is designed for use in a He transport vessel. The sample is attached to a copper head fixed at the end of a stainless steel tube (a). Two other concentric tubes, (b) and (c), allow the different volumes to be evacuated separately. To avoid thermal oscillations and to reach an equilibrium between the sample and the environment, the adjustment of the cooling power during the sweeps is quite critical. The inner most volume is generally filled with He as

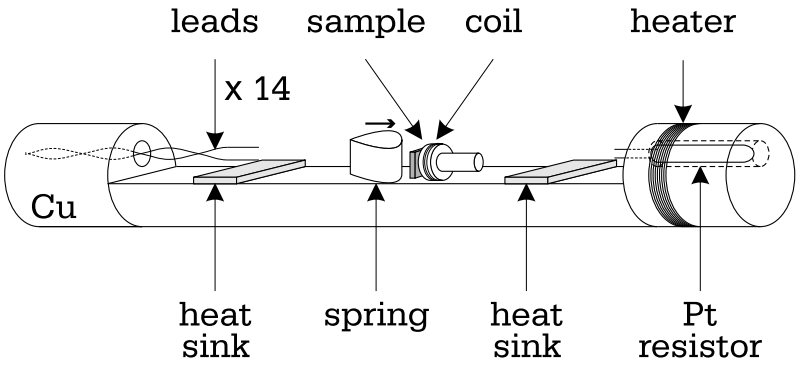

Figure 4.10: *Detail of copper head of the setup used for the measurement of T_c.*

a contact gas. In principle such volume can be filled with He and pumped in order to reach temperatures below 4.2 K. The outer volume is either evacuated for thermal insulation or filled with low pressure gas for cooling.

On the copper head (Fig. 4.10) the heat sinks for the electric leads, the coil on which the sample is pressed by a capton spring, and a heater, made of a twisted pair of manganin wires, are placed. The temperature is measured by a platinum resistor inserted into a hole and fixed with an stainless steel spring.

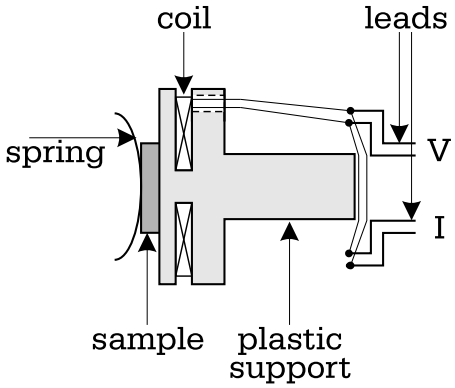

Figure 4.11: *Detail of the sample and coil mounting.*

The sample is pressed against a pancake-coil (Fig. 4.11). The coil is made of 140 turns of 66 μm wire, wound by filling in a groove in plastic (vespel) support. This guarantees the stability of the coil, since glues like GE varnish cannot be used if this setup has to be used in UHV. To have a good signal to noise ratio it is important that the coupling between the coil and the sample is maximized. With the sample pressed on the plastic support the distance between the coil and sample is approximately 0.5 mm.

The leads carrying the current to the coil and the heater are copper wires with a diameter of 0.1 mm; all the others are manganin wires of the same diameter. Generally twisted pairs are used. The leads carrying the high frequency signal to and from the coil are inside separate German silver tubes over the entire length to screen the high frequencies used.

The electronic setup is shown in Fig. 4.12. The sinusoidal potential that drives

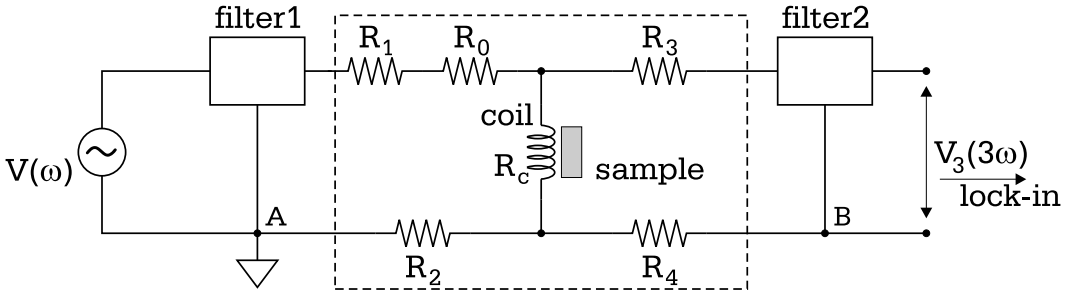

Figure 4.12: *Schema of the electronic setup used for the T_c measurements. $V(\omega)$ and $V_3(3\omega)$ are the exciting and measured voltages, respectively. R_1-R_4, R_0 and R_c are resistances, and A and B mark two points were the ground of the circuit can be disconnected.*

the coil is generated by the internal generator of a lock-in amplifier Stanford SR810. The frequency of the excitation signal selected was $\omega = 33.31$ kHz and its amplitude between 0.1 and 0.5 V. The output of the generator has to be filtered (filter 1) to suppress the higher harmonic components which are emitted together with the ground wave. This is particularly important because the measured signals are in the range from some tens of nV to a few μV depending on the size of the sample. The second filter (filter 2) is a Q-filter which allows only the frequency 99.94 kHz to pass and has a rejection of the fundamental frequency greater than 140 dB. This reduces considerably the signal at the entrance of the lock-in and allows the use of high sensitivities without saturating the internal amplifier of the lock-in.

The resistance of the Cu wires, represented as R_1 and R_2 in Fig. 4.12, is 52 Ω; that of the manganin wires, R_3 and R_4, is 176 Ω. In series with the resistance of the incoming wire there is a resistance $R_0 = 27$ Ω on which most of the potential drop is expected to happen. The coil has a resistance $R_c = 6.0$ Ω.

The insulation of the electronic circuit from the noise of the net and the grounding of the different electronic instruments is particularly important in this measurement, due to low level of the signal arising from the typically 0.5 mm$^2\times$ 0.05 mm size of the samples. For this reason the ground of the circuit can be broken at two points, A and B in Fig. 4.12. By careful filtering the non-linearity of the function generator the noise level can be reduced below 50 nV, achieving a signal to noise of ~ 40.

The temperature sweeps are performed using an ITC503 Oxford Instruments temperature controller, which allows the range and duration of the sweep to be programmed with good accuracy. The proper measurement of the temperature dependence of the third harmonic signal requires also that the cooling rate is not too high and thermal equilibrium of the sample with the environment has to be achieved. In case the temperature sweep is too fast the third harmonic curves show a strong hysteresis during the thermal cycle which can be as large as 5 K. Therefore, a fast sweep with a rate of 1 K per 30 s is performed initially to identify the approximate transition temperature, and afterwards the actual measurements are performed with a slower sweep of 1 K per min in a small window around the T_c. Then the hysteresis is negligible.

4.2.3 Sample measurements

In this section, the measurements for the optimally doped BSCCO sample Opt95 are described. In Fig. 4.13 the absolute value of the signal at 3ω is shown for two different excitation voltages applied to the coil, 0.5 and 0.2 V. The critical

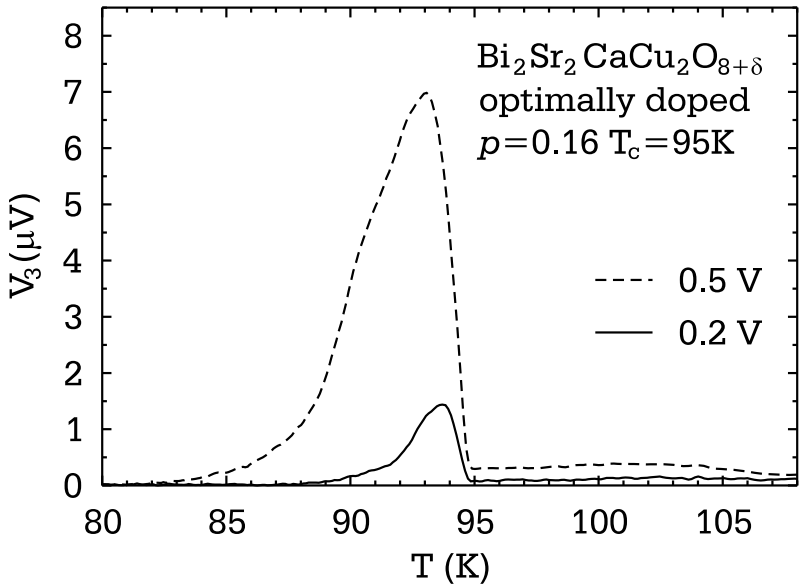

Figure 4.13: *Third harmonic signal for the optimally doped Opt95 BSCCO as a function of temperature for two values of the applied voltage to the coil.*

temperature of the sample is 95 K and the sharpness of the onset demonstrates the homogeneity and the good quality of the crystal. As expected (Fig. 4.8), the third-harmonic signal rises abruptly as the sample is cooled below T_c. The increase in magnitude of $|\chi_3|$ with increasing H_{ac} reflects the increase in nonlinearity, including hysteresis, in the magnetization as a function of field.

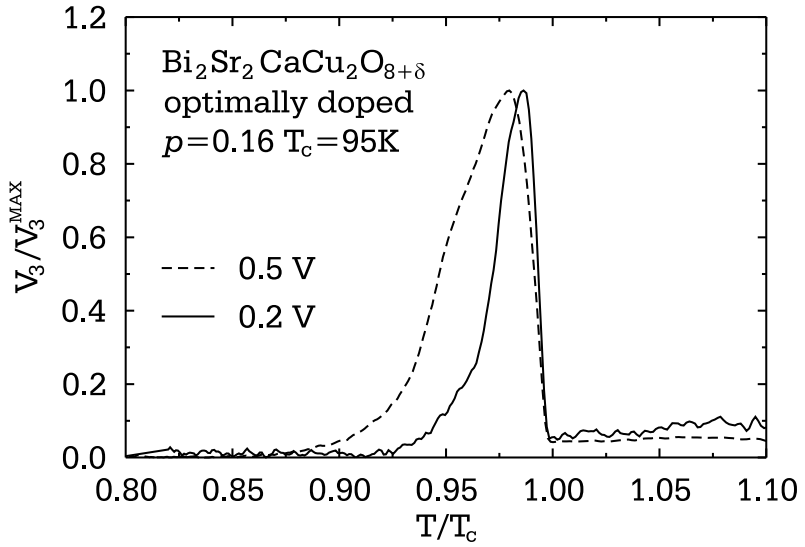

Figure 4.14: *Third harmonic signal for the optimally doped Opt95 BSCCO normalized to the maximum as a function of reduced temperature for two values of the applied voltage to the coil.*

The two curves are best compared if the data are divided by the respective maximum value of the $|\chi_3|$ and plotted as a function of the reduced temperature, as shown in Fig. 4.14. As predicted (Fig. 4.8), the temperature at which the signal first appears does not change with the magnitude of the applied field. The curve itself, however, becomes broader and the maximum shifts to lower values when H_{ac} is increased. Therefore, although the total signal is lower, it is preferable to use a small excitation signal.

4.3 Setup for the Raman experiments

The optical setup for Raman measurements is schematically shown in Fig. 4.15. The

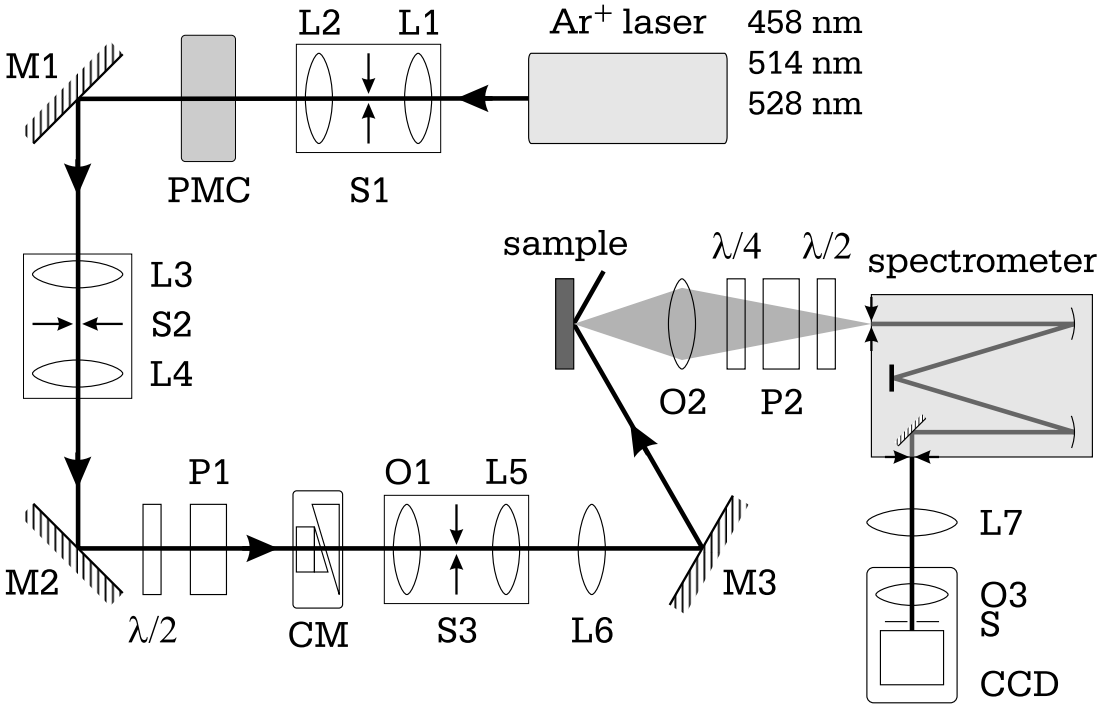

Figure 4.15: *Schema of the Raman experimental setup. L1-L7 are achromatic lenses; S1-S3 pin-holes or slits; PMC is a prism-monochromator; M1-M3 mirrors, P1-P2 polarizers; CM compensator; O1-O3 objectives; S shutter.*

light source is an Ar^+ ion laser, Coherent Innova 304. Different lines of the laser at 458 nm, 514 nm and 528 nm have been used to investigate the dependence of the inelastically scattered light upon the excitation energy. In addition, measurements at 647 nm have been performed using the light emitted by a Kr^+ ion laser, Coherent Innova 400.

A first spatial filter, composed of two achromatic lenses with focal lengths $f =$ 30 mm (L1) and $f = 50$ mm (L2) and a pin-hole with diameter 30 μm (S1), is used. As a result, the contribution of the plasma radiation from the laser tube, which is characterized by a much higher divergence as compared to the coherent laser mode, is eliminated. A finer spectral filtering can then be achieved by the prism-monochromator (PMC). An adjustable slit (S2) between two achromatic lenses both with $f = 100$ mm (L3 and L4) allows the rejection of the undesired lines which differ from the laser line by more than 30 cm^{-1}.

With a Glan-Thompson polarizer (P1) it is possible to prepare strictly linearly polarized light. The $\lambda/2$-retardation plate placed just before the polarizer rotates the polarization of the outcoming laser light and allows adjustment of the power incident on the sample. In order to make the spectra directly comparable, it is important that the power absorbed by the sample is independent of the polarization configuration. A precise adjustment of the polarization of the light incident on the sample is achieved with a Soleil-Babinet compensator (CM) described in more detail in Sect. 4.4.3.

An additional spatial filter, composed of a microscope objective lens (Spindler and Hoyer, $\times$10) (O1), a pin-hole with diameter 20 μm (S3), and an achromatic lens with focal length $f = 30$ mm (L5), is finally used to obtain a homogeneous Gaussian beam. The light is then focussed on the sample surface with another achromatic lens with $f = 250$ mm (L6). The angle of incidence of the beam is adjusted according to the optical constants of the sample so to have minimum reflected intensity for parallel polarized light.

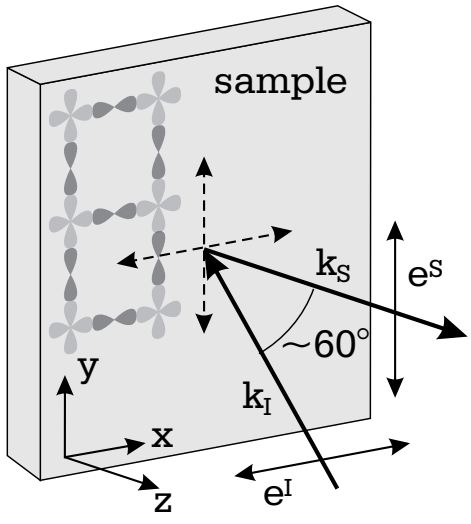

Figure 4.16: *Detail of the sample orientation and polarization adjustment.*

The sample is placed in a cryopumped vacuum of $\approx 5 \times 10^{-7}$ mbar of a He-flow cryostat. Through the thermal contact with a cold finger it is possible to maintain the sample at temperatures between 1.8 K and 330 K. The temperature is measured by a Si diode on the sample holder. More details of the cryogenic equipment can be found in reference [65].

The correct alignment of the sample is fundamental to exploit properly the Raman selection rules. For this reason, a Laue image is taken after mounting the crystal on a gold-plated sample holder, so that the sample can

be placed with the Cu-O bonds parallel or at 45° with respect to the xyz laboratory frame (Fig. 4.16). The incoming polarized light hits the surface at an angle of incidence of approximately 60°; the light reflected by the sample is absorbed by a beam stopper.

In Fig. 4.16 an example of the measuring geometry is shown: the polarizations of the incident and of the scattered light are along the x and y directions, respectively, corresponding therefore (see Sect. 3.6.2 and Fig. 3.7) to the $A_{2g} + B_{2g}$ symmetry components.

The inelastically scattered light is collected by a camera objective (O2) (Minolta, $f = 58$ mm, 1:1.4). The selection of the polarization of the scattered light is achieved by a $\lambda/4$-retardation plate and a second polarizer (P2). For linear polarizations, the retardation plate is not necessary and is therefore oriented with its fast or slow axis parallel to the transmission axis of the polarizer P2. However, when circular polarizations are of interest, the retardation plate is used to transform the circular polarization into a linear one. An additional $\lambda/2$-retardation plate in front of the entrance slit of the spectrometer rotates the linearly polarized light into the direction of maximal transmission of the spectrometer.

The spectrometer is a Jarrel-Ash 25-100 double monochromator with the gratings mounted in the Czerny-Turner configuration. The two monochromator stages are symmetrical and subtractively coupled (Fig. 4.17). The light focussed on the

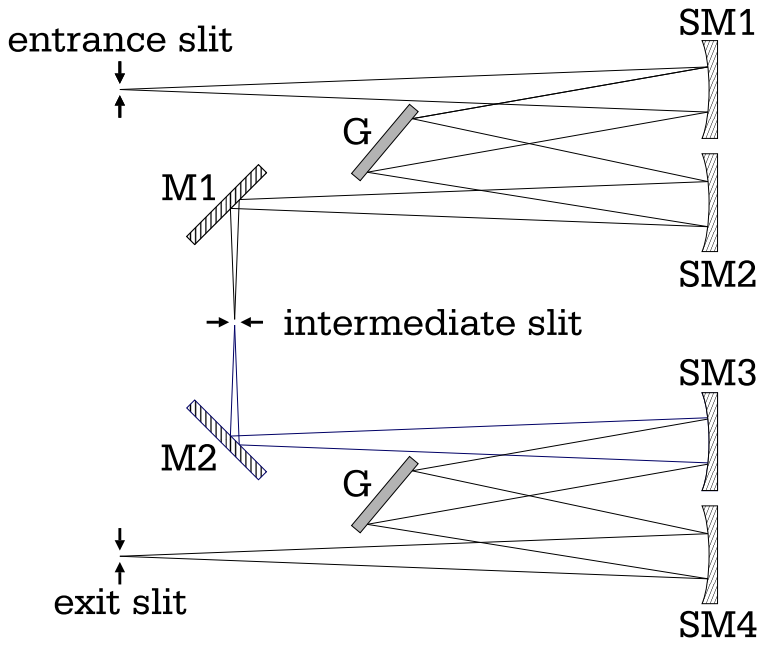

Figure 4.17: *Double monochromator used for the Raman measurements; SM1-SM4 are spherical mirrors, M1-M2 plane mirrors and G gratings.*

entrance slit is collimated by the first spherical mirror (SM1) and reflected as parallel light on the grating (G). The dispersed light is collected by the second spherical mirror (SM2) and focussed on the intermediate slit to enter the second identical stage.

The light outcoming from the exit slit is focussed by an achromatic lens with focal length $f = 200$ mm (L7) and a camera objective (O3) (Nikon, $f = 50$ mm, 1:1.18) on the CCD chip (Tektronix TK-512), cooled by liquid nitrogen to -110°C. Since the scanning spectrometer is operated in subtractive mode, the detection is single-channel and the CCD is virtually used as a photomultiplier. The advantage over the latter is that for long-time acquisition the signal-to-noise ratio is much higher because the read-out noise being the main source does not increase with the acquisition time.

The intensity of the spectra is given in units of photon counts per second (cps) normalized to the power absorbed by the sample. The temperatures reported in this work have been corrected for the heating of the sample due to the absorption of the laser light. For details of the determination of the sample temperature see [34, 65]. The total intensity is subject to variations because of several sources not sufficiently controllable, such as the influence of adsorbed surface layers. To correct for these effects, the spectra are adjusted so to coincide between 800 and 1000 cm^{-1}. This procedure is justified by the temperature independence of the mean value of the scattered intensity in this spectral range [30].

4.4 Polarization analysis

As introduced in Chapter 3, the capability to probe different symmetries is achieved by adjusting the polarization states of the incoming and scattered light. However, independent of the polarization state selected, the light is always a sum of two different symmetries and without a complete set of polarization configurations it is not possible to extract the pure symmetries (see Sect. 3.6.2). Up to now the extraction of the different contributions has been based on the assumption that the A_{2g} symmetry is not active in cuprate materials [66]. However, inconsistencies in the high energy analysis of the Raman spectra [30], together with the proposal of chiral excitations in cuprate superconductors [67, 68] have motivated a more detailed polarization analysis.

The proper adjustment of the polarization state is a challenging task because it requires the knowledge of the optical properties of the material and of the effects induced by the optical components in the light path before the sample. These are in

fact necessary elements to finally calculate the polarization state inside the sample.

4.4.1 Electrodynamics of metals

The propagation of the electromagnetic field into the sample can be studied by modeling it as a metal, and considering the Fresnel formulas for the transmitted and reflected waves [69]. Given an incident plane wave, with $A_{\parallel}$ and $A_{\perp}$ the amplitude components of the electric field parallel and perpendicular to the plane of incidence, respectively, the amplitudes of the transmitted wave are

$$\begin{cases} T_{\perp} &= \dfrac{2n_1 \cos\theta_1}{n_1 \cos\theta_1 + \hat{n}_2 \cos\theta_2} A_{\perp} \\ T_{\parallel} &= \dfrac{2n_1 \cos\theta_1}{\hat{n}_2 \cos\theta_1 + n_1 \cos\theta_2} A_{\parallel} \ , \end{cases} \tag{4.4}$$

and of the reflected wave

$$\begin{cases} R_{\perp} &= \dfrac{n_1 \cos\theta_1 - \hat{n}_2 \cos\theta_2}{n_1 \cos\theta_1 + \hat{n}_2 \cos\theta_2} A_{\perp} \\ R_{\parallel} &= \dfrac{\hat{n}_2 \cos\theta_1 - n_1 \cos\theta_2}{\hat{n}_2 \cos\theta_1 + n_1 \cos\theta_2} A_{\parallel} \ . \end{cases} \tag{4.5}$$

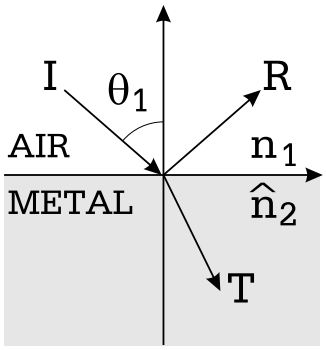

Figure 4.18: *Incident (I), reflected (R) and transmitted (T) waves at the air-metal interface.*

Here n_1 and $\hat{n}_2$ are the indices of refraction of air and of the metal, respectively, and θ_1 is the angle of incidence (Fig. 4.18). The index of refraction must be taken as complex, $\hat{n}_2 = n_2(1 + i\kappa_2)$; κ_2 is called the attenuation index. For the angle θ_2 the law of refraction still holds

$$\sin\theta_2 = \frac{1}{\hat{n}_2} \sin\theta_1. \tag{4.6}$$

Since $\hat{n}_2$ is complex, so is θ_2, which therefore has no longer the simple meaning of the angle of refraction.

To evaluate the propagation of light in the material it is useful to introduce the transmission and reflection coefficients for the electric field amplitude

which are defined as

$$\begin{cases} t_{\perp} &= \dfrac{T_{\perp}}{A_{\perp}} &= t'_{\perp} + i\, t''_{\perp} &= \tau_{\perp} e^{i\phi_{\perp}} \\ t_{\parallel} &= \dfrac{T_{\parallel}}{A_{\parallel}} &= t'_{\parallel} + i\, t''_{\parallel} &= \tau_{\parallel} e^{i\phi_{\parallel}} \end{cases} \tag{4.7}$$

and

$$\begin{cases} r_\perp &= \dfrac{R_\perp}{A_\perp} &= r'_\perp + i\, r''_\perp &= \rho_\perp e^{i\chi_\perp} \\ r_\parallel &= \dfrac{R_\parallel}{A_\parallel} &= r'_\parallel + i\, r''_\parallel &= \rho_\parallel e^{i\chi_\parallel} \ . \end{cases} \tag{4.8}$$

Transmitted field

The relevant question for the measurements is how the two components perpendicular and parallel to the plane of incidence are absorbed and phase shifted due to the interface. This, in fact, allows the determination of how any specific polarization, which can always be decomposed into a sum of a perpendicular and a parallel component, is transformed inside the sample. In particular, the absorption and the phase difference are described by τ_i and ϕ_i (with $i = \perp, \parallel$), respectively. To determine explicitly these quantities from Eq. (4.4) it is most convenient to introduce two functions u_2 and v_2 such that [69]

$$\hat{n}_2 \cos\theta_2 = u_2 + i\ v_2 \ . \tag{4.9}$$

From Eq. (4.6) and Eq. (4.9) u_2 and v_2 are given by

$$\begin{cases} 2u_2^2 &= n_2^2(1-\kappa_2^2) - n_1^2 \sin^2\theta_1 + \sqrt{\left[n_2^2(1-\kappa_2^2) - n_1^2\sin^2\theta_1\right] + 4n_2^2\kappa_2^2} \\ 2v_2^2 &= -\left[n_2^2(1-\kappa_2^2) - n_1^2\sin^2\theta_1\right] + \sqrt{\left[n_2^2(1-\kappa_2^2) - n_1^2\sin^2\theta_1\right] + 4n_2^2\kappa_2^2} \ . \end{cases} \tag{4.10}$$

With these two functions, it is finally possible to extract ϕ_i and τ_i from Eq. (4.4) as functions only of the angle of incidence and the optical constants of the material. The resulting expressions for the perpendicular component are

$$\begin{cases} \phi_\perp &= \arctan\left(\dfrac{-v_2}{n_1\cos\theta_1 + u_2}\right) \\ \tau_\perp^2 &= \dfrac{4n_1^2\cos^2\theta_1}{n_1^2\cos^2\theta_1 + 2n_1\cos\theta_1 u_2 + u_2^2 + v_2^2} \end{cases} \tag{4.11}$$

and for the parallel component

$$\begin{cases} \phi_\parallel &= \arctan\left(\dfrac{-n_2^2\kappa_2\cos\theta_1(1+\kappa_2^2) + n_1(u_2\kappa_2 - v_2)}{n_2^2\cos\theta_1(1+\kappa_2^2) + n_1(u_2 + \kappa_2 v_2)}\right) \\ \tau_\parallel^2 &= \dfrac{4n_1^2n_2^2\cos^2\theta_1(1+\kappa_2^2)}{[n_2^2(1-\kappa_2^2)\cos\theta_1 + n_1u_2]^2 + [2n_2^2\kappa_2\cos\theta_1 + n_1v_2]^2} \ . \end{cases} \tag{4.12}$$

These expressions are all that is needed to determine fully the propagation in the sample, once the angle of incidence of the laser light on the sample (θ_1) is determined and the optical constants are measured. The method to determine $\hat{n}_2$, established

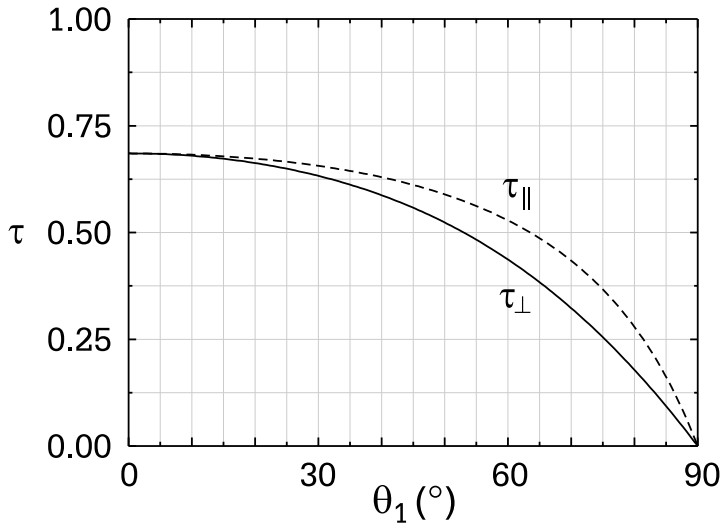

Figure 4.19: *Amplitude of the transmission coefficients of the sample for the electric field parallel ($\tau_{\|}$) and perpendicular ($\tau_{\perp}$) to the plane of incidence as a function of the angle of incidence θ_1. The plots are calculated for $\hat{n}_2 = 1.83(1 + i\ 0.39)$.*

during this work, is described in Sect. 4.4.2. An example of the absorption and of the phase shift experienced by the electric field inside the sample as a function of the angle of incidence are shown in Figs. 4.19 and 4.20, respectively. The plots are

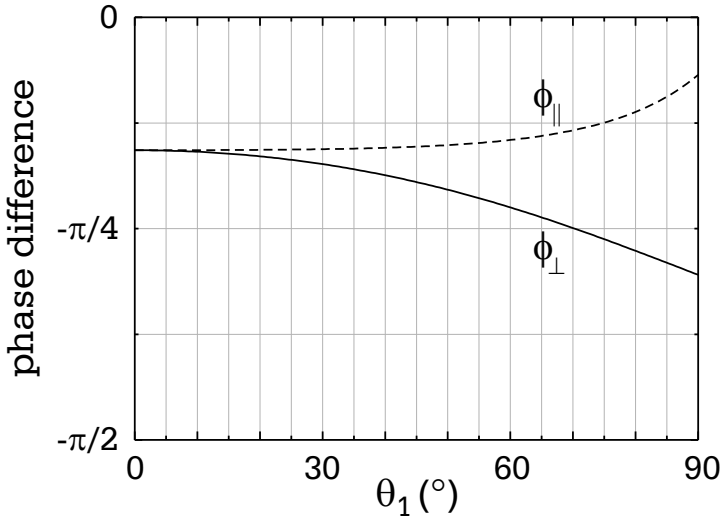

Figure 4.20: *Phase difference experienced at the interface by the transmitted electric field parallel ($\phi_{\|}$) and perpendicular ($\phi_{\perp}$) to the plane of incidence as a function of the angle of incidence θ_1. The plots are calculated for $\hat{n}_2 = 1.83(1 + i\ 0.39)$.*

calculated taking for the index of refraction the values obtained for an optimally

doped YBCO sample $\hat{n}_2 = 1.83(1 + i\ 0.39)$.

It is worth noticing that high temperature superconductors have in general highly anisotropic optical properties. Therefore, the measurement of n_2 and κ_2 must be performed in exactly the same geometrical configuration as used for the Raman measurements.

Reflected field

The interest in the reflected field is related to the necessity to measure the complex index of refraction $\hat{n}_2$ of the samples, before being able to adjust the proper polarization state. The optical constants of the sample can be determined by measuring how the light with a given polarization state transforms due to the reflection on the sample surface.

It is convenient to introduce the ratio between the reflection coefficients, P, the difference in phase shift, Δ, and an angle ψ as

$$\begin{cases} P & \equiv & \tan\psi = \dfrac{\rho_\perp}{\rho_\parallel} \\ \Delta & = & \chi_\parallel - \chi_\perp \ . \end{cases} \tag{4.13}$$

It can be shown [69] that from Eq. (4.5) and Eq. (4.6) the following expression holds for the complex index $\hat{n}_2$

$$\frac{\sqrt{\hat{n}_2^2 - \sin^2\theta_1}}{\sin\theta_1 \tan\theta_1} = -\frac{\cos 2\psi + i \sin 2\psi \sin\Delta}{1 + \sin 2\psi \cos\Delta} \ . \tag{4.14}$$

From this expression, the optical constants n_2 and κ_2 of the sample can be determined by measuring P and Δ, and the angle of incidence θ_1. The practical realization is described in the next paragraph.

4.4.2 Measurement of the optical constants of the samples

Since P and Δ characterize the difference in absorption and phase shift of the reflected parallel and perpendicular components, they can be directly measured by fixing a convenient polarization state before the sample and measuring the resulting elliptical polarization of the reflected light.

The setup for this measurement is shown in Fig. 4.21. The incoming light is linearly polarized by the first polarizer (P1) at 45° with respect to the x direction of the laboratory frame, so that the parallel and perpendicular components have the same amplitude and phase. Through a lens L6 (see Fig. 4.15) the light is focussed on small flat piece of the sample surface, typically of size of 0.5 mm^2, to obtain a uniformly reflected spot. The reflected light is absorbed by a power meter (PM), which

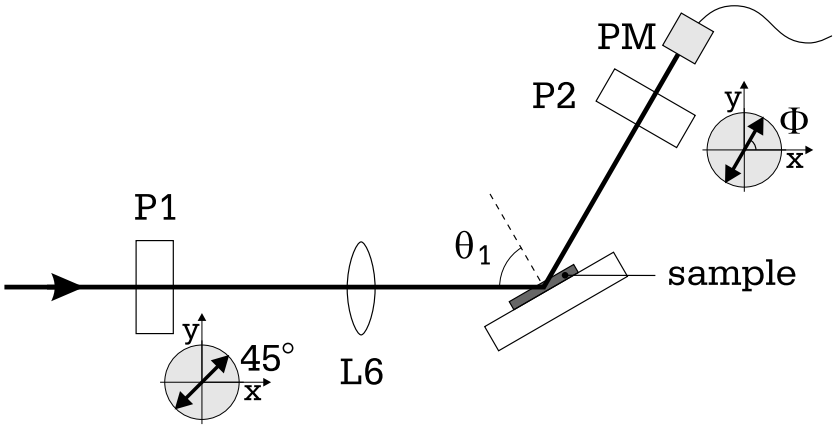

Figure 4.21: *Setup used for the measurement of optical constants of the sample. P1-P2 are polarizers, L6 a lens and PM the power meter. The transmission axis of each polarizer is marked by the double arrow in the x-y plot. θ_1 is the angle of incidence and Φ the angle between the transmission axis of the second polarizer and the x direction of the laboratory frame.*

measures the intensity as a function of the angle Φ between the transmission axis of the second polarizer (P2) and the x direction of the laboratory frame. Since the two incident waves have the same phase and amplitude, the ellipticity measurement of the reflected light gives directly P and Δ.

An example of the elliptically polarized reflected light intensity is shown in Fig. 4.22, where the intensity is plotted as a function of Φ for an optimally doped YBCO sample (see Tab. 4.2). The measured intensity is related to the ellipticity of the light by the expression

$$I(\Phi) = \frac{a_1^2}{2}\cos^2\Phi + \frac{a_2^2}{2}\sin^2\Phi + \frac{a_1 a_2}{2}\sin^2 2\Phi\cos\delta \qquad (4.15)$$

where a_1 and a_2 are the x and y components of the electrical field, respectively, and δ is the phase difference between the y and x components. By fitting the data, as shown in Fig. 4.22, a_1, a_2 and δ are directly determined. Since in this configuration the x direction is parallel to the plane of incidence, it is clear that $P \equiv \tan\psi = a_2/a_1$ and $\Delta = -\delta$. For this sample the resulting optical constants are $\hat{n}_2 = 1.83(1+i\,0.39)$.

4.4.3 Calibration of the Soleil-Babinet Compensator

For the adjustment of the proper polarization state outside the sample a Soleil-Babinet compensator (Bernhard Halle Nachfolger) has been used [69]. As shown in Fig. 4.23, it is composed of three quartz pieces, two wedges (b,c), and a plane-parallel slab (a), with the optical axis oriented perpendicular to the optical axes of the two wedges.

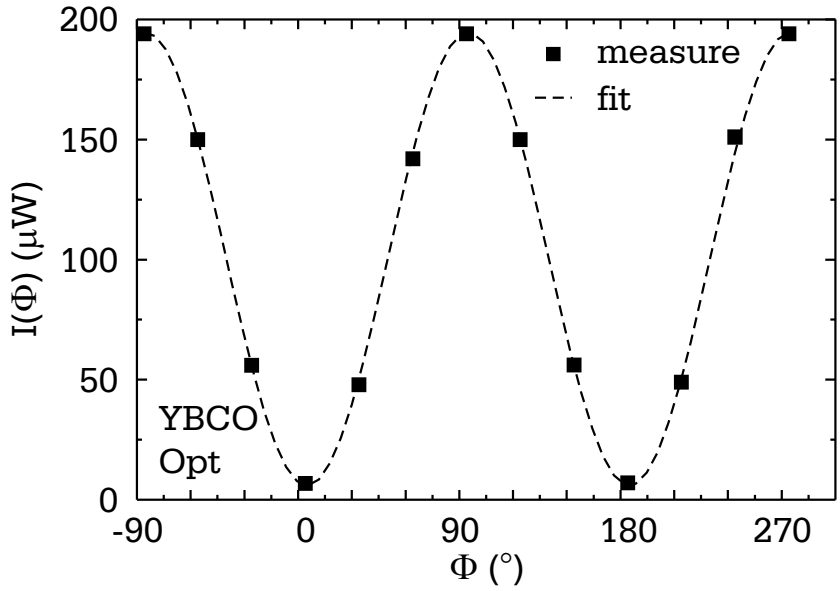

Figure 4.22: *Intensity of the light reflected by the YBCO sample Opt (Tab. 4.2) as a function of the angle Φ of the second polarizer, measured at an angle $\theta = 60°$. The dashed line is the best fit using Eq. (4.15).*

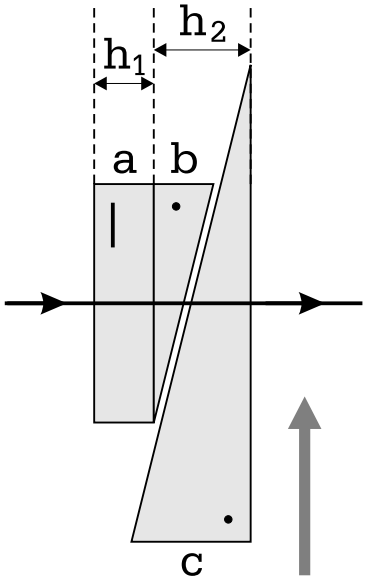

Figure 4.23: *Sketch of the Soleil-Babinet compensator. The optical axis of the first slab (a) is perpendicular to the axes of (b) and (c). The grey arrow marks the direction of movement of wedge (c) for increasing values of d.*

Therefore, the compensator has two degrees of freedom, the optical path inside the material, and the angle between the polarization of the incident light and the optical axis of the first element. In practice the optical path can be modified by changing the position of the wedge (c) with respect to (a) and (b), as indicated by the grey arrow in Fig. 4.23. This shift between (c) and (b) is controlled by a micrometer screw and is measured through the quantity d. The angle of the optical axis of (a) can be adjusted through another micrometer screw to within 1/20 of degree. It is therefore possible with the Soleil-Babinet compensator to prepare any desired type of elliptically polarized light. If the optical axis of piece (a) is along the y direction of the laboratory reference frame, the phase shift between the x and y components is given by

$$\delta_y - \delta_x = \frac{2\pi}{\lambda}[|n_o - n_e|(h_1 - h_2)] \tag{4.16}$$

with λ the wavelength of the incoming light, n_0 and n_e the ordinary and extraordinary indices of refraction of the material ($n_0 = 1.544$ and $n_e = 1.553$ at $\lambda = 589$ nm).

To be able to use the compensator, a proper calibration of the instrument is necessary at each specific wavelength used. This is performed by determining the relative position of the two wedges (b) and (c), h_2, and the exact orientation of the optical axes of the three pieces. A possible configuration for the calibration of the compensator is shown in Fig. 4.24.

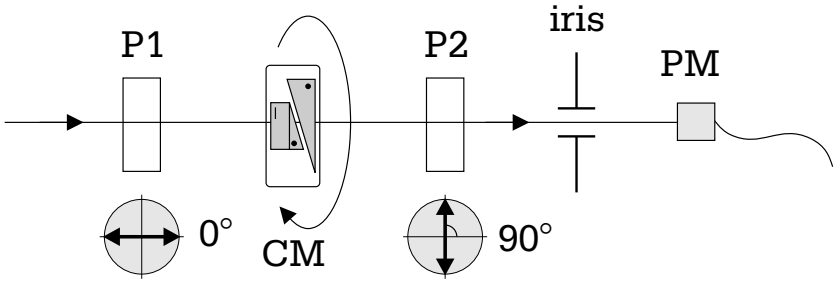

Figure 4.24: *Setup used for the calibration of the compensator. P1-P2 are polarizers, CM the compensator and PM the power meter. The transmission axis of each polarizer is marked by the double arrow in the x-y plot.*

The compensator is placed between two crossed polarizers (P1 and P2), and the power meter (PM) measures the intensity transmitted by the second polarizer. An iris diaphragm is necessary to block the multiple reflections coming out of the compensator. In this configuration, assuming that the wedges are placed so that $\delta \neq 0$, a rotation of the compensator around the optical axis will have the effect of changing the angle between the incoming polarization and the optical axis of the first piece (a). It is therefore clear that a minimum of the intensity is measured by the power meter when this axis is parallel or perpendicular to the transmission axis of the first polarizer, since in this case no phase difference is introduced between the x and y component and the light will be blocked by the second polarizer. Once the position of the optical axis with respect to the laboratory frame is determined, the phase difference as a function of the shift of the wedges, measured by a parameter d, can be determined measuring the maxima and minima of the transmission intensity when only d is varied. The distance between two maxima or minima corresponds to a phase shift of 2π.

The variation of the phase shift with the wavelength is summarized in Tab. 4.5, where λ_L is the laser wavelength, d_0 represents the $\delta = 0$ position and Δd_π is the variation of the parameter d corresponding to a phase shift of $\delta = \pi$. The small variations of the value of d_0, which should be independent of λ, are probably due to a slight misalignment of the compensator.

λ_L (nm)	d_0 (mm)	Δd_π (mm)
458	14.87	2.91
531	14.82	3.43
633	14.82	4.16

Table 4.5: *Wavelength dependence of the phase shift of the compensator. λ_L is the laser wavelength, d_0 the $\delta = 0$ position, and Δd_π is the variation of d corresponding to a phase shift of $\delta = \pi$.*

4.4.4 Preparation of the polarization state of the incident light

Once the compensator is calibrated and aligned, and the properties of the sample are measured, the polarization state of the incoming scattered light can be adjusted. First, the ellipticity necessary to produce the desired polarization state inside the sample must be determined. Then, after adjusting the compensator to produce the proper phase difference, the polarization state of the light just in front of the entrance window of the cryostat has to be measured, using Eq. (4.15). Although the calibration described in Sect. 4.4.3 allows the determination of the compensator settings corresponding to a certain phase shift, minor adjustments are always required, mainly because of the mirror M3 (Fig. 4.15).

The polarization states adjusted before the sample and expected inside the sam-

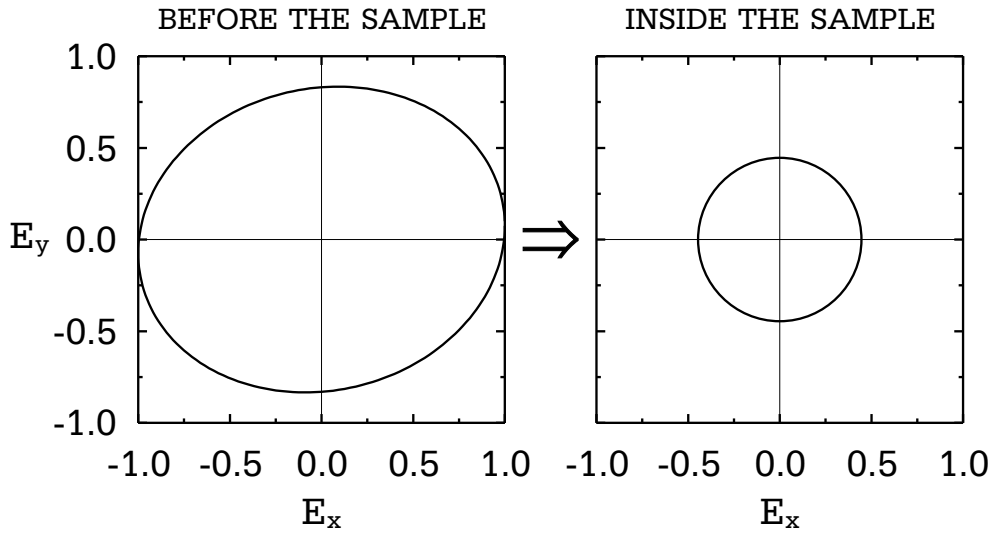

Figure 4.25: *Example of preparation of the polarization state to have circularly polarized light inside the sample. The sample is the optimally doped YBCO sample (Opt in Tab. 4.2).*

ple are shown in Fig. 4.25 for the optimally doped YBCO sample (Opt in Tab. 4.2).

Note that the scattered light, being measured at normal incidence, is not affected by the propagation in the metal, and no corrections are required.

Chapter 5

Two-particle and single-particle relaxation rates: experimental and theoretical results

In this chapter experimental angle-resolved photoemission spectroscopy (ARPES) data of an overdoped BSCCO sample are analyzed to determine the single-particle properties of the carriers. These results are then used to calculate the Raman response, which is finally compared to the experimental observations. Since photoemission is a single-particle probe in contrast to Raman, which is a two-particle probe, this approach allows the identification of those features of the Raman spectra which can be traced back to single-particle properties.

5.1 Loose ends in the normal state Raman observations

The normal-state Raman spectra are characterized by several features which are still not at all understood. In addition to the anisotropy between B_{1g} and B_{2g} symmetries, which becomes more and more pronounced with underdoping, a large scattering intensity is observed in all symmetries up to energies of at least 1 eV. As introduced in Sect. 3.3.1, the self energy is not only necessary to observe inelastic light scattering in the normal state, but is crucial for the understanding of the spectral shape. At present, however, there is no agreement on the form of the self energy since the electronic interactions in the cuprates are still an open issue.

Different theoretical models have been proposed so far. The effect of an impurity potential on free electrons, for example, has been studied [70]. In this picture, the

spectra have a peak at an energy of the order of the scattering rate and then fall off at large frequencies and can therefore not fit the large flat continuum observed up to energies of 1 eV. The response of a nested Fermi liquid was also calculated, leading to a frequency and temperature dependent scattering rate $1/\tau^* = \max\{\beta T, \alpha\omega\}$, where α and β are constant prefactors [71]. This form of the scattering rate, while yielding a qualitatively good agreement between the theoretical curves and the measured spectra at high frequencies, does not explain the channel dependence observed. More recently the model of a nearly antiferromagnetic Fermi liquid was explored and the Raman spectra calculated [72]. The idea is that the strong magnetic interactions between the quasiparticles are peaked at or near the antiferromagnetic wavevector $\mathbf{Q} = (\pi/a, \pi/a)$ (Sect. 2.6 and [27]) and lead to an anisotropic self energy. Although a qualitative agreement with the experiments is achieved at low frequencies, substantial deviations are observed at high frequencies.

In this work a new type of approach is used which is based on the determination of the single-particle self energy from photoemission data. The form of the self energy obtained is then used to calculate the Raman response and allows the understanding of the experimental spectra in a large energy range.

5.2 What photoemission spectroscopy measures

Angle-resolved photoemission (ARPES) essentially measures the probability of creating a photoelectron with an energy $\hbar\omega_f$ and wave vector $\mathbf{k}_f$ by an electron with energy $\hbar\omega$ and wave vector $\mathbf{k}$ inside a solid. Under the assumption that the photoelectron leaves the sample so quickly that the interaction with the photohole left behind is negligible ("sudden approximation") the intensity of the photocurrent can be written as [73, 74]

$$I(\mathbf{k},\omega) = |M(\mathbf{k})|^2 [A(\mathbf{k},\omega) n_F(\omega)] \otimes R_{\omega,\mathbf{k}} + B(\omega) \tag{5.1}$$

where $M(\mathbf{k})$ represents the matrix element linking the initial and final electronic states, $A(\mathbf{k},\omega)$ is the single-particle spectral function, $n_F(\omega)$ is the Fermi-Dirac distribution function, and $\otimes$ marks the convolution with the energy and momentum resolution function $R_{\omega,\mathbf{k}}$. $B(\omega)$ is an energy dependent background, which contains extrinsic effects such as inelastic scattering of the photoelectrons, and which is only weakly momentum dependent.

The information related to the single-particle properties are contained in the spectral function. In fact, $A(\mathbf{k},\omega)$ is related to the imaginary part of the single-particle Green function $G(\mathbf{k},\omega)$ as $A(\mathbf{k},\omega) = -2G''(\mathbf{k},\omega)$ [40], where $G(\mathbf{k},\omega) =$

$G'(\mathbf{k},\omega)+iG''(\mathbf{k},\omega)$. From Eq. (3.13), after performing the analytical continuation, the spectral function can be written as

$$A(\mathbf{k},\omega) = -\frac{2\Sigma''(\mathbf{k},\omega)}{[\omega - \xi_{\mathbf{k}} - \Sigma'(\mathbf{k},\omega)]^2 + [\Sigma''(\mathbf{k},\omega)]^2} \tag{5.2}$$

where $\Sigma = \Sigma' + i\Sigma''$ is the self energy (Sect. 3.3), $\xi_{\mathbf{k}} = \varepsilon_{\mathbf{k}} - \mu$ the band dispersion (Sect. 3.5). The convention $\hbar = 1$ and $k_B = 1$ is used. Therefore $A(\mathbf{k},\omega)$ must be extracted from the measured intensity expressed by Eq. (5.1).

The influence of the matrix elements, which can produce dramatic variations in the angular distribution of photoelectrons [75, 76], can be accounted for using a "self-normalization-procedure". The measured intensity is divided by a quantity which mimics the matrix-element effects but at the same time is a slowly varying function of momentum. Two methods successfully applied to the determination of the Fermi surface topology consist in dividing the data by the signal at the highest binding energy available or by the intensity integrated over all energies [74]; the former method will be used in this work.

The knowledge of the spectral function, or equivalently of the imaginary part of the single-particle Green function, is all that is needed to calculate the Raman response function (Sect. 3.3). The derivation of $A(\mathbf{k},\omega)$ from the measured intensity in Eq. (5.1) is however non-trivial and depends substantially on the quality of the experimental data. It is also worth noticing that to calculate a response the spectral function has to be determined for all frequencies ($-\infty < \omega < \infty$), while ARPES only probes occupied states ($\omega < 0$ at $T = 0$ if the Fermi level is taken as reference), as implied by the Fermi-Dirac distribution function in Eq. (5.1). To overcome this problem particle-hole symmetry is assumed, that is $A(\omega) = A(-\omega)$ [77]. While holding for low frequencies ($\omega \lesssim T$), this approximation probably fails for large ω [77]. The direct extraction of the spectral function from the measured intensity is further hampered by the lack of detailed knowledge of the additive extrinsic background $B(\omega)$ which itself is ω-dependent.

The new electron analyzers employed in the last few years allow the simultaneous measurement of the photoemitted intensity as a function of both energy and momentum. This permits a new approach, used in this work, which explores the momentum rather than the traditional energy dependence of the spectral function in Eq. (5.1). Given the set of measurements analyzed in this thesis this approach is preferable also because of the much finer mesh of data in $\mathbf{k}$-space as compared to the energy space.

For $\mathbf{k}$ near the Fermi wavevector $\mathbf{k}_F$, and varying normal to the Fermi surface,

the band dispersion can be linearized as

$$\xi_{\mathbf{k}} \simeq v_F^0(k - k_F) \tag{5.3}$$

where v_F^0 is the bare Fermi velocity and the band dispersion is measured with respect to the Fermi level. The real part of the self energy can also be expanded around the Fermi surface as $\Sigma'(\omega) \simeq \omega(\partial\Sigma'/\partial\omega)_{\omega=0}$, since $\Sigma'(\omega = 0) = 0$ [40]. Then Eq. (5.2) can be written

$$A(\mathbf{k},\omega) = -\frac{2\Sigma''(\mathbf{k},\omega)}{[\omega(1 - (\partial\Sigma'/\partial\omega)_{\omega=0}) - v_F^0(k - k_F)]^2 + [\Sigma''(\mathbf{k},\omega)]^2} \tag{5.4}$$

and, introducing the renormalized Fermi velocity $\tilde{v}_F = v_F^0/[1 - (\partial\Sigma'/\partial\omega)_{\omega=0})]$, Eq. (5.4) can be rewritten to emphasize the k-dependence as

$$A(\mathbf{k},\omega) = -\frac{2\Sigma''(\mathbf{k},\omega)/(v_F^0)^2}{\left[k - (k_F + \frac{\omega}{\tilde{v}_F})\right]^2 + \left[\frac{\Sigma''(\mathbf{k},\omega)}{v_F^0}\right]^2} \tag{5.5}$$

Assuming that $\Sigma(\mathbf{k},\omega)$ is not strongly dependent on $\mathbf{k}$, Eq. (5.5) implies that the intensity measured at a fixed ω, as a function of k perpendicular to the Fermi surface is essentially a Lorentzian centered at

$$k_{max} = k_F + \omega\frac{1}{\tilde{v}_F} \tag{5.6}$$

and with a half width at half maximum (HWHM) of

$$\Delta k = |\Sigma''(\omega)|/(v_F^0) \tag{5.7}$$

The validity of these approximations will then be tested analyzing the intensity as a function of a $\mathbf{k}$ normal to the Fermi surface at different angles on the Fermi surface ϕ.

The conventions used in this work to label any $\mathbf{k}$-point through the angle ϕ and the magnitude of the wave vector $k = |\mathbf{k}|$, measured starting from the point $(\pi/a, \pi/a)$, are shown in Fig. 5.1. The momentum dependence of the measured intensity is derived keeping the angle ϕ fixed and varying the magnitude of the wave vector k, represented schematically by the arrows in Fig. 5.1. These "cuts" in momentum space at a fixed binding energy are called momentum distribution curves (MDCs). The advantage of this method of performing MDC is that the cuts are approximately perpendicular to the Fermi surface. Whenever the curve strongly deviates from a Lorentzian, the dependence of the self energy on the amplitude momentum is not negligible, and the approximations of Eq. (5.6) and Eq. (5.7) are not valid any longer.

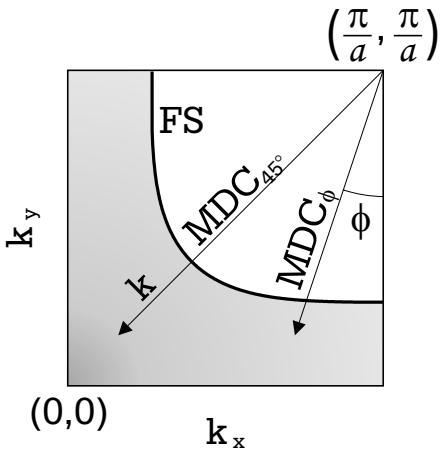

Figure 5.1: *Method used to obtain momentum distribution curves (MDC) from cuts in momentum space at a fixed binding energy. ϕ is the angle around the Fermi surface; the cuts are labeled by the angle.*

If the intensity at fixed momentum $\mathbf{k}$ is measured as a function of the binding energy, energy distribution curves (EDCs) are obtained, which, as evident from Eq. (5.2), have a non-Lorentzian lineshape whenever the self energy depends on ω, as is expected in the cuprates.

These considerations alone already show the advantage of an analysis based on the MDCs. Another motivation for this choice is that MDCs have a constant background since measured at a fixed energy, which therefore does not affect the determination of the quantities k_{max} and Δk. In addition, these curves show a well defined peak in the normal state at all points on the Fermi surface even if a peak in the EDC is not visible any longer [78]. Finally, given the set of data available for this study, with a relatively coarse mesh of energies and with an energy resolution of only 20 meV, an analysis based on interpretation of the MDC is more robust.

5.3 Photoemission results on overdoped $Bi_2Sr_2CaCu_2O_{8+\delta}$

In this section raw photoemission data of an overdoped Pb-BSCCO sample with $T_c = 71.9$ K are analyzed [15]. The advantage of partially substituting Pb for Bi in BSCCO samples is that the structural modulation along the crystallographic b direction characteristic of BSCCO disappears, simplifying the observed MDCs. The experiments were performed by S. Borisenko and co-workers at the Institute for Solid State and Material Research, IFW Dresden, using monochromatic, unpolarized He I radiation and a SCIENTA SETS200 analyzer [74]. The energy covers a range from -220 meV to 120 meV in steps of 10 meV around the Fermi energy; in momentum space a mesh of 4117 $\mathbf{k}$-values covers roughly half of the Brillouin zone. The temperature of the sample was 300 K, and the resolution achieved was 0.014 Å^{-1} × 0.035 Å^{-1} × 19 meV for the full width at half maximum (FWHM) momentum (parallel and perpendicular to the analyzer's entrance slit) and energy resolution, respectively.

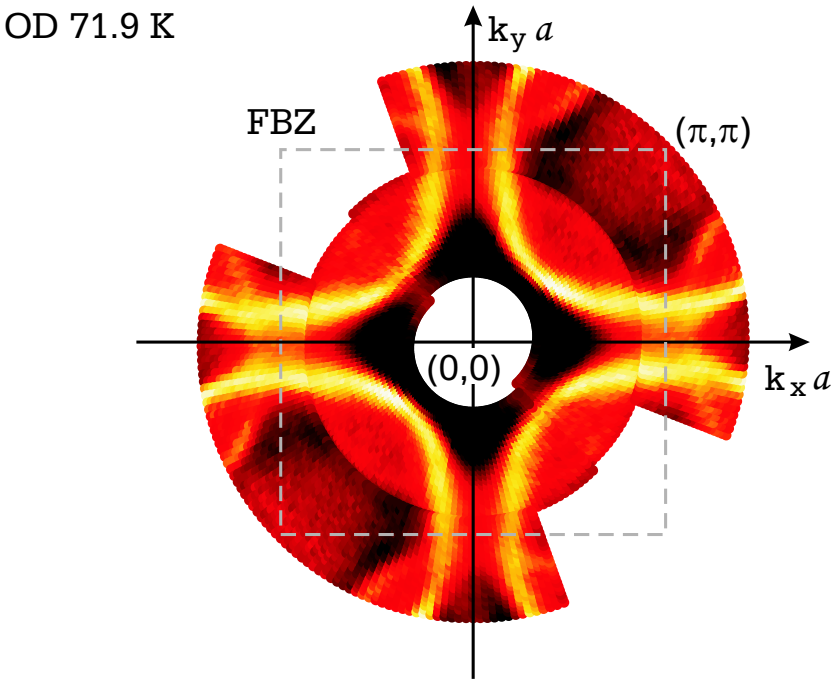

Figure 5.2: *Momentum distribution map (MDM) at the Fermi energy measured at 300 K. Light colors correspond to higher intensities. The raw data cover half of area shown and have been rotated by* 180° *around the* $(0,0)$ *point to produce an image over the entire first Brillouin zone (FBZ) marked with a dashed line.*

The analysis of these data is performed starting from the momentum distribution maps (MDMs), which are images of the Brillouin zone, taken at fixed binding energy. The momentum distribution map at the Fermi energy is shown in Fig. 5.2, where the intensity at the Fermi level divided by the intensity integrated over the entire available range is plotted. The bright points determine the location of the Fermi surface. From these data the lattice constant a turns out to be about 3.9 Å, in good agreement with the tabulated value [79].

5.3.1 Experimental Fermi surface and Fermi velocity

The topology and character of the normal state Fermi surface can be effectively investigated by photoemission spectroscopy. The experiments confirmed the existence of a large hole-like surface centered at the corners of the Brillouin zone as predicted by band structure calculations [80, 81]. The improvements in energy and momentum resolution achieved in the last years have allowed to settle controversial issues such as the existence of shadow Fermi surfaces and diffraction replica [82] and, quite recently, the existence of a splitting of the bands due to the interaction between the CuO_2 layers [83, 84, 85].

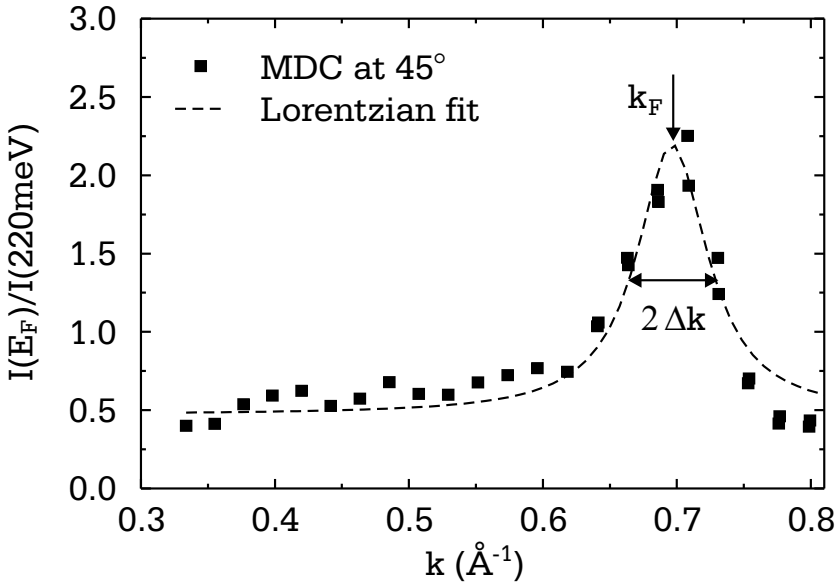

Figure 5.3: *MDC at $\phi = 45°$ and zero binding energy. The dashed line is the best Lorentzian fit to the data. The maximum of the curve determines the Fermi wavevector $k_F(45°)$, and the HWHM is called $\Delta k(45°)$.*

Fermi surface

To remove the effect of the matrix elements, the data are self-normalized by dividing the signal at the binding energy of interest by the signal at the highest binding energy available, i.e. 220 meV. As mentioned in Sect. 5.2, this operation is necessary to obtain the single-particle spectral function. The Fermi surface is determined from Eq. (5.6) as the locus of the k_{max}-values in the MDM taken at the Fermi energy (Fig. 5.2). Therefore cuts in the Brillouin zone as shown in Fig. 5.1 are taken at every two degrees for $0° < \phi < 90°$. Each curve is characterized by a peak with an approximately symmetrical form which is fitted by a Lorentzian curve to determine $k_{max}(\phi, \omega = 0) \equiv k_F(\phi)$ and $\Delta k(\phi)$. As an example, the MDC obtained at $\phi = 45°$ and $\omega = 0$ is shown in Fig. 5.3.

The resulting Fermi surface is plotted in Fig. 5.4. The dashed line corresponds to a fit using the tight-binding band given in Eq. (3.27)

$$-2t[\cos(k_x a) + \cos(k_y a)] + 4t' \cos(k_x a)\cos(k_y a) - \mu = 0 \ .$$

The parameters obtained from the fit are $t'/t = 0.45$ and $\mu/2t = -0.55$.

To investigate more carefully the effect of the matrix elements the results for $k_F(\phi)$ and $\Delta k(\phi)$ for different self-normalization procedures have been investigated in this work. While the Fermi surface itself is completely robust, the momentum width of the MDCs, $\Delta k(\phi)$, is most precisely determined when the self-normalization

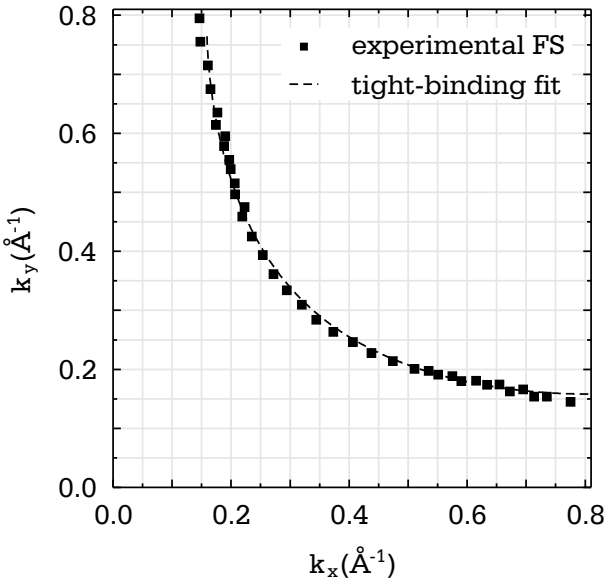

Figure 5.4: *Fermi surface obtained from the maximum of the MDCs. The dashed line is a fit within the tight-binding model of Eq. (3.27), with* $t'/t = 0.45$ *and* $\mu/2t = -0.55$.

is performed by dividing the spectra by the intensity at the highest binding energy. This is clearly related to a better elimination of matrix element effects which allows

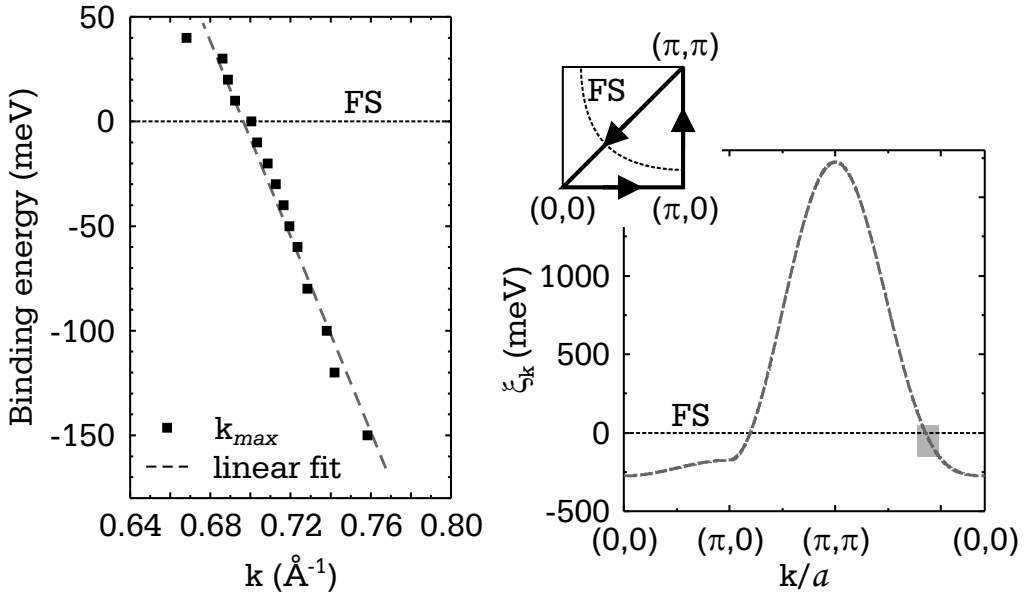

Figure 5.5: *Dispersion resulting from MDCs at* $\phi = 45°$ *at different binding energies (left panel). Band dispersion for the tight-binding model band of Eq. (3.27) (right panel). The grey rectangle marks the area investigated in the left panel. FS is the Fermi surface.*

a relatively flat background and consequently a reduction of the errors on the width determination.

Fermi velocity

To obtain the imaginary part of the self energy from in Eq. (5.7), the Fermi velocity as a function of the angle ϕ, $v_F^0(\phi)$, must also be determined. However, the Fermi velocity determined from the band dispersion corresponds to the renormalized Fermi velocity $\tilde{v}_F$ [86], and the bare one $v_F^0(\phi)$, cannot be measured. For this reason, $\tilde{v}_F$ is used in practice to determine the self energy [87].

The band dispersion resulting from the maximum of the MDCs at $\phi = 45°$ at different binding energies is clearly linear, and is shown in Fig. 5.5. From a linear fit to these data the Fermi velocity results $\tilde{v}_F(\phi = 45°) \simeq 2.2$ eV Å $\simeq 3.3\times10^7$ cm s^{-1}, consistent with previous results on the same material [74].

The angular (ϕ) dependence of the mean velocity of the electrons is derived from the variations of the band structure $\varepsilon_{\mathbf{k}}$, determined as in Fig. 5.4, for k-intervals perpendicular to the Fermi surface or, restoring $\hbar$,

$$\tilde{v}_F \simeq \frac{1}{\hbar}\frac{\Delta\varepsilon_{\mathbf{k}}(\phi)}{\Delta k} \ . \qquad (5.8)$$

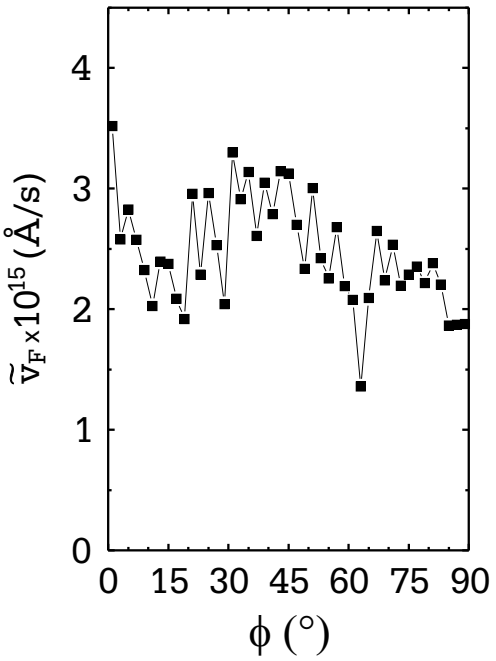

Figure 5.6: *Renormalized Fermi velocity as a function of the angle around the Fermi surface.*

The symbol Δ is used because of the discreteness of the experimental data ($\Delta\varepsilon_{\mathbf{k}} = \pm10, 20, ...$ meV). The result of averaging over different $\Delta\varepsilon_{\mathbf{k}}$ is shown in Fig. 5.6. The Fermi velocity has a small angular modulation, being maximal at the nodal direction, $\tilde{v}_F(\phi = 45°) \simeq 3 \times 10^7$ cm s^{-1}, and minimal at the antinodal directions $\tilde{v}_F(\phi = 0°, 90°) \simeq 2 \times 10^7$ cm s^{-1}.

5.3.2 Momentum dependence of the self energy

The observation that the spectral function for Fermi surface crossing along the $(\pi, 0) - (\pi, \pi)$ direction in the Brillouin zone (antinodal or "hot" region) is smeared by strong scattering as compared to the spectrum along the $(0, 0) - (\pi, \pi)$ direction (nodal or "cold" region) [83] has been ascribed to a strong momentum dependence of

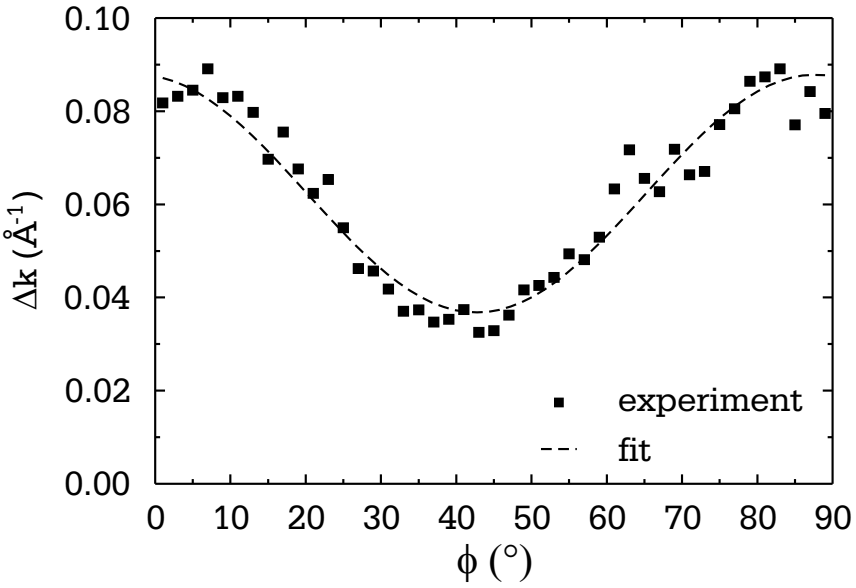

Figure 5.7: *Half width at half maximum Δk of the MDCs as a function of the angle ϕ around the Fermi surface. The dashed line is the fit to the data obtained using Eq. (5.9).*

the quasiparticle self energy, whose imaginary part is responsible for the scattering rate. Now, from the width of the MDCs it is finally possible to verify the extent of the anisotropy of the single-particle self energy and therefore of the quasiparticle scattering rate.

The half width at half maximum Δk (Fig. 5.3) at different angles ϕ on the Fermi surface is shown in Fig. 5.7. Δk shows a modulation and is maximal at the antinodal points ($\phi = 0°, 90°$) and smallest at the nodal direction ($\phi = 45°$). The angular dependence of the Δk can be described by the function

$$\Delta k(\phi) = \Delta k_0 + \Delta k_1 \cos^2(2\phi) \tag{5.9}$$

The parameters resulting from a fit to the data are $\Delta k_0 = 0.037$ Å^{-1} and $\Delta k_1 = 0.051$ Å^{-1}. These values are consistent with those in Ref. [15].

Using Eq. (5.7) it is finally possible to evaluate the momentum dependence of the imaginary part of the self energy at the Fermi energy ($\omega = 0$), which is shown in Fig. 5.8. From a fit to the data with the same angular dependence of $\Delta k(\phi)$ the modulation of $|\Sigma''|$ around the Fermi surface results as

$$C_1(\phi) \equiv |\Sigma''(\phi, \omega = 0)| - |\Sigma''(45°, \omega = 0)| \approx (67 \text{ meV}) \cdot \cos^2(2\phi) \ . \tag{5.10}$$

Since the momentum width (Fig. 5.7) and $\tilde{v}_F(\phi)$ (Fig. 5.6) have different dependences upon ϕ, the strong variation of $\Delta k(\phi)$ is partially compensated in the self

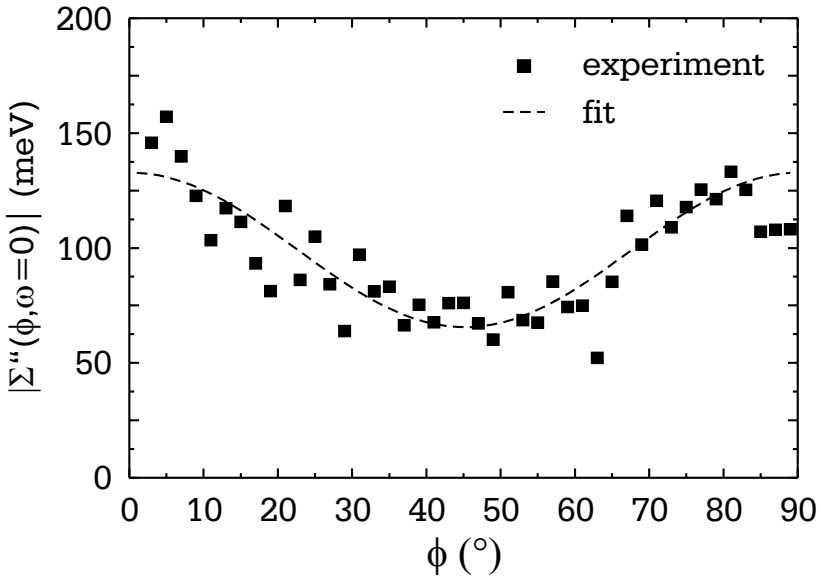

Figure 5.8: *Absolute value of the imaginary part of the self energy at the Fermi energy as a function of the angle ϕ around the Fermi surface. The dashed line is the fit to the data.*

energy. Still, $|\Sigma''|$ is maximal at the antinodal directions marking a stronger scattering rate as compared to the nodal directions where it is minimum, as expected from other indirect observations [78, 86].

5.4 Derivation of the Raman response from single-particle properties

In the traditional Fermi liquid picture, an electron in a solid becomes "dressed" with a "cloud" of excitations acquiring a different effective mass but still behaving like a single-particle excitation or a "quasiparticle". In the cuprates, where the electrons are strongly correlated and highly interacting with different excitations, the question as to the appropriateness of this picture is still under debate. At optimum doping and in the underdoped region of the phase diagram several experiments seem to indicate a breakdown of this scenario [87, 3].

As introduced in Chapter 3, it is the single-particle self energy $\Sigma(\mathbf{k}, \omega)$ that reflects fundamental interactions in a many-body system; Σ has a two-fold effect: it renormalizes the dispersion relation $\xi_{\mathbf{k}}$ and introduces a finite spectral linewidth $\Gamma = -2\Sigma''$; $\tau = \hbar/\Gamma$ is the lifetime of the quasiparticles in the interacting system. Here, the self energy directly derived from the photoemission data is used to calculate the Raman response for overdoped samples.

5.4.1 Single-particle self energy

From the analysis of the raw photoemission data the momentum dependence of the self energy is obtained in this work. However, due to the poor energy resolution and the lack of measurements at various temperature, the energy and temperature dependence of the self energy is taken from experimental observations on comparable samples by other groups [78, 74].

Recent photoemission studies in optimally doped BSCCO have provided evidence that the imaginary part of the self-energy has a linear temperature dependence along the Brillouin zone diagonals independent of the binding energy for small energies and a linear energy dependence independent of temperature for large binding energies [87]. This behaviour seems to support a marginal-Fermi liquid picture [88, 89].

The temperature dependence of the full width at half maximum Δk of the MDCs of an optimally doped BSCCO sample is shown in Fig. 5.9. [78]. Δk is linear in

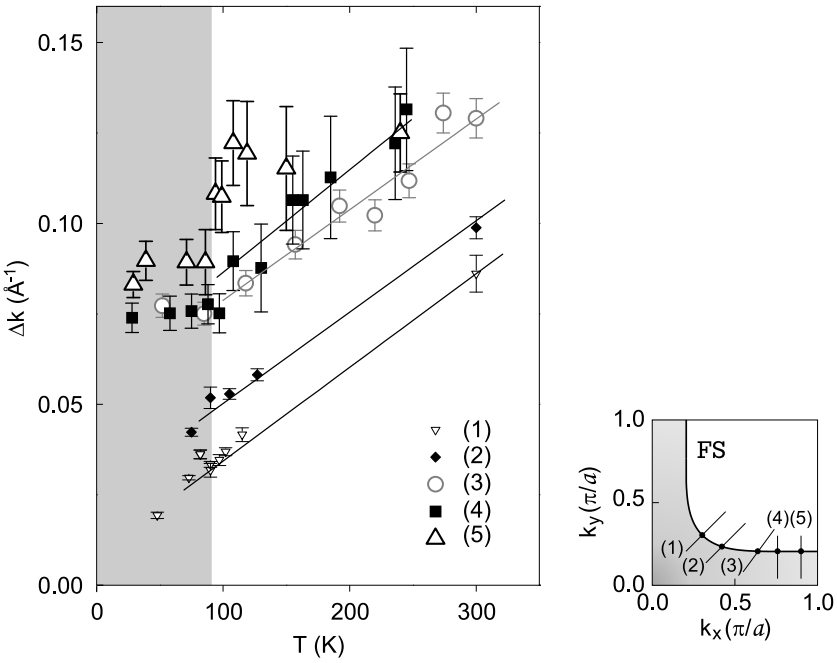

Figure 5.9: *Full width at half maximum Δk of the MDCs as a function of temperature for different positions on the Fermi surface for an optimally doped BSCCO from Ref. [78]. The different cuts are shown in the right panel. FS is the Fermi surface. The widths are measured at the Fermi level and at the leading edge in the normal and in the superconducting (grey region), respectively.*

T, being reminiscent of the temperature dependence of the resistivity [41], with a small zero-temperature intercept $C_0 \approx 9$ meV.

Including the dependence on the angle ϕ around the Fermi surface, the imaginary

part of the self energy can be represented as

$$\Sigma''(\phi,\omega,T) = -\left[C(\phi) + \sqrt{(\alpha\omega)^2 + (\beta T)^2}\right] \ . \tag{5.11}$$

$C(\phi)$ includes the zero-temperature contribution (C_0) and the angular modulation ($C_1(\phi)$) given by Eq. (5.10)

$$C(\phi) = C_0 + C_1(\phi) \tag{5.12}$$

α and β are two dimensionless constants which characterize the variation of the self energy with energy and temperature, respectively. From other measurements by the same group on similar samples, it has been shown that the experimental EDCs are consistent with the values $\alpha = 1.1$ and $\beta = 2$ [74]. Therefore these values are used in this calculation. Since the self energy represents the scattering rate of the quasiparticles, it cannot become arbitrarily large for increasing ω, implying an unphysical, vanishingly small mean free path. Therefore, a smooth cutoff ω_0 is introduced by multiplying the imaginary part of the self energy (Eq. (5.11)) by a Lorentzian, and a constant value equal to the maximum of the function is taken for the energy dependent term at high frequencies. In Fig. 5.10 the low energy dependence of the imaginary part of the self energy is plotted in the nodal ($\phi = 45°$) and antinodal ($\phi = 90°$) directions, for three temperatures. In Appendix A the high-energy properties of Σ'' are shown in more detail.

The real part of the self energy is calculated analytically by Kramers-Krönig transformation of the imaginary part to satisfy causality. The explicit analytic expression of the real part is reported in Appendix A.

5.4.2 Raman response

As described in Sect. 3.3.1, the Raman response function in the normal state is given by (Eq. (3.16))

$$\chi''_{\gamma\gamma}(\omega) = \sum_{\mathbf{k}} \gamma_{\mathbf{k}}^2 \int_{-\infty}^{\infty} \frac{dy}{\pi} G''(y,\mathbf{k}) G''(y-\omega,\mathbf{k}-\mathbf{q}) \left[n_F(y) - n_F(y-\omega)\right] \tag{5.13}$$

where n_F is the Fermi-Dirac distribution function and $\gamma_{\mathbf{k}}$ is the Raman vertex. The imaginary part of the renormalized electronic Green function $G''(y,\mathbf{k})$ is

$$G''(y,\mathbf{k}) = \frac{\Sigma''(y,\mathbf{k})}{(y - \xi_{\mathbf{k}} - \Sigma'(y,\mathbf{k}))^2 + (\Sigma''(y,\mathbf{k}))^2} \tag{5.14}$$

with $\xi_{\mathbf{k}}$ the band dispersion.

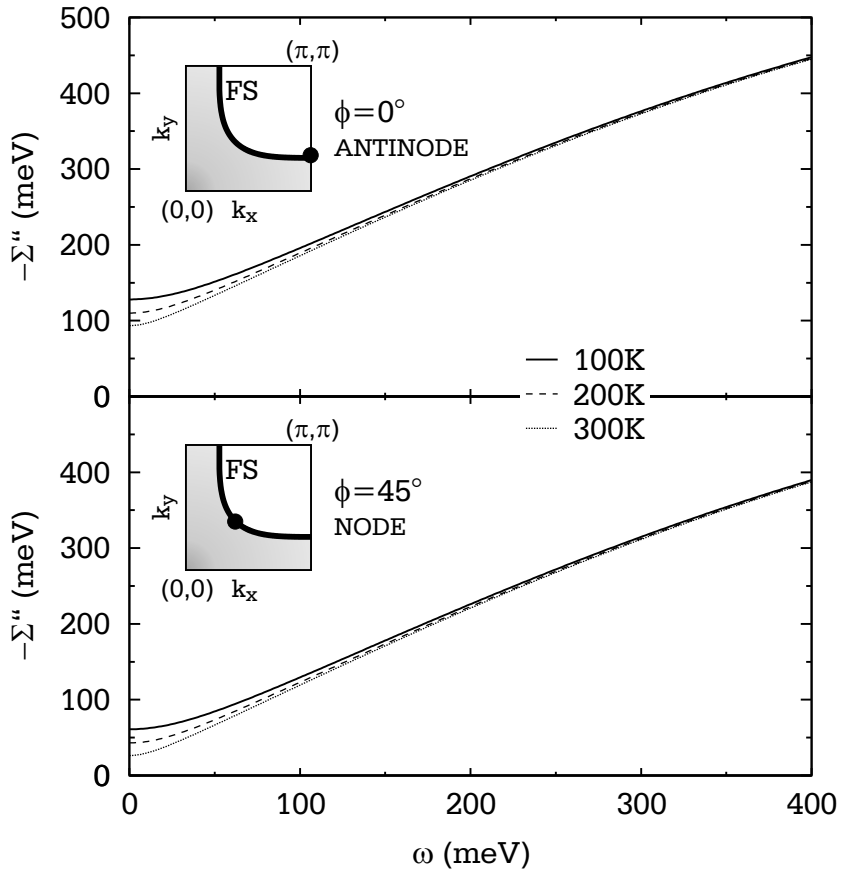

Figure 5.10: *Variations of the imaginary part of the self energy with frequency at three temperatures at the antinodal ($\phi = 0°$, panel (a)) and nodal ($\phi = 45°$ panel (b)) directions.*

The analytical calculation is further simplified by approximating the Fermi surface as cylindrical and by changing the 2D $\mathbf{k}$-sum in an energy and an angular integration around the Fermi surface

$$\sum_{\mathbf{k}} \rightarrow \int_0^{2\pi} d\phi \int_{-\infty}^{\infty} d\epsilon N(\epsilon) \tag{5.15}$$

where $N(\epsilon)$ is the density of states, which is considered constant and equal to its value at the Fermi level $N(\epsilon) \sim N(\epsilon = \epsilon_F) \equiv N_F$ since the electrons participating in the interaction are mainly those with energies around the Fermi energy. Within these simplifications and for $\mathbf{q} \rightarrow 0$, it is possible to write the response function as

$$\begin{aligned} \chi''_{\gamma\gamma}(\omega) &= N_F \int_0^{2\pi} d\phi \int_{-\infty}^{\infty} d\epsilon\, \gamma^2(\phi) \int_{-\infty}^{\infty} \frac{dy}{\pi} \left[n_F(y) - n_F(y-\omega)\right] \\ & \quad G''(y,\epsilon,\phi) G''(y-\omega,\epsilon,\phi) \ . \end{aligned} \tag{5.16}$$

The energy integration can be performed analytically assuming that the self

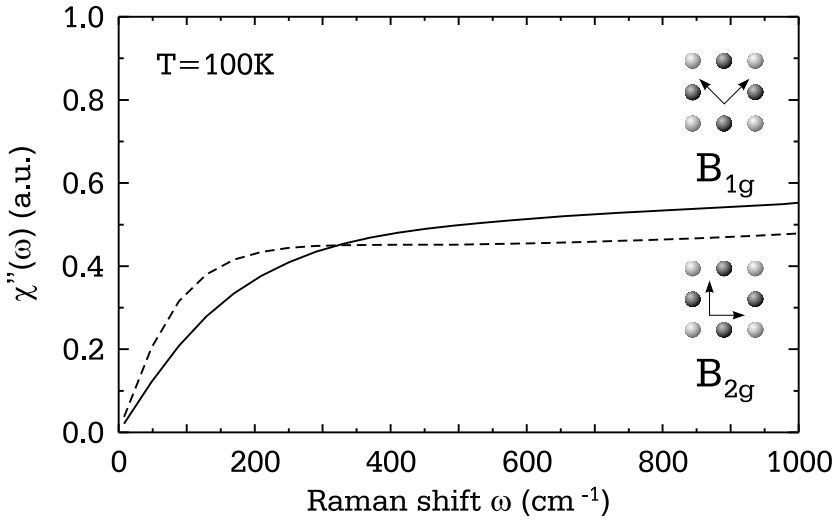

Figure 5.11: *Theoretical Raman response in B_{1g} and B_{2g} symmetries. The parameters used for the plot are $\alpha = 1.1$, $\beta = 2$, $T = 100$ K, $C_0 = 9$ meV, and $\omega_0 = 1$ eV.*

energy depends on $\mathbf{k}$ only through the angle ϕ around the Fermi surface. The resulting expression for the Raman response is

$$\chi''_{\gamma\gamma}(\omega) = N_F \int_{-\infty}^{\infty} dy\, [n_F(y-\omega) - n_F(y)] \int_0^{2\pi} d\phi \gamma^2(\phi) \frac{\Sigma''(y-\omega,\phi) + \Sigma''(y,\phi)}{[\Sigma'(y-\omega,\phi) - \Sigma'(y,\phi) + \omega)]^2 + [\Sigma''(y-\omega,\phi) + \Sigma''(y,\phi)]^2} . \quad (5.17)$$

In Fig. 5.11 the Raman response given by Eq. (5.17) is plotted for B_{1g} and B_{2g} symmetries. The values of the parameters used are $\alpha = 1.1$, $\beta = 2$, $T = 100$ K, $C_0 = 9$ meV, and $\omega_0 = 1$ eV.

The evolution with temperature of the response is shown in Fig. 5.12 for the B_{1g} (panel (a)) and B_{2g} (panel (b)) channels. The curves are calculated for $T = 100$, 200, 300 K; the other parameters have the same values used for Fig. 5.11. The spectra have been adjusted at $\omega = 1000$ cm^{-1} to allow a better comparison of the low frequency spectral shape. In both symmetries the initial slope of the spectra, which is proportional to the lifetime of the carriers, increases with decreasing temperatures. This result is consistent with experimental Raman observations, as will be discussed in detail in Sect. 6.1 (see for comparison Fig. 6.3).

5.4.3 Comparison with Raman experimental results

The comparison of the theoretical curves and the experimental Raman observations is shown Fig. 5.13. The data correspond to the overdoped BSCCO single crystal

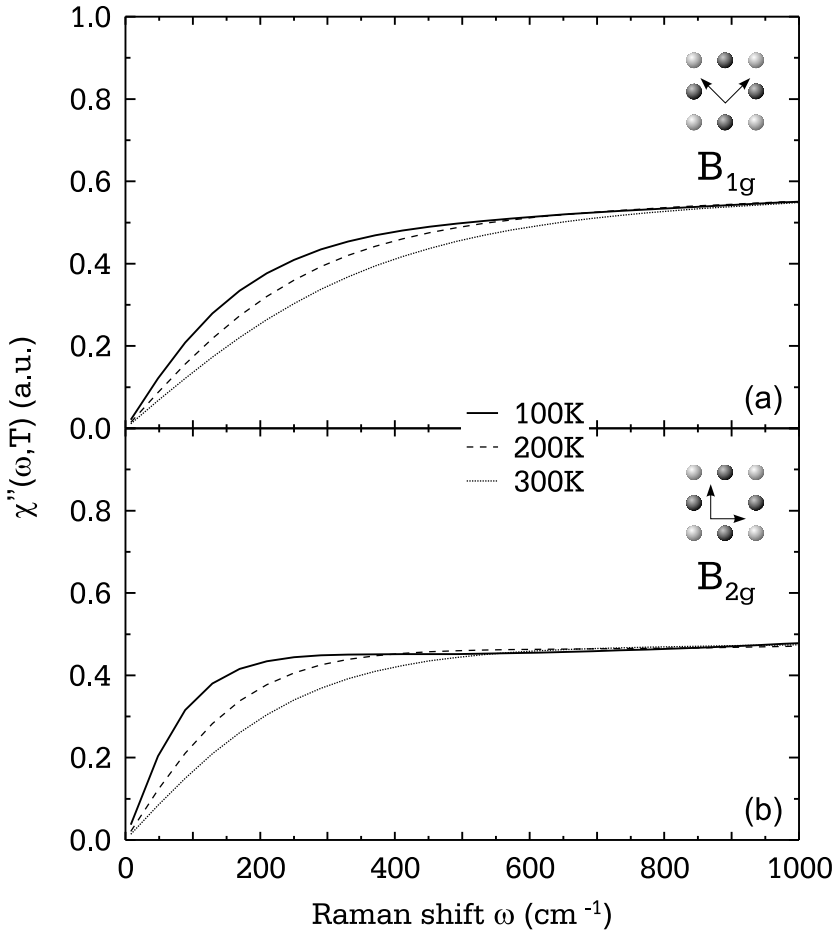

Figure 5.12: *Temperature dependence of the theoretical response in B_{1g} (a) and in B_{2g} (b) symmetries. The parameters used for the plot are $\alpha = 1.1$, $\beta = 2$, $C_0 = 9$ meV, and $\omega_0 = 1$ eV.*

with $T_c = 78$ K and $p = 0.20$ (see Tab. 4.3). The fit to the data is performed by adjusting the cutoff frequency $\omega_0 = 5$ meV, which is the only parameter not derived from experimental ARPES measurements. The other parameters are $\alpha = 1.1$, $\beta = 2$, $T = 200$ K and $C_0 = 9$ meV.

As is clear from Fig. 5.13, a good agreement between the theoretical curves and the experimental data is obtained both for the low-frequency spectral shape and the high-frequency continuum in B_{1g} and B_{2g} symmetries. From this analysis it appears that the two spectroscopic techniques are consistent in the overdoped regime. In other words, the Raman observations can be understood qualitatively in terms of single-particle properties as detected by photoemission.

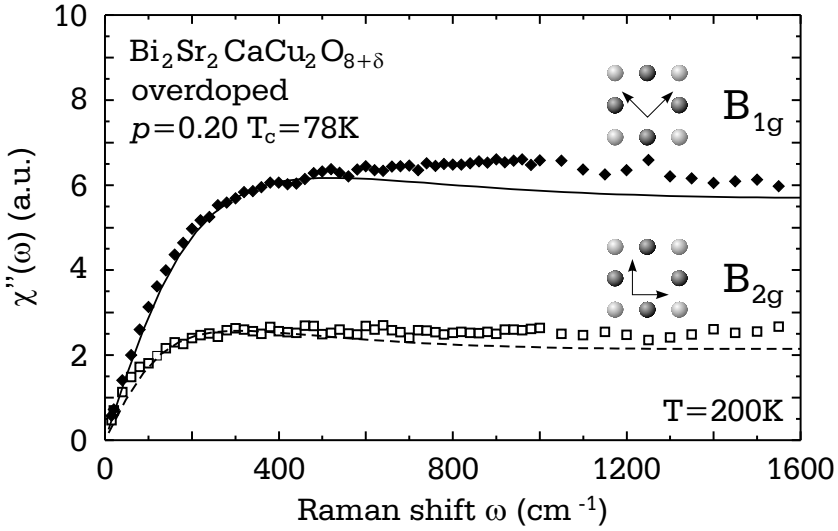

Figure 5.13: *Comparison between the experimental measurements (points) and the calculated response (lines) in B_{1g} and in B_{2g} symmetries. The parameters used for the plot are $\alpha = 1.1$, $\beta = 2$, $T = 200$ K, $C_0 = 9$ meV, and $\omega_0 = 5$ eV.*

5.5 Experimental indications of many-body effects

In conclusion, through the approach described in this work the experimental Raman spectra can be traced back to an energy, momentum and temperature dependent self energy consistent with photoemission results.

When the carrier concentration is reduced, substantial modifications in the properties of the excitations are expected. From the Raman spectra the anisotropy between the B_{1g} and the B_{2g} responses is strongly doping dependent. In particular, in B_{1g} symmetry the Raman lifetime in the static limit becomes shorter with decreasing carrier concentrations in contrast to the B_{2g} where the doping dependence is only moderate [30]. The question whether this can still be attributed to single-particle self energy properties arises.

The evolution of $\Delta k(\phi)$ with doping has been recently studied in BSCCO by photoemission [15]. Surprisingly, the ϕ dependence of the momentum widths was essentially doping independent. The authors argue that the observed anisotropy could actually be the result of two contributions, the splitting of the band due to the presence of two CuO_2 planes (bilayer splitting) and the angular dependence of the coupling to the interactions. In principle, the two effects could have opposite doping dependences. However, since the anisotropy of the self energy is unaffected by the carrier concentration, it is clear that this alone cannot account for the experimental

Raman results in the optimally and underdoped regimes. These results indicate that the evolution of the Raman spectra with doping cannot be derived only from single-particle properties and is probably to be ascribed to many-body effects.

In Chapter 6 the evolution with doping of the Raman spectra is investigated in detail and discussed within a scenario where a putative quantum phase transition happening in the phase diagram of the cuprates (see also Sect. 2.3) is considered.

Chapter 6

Observation of an unconventional metal-insulator transition above the critical temperature

In the overdoped region of the phase diagram, the observed Raman spectra are consistent with angle-resolved photoemission spectroscopy (ARPES) results, as discussed in Chapter 5. However, when the carrier concentration is reduced the two spectroscopic techniques seem to reveal different properties of the dynamics of the carriers. In fact, while the single-particle self energy (see Sect. 5.4.1) does not display substantial variations with doping [15], the Raman spectra undergo dramatic modifications [30].

To solve this inconsistency, detailed measurements of the Raman spectra in BSCCO in the normal state over a wide doping range are presented in this chapter. As a result of the study of the temperature and symmetry dependence of the Raman measurements, a strong anisotropy of the electronic relaxation rates is observed which cannot be explained by single-particle properties alone. Therefore, a new phenomenological model is developed here, which allows a quantitative understanding of the Raman results in terms of an unconventional metal-insulator transition. The results in other compounds, YBCO and LSCO, are also presented for comparison.

6.1 Experimental results in $Bi_2Sr_2CaCu_2O_{8+\delta}$

The experiments on BSCCO have been performed on the set of crystals Opt92, OD78, OD62 and OD56 (Tab. 4.3). The samples in the crucial doping range (OD62, OD56) were obtained from the same extremely homogeneous overdoped single crystal (OD78) cut in pieces and annealed in different oxygen partial pressures, as de-

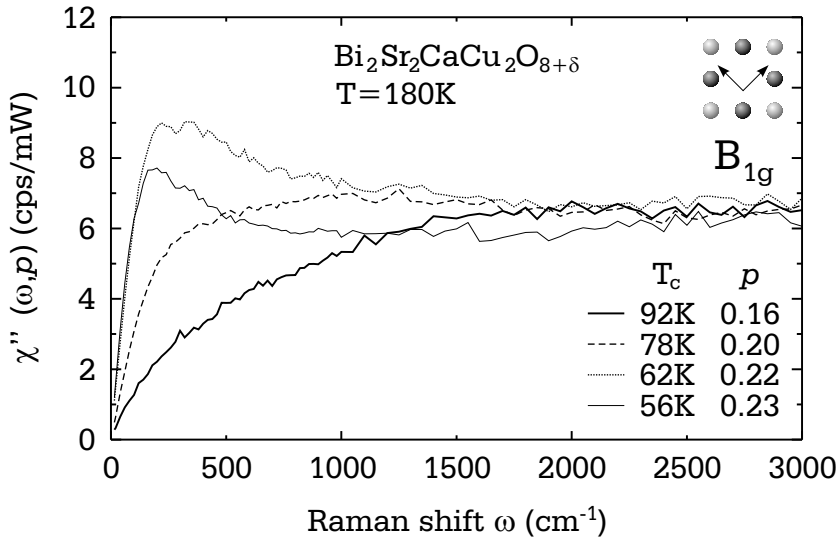

Figure 6.1: *Electronic Raman response at $T = 180$ K in B_{1g} symmetry of differently doped samples. The critical temperature and the doping level are indicated.*

scribed in Sect. 4.1.3.

The electronic Raman response $\chi''(\omega, p)$ for differently doped samples at a fixed temperature $T = 180$ K is shown in Fig. 6.1 for B_{1g} symmetry and in Fig. 6.2 for B_{2g} symmetry. The contribution of the lattice vibrations has been subtracted out. The overall intensities of the spectra are adjusted by a multiplicative constant to allow the comparison of the spectral shapes at low frequencies. The doping dependence of the intensity at $800 - 1000$ cm^{-1} is discussed in Sect. 7.1 and in [30].

By comparing the sets of spectra in the two symmetries, it is clear that the Raman response $\chi''(\omega, p)$ shows a very different evolution with doping. In B_{1g} symmetry (Fig. 6.1) the response is strongly suppressed below 2000 cm^{-1}, indicating the opening of a gap in the electronic excitation spectrum upon decreasing carrier concentration. In contrast, in B_{2g} symmetry (Fig. 6.2) there is only a very weak doping dependence, as if a gap would exist only for the antinodal quasiparticles.

The evolution of the spectra with the carrier concentration is best evinced when also the temperature dependence is studied. In Fig. 6.3 the raw Raman spectra of the strongly overdoped sample OD62 are shown for B_{1g} (a) and for B_{2g} (b) symmetries in the normal state at 206 K, 114 K and 80 K. The temperatures discussed here are already corrected to include the heating of the sample due to the absorption of the laser light. The sharper features superimposed on the broad electronic continuum are due to lattice vibrations. The low-frequency response ($\omega < 200$ cm^{-1}) depends

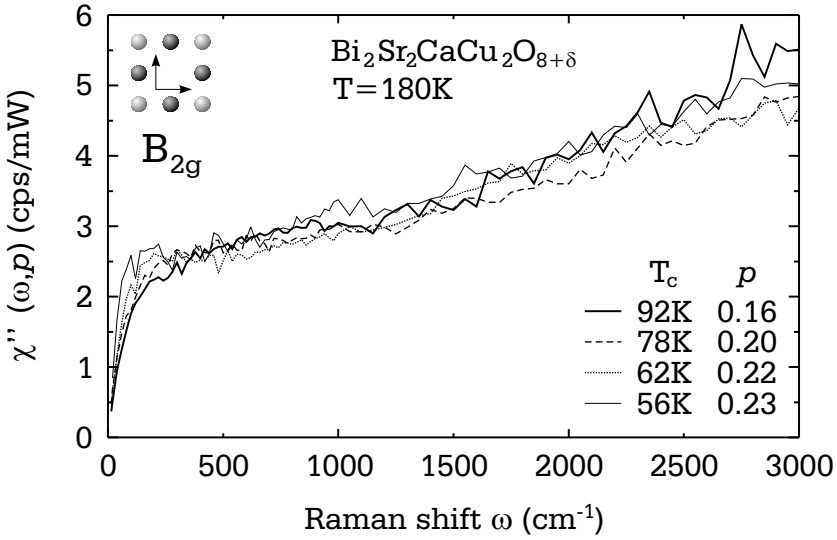

Figure 6.2: *Electronic Raman response at $T = 180$ K in B_{2g} symmetry of differently doped samples. The critical temperature and the doping level are indicated.*

on temperature in a rather similar way in the two symmetries: the initial slope of the spectra, which is proportional to the lifetime of the carriers, decreases with increasing temperature, indicating typical metallic behaviour.

The previous observations can be compared with measurements for another overdoped sample (OD78) with a smaller carrier concentration. The Raman response in B_{2g} symmetry is shown in Fig. 6.4 (b) at the three temperatures, 242 K, 190 K and 91 K. The spectra in this symmetry are similar in shape and temperature evolution to those of the strongly overdoped sample (OD62, Fig. 6.3 (b)). In the B_{1g} channel, however, there is hardly any temperature dependence at all for the sample with $p = 0.20$ (Fig. 6.4 (a)).

Finally, the results for a slightly underdoped sample with $T_c = 92$ K and $p = 0.15$ [90] are shown for comparison in Fig. 6.5. While in B_{2g} symmetry (panel (b)) there is still a decrease of the slope at low frequencies with increasing temperature, just the opposite temperature dependence is observed in B_{1g} symmetry (panel (a)). With increasing temperature the slope of the spectra and, therefore, the lifetime of the carriers also increases indicating non-metallic behaviour.

Summarizing, while the overall continuum in B_{2g} geometry is relatively doping independent and has a temperature evolution typical for metallic behaviour, it shows a non-trivial dependence on doping and temperature in B_{1g} symmetry: the slope of the low-frequency response decreases with increasing T in a way similar to that in

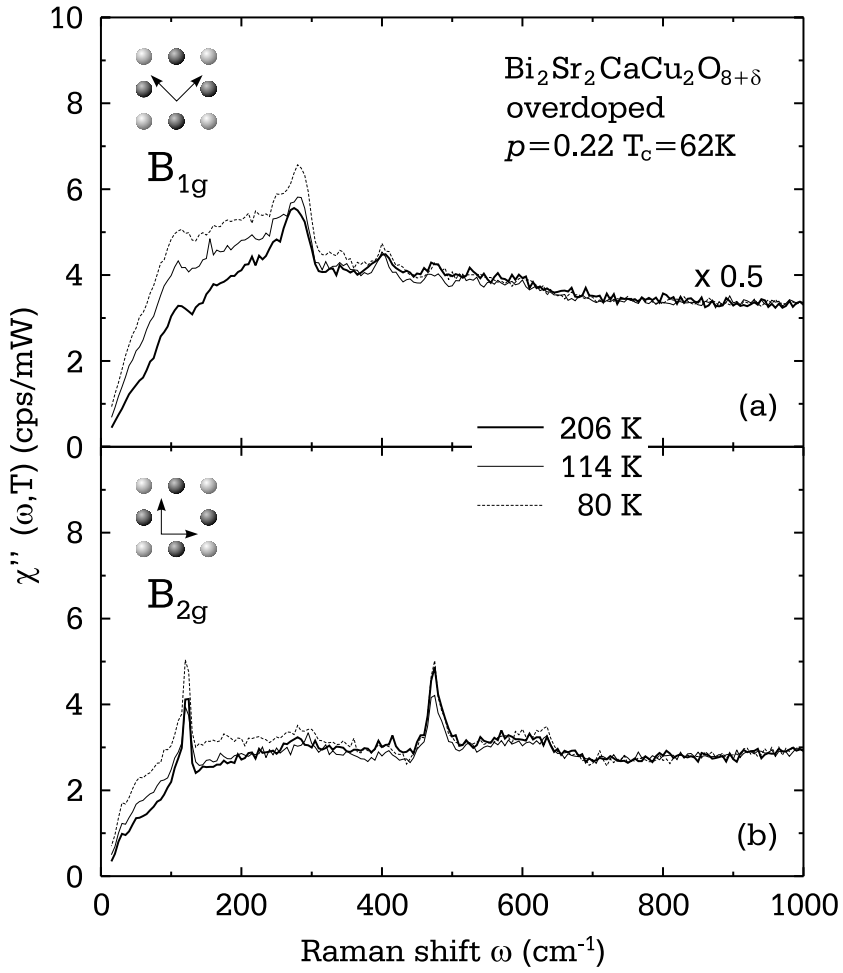

Figure 6.3: *Raman response $\chi''(\omega, T)$ of the overdoped BSCCO sample OD62 at different temperatures as indicated in the figure. In panels (a) and (b) B_{1g} and B_{2g} symmetries, respectively, are shown. The spectra in B_{1g} symmetry have been multiplied by 0.5 to show the data on the same scale as in Fig. 6.4 and Fig. 6.5.*

B_{2g} symmetry for the strongly overdoped sample (Fig. 6.3), becomes temperature independent near optimal doping $p \geq 0.16$ (Fig. 6.4), and starts to increase with increasing T just below optimal doping (Fig. 6.5).

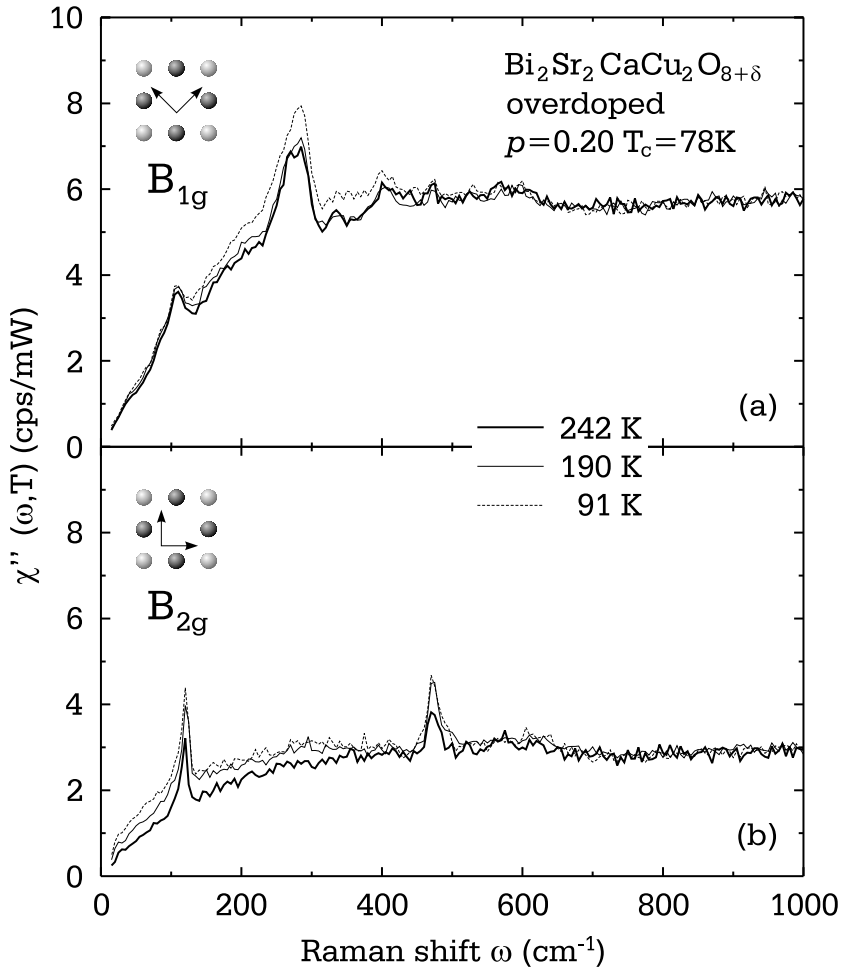

Figure 6.4: *Raman response $\chi''(\omega, T)$ of the overdoped BSCCO sample with $T_c = 78$ K at different temperatures as indicated in the figure. In panels (a) and (b) B_{1g} and B_{2g} symmetries, respectively, are shown.*

6.2 Doping dependence of the Raman relaxation rates

To better quantify the dynamics of the carriers and to study its evolution with temperature and doping, the Raman relaxation rates can be extracted from the measured response $\chi''(\omega, T, p)$. The method to calculate $\Gamma(\omega, T, p)$ is briefly described in Sect. 3.4.

The dynamical relaxation rates for the samples OD62 and OD78, whose raw Raman spectra are shown in Fig. 6.3 and Fig. 6.4, are displayed as a function of temperature in Fig. 6.6. Both in B_{1g} (a,b) and B_{2g} (c,d) symmetries, the frequency dependence of the quasiparticle relaxation rates shows only little dependence on momentum and doping. As compared to results at lower doping levels [30] a ten-

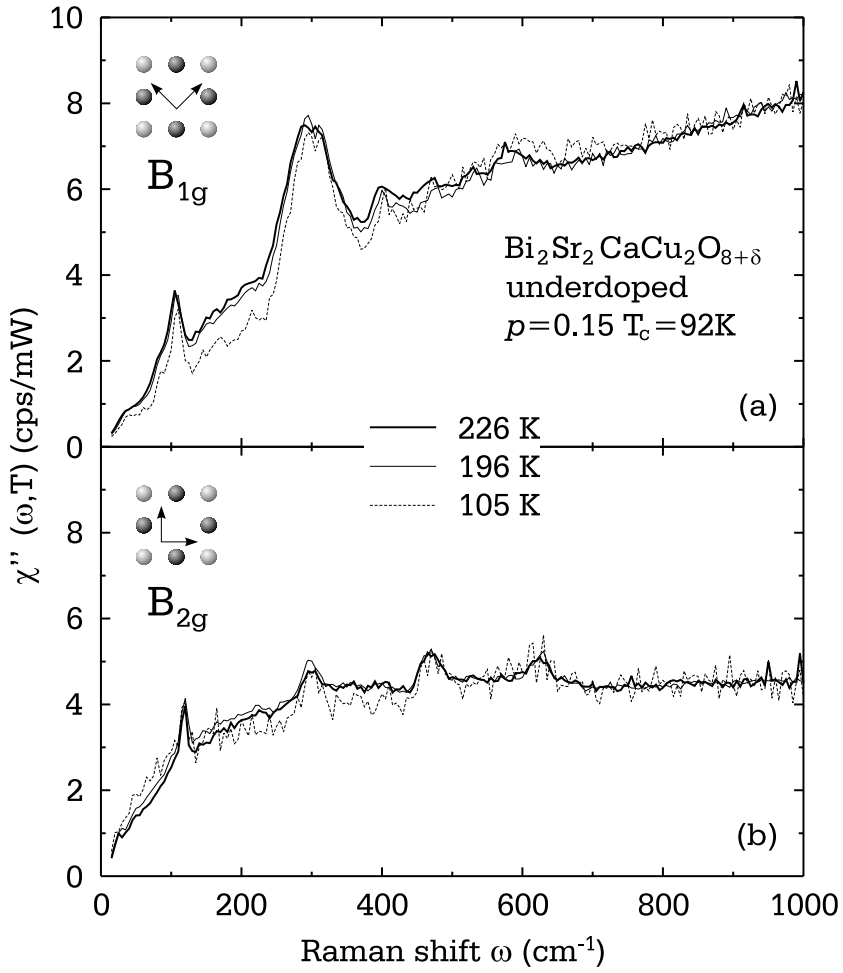

Figure 6.5: *Raman response $\chi''(\omega, T)$ of an underdoped BSCCO sample with $p = 0.15$ at different temperatures from Ref. [90]. In panels (a) and (b) B_{1g} and B_{2g} symmetry results are shown, respectively.*

dency to a more quadratic frequency dependence below approximately 400 cm^{-1} in B_{1g} symmetry is found here, possibly indicating more conventional quasiparticle dynamics.

The static relaxation rate obtained in the *dc* limit, $\Gamma_0(T) \equiv \Gamma(\omega \to 0, T)$, represents the inverse of the quasiparticle lifetime and therefore has a significance similar to the transport resistivity in a conventional metal. As visible from Fig. 6.6, the dependence of the *dc* limit of the relaxation rates on temperature evolves differently with doping in the two symmetries: while $\Gamma_0^{B_{2g}}(T)$ decreases with temperature at both doping levels (Fig. 6.6 (c,d)) consistent with ordinary and optical transport [91], $\Gamma_0^{B_{1g}}(T)$ is essentially temperature independent for $p = 0.20$ and assumes the

B_{2g} behaviour at $p \geq 0.22$ [92].

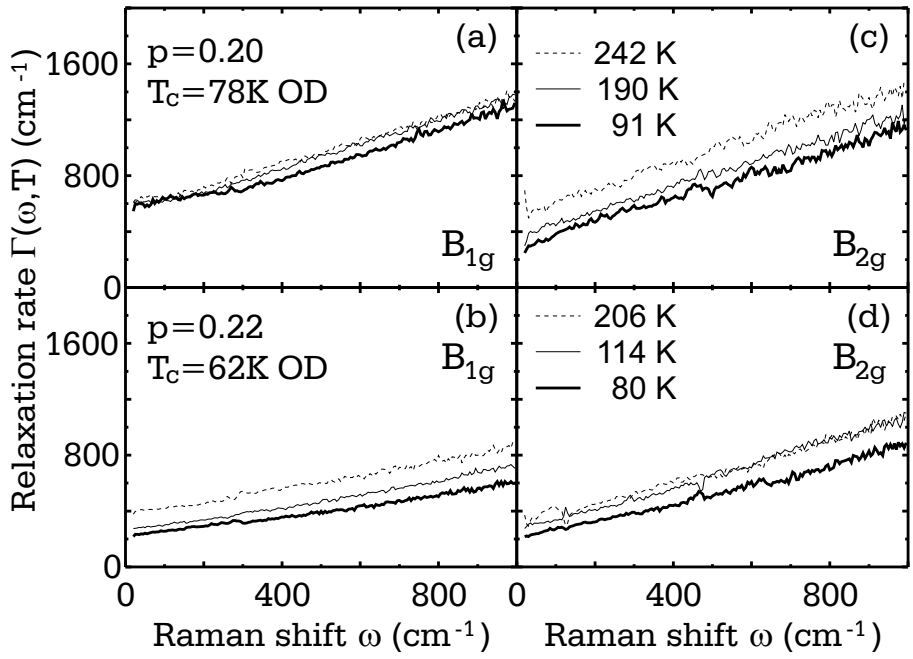

Figure 6.6: *Relaxation rates in B_{1g} (a,b) and B_{2g} (c,d) symmetries at different temperatures for the two overdoped samples OD78 and OD62.*

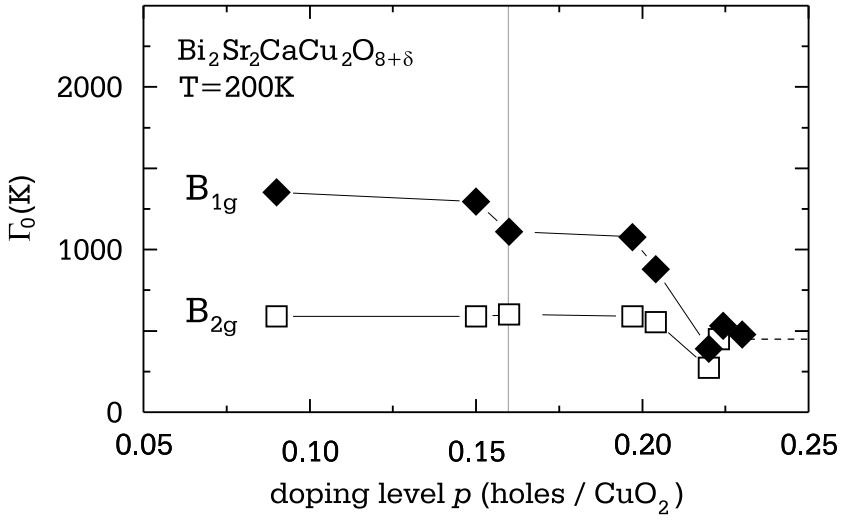

Figure 6.7: *Static relaxation rates in B_{1g} and B_{2g} symmetries as a function of doping p at a fixed temperature $T = 200$ K. Results from previous measurements [90] are also included. The grey line marks optimal doping.*

The doping dependence of the static relaxation rates at a fixed temperature $T = 200$ K is summarized in Fig. 6.7, where results from previous measurements [90] are included for completeness. The error on Γ_0 is of the size of the points in Fig. 6.7. The strong anisotropy between the two symmetries is clearly visible up to $p \simeq 0.21$. The magnitude of $\Gamma_0^{B_{1g}}$ decreases by approximately 70% for $0.09 \leq p \leq 0.22$ while $\Gamma_0^{B_{2g}}$ is almost constant up to $p \simeq 0.20$ and changes by only 30% in the narrow range $0.20 < p < 0.22$. In particular, a crossover for $0.20 < p < 0.22$ is clearly visible where the Raman relaxation rates rapidly decrease, and the anisotropy vanishes. Since the changes for $0.20 < p < 0.22$ are observed for a set of samples prepared from a single homogeneous piece, the observed features are robust and not related to differences in sample quality.

The variations of the relaxation rates with temperature $\partial\Gamma_0(T,p)/\partial T$ as a function of doping are shown in Fig. 6.8 (a) at a fixed temperature $T = 200$ K. The error in both panels of Fig. 6.8 is of the size of the points. In B_{1g} symmetry, which probes mainly the nodal quasiparticles (see Sect. 2.6), $\partial\Gamma_0(T,p)/\partial T$ deviates only little from 2 in the entire doping range. The logarithmic derivative $\partial[\ln\Gamma_0^{B_{2g}}(T)]/\partial(\ln T)$ in Fig. 6.8 (b) demonstrates that $\Gamma_0^{B_{2g}}(T)$ varies essentially linearly with temperature. The two observations suggest that $\Gamma_0^{B_{2g}}(T)$ varies as $\Gamma_0^{B_{2g}}(T,p) \simeq 2k_BT$. In contrast, $\partial\Gamma_0^{B_{1g}}(T,p)/\partial T$, which reflects the dynamics of the anti-nodal quasiparticles, is strongly temperature dependent, increases continuously with p and changes sign close to optimal doping. For $p \geq 0.22$, also for $\partial\Gamma_0^{\mu}(T,p)/\partial T$, with $\mu = B_{1g}, B_{2g}$, any kind of anisotropy disappears.

It is both the apparent symmetry dependence of the relaxation rates, $\Gamma_0^{B_{2g}} < \Gamma_0^{B_{1g}}$ (Fig. 6.7 (a)), and the characteristic increase of the relaxation rate toward lower temperature, $\partial\Gamma_0^{B_{1g}}(T)/\partial T < 0$ for $p \leq 0.16$ (Fig. 6.7 (b)), which indicate that there is not only a gap but also a strong anisotropy in momentum space. In particular, since the strongest effects are observed in B_{1g} symmetry, the maxima of such a gap must be located around the Brillouin zone axes (anti-nodal or "hot" region). Thus the "hot" quasiparticles show a crossover from metallic to insulating behaviour near optimal doping while the "cold" quasiparticles are metallic for all dopings at the temperatures examined. In this sense, the observed evolution with doping indicates the existence of an anisotropic or unconventional metal-insulator transition. This is different from a conventional Mott transition [93] since the charge excitations become gapped only on specific areas of the Fermi surface, and the overall *dc* transport remains still metallic.

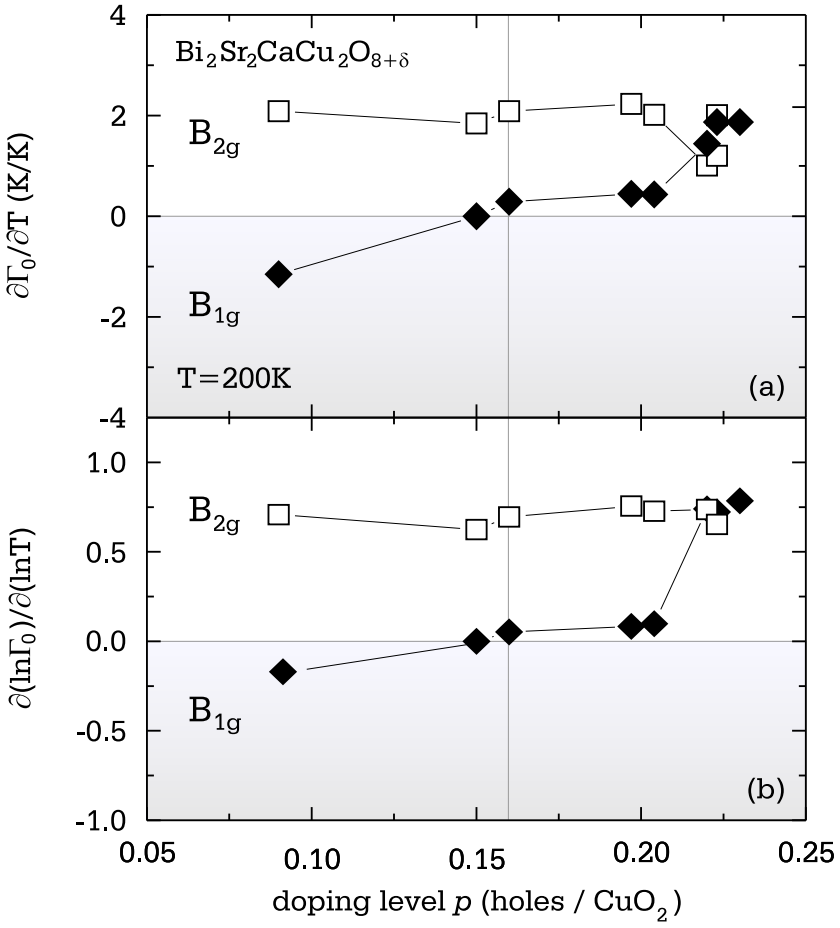

Figure 6.8: *(a) Variation with temperature of the static relaxation rates in B_{1g} and B_{2g} symmetries as a function of doping p at a fixed temperature $T = 200$ K. (b) Logarithmic derivatives of the Raman relaxation rates indicating power-law behaviour in the temperature dependence in B_{2g} symmetry. The grey line marks optimal doping.*

6.3 Theoretical model for the metal-insulator crossover

These experimental results can be understood in terms of an anisotropic gap which develops near the hot spots to minimize strong interactions between the electrons [94]. An exact treatment of non-resonant electronic Raman scattering in systems displaying a quantum-critical MIT in the limit of infinite dimensions has been formulated for Hamiltonians displaying both Fermi-liquid and non-Fermi-liquid ground states [95, 96]. However, the development of an anisotropic gap and its effect on the Raman response have not been investigated yet. Therefore, a phenomenological

treatment for a system near a quantum phase transition has been considered in this work, focusing on the effect of an anisotropic, doping-dependent gap in the charge channel, $\Delta_C(p)$.

The observation of non-metallic behaviour of quasiparticles with momenta along the axes of the Brillouin zone indicates that the gap is compatible with $\mid d_{x^2-y^2} \mid$ symmetry. Therefore, the simplest form which is maximal along the axes and vanishes along the Brillouin zone diagonals is considered here

$$\Delta_C(p,\phi) = \Delta_C(p)\cos^2(2\phi) \tag{6.1}$$

with ϕ the azimuthal angle on a cylindrical Fermi surface and $\Delta_C(p)$ the doping dependent magnitude. The doping dependence is postulated to be of the form

$$\Delta_C(p) = \Delta_C(0)\left(1-\frac{p}{p_c}\right)^{\zeta} \tag{6.2}$$

with p_c the critical doping and $\Delta_C(0)$ the maximum value of the gap that, together with the exponent ζ, has to be determined by comparison with the experimental results.

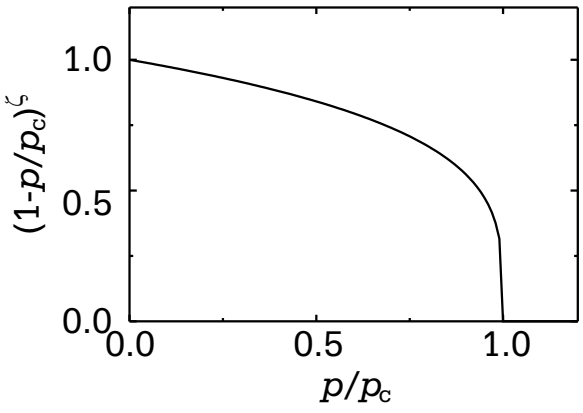

Figure 6.9: *Doping dependence of the charge gap in normalized units.*

The doping dependence of the gap given by Eq. (6.2) is shown in Fig. 6.9 for the exponent $\zeta = 1/4$. For doping levels larger than p_c the gap is closed and the dynamics of the quasiparticles is metallic. For $p < p_c$ the gap increases in magnitude with decreasing p.

The effect of this gap is to reduce the number of states participating in the conduction of "hot" quasiparticles by depleting the conduction band as shown schematically in Fig. 6.10. The available states are those located in either part of the band with a total width E_b separated symmetrically with respect to the chemical potential by $\pm\Delta_C/2$. Note that the gap Δ_C should be considered an activation energy for moving a particle rather than a single particle gap.

As described in Sect. 3.3.1, the Raman response function in the normal state in given by (Eq. (3.16))

$$\chi''_{\gamma\gamma}(\omega) = \sum_{\mathbf{k}} \gamma_{\mathbf{k}}^2 \int_{-\infty}^{\infty} \frac{dy}{\pi} G''(y,\mathbf{k})G''(y-\omega,\mathbf{k}-\mathbf{q})\left[n_F(y)-n_F(y-\omega)\right] \tag{6.3}$$

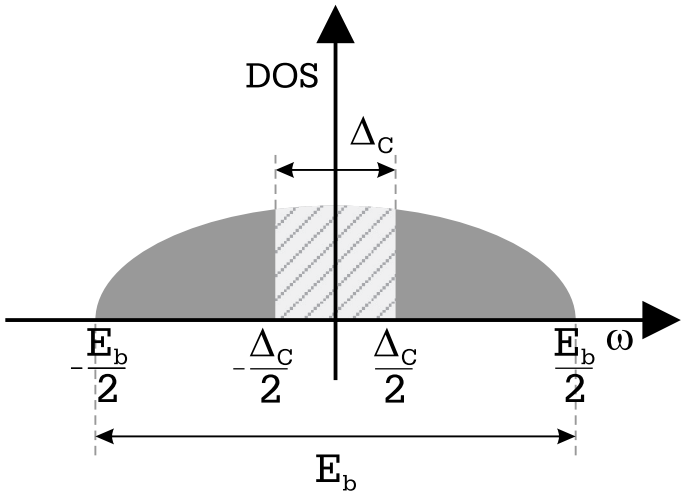

Figure 6.10: *Effect of the opening of a normal state gap, Δ_C, in the band E_b. The energies are referred to the chemical potential.*

where n_F is the Fermi-Dirac distribution function, $\gamma_{\mathbf{k}}$ is the Raman vertex. $\hbar = 1$ and $k_B = 1$ are considered. $G''(y, \mathbf{k})$ is the imaginary part of the renormalized electronic Green function

$$G''(y, \mathbf{k}) = \frac{\Sigma''(y, \mathbf{k})}{(y - \xi_{\mathbf{k}} - \Sigma'(y, \mathbf{k}))^2 + (\Sigma''(y, \mathbf{k}))^2} \tag{6.4}$$

with $\xi_{\mathbf{k}} = \varepsilon_{\mathbf{k}} - \mu$ the band dispersion.

Following the same approximations as in Sect. 5.4.2, the Raman response can be finally written (Eq. (5.17)) as

$$\chi''_{\gamma\gamma}(\omega) = N_F \int_{-\infty}^{\infty} dy \, [n_F(y - \omega) - n_F(y)] \int_0^{2\pi} d\phi \gamma^2(\phi) \frac{\Sigma''(y - \omega, \phi) + \Sigma''(y, \phi)}{[\Sigma'(y - \omega, \phi) - \Sigma'(y, \phi) + \omega)]^2 + [\Sigma''(y - \omega, \phi) + \Sigma''(y - \omega, \phi)]^2} \tag{6.5}$$

Next, some modeling is necessary for the momentum, energy and temperature dependence of the self energy. In this chapter $\Sigma''(\mathbf{k}, \omega)$ is approximated to be momentum independent. Although as described in Chapter 5 the self energy possesses a modulation along the Fermi surface with the maximum at the "hot" spots and the minimum along the Brillouin zone diagonals (Fig. 5.8), this effect does not essentially vary with doping [15] and, therefore, cannot account for the evolution of $\Gamma_0^{B_{1g}}$ and $\Gamma_0^{B_{2g}}$ with the carrier concentration. So, the self energy is taken as

$$\Sigma''(\mathbf{k}, \omega) \equiv \Sigma'' = \text{const} \ . \tag{6.6}$$

Photoemission results have also shown that $\Sigma''(\mathbf{k}, \omega)$ does not display any energy dependence for $\omega < 2.5\, T$,(Fig. 5.10), but rather increases linearly with temperature

[97, 78]. As the calculation is performed in the static limit ($\omega \to 0$), the self energy can be consistently approximated by $\Sigma''(T) \propto T$.

With these approximations Eq. (6.5) reduces to

$$\chi''_{\gamma\gamma}(\omega) = N_F \int_{band} dy \, [n_F(y-\omega) - n_F(y)] \int_0^{2\pi} d\phi \gamma^2(\phi) \frac{2\Sigma''}{\omega^2 + [2\Sigma'']^2} \tag{6.7}$$

The energy integration is performed over the states participating in conduction (schematically colored in dark grey in Fig. 6.10). Finally, taking the limit $\omega \to 0$ in Eq. (6.7) the Raman response becomes

$$\chi''_{\gamma\gamma}(\omega \to 0) = N_F \int_0^{2\pi} d\phi \; \gamma^2(\phi) \int_{band} \frac{dy}{\pi}(-\omega) \frac{\partial n_F(y)}{\partial y} \frac{1}{2\Sigma''} \tag{6.8}$$

Given the symmetry of the integrand function, Eq. (6.8) can be rewritten as

$$\chi''_{\gamma\gamma}(\omega \to 0) = -\omega \; \frac{N_F}{2\Sigma''} \; \frac{2}{\pi} \int_0^{2\pi} d\phi \gamma^2(\phi) \left[n_F\left(\frac{E_b}{2}\right) - n_F\left(\frac{\Delta_C(\phi,p)}{2}\right)\right] \tag{6.9}$$

with $\Delta_C(\phi, p)$ given by Eq. (6.1) and Eq. (6.2). The static Raman relaxation rate is defined as the inverse of the slope of the Raman spectra for vanishing frequencies, that is

$$\Gamma_0(T,p) = \left(\frac{\partial \chi''}{\partial \omega}(\omega \to 0) \right)^{-1} \tag{6.10}$$

From Eq. (6.9) it follows that

$$\Gamma_0(T,p) = \left\{ \frac{N_F}{\pi\Sigma''} \int_0^{2\pi} d\phi \left[\gamma^2(\phi) n_F\left(\frac{\Delta_C(\phi,p)}{2}\right)\right] - 4 n_F\left(\frac{E_b}{2}\right) \right\}^{-1} . \tag{6.11}$$

In the limit $E_b \gg T$, which applies because E_b of the order of 10^5 K and T of the order of 10^2 K,

$$\Gamma_0(T,p) = \frac{\pi\Sigma''}{N_F} \left\{ \int_0^{2\pi} d\phi \left[\gamma^2(\phi) n_F\left(\frac{\Delta_C(\phi,p)}{2}\right)\right] \right\}^{-1} . \tag{6.12}$$

The relaxation rates calculated from Eq. (6.12) are plotted in Fig. 6.11 for B_{1g} (panel (a)) and B_{2g} (panel (b)) symmetries for different doping levels p/p_c. The temperature corresponding to the experiments is also marked. From the figure it is possible to see that, when the doping level is reduced from $p/p_c = 1$, the slope of the relaxation rates in the B_{1g} symmetry at a fixed temperature decreases and eventually changes sign at a doping concentration which depends on the temperature. In B_{2g} symmetry no substantial variations are observed.

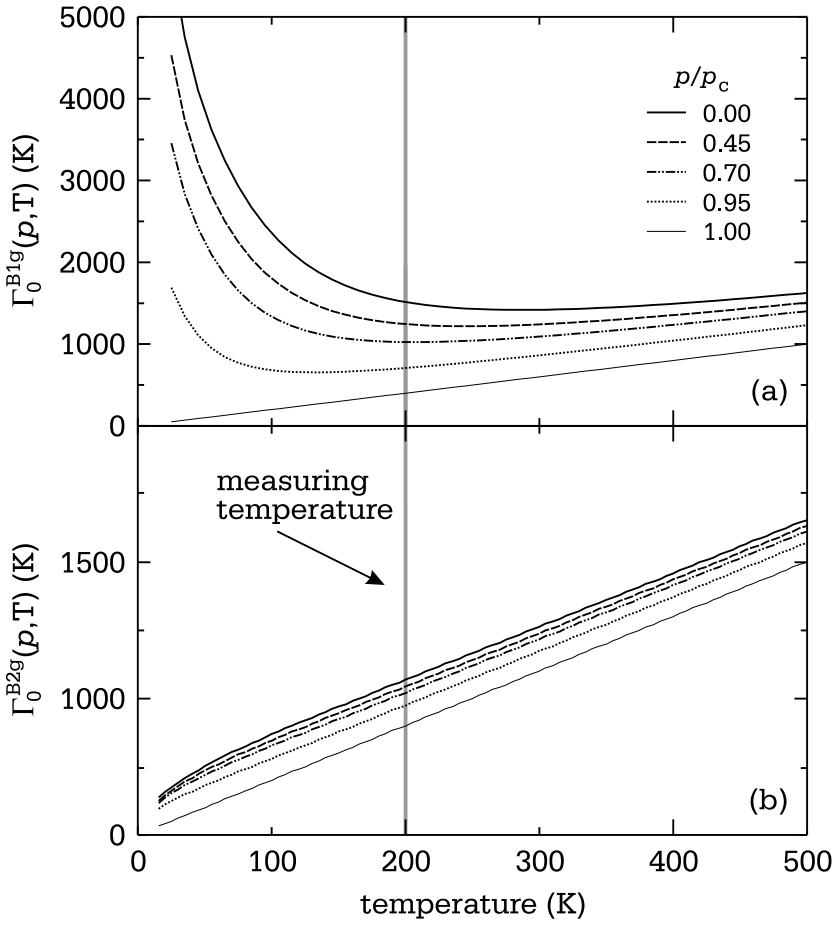

Figure 6.11: *Temperature dependence of the static relaxation rates in the B_{1g} and B_{1g} symmetries for different doping levels p/p_c. The temperatures at which the experiments are performed is indicated.*

6.4 Unconventional metal-insulator transition in the overdoped regime

The comparison between the experimental static relaxation rates (Fig. 6.7) and the model described (Sect. 6.3) is shown in Fig. 6.12. The theoretical curves have been calculated from Eq. (6.12) with $\Delta_C(0) = 1100$ K, and $\zeta = 0.25$. In B_{2g} symmetry which reflects *dc* and optical transport properties [30], the influence of the gap is weak, and the temperature dependence comes essentially from $\Sigma''(T)$. This explains why in conventional transport the MIT is observed at much lower temperatures if at all. The general trend of the B_{1g} rates, in particular the sign change, is well reproduced by the phenomenology in spite of the simplified form considered for Σ'' and for the gap.

These observations strongly suggest that a putative quantum critical point for

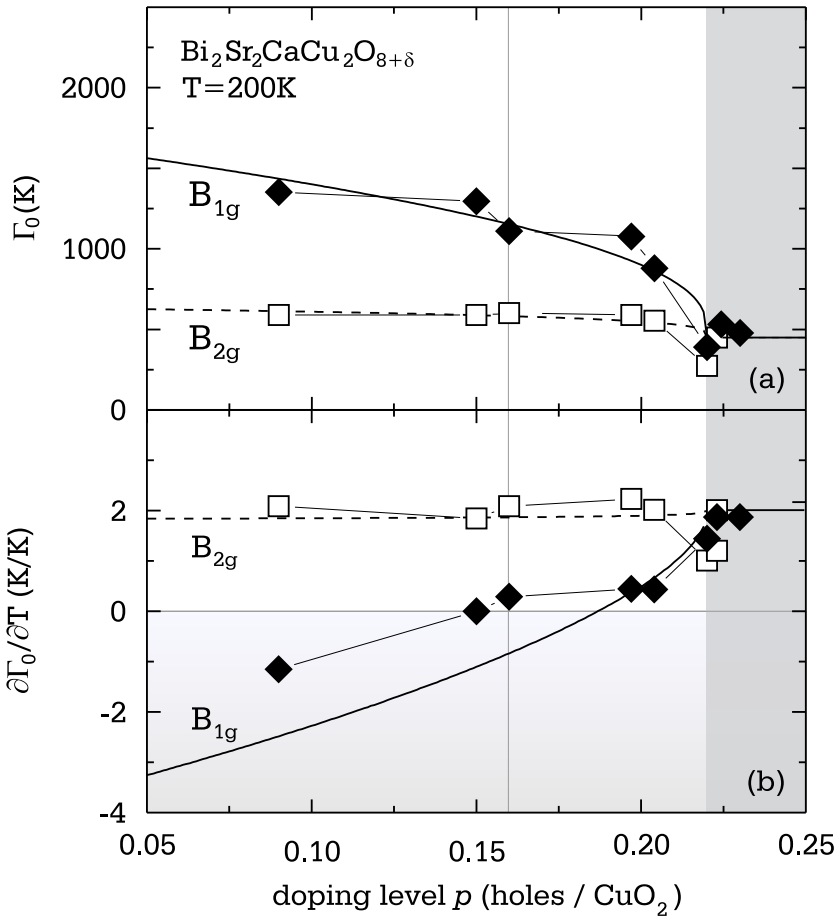

Figure 6.12: *Static relaxation rates, (a), and variation with temperature of the relaxation rate, (b), in B_{1g} and B_{2g} symmetries as a function of doping p at a fixed temperature $T = 200$ K. The solid lines are fits to the data with the parameters $p_c = 0.22$, $\Delta_C(0) = 1100$ K, and $\zeta = 0.25$.*

this material would lie at a doping of $p_c \simeq 0.22$ [98]. Even if this value is higher than $p_c \simeq 0.19$ derived from transport properties [8, 99, 100, 101], the two phenomena are probably directly linked. The differences in the critical doping in transport and Raman can be understood in terms of different selection rules and are a direct effect of the unconventional anisotropic nature of the gap controlling the transition. In fact, while transport is most sensitive to quasiparticles located in the "cold" spots, the possibility of differently weighting the regions on the Fermi surface allows Raman to resolve the MIT up to its very onset at p_c. Since $p_c \simeq 0.22$ is also inferred from the T^0 line [102], Raman scattering probably captures the first onset of non-Fermi liquid behaviour in this compound and can trace it back to a correlation-induced localization of carriers. On the other hand, the pseudogap at T^* does not

fit straightforwardly into this scenario. It either marks a pairing or charge-ordering instability or is connected to T^0 in a more complicated way through fluctuation effects [9].

6.5 Results in other compounds

Finally, the results obtained in BSCCO are compared to those obtained in two other cuprates, YBCO and LSCO.

The temperature dependence of the static relaxation rates in YBCO and its evolution with doping reproduced from [90] is shown in Fig. 6.13. For both symmetries

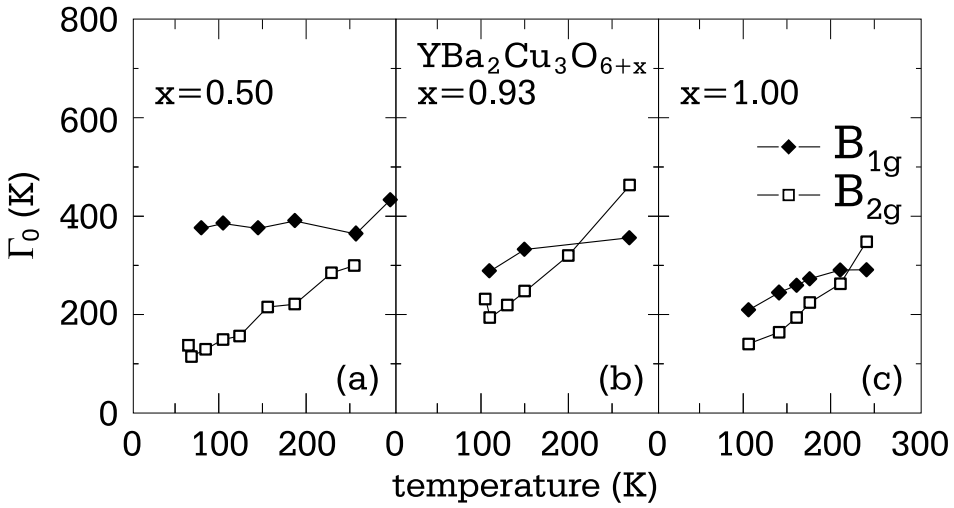

Figure 6.13: *Temperature dependence of the static relaxation rates in YBCO in B_{1g} and B_{2g} symmetries, at different doping levels form [90].*

the overall behaviour is similar to what is observed in BSCCO, especially strong reduction or disappearance of the anisotropy in the scattering rates in the overdoped sample with $x = 1.00$ or $p = 0.19$. As in BSCCO, Γ_0 is linearly increasing with doping in B_{2g} symmetry at all doping levels consistently with transport measurements. Again, $\Gamma_0^{B_{1g}}(T)$ displays an approximately linear temperature dependence only in the overdoped sample, while it becomes almost and completely temperature independent in the optimally ($x = 0.93$) and underdoped ($x = 0.50$) samples, respectively. Hence, the "cold" electrons probed by B_{2g} symmetry display metallic behaviour in the entire doping range studied, while the "hot" ones, probed by B_{1g} symmetry, are metallic only in the overdoped regime. Since $p \geq 0.19$ cannot be

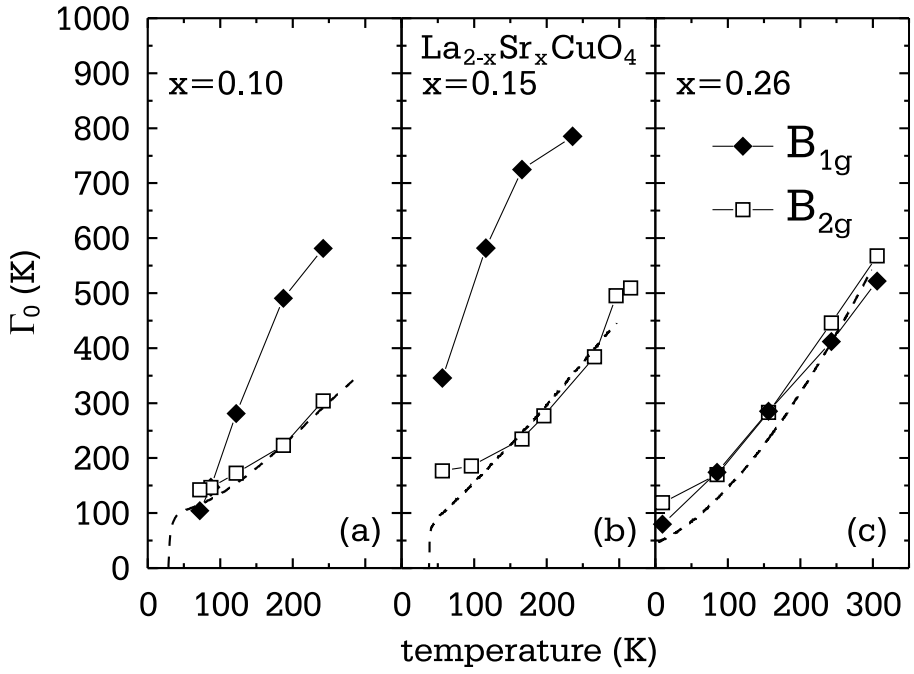

Figure 6.14: *Temperature dependence of the static relaxation rates in LSCO at different doping level as indicated in B_{1g} and B_{2g} symmetries. The dashed lines are relaxation rates calculated from the resistivity through Eq. (6.13).*

accessed in this compound by oxygen doping alone, it is not possible to determine p_c.

The static relaxation rates in the three LSCO samples measured (Tab. 4.1), underdoped ($x = 0.10$), optimally doped ($x = 0.15$) and overdoped but no longer superconducting ($x = 0.26$), are shown in Fig. 6.14. The error on Γ_0 is of the size of the points. In the figure are also plotted (dashed line) the relaxation rates calculated from the resistivity shown in Fig. 4.2 using the Drude expression

$$\Gamma_0(T) = \rho(T)\epsilon_0\omega_{pl}^2 \tag{6.13}$$

with ϵ_0 the permittivity of vacuum and ω_{pl} the plasma frequency. ω_{pl} has been used as a parameter to scale the transport relaxation rates to those measured by Raman; the values used in Fig. 6.14 are $\omega_{pl} = 0.57$, 0.96 and 1.75 eV in the underdoped, optimally and overdoped sample, respectively. The plasma frequencies obtained are close to those extracted from infrared reflectivity [103]. The doping dependence is somewhat stronger, but, given the simplicity of the approach, discrepancies on this scale are not surprising.

Similarly to BSCCO and YBCO, LSCO is also characterized by an anisotropy be-

tween the two symmetries, which vanishes in the overdoped sample, where $\Gamma_0^{B_{1g}}$ and $\Gamma_0^{B_{2g}}$ practically coincide. Also the agreement between $\Gamma_0^{B_{2g}}$ and transport (dashed lines in Fig. 6.14) is observed at all doping levels. However, while a consistent picture for all high-temperature superconductor families studied so far is evolving from the analysis of B_{2g} symmetry, the results in B_{1g} symmetry are quite surprising. They can not be straightforwardly reconciled with the metal-insulator-crossover scenario. It is possible that the expected transition from an essentially isotropic material to a strongly anisotropic one is still occurring when the hole concentration is reduced. Specifically, at high temperatures the magnitudes of the B_{1g} relaxation rates $\Gamma_0^{B_{1g}}$ are much larger than $\Gamma_0^{B_{2g}}$ similarly as in BSCCO and YBCO. However, the increase of $\Gamma_0^{B_{1g}}$ upon cooling, which is considered to be an indication of a gap, is completely absent. At $T < 100$ K $\Gamma_0^{B_{1g}}$ becomes even smaller than $\Gamma_0^{B_{2g}}$ for the underdoped sample with $x = 0.10$ (Fig. 6.14 (a)).

Additional information which can help the understanding of these observations is provided by the comparison with results from other experimental methods. As will described in Chapter 8, there seems to be a clear indication for charge ordering in LSCO with a relatively large correlation length of the one-dimensional domains, that influences also the correlation properties [104]. Therefore, a superposition of two effects is probably observed: at high temperatures the metal-insulator transition dominates the dynamics in B_{1g} symmetry as in the other compounds. For this reason $\Gamma_0^{B_{1g}}$ is still larger than $\Gamma_0^{B_{2g}}$ for almost the entire temperature range. At low temperatures, however, the effect of the gap is overcompensated by the influence of charge ordering which leads to an enhanced conductivity along the principal directions.

6.6 Quantum critical point in the phase diagram of cuprates

The Raman results indicate the existence of a crossover that is at a critical doping $p_c = 0.22$ at $T = 200$ K. This result needs to be compared with the present understanding of the complex phase diagram which characterizes all cuprates (Fig. 2.4).

In the normal state several crossover lines separating regions of the phase diagram with different physical properties are detected by different experimental probes [9]. As introduced in Sect. 2.3, the temperature T^* scale usually identified with the opening of a pseudogap has been observed in many experiments which probe both single-particle properties such as specific heat and angle-resolved photoemission spectroscopy, and many-particle properties such as NMR and transport [16].

An additional crossover at higher temperatures and doping has been determined from anomalies in NMR at T^0 [105, 106].

It has been recently proposed that the peculiar properties of the cuprates both in the normal and in the superconducting states are controlled by a quantum critical point (QCP), which is located in the optimally or slightly overdoped region of the phase diagram [101, 107].

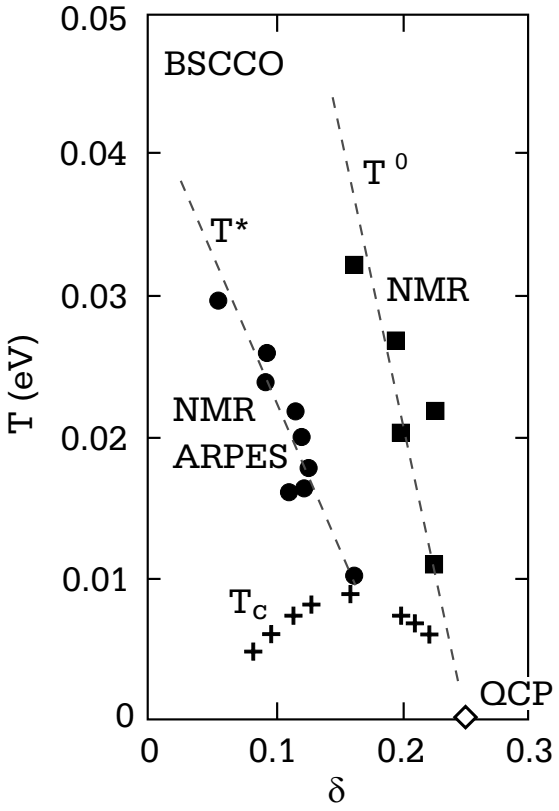

Figure 6.15: *Summary of the relevant energy scales in the phase diagram of BSCCO [9]. The symbols correspond to different experimental measurements, the dashed lines represent the possible crossovers.*

The doping dependence of the relevant energy scales observed in BSCCO by various experimental methods is summarized in Fig. 6.15 [9]. The squares correspond to NMR Knight shift measurements, the circles to ARPES and NMR measurements, and the crosses mark the T_c of part of the samples. The position of the QCP is in the overdoped region around $p \simeq 0.23$. The line T^0 (sometimes also referred to as "weak-pseudogap" crossover [108]) is the critical line which, starting from the QCP, marks the appearance of phonon-induced charge ordering and of the subsequent depression of the single-particle density of states. For $T < T^0$ (p) the critical charge-ordering fluctuations are expected to become substantial. These, which are proposed by the authors of [9] to mediate the effective critical interaction, shift the critical line to T^* at lower temperatures, called "strong-pseudogap" crossover.

Indeed, the existence of a quantum critical point is supported by recent transport experiments on copper oxides with relatively low superconducting transition temperatures T_c [8, 99, 100]. In these materials a metal-insulator transition (MIT) has been observed at very low temperatures in magnetic fields high enough to suppress superconductivity. In fact, the resistivity $\rho(T)$ exhibits a minimum, and such minimum moves to zero temperature with increasing p and disappears close to opti-

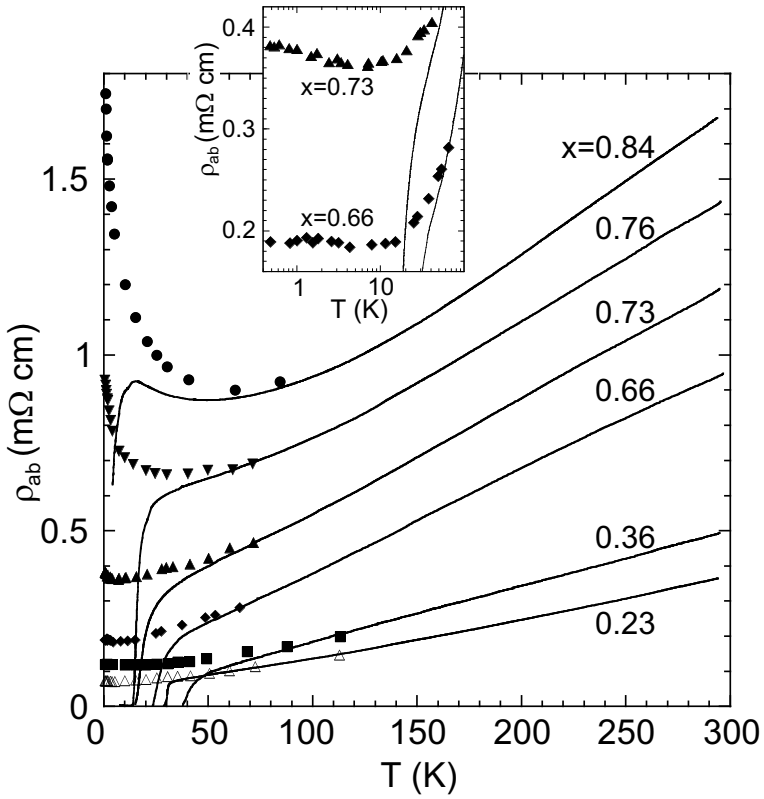

Figure 6.16: *Temperature dependence of the in-plane resistivity ρ_{ab} of differently doped $Bi_2Sr_{2-x}La_xCuO_{6+\delta}$ crystals measured without (solid lines), and with (points) applied magnetic field [99]. The inset shows the low temperature behaviour of the $x = 0.66$ and $x = 0.73$ samples.*

mal doping, $p \simeq 0.16$. This is shown in Fig. 6.16 where the temperature dependence of the in-plane resistivity ρ_{ab} is plotted for differently doped $Bi_2Sr_{2-x}La_xCuO_{6+\delta}$ crystals [99]. In zero magnetic field applied (solid lines) all samples except for the most underdoped one with $x = 0.84$ display a metallic behaviour above T_c. When a magnetic field of 60 T is applied (points), a clear upturn is observed in the resistivity indicating non metallic behaviour. The inset shows the low temperature behaviour of the samples with $x = 0.66$ and $x = 0.73$, the doping values at which the upturn starts to be observed. The doping dependence of the minimum in the resistivity curves is also visible in Fig. 6.16. Since $\rho(T)$ has no characteristic energy scale other than the temperature itself, this MIT has been ascribed to the existence of a nearby quantum-critical point (QCP). Although many scenarios have been proposed, there is not yet a picture which has been able to reproduce the complex behaviour of the electron dynamics over a wide range of doping levels and reconcile the results from various experimental methods.

In conclusion, the existence of a quantum phase transition seems to be a general

feature of the cuprates although the critical doping depends on the material class as demonstrated for low T_c compounds [8, 99, 100]. This quantum phase transition can be described phenomenologically in terms of a generalized metal-insulator transition with a strongly anisotropic doping dependent gap. In LSCO the influence of such a transition on the Raman spectra seems to be masked by a charge-ordering instability.

Chapter 7

Electronic anisotropies below the critical temperature

The observation of an unconventional metal-insulator transition in the overdoped region of the phase diagram raises the question of whether there is a corresponding phenomenon below the critical temperature. It is therefore of great interest to study the anisotropy in the electronic properties and its evolution with carrier concentration in the superconducting state. Indeed, from the analysis of the polarization dependent response the d-wave character of the superconducting energy gap has been successfully observed [109].

Raman studies of the electron properties below T_c have already been carried out for various doping levels in BSCCO, YBCO and LSCO [30, 110, 111, 112]. However, several issues remain still unclarified, particularly the evolution of the electronic properties with the carrier concentration. The superconducting energy gap itself, fundamental for the quest of the pairing mechanism, seems to elude clear understanding. This manifests itself most clearly in the different energy scales obtained by different investigation techniques [25].

In this chapter a detailed characterization of the superconducting spectra is presented throughout a wide region of the phase diagram. The different evolution of the electronic contributions detected in B_{1g} and B_{2g} symmetries may play a key role in understanding the nature of the pairing state.

7.1 Doping dependence of the electronic Raman spectra

The Raman experiments were performed on differently doped BSCCO (Opt92, OD78, OD62 and OD56 in Tab. 4.3), and on underdoped and optimally doped LSCO single crystals (UD and Opt in Tab. 4.1).

The evolution with carrier concentration p of the spectra in B_{1g} symmetry at approximately 10 K and 90 K is shown in Fig. 7.1. The spectra of two underdoped samples measured previously [113] are also included for comparison. The B_{2g} spectra of the same samples are shown in Fig. 7.2. The contribution from phonon excitations has been subtracted out in all spectra except in the B_{2g} response of the OD56 sample (Fig. 7.2 (a)). The data are plotted as a function of energy normalized to the respective transition temperatures of the samples to separate the scaling with T_c from other changes as a function of the doping level.

The superconductivity-induced features in B_{1g} and B_{2g} symmetries show a very different scaling behaviour with the carrier concentration. In B_{1g} symmetry, as the carrier concentration decreases from overdoped, Fig. 7.1 (a), to underdoped, Fig. 7.1 (e), the spectrum undergoes substantial modifications. In particular, the intensity is strongly suppressed upon reducing the doping level. In the strongly underdoped sample ($p < 0.15$, Fig. 7.1 (e)) there is no evidence of a superconductivity-induced feature, consistent with what was previously reported in YBCO [111]. The energy of the superconductivity-induced feature $\hbar\omega_{peak}^{B_{1g}}$, marked by a dark-grey arrow, is also strongly affected by doping, moving from $\hbar\omega_{peak}^{B_{1g}}/k_BT_c \approx 4.5$ in the most overdoped sample (Fig. 7.1 (a)) to $\hbar\omega_{peak}^{B_{1g}}/k_BT_c \approx 9.4$ in the slightly underdoped one (Fig. 7.1 (d)). In conclusion, the energy of the superconductivity-induced peak in B_{1g} symmetry does not scale with T_c but rather has a stronger dependence on doping p.

In contrast, the B_{2g} spectra (Fig. 7.2) show a superconducting peak at all doping levels. The maxima of the superconducting spectra $\hbar\omega_{peak}^{B_{2g}}/k_BT_c$ are approximately constant between 6 and 6.5, with the exception of the most overdoped sample (Fig. 7.2 (a)).

The intensity of the spectra at high energies ($\hbar\omega > 12k_BT_c$) in the two symmetries depends differently on doping. In B_{2g} symmetry a stronger dependence is observed: the intensity increases by a factor of two from the most overdoped (Fig. 7.2 (a)) to the optimally doped sample (Fig. 7.2 (c)), being maximal in the slightly underdoped one (Fig. 7.2 (d)) and decreasing again toward stronger underdoping (Fig. 7.2 (e)). In B_{1g} symmetry no substantial change is observed from

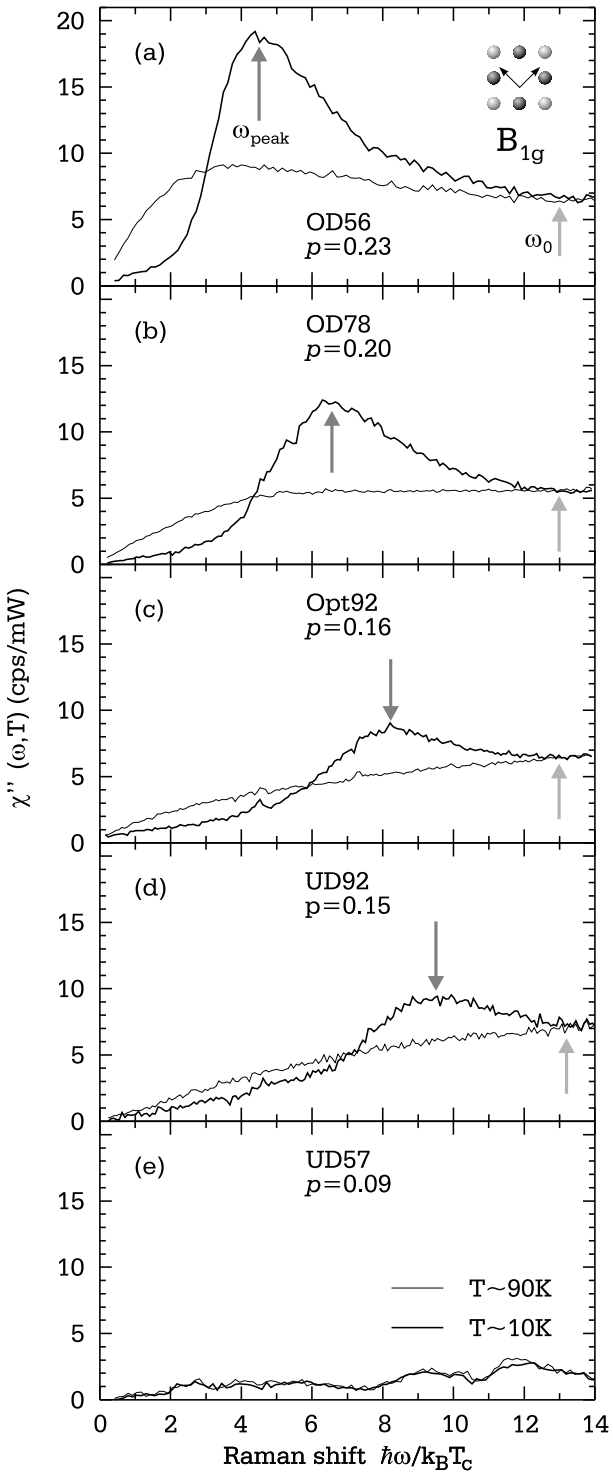

Figure 7.1: *Doping dependence of the Raman response $\chi''(\omega)$ in B_{1g} symmetry in the normal and superconducting states. Panels (d,e) are from [113]. The data are plotted as a function of energy normalized to the respective transition temperatures T_c of the samples. The arrows mark the energies ω_{peak} and ω_0.*

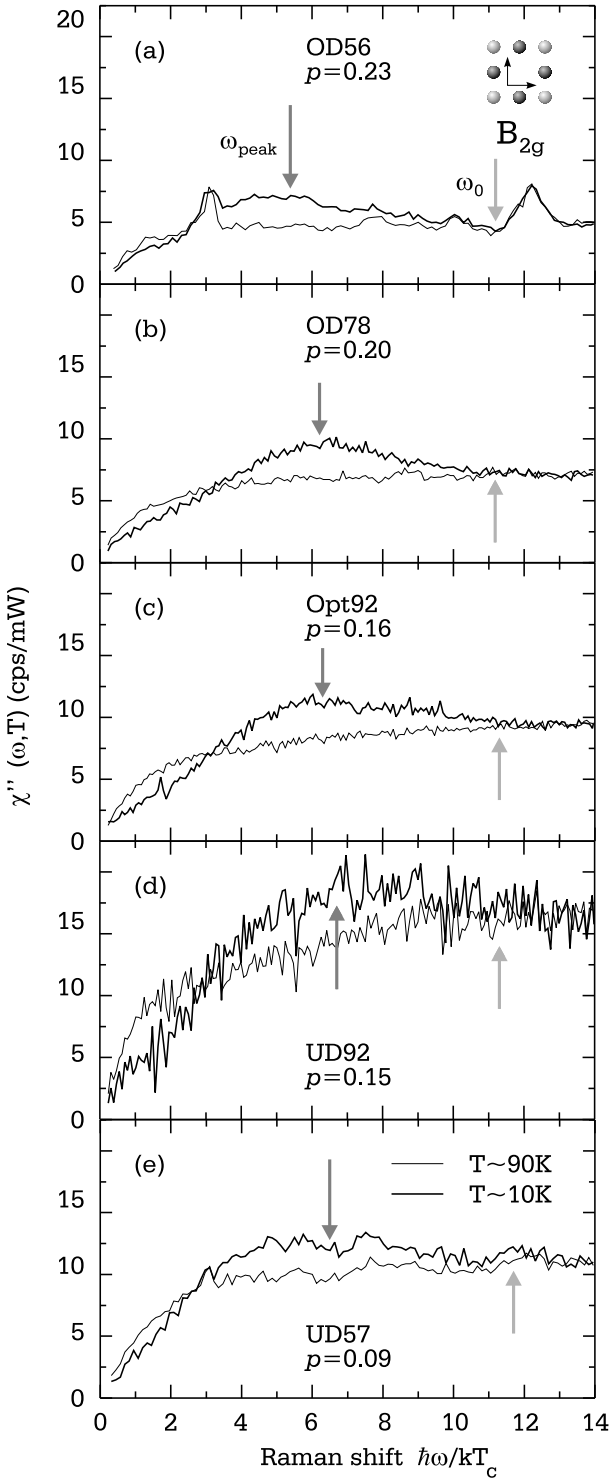

Figure 7.2: *Doping dependence of the Raman response $\chi''(\omega)$ in B_{2g} symmetry in the normal and superconducting states. Panels (d,e) are from [113]. The data are plotted as a function of energy normalized to the respective transition temperatures T_c of the samples. The arrows mark the energies ω_{peak} and ω_0.*

optimally to overdoped samples, but the intensity is strongly suppressed in the underdoped sample (Fig. 7.1 (e)). These results are consistent with previous observations in the same compound [90].

In Figs. 7.1 and 7.2 the energy at which the superconducting and normal state spectra merge, ω_0, is marked by a light-grey arrow. Clearly, this energy scales with T_c in both symmetries.

In Fig. 7.3 the measurements in the superconducting state are summarized for both B_{1g} (panel (a)) and B_{2g} (panel (b)) symmetries. The intensity normalized to the respective value at high energies ($\sim 14 k_B T$) to allow a direct comparison of the

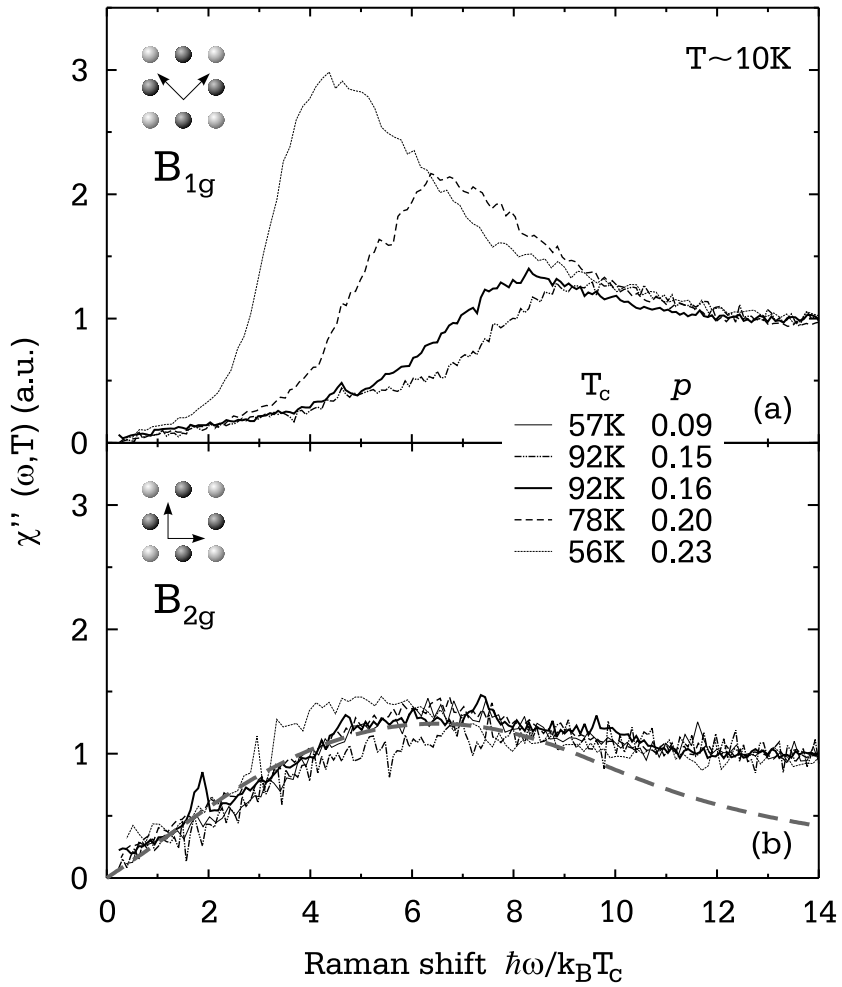

Figure 7.3: *Doping dependence of the superconducting Raman response $\chi''(\omega)$ of BSCCO in B_{1g} (a) and B_{2g} (b) symmetries. The data are plotted as a function of energy normalized to the respective transition temperatures of the samples. The dashed line in panel (b) is the theoretical prediction for a d-wave superconducting gap with Δ_0 (Eq. (7.1)) scaling with T_c upon doping. The parameters used are described in the text.*

response. In B_{2g} symmetry all the data are consistent with a d-wave superconducting gap (see Sect. 2.5) of the form

$$\Delta(\phi) = \Delta_0 \cos(2\phi) \ . \tag{7.1}$$

In fact, if the only effect of doping is to modify T_c and to change Δ_0 proportionally, then the spectra plotted as a function of normalized energy $\hbar\omega/k_BT_c$ are expected to scale one on top of each other. This is emphasized by the theoretical curve (dashed line in Fig. 7.3 (b)) which is calculated using Eqs. (3.19) and (3.20) and $\Delta_0/k_BT_c = 5$. The other parameters used for the plot are $\mu/t = -1.373$, $t'/t = 0.45$ and $t = 250$ meV; a phenomenological damping of $\Gamma/t = 0.05$ has been used to mimic the effect of impurities.

In the B_{1g} channel (Fig. 7.3 (a)), the superconducting spectra become sharper and gain intensity when the carrier concentration p is increased. The evolution of the spectra with p cannot be explained consistently in B_{1g} and B_{2g} symmetries without introducing additional, so far unidentified physical effects.

The doping dependence of the redistribution of the intensity in the superconducting state is shown in Fig. 7.4. The inverse of the normalized maximum intensity is plotted as a function of doping. Results from previous measurements [113] are also included. The dashed line is a linear fit to the data. The inverse of the peak intensity decreases linearly with doping and extrapolates to zero at approximately

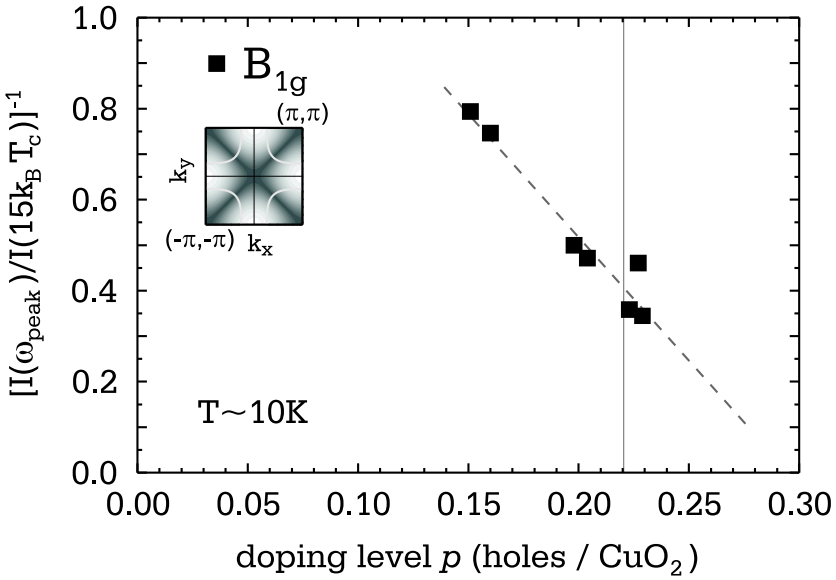

Figure 7.4: *Doping dependence of the inverse of the peak intensity in B_{1g} spectra of BSCCO at 10 K. The dashed line is a linear fit to the data. The grey line marks the critical doping at which the metal-insulator transition is observed in the normal state (Chapter 6).*

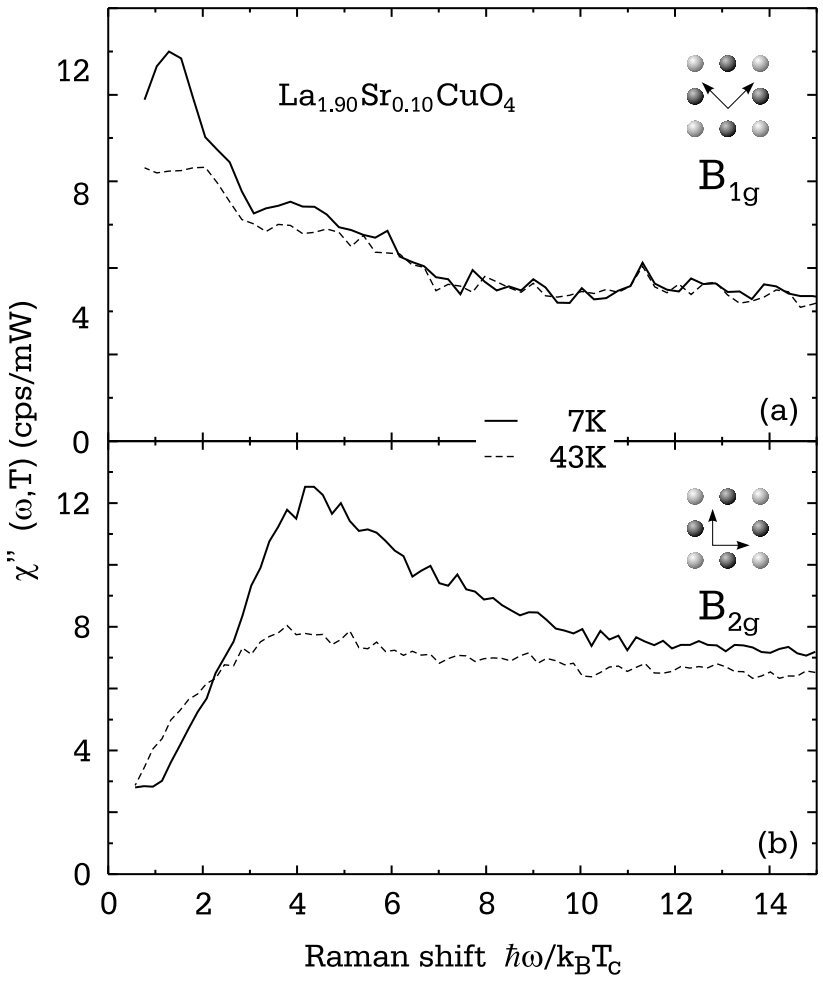

Figure 7.5: *Raman response $\chi''(\omega, T)$ of the underdoped LSCO in the superconducting and normal states . In panels (a) and (b) are shown B_{1g} and B_{2g} symmetries.*

$p \simeq 0.29$. This value is close to the doping level $p \simeq 0.27$ where T_c vanishes (as determined from Eq. (4.1)). The grey line marks the critical doping $p_c = 0.22$ at which the metal-insulator transition is observed in the normal state (Chapter 6). From Fig. 7.4 it is clear that no changes in the evolution of the peak intensity are observed when $p_c = 0.22$ is crossed. Therefore, no indications of the metal-insulator transition are found in the superconducting state from this analysis.

The electronic Raman response of underdoped LSCO is shown in Fig. 7.5 in the superconducting and in the normal state at 7 K and 43 K, respectively. As for BSCCO, the data are plotted as a function of energy normalized to the respective transition temperatures of the samples. The lack of a superconductivity-induced peak in B_{1g} symmetry is similar to what is observed in BSCCO (Fig. 7.1 (e)) and is consistent with previous results in LSCO [112]. In addition, an anomalously strong

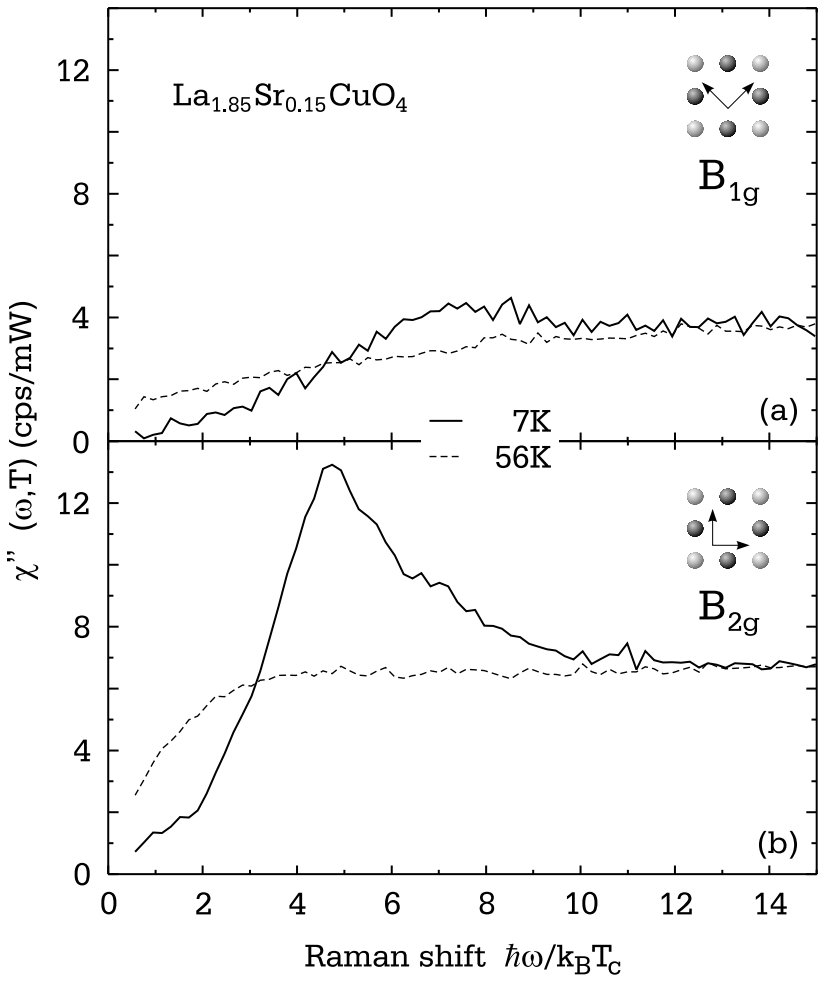

Figure 7.6: *Raman response $\chi''(\omega, T)$ of the optimally LSCO in the superconducting and normal states . In panels (a) and (b) are shown the B_{1g} and B_{2g} symmetries.*

increase of the low-frequency response is observed. This anomaly is studied in detail in Sect. 8.4.2 and is interpreted as an indication of charge ordering in underdoped LSCO.

The electronic Raman response in optimally doped LSCO in the superconducting and in the normal state at 7 K and 56 K, respectively, is shown in Fig. 7.6. In B_{2g} symmetry the spectrum at the lowest temperature (7 K) is characterized by a strong superconductivity-induced peak, similarly to what is observed in the underdoped sample. Such a feature is now visible also in B_{1g} symmetry with a maximum (190 cm^{-1}) slightly higher than in B_{2g} symmetry (120 cm^{-1}). The maximum magnitude of the superconducting energy gap is usually estimated from the position of the B_{1g} peak [32], since $\omega_{peak}^{B_{1g}} \simeq 2\Delta_{max}$ (see Sect. 3.3.2). Then $\Delta_{max} \simeq 95$ cm^{-1} consistent with previous Raman measurements [114] and with estimates from angle-

resolved photoemission experiments where the shift of the leading edge midpoint is analyzed [115].

7.2 Low-frequency power laws

The low-frequency behaviour of the spectra depends on the symmetry of the energy gap in a characteristic way for ordered and disordered systems. In disordered unconventional superconductors with d-wave pairing, the frequency dependence of the electronic Raman response for $\omega \to 0$ is linear in B_{2g} symmetry and changes from ω to ω^3 at a characteristic frequency ω^* in B_{1g} symmetry. The scale ω^* is expected to grow with increasing impurity concentration as $\omega^* \sim \sqrt{\Gamma\Delta_0}$ [116]. In B_{2g} symmetry the slope of the spectra is related to Δ_0 as

$$\chi''_{B_{2g}}(\omega \to 0) \propto \left(\frac{\hbar\omega}{\Delta_0}\right) \tag{7.2}$$

The study of the low-frequency behaviour in both symmetries can therefore be used to study the evolution with carrier concentration of both the magnitude and the anisotropy of the gap. In Fig. 7.7 the B_{2g} spectra of four differently doped samples are plotted in double logarithmic scale to show the low-frequency power laws. The intensities have been normalized at high energies. The power-law exponent obtained from the fit to the data of the overdoped sample OD78 (T_c = 78 K, p = 0.2) is

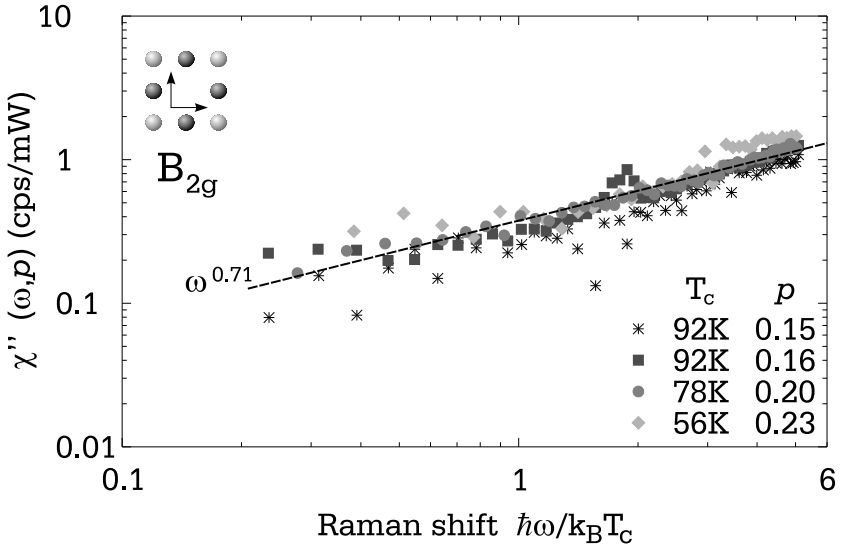

Figure 7.7: *Low-frequency power laws of the Raman response $\chi''(\omega)$ of BSCCO in B_{2g} symmetry for differently doped samples. The spectra have been normalized to 1 at high energies. The dashed line is a linear fit to the data of the sample OD78 (T_c = 78 K, p = 0.2).*

0.71, indicating a variation with ω close to linear as expected. However, the most relevant result shown in Fig. 7.7 is that the spectra of all samples collapse on one curve. Therefore, not only the position of the maximum of the intensity but also the low-frequency part of the spectra indicate that the gap maximum Δ_0 (Eq. (7.1)) scales strictly with T_c.

The low-frequency behaviour of the B_{1g} spectra is shown in Fig. 7.8 in double logarithmic scale. At all doping levels the spectra are characterized by a crossover from linear to cubic power laws as expected in the case of a disordered d-wave superconductor [116]. The crossover frequency is found to be doping dependent, as shown in Fig. 7.9, where results from previous measurements [90] are also included. The dashed line is a linear fit to the data and the grey line marks the critical doping $p_c \simeq 0.22$. ω^* decreases linearly with increasing p and extrapolates to zero approximately at $p \simeq 0.25$. Similarly to what is observed for the intensity of the peak, the crossover frequency does not display any deviation from the linear dependence for $p \geqslant p_c$ either.

Since ω^* is obtained directly from the measurements (Fig. 7.9) and Δ_0 can be derived from the superconducting peak maximum, $\Gamma \propto (\omega^*)^2/\Delta_0$ can be estimated. However, $\omega_{peak}^{B_{1g}}$ and $\omega_{peak}^{B_{2g}}$ exhibit different doping dependences and, therefore, are both considered: $\Delta_0 = \omega_{peak}^{B_{1g}}/2$ and $\Delta_0 = \omega_{peak}^{B_{2g}}/1.7$ [117]. The resulting Γs are shown in Fig. 7.10 in panels (a) and (b), respectively. The first observation is that, independently of the choice of Δ_0, Γ possesses a strong doping dependence, decreases upon increasing doping level and changes by an order of magnitude. If Γ were attributed entirely to impurities [116] then, in a first approximation, no doping dependence would be expected, since oxygen doping does not introduce defects in the CuO_2 planes. Apparently, it has a different origin. For this reason the normal state relaxation rate Γ_0 in B_{1g} symmetry extrapolated to zero temperature is also plotted in Fig. 7.10. The comparison with the normal state scattering confirms that no indication of a metal-insulator transition, clearly visible as a jump in Γ_0, is observed below T_c.

In conclusion, the doping evolution of the superconducting state spectra still remains puzzling. The analysis of the spectra at low energy in both symmetries is consistent with a disordered d-wave superconductor with a maximum gap magnitude Δ_0 which scales with the carrier concentration similarly to T_c. However the doping dependence of Γ and the different scaling of ω_{peak} with p in the two symmetries indicate that some additional phenomena are involved in the superconducting state. Below T_c no anomaly is found at p_c.

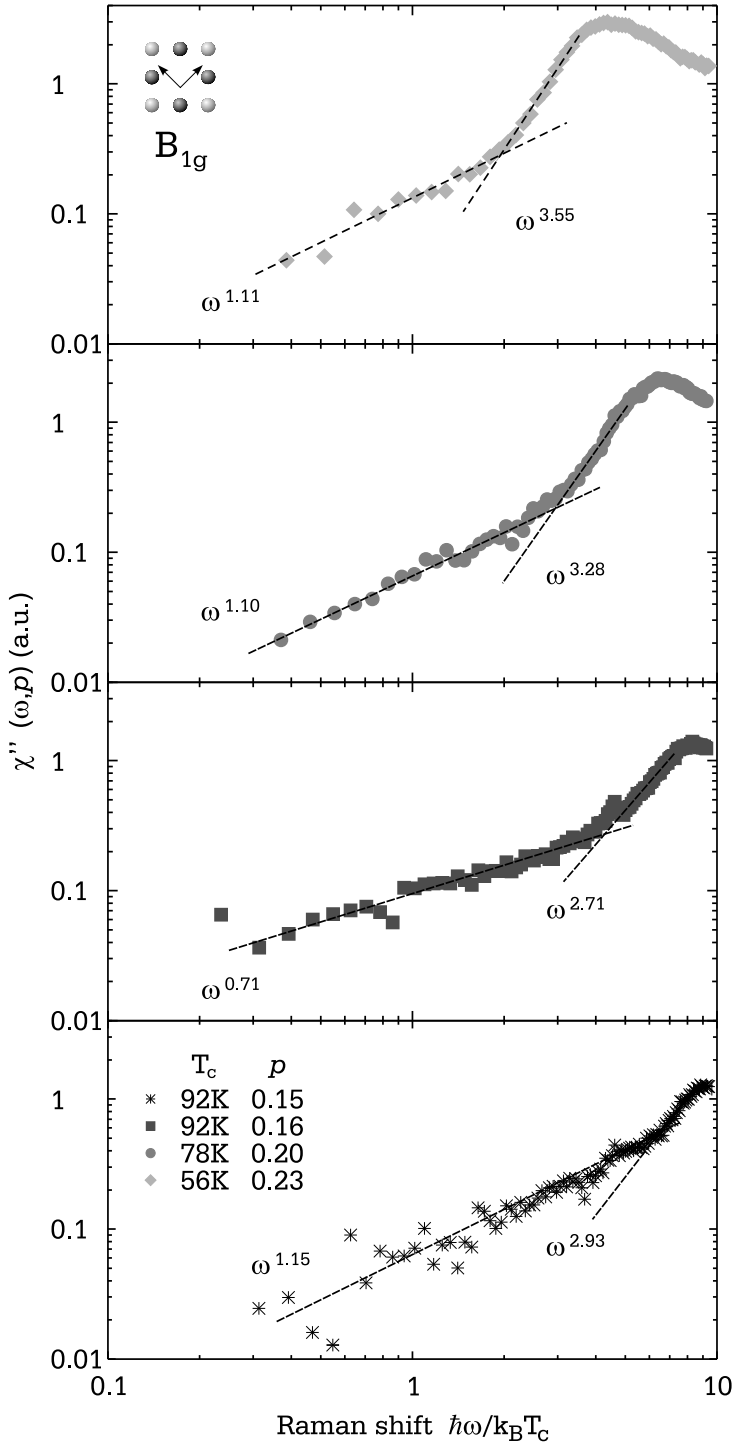

Figure 7.8: *Low-frequency power laws of the Raman response $\chi''(\omega)$ of BSCCO in B_{1g} symmetry for differently doped samples. The spectra have been normalized to 1 at high energies. The dashed lines are a linear fits to the data in logarithmic scale. The obtained exponents are indicated.*

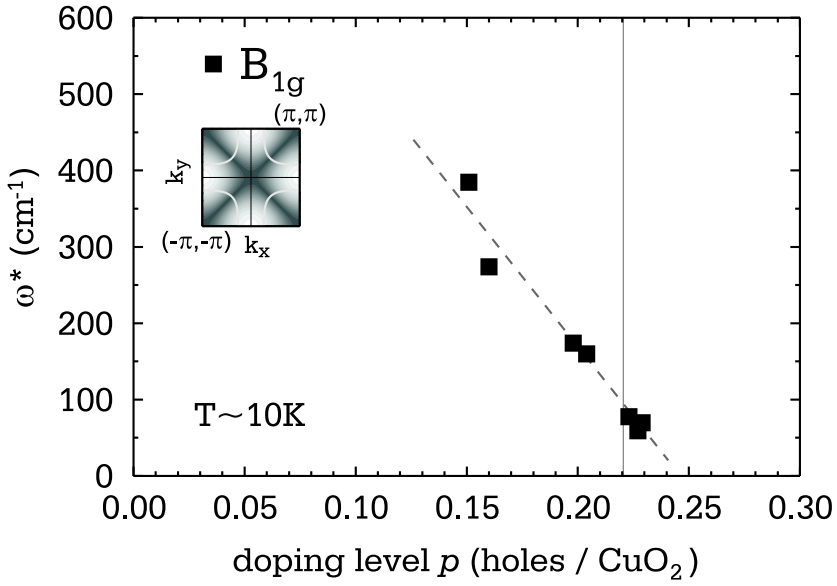

Figure 7.9: *Crossover frequency ω^* as a function of doping in B_{1g} symmetry in BSCCO. Results from previous measurements are also included [90]. The dashed line is a linear fit to the data. The grey line marks the critical doping at which the metal-insulator transition is observed in the normal state (Chapter 6).*

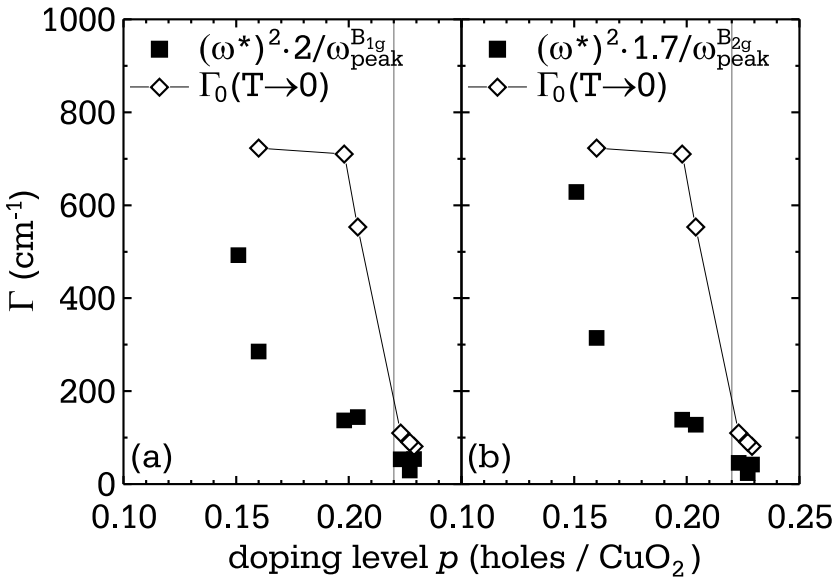

Figure 7.10: *Doping dependence of the scattering rate Γ extracted from the crossover frequency ω^*. The superconducting gap is considered to posses the doping dependence of either $\omega_{peak}^{B_{1g}}$ (a) or of $\omega_{peak}^{B_{1g}}$ (b). $\Gamma_0(T \to 0)$ is the static relaxation rate in the normal state in B_{1g} symmetry extrapolated to zero temperature. The grey lines mark $p_c = 0.22$.*

7.3 Two energy scales in the superconducting state?

The evolution of the energy gap with doping as determined by the position of the superconductivity-induced feature ω_{peak} in B_{1g} and B_{2g} symmetries is summarized in Fig. 7.11. Results from previous measurements [113] are also included. The dotted line represents the scaling of T_c with doping as given from Eq. (4.1) and is adjusted to fit the B_{2g} results as $6k_BT_c(p)$. The dashed line is a linear fit to the B_{1g} peak position.

While the B_{2g} peak position follows closely the evolution of T_c, $\omega_{peak}^{B_{1g}}$ scales linearly with the doping in the range studied. In the strongly underdoped ($p = 0.09$) sample no superconducting peak was observed in B_{1g} symmetry. It is therefore hard to discuss how the superconductivity-induced peak behaves in the range $0.09 < p < 0.15$. Previous measurements do not provide a definite answer since contradictory results were obtained. While in [110] $\omega_{peak}^{B_{1g}}$ is found to continuously increase for decreasing p, in [118] it is reported to be constant for $p \leqslant 0.1$.

The two peak positions merge in the overdoped region at $p \simeq 0.20$, where cuprates are believed to recover a BCS character. A similar analysis has been per-

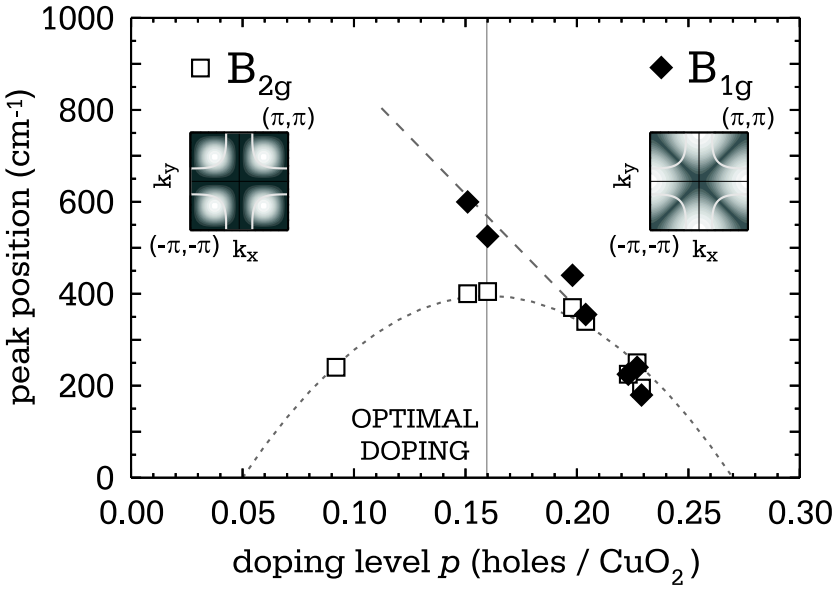

Figure 7.11: *Position of ω_{peak} in the B_{1g} and B_{2g} spectra of differently doped BSCCO samples. Previous results are also included [113]. The dotted line is 6 $k_BT_c(p)$, with $T_c(p)$ given by Eq. (4.1); the dashed line is a linear fit to the B_{1g} peak position. The regions of the Brillouin zone where the vertex is most sensitive are shown in the insets with light colors.*

formed on YBCO [30], and a comparable evolution with p of the superconductivity-induced peak has been observed.

The scaling of Δ_0 with T_c as derived from the low-energy analysis of the B_{2g} symmetry spectra is consistent with the results for the superconducting energy gap derived from the magnetic penetration depth [119], electron tunneling for bias voltages well below the gap [120, 121], as well as Andreev reflection measurements [25]. However, if the B_{1g} peak energy $\omega_{peak}^{B_{1g}}$ is considered, Raman scattering seems to reveal a different energy scale which increases monotonically upon decreasing carrier concentration. This result is in agreement with the doping dependence determined from the conductance peaks in the tunneling experiments [122] and with photoemission observations [123].

To reconcile the different energy scales observed, different proposals have been put forward but still there is no accepted model. It has been proposed that there are two relevant energy scales [25, 124]. The single-particle excitation energy as probed by photoemission and tunneling spectroscopies increases with decreasing doping and reflects the increase of the inter-particle interaction towards the antiferromagnetic phase. This seems to be the energy scale detected by the B_{1g} Raman response.

The second energy scale is related to coherence in the superconducting phase and can be measured by two-particle probes, such as Andreev reflections or B_{2g} Raman scattering. These two energies approach the same value at high doping levels, but become increasingly different at low doping levels. The interpretation of these energy scales and their relationship remains, however, an unsolved question. More recently the existence of an additional order parameter competing with the superconducting gap has been proposed to be the origin of the the complex phenomenology of cuprates [67]. The d-wave character of this order parameter mostly affects the B_{1g} Raman response and could account for some of the experimental observations [125].

A different proposal is that the anisotropy of the superconducting gap changes with doping [121]. In particular, Δ_0 in Eq. (7.1) is suggested to be no longer constant but to posses an additional ϕ dependence. So, while $\Delta_0(\phi = \pi/4)/k_BT_c$ is constant and represents the mean-field gap, $\Delta_0(\phi = 0, \pi/2)/k_BT_c$ is doping dependent because of its interplay with the normal state gap or pseudogap [16]. In this scenario the discrepancies between the results from different techniques [25] are related to the different regions of the Brillouin zone: along $\phi = 0, \pi/2$ by tunneling and $\phi = \pi/4$ by penetration depth, for example.

In summary, in the superconducting state two energy scales with distinctively different doping dependences are observed by Raman in the two symmetries which probe different regions of the Brillouin zone (see insets in Fig. 7.11). The B_{1g} scat-

tering geometry is most sensitive in regions where the energy gap is maximum. Therefore the excitations with energy high enough to overcome the maximal superconducting binding energy are mainly contributing. The B_{2g} channel, instead, probes regions where the gap is vanishing. So, low-lying quasiparticles contribute mainly to this symmetry. Although the significance and the interplay of these two energy scales is still controversial, the Raman results indicate that the energy scale emerging from the B_{1g} spectra is related to single-particle properties while that emerging from the B_{2g} spectra reveals thermodynamical properties.

7.4 Detailed temperature dependence below T_c

The evolution of the spectra with temperature in the superconducting state is shown in Fig. 7.12 for two overdoped samples OD78 (a) and OD56 (b). Only the B_{1g} spectra are shown where the strong superconducting signal allows a clear temperature char-

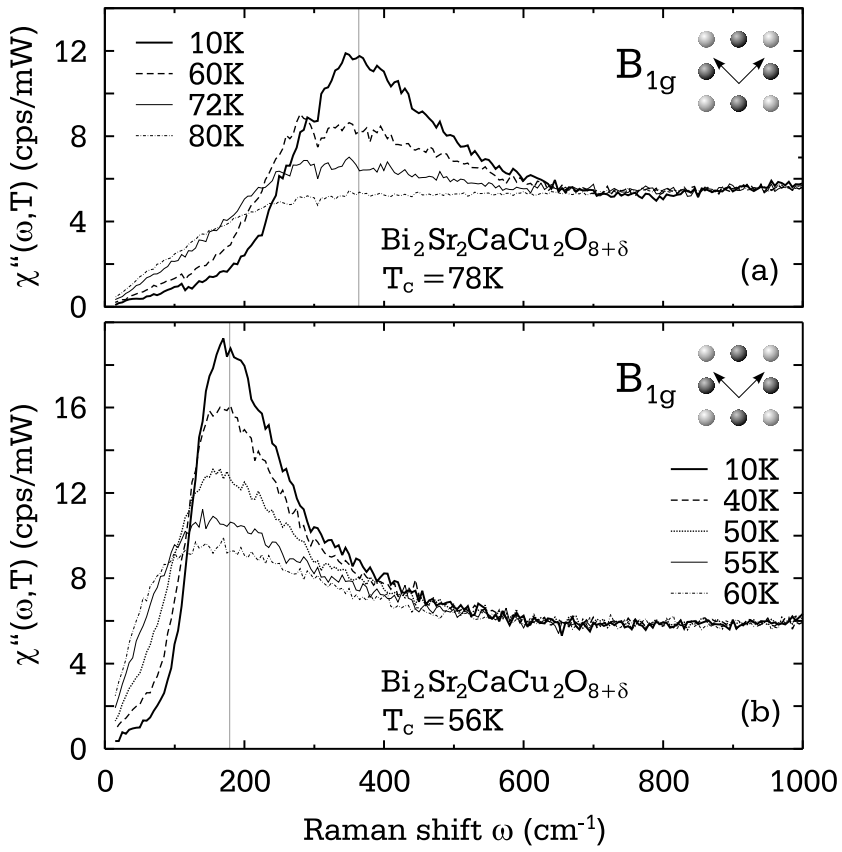

Figure 7.12: *Temperature evolution of the Raman response $\chi''(\omega, T)$ in B_{1g} symmetry for the overdoped samples OD78 (a) and OD56 (b). The grey line marks the position of the peak at the lowest temperature measured.*

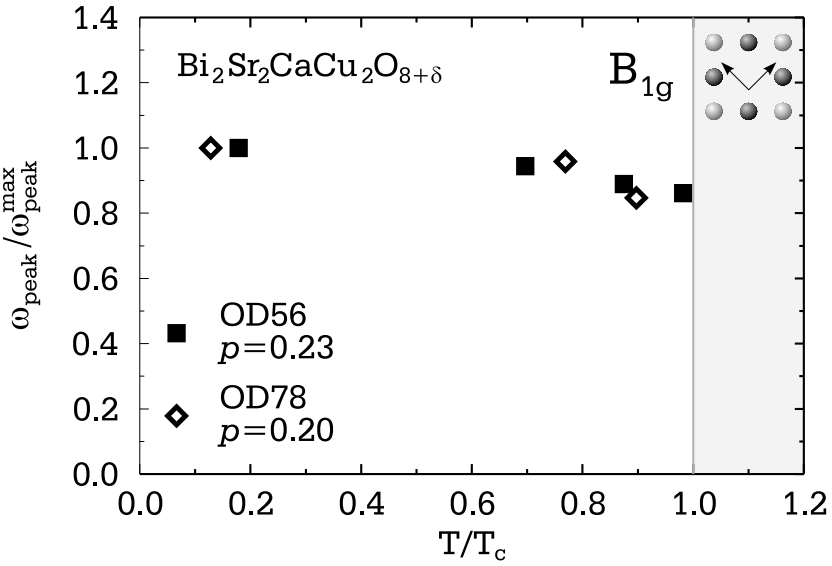

Figure 7.13: *Temperature dependence of the superconductivity-induced peak in B_{1g} symmetry for the overdoped samples OD78 and OD56. The temperature is scaled to the corresponding T_c and the peak positions by the value at the lowest temperature. The grey area marks the normal state.*

acterization. With increasing temperature the intensity of the superconductivity-induced peak is reduced and vanishes at T_c. No indication of partially coherent states above the critical temperature are therefore found as opposed to what is claimed in [126]. This result is not only characteristic of the overdoped regime but was also observed in the slightly underdoped sample (UD92) where the superconductivity-induced peak in B_{1g} symmetry is still visible [90].

The frequency of the maximum intensity decreases slightly with increasing T. The temperature dependence of $\omega_{peak}^{B_{1g}}$ for the two overdoped samples of Fig. 7.12 (OD78 and OD56) is summarized in Fig. 7.13. To compare the results of the two samples, the temperatures are normalized to the respective T_cs and the peak positions to the values at the lowest temperature (10 K). The error on the data is approximately of the size of the points. Apparently, $\omega_{peak}^{B_{1g}}$ depends only weakly on temperature, in contrast to what is expected if the peak would directly reflect a BCS-like d-wave superconducting gap [127]. It is also interesting to notice that, in agreement with the results from the peak intensity (Fig. 7.4) and from the crossover frequency (Fig. 7.9), the superconducting state does not seem to reflect the metal-insulator transition observed at $p_c \simeq 0.22$ in the normal state. In fact, the two samples with $p < p_c$ (OD78) and $p > p_c$ (OD56) are characterized by the same temperature dependence.

7.5 Resonance properties of the gap feature

In order to gain additional information on the superconductivity-induced features, the dependence of the spectra on the excitation energy can be studied. In fact, it has been previously argued that the pair-breaking excitations show clear resonance properties in strongly overdoped BSCCO samples (with $T_c < 82$ K) in B_{1g} symmetry [128]. The resonances were analyzed in connection with two-magnon excitations and were interpreted as a signature of the crossover from persisting antiferromagnetic order at lower doping levels to an antiferromagnetically correlated Fermi liquid in the strongly overdoped regime.

The purely electronic Raman spectra of the overdoped BSCCO samples OD78, OD62, and OD56 at 10 K for excitation energies between 1.9 eV ($\lambda_{laser} = 647$ nm) and 2.7 eV ($\lambda_{laser} = 458$ nm) are shown in Fig. 7.14 for the B_{1g} and B_{2g} scattering geometries.

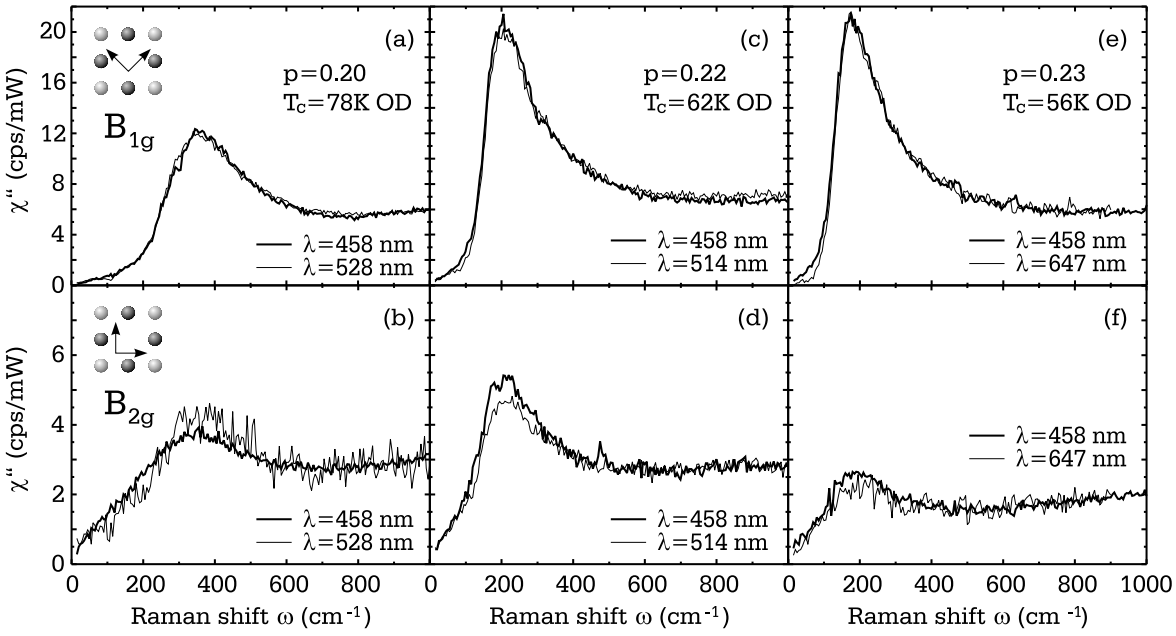

Figure 7.14: *Raman response $\chi''(\omega)$ in B_{1g} and B_{2g} symmetries of the overdoped BSCCO samples OD78 (a,b), OD62 (c,d) and OD56 (e,f) at 10 K at different excitation energies.*

To enable an optimum comparison of the shape of the Raman response the overall spectra at wavelengths $\lambda_{laser} \neq 458$ nm have been multiplied by a factor, ranging from 0.7 to 2, to adjust the intensity at 800-1000 cm^{-1} to the spectra at $\lambda_{laser} = 458$ nm.

As is clear from Fig. 7.14 there is no significant variation of the lineshape of the spectra with excitation energy in any symmetry and doping level studied. While

in the B_{1g} spectra the total intensity does hardly display a wavelength dependence, a reduction of the overall intensity is observed in B_{2g} symmetry upon decreasing photon energies. This reduction is not visible in Fig. 7.14 since the overall spectra at wavelengths $\lambda_{laser} \neq 458$ nm have been adjusted to the spectra at $\lambda_{laser} = 458$ nm.

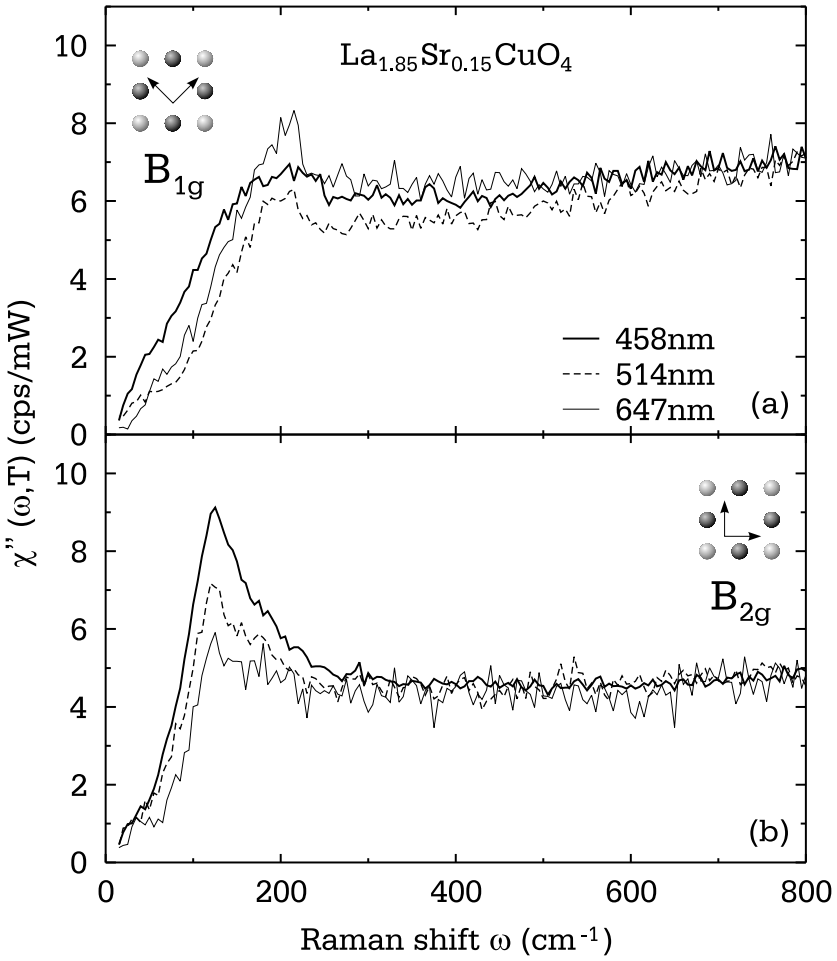

Figure 7.15: *Raman response $\chi''(\omega)$ in B_{1g} (a) and B_{2g} (b) symmetries of the optimally doped LSCO crystal at 10 K for different excitation energies.*

Stronger effects are observed in LSCO. In Fig. 7.15 the electronic contribution of the optimally doped sample at 10 K is shown for different wavelengths in B_{1g} (a) and B_{2g} (b) scattering geometries. Also in this sample the spectra have been adjusted by a multiplicative factor to make them coincide at 600-800 cm^{-1}. While the overall intensity in B_{1g} symmetry does not change with the excitation energy, the intensity in B_{2g} symmetry is reduced by a factor of four upon reducing the photon frequency. In both symmetries the lineshape of the spectra is modified with the wavelength, but the effect is more severe in the B_{2g} channel, where the clear peak observed with

$\lambda_{laser} = 458$ nm is almost completely washed out at $\lambda_{laser} = 647$ nm.

In conclusion, while in BSCCO no specific variation of the superconductivity-induced peak is observed at any excitation energy, strong resonance effects are observed in LSCO in B_{2g} symmetry where the superconducting peak is strongly suppressed upon reducing the energy of the exciting photons. The overall cross section displays a dependence on the wavelength, which is strongest in LSCO, only in the B_{2g} response.

The different dependence of the lineshape on the wavelength in the two materials could arise from different phenomena. The independence of the lineshape observed in BSCCO is similar to what observed not only in YBCO [129] but also in the electron-doped NCCO [130]. In the latter material, however, the resonance effects have the opposite dependence on λ_{laser}. The change of the lineshape of the spectra in LSCO could be related to superconductivity-induced phonon renormalization effects [131]. The A_{1g} phonons at 125 and 145 cm^{-1} are in fact peaked at approximately the same energy as the pair-breaking feature. On the other hand, it has been proposed recently that the band structure-related resonance effects might strongly modify both the intensity and the shape of the spectra [132].

Chapter 8

Role of antiferromagnetic correlations

The analysis of the normal-state Raman spectra of several cuprates (Chapter 6) reveals a doping dependent anisotropy in the relaxation rates. The study of the evolution with temperature and doping indicates that the "hot" quasiparticles with momenta along the Brillouin zone axes (see Sect. 2.6) do not carry current any more when the doping level is reduced, while the "cold" quasiparticles with momenta along the Brillouin zone diagonals remain metallic for all samples studied. These experimental observations are explained in terms of an unconventional metal-insulator transition which can be observed for $p < p_c = 0.22$ [98].

What drives such a transition remains, however, unclarified. A possible connection with antiferromagnetic fluctuations is explored in this chapter. In particular, the role of antiferromagnetic correlation is investigated, focusing on different aspects of the interaction between magnetic excitations and electrons. The contribution of the scattering by spin excitations to the Raman spectra in the superconducting state is discussed first, then a new theoretical model is introduced which allows the understanding of the A_{1g} symmetry component in the superconducting state. The possible existence of chiral spin fluctuations is investigated by performing a complete symmetry analysis. An A_{2g} symmetry component is clearly resolved for the first time in metallic cuprates. Finally, the spin and charge order is studied in LSCO.

8.1 Metal-insulator transition and two-magnon scattering

The normal state properties of the Raman spectra have been interpreted in terms of an anisotropic gap which opens below a critical doping p_c (Sect. 6.3). When the carrier concentration is further reduced, the magnitude of the gap increases, reducing the states available for conduction. The momentum dependence of this charge gap is compatible with $\mid d_{x^2-y^2} \mid$ symmetry, and a possible connection to the superconducting gap or to the pseudogap could be proposed on the basis of the similar $\mathbf{k}$ dependence [16, 133]. However, the presence of precursor superconductivity due to strong pairing attraction above T_c [134] can be safely excluded because of the high temperature (200 K) and doping level ($p > 0.19$) at which the crossover is observed (Sect. 6.4). Also the pseudogap scenario must be ruled out, because the onset temperature T^* at which the pseudogap starts to be visible is of the order of T_c around optimal doping $p \simeq 0.16$ [101] and increases only for decreasing carrier concentrations (see Fig. 6.15).

On the other hand, the proximity of superconductivity and antiferromagnetism in the phase diagram raises the question of the persistence of antiferromagnetic fluctuations also for high carrier concentrations.

In an antiferromagnet the electric field of the incoming photon can excite two magnons of opposite momenta [135]. A simple picture for the two-spin flip process in the CuO_2 plane can be obtained if the microscopic process is decomposed into individual electron hoppings as visualized in Fig. 8.1. The incoming photon couples to a down-spin electron on a Cu site (a) inducing a charge transfer to a neighboring oxygen orbital (b). This is followed by an exchange process with a neighboring Cu spin (c). Finally, an up-spin electron hops back to the initial Cu site emitting the outgoing photon (d) [136]. Due to the form of the nearest-neighbor light scattering Hamiltonian, the Raman intensity arising from two spin flips will appear only in B_{1g} symmetry [135]. A more detailed study of the Raman intensity in the resonant regime [137], which considers the effect of final state interaction, qualitatively explains the lineshape of the spectra in an antiferromagnet. Within this model the excitation of a pair of zone-boundary magnons leads to a peak at $\omega_{2M} \simeq 2.8J$ in the B_{1g} spectra, where J is the exchange coupling constant. When holes are doped into the antiferromagnet, the two-magnon feature in the Raman weakens and shifts to lower energies, but is still present in the superconducting and metallic phases.

In Fig. 8.2 the B_{1g} and B_{2g} normal state spectra are shown for differently doped BSCCO samples covering the range from optimal doping (Opt95) to the strongly

overdoped regime (OD78, OD62 and OD56) (Tab. 4.3).

The sharp features below 800 cm^{-1} are due to lattice vibrations. The two-magnon peak is clearly visible in the optimally doped sample (panel (a)) as a broad feature in the B_{1g} spectrum at $\omega_{2M} \simeq 1500$ cm^{-1}. ω_{2M} shifts toward lower frequencies for increasing carrier concentrations p. While still visible in the overdoped sample with $p = 0.20$ (panel (b)) it cannot clearly be identified in the two strongly overdoped samples (panels (c,d)). As expected, no structures are observed in the B_{2g} spectra, which have almost no doping dependence (see Fig. 6.2).

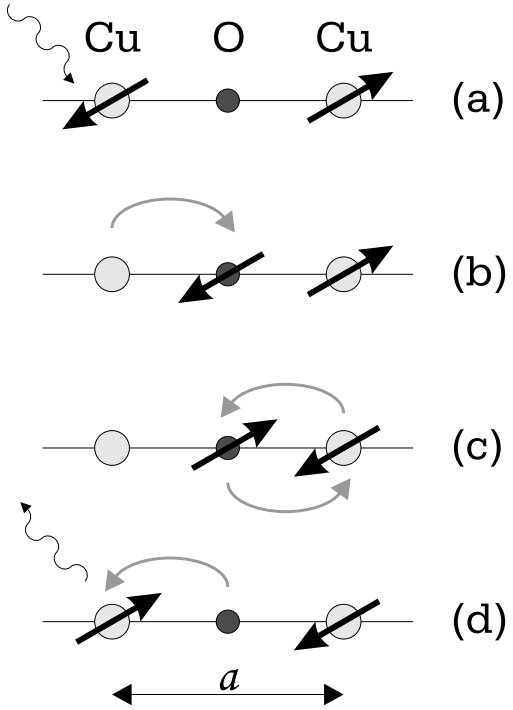

Figure 8.1: *Schematic picture of the two-spin flip process in a CuO_2 plane. (a) The incoming photon is absorbed creating (b) a charge transfer excitation from a Cu to an O orbital. After the exchange process (c) the electron hops back from O to Cu site with the emission of the outgoing photon [136].*

The analysis of the B_{1g} spectra indicates that short range antiferromagnetic coupling persists in the superconducting metallic phases. In fact, Raman detects the contribution of the scattering from spin-flip excitations well beyond optimal doping (Fig. 8.2 (a)). It is interesting to notice that such a contribution seems to disappear for $p > 0.21$ (Fig. 8.2 (c,d)), doping level at which also the anisotropy between the relaxation rates in the two symmetry channels B_{1g} and B_{2g} vanishes (Fig. 6.7). This observation suggests a possible relationship between the two phenomena.

8.2 Antiferromagnetic correlations below T_c

If, in general, antiferromagnetic correlations persist in the metallic phase, they seem particularly important in the superconducting state where spin susceptibility studies have revealed the existence of a resonant spin excitation. Such an unusual spin collective mode, most extensively studied by inelastic neutron scattering, is unique to high-temperature superconductors and is believed to be a key factor in the phe-

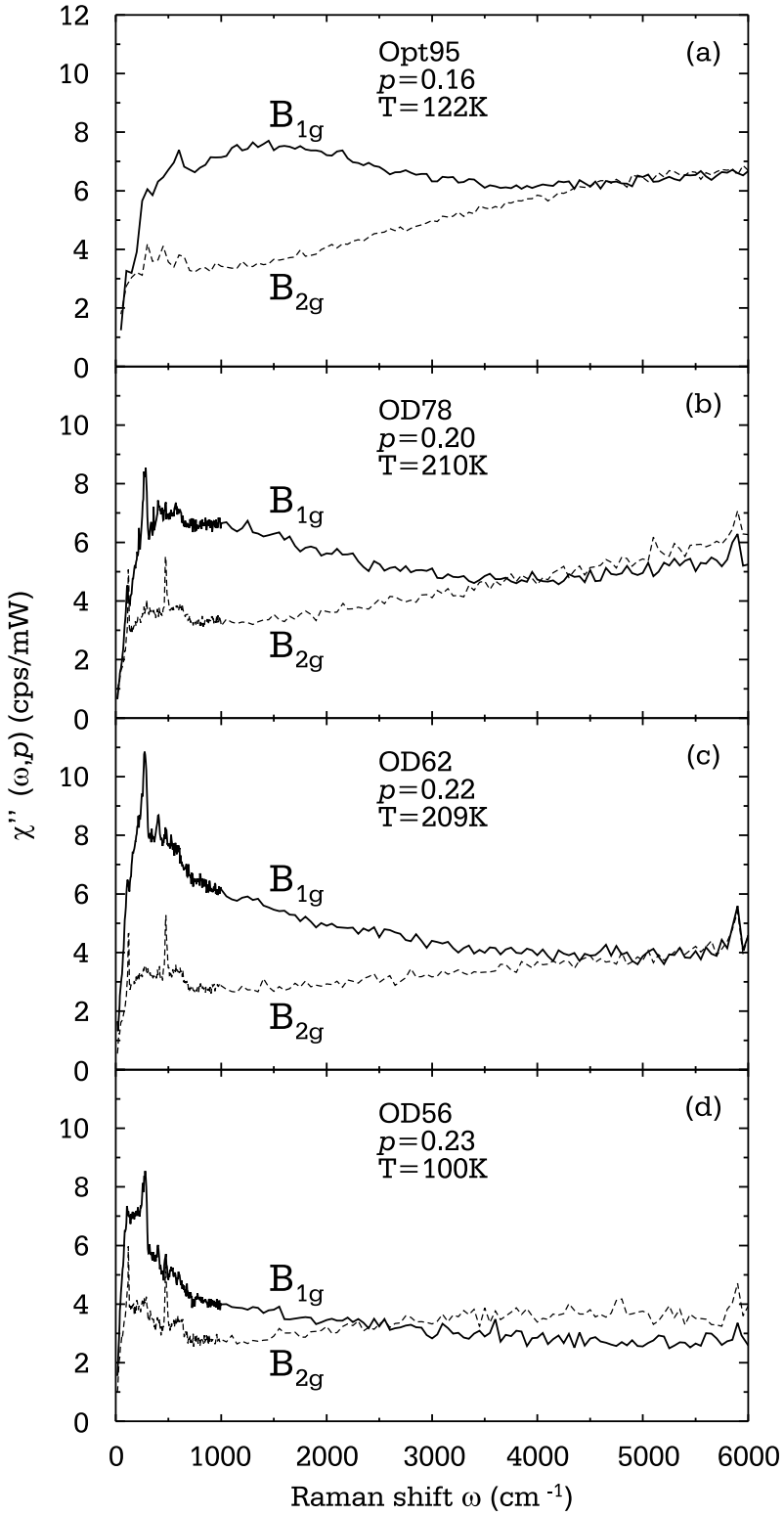

Figure 8.2: *Doping dependence of the Raman response in B_{1g} and in B_{2g} symmetries in the normal state for differently doped BSCCO samples.*

nomenology of the cuprates.

First observed in YBCO [44, 138, 139], it has been also identified in BSCCO [140] and in TBCO [46] at various doping levels. The magnetic resonance peak is a sharp collective mode that occurs at an energy of $\omega_R \simeq$ 41 meV in optimally doped samples and at a momentum $\mathbf{Q} = (\pi/a, \pi/a)$, where a is the nearest-neighbor Cu-Cu distance. Its intensity decreases continuously with increasing temperature, and vanishes above the transition temperature T_c. The energy of the mode is found to scale linearly with T_c with a maximum value $\omega_R \simeq$ 41 meV in YBCO and BSCCO [140] and $\omega_R \simeq$ 47 meV in TBCO [46].

These observations have inspired numerous theoretical studies of the interplay between electrons and collective spin excitations. The anomalies in the spectra observed close to T_c by photoemission, tunneling and optical conductivity [141, 142] have been interpreted as evidence of coupling to the neutron mode.

Here, the Raman response of a $d_{x^2-y^2}$ superconductor including the contribution from a spin fluctuation identified with the resonance near $\omega_R \approx 41$ meV is calculated.

8.2.1 Theory of Raman scattering from spin fluctuations

There is a clear experimental indication of the interplay between antiferromagnetism and superconductivity from inelastic neutron scattering. Several fundamentally different microscopic descriptions have been proposed to explain it. In this work it is modeled considering a magnon-like collective mode in the superconducting state [143].

Spin fluctuation collective mode

The spin susceptibility χ_s is modelled by extending the weak-coupling BCS form for a superconductor in a $d_{x^2-y^2}$ pairing state to include antiferromagnetic spin fluctuations by a random-phase-approximation (RPA) form [144, 145]

$$\chi_s(\mathbf{q},\omega) = \frac{\chi_0^{BCS}(\mathbf{q},\omega)}{1 - \bar{U}\chi_0^{BCS}(\mathbf{q},\omega)} \tag{8.1}$$

where $\bar{U}$ is taken as an effective interaction strength. χ_0^{BCS} is the BCS susceptibility [43]

$$\chi_0^{BCS}(\mathbf{q}, i\omega) = \frac{1}{\beta}\mathrm{Tr}\sum_{\mathbf{k},i\omega'} \hat{G}(\mathbf{k}, i\omega')\hat{G}(\mathbf{k}+\mathbf{q}, i\omega'+\omega) \tag{8.2}$$

where $\hat{G}(\mathbf{k}, i\omega')$ is the matrix form of the electronic propagator explicitly written in Eq. (3.17), Tr denotes the trace, $\beta = T^{-1}$, and the conventions $\hbar = 1$ and $k_B = 1$ are used. In Eq. (8.1) χ_0^{BCS} includes the superconducting pairing correlations, while

the RPA structure of the response and the strength of the effective interaction $\bar{U}$ represent the antiferromagnetic correlations.

The band structure is described by a tight-binding model for a tetragonal system (see Sect. 3.5, Eq. (3.27)), with the addition of a term describing the hopping between the CuO_2 planes of a bilayer

$$\xi_{\mathbf{k}} = -2t[\cos(k_x a) + \cos(k_y a)] + 4t' \cos(k_x a)\cos(k_y a) - t_\perp(\mathbf{k}) - \mu \ . \tag{8.3}$$

a and c are the lattice constants; $t_\perp(\mathbf{k})$ represents the inter-plane hopping term and is given by [143]

$$t_\perp(\mathbf{k}) = 2t_\perp \cos(k_z c)[\cos(k_x a) - \cos(k_y a)]^2 \tag{8.4}$$

where k_z is 0 or π/c for the bonding or anti-bonding band of the bilayer, respectively. The corresponding two Fermi surfaces are shown in Fig. 8.3. The band structure parameters in this work are always chosen to be applicable to optimally doped systems and are $\langle n \rangle = 0.85$, $t'/t = 0.45$, and $t_\perp/t = 0.1$ [145]. The double arrows

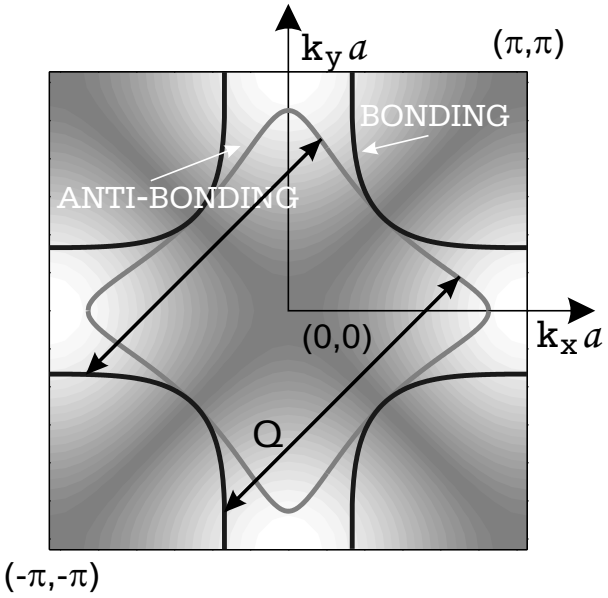

Figure 8.3: *Bonding and antibonding Fermi surfaces. The arrow labeled* **Q** *correspond to a* $(\pi/a, \pi/a, \pi/c)$ *momentum transfer. The parameters used for the plot are* $\langle n \rangle = 0.85$, $t'/t = 0.45$, *and* $t_\perp/t = 0.1$. *The light and dark colors in the background mark the regions where the d-wave superconducting gap is maximal and minimal, respectively.*

labeled by **Q** correspond to a momentum transfer of $(\pi/a, \pi/a, \pi/c)$, which connects states on the bonding Fermi surface to states on the anti-bonding Fermi surface.

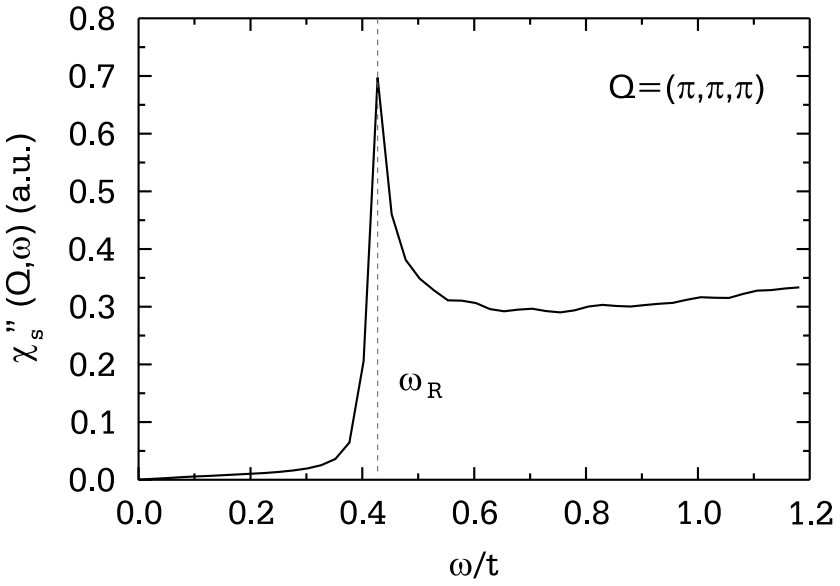

Figure 8.4: *Spin susceptibility for* $\mathbf{Q} = (\pi/a, \pi/a, \pi/c)$. *The parameters used for the plot are* $\langle n \rangle = 0.85$, $t'/t = 0.45$, $t_\perp/t = 0.1$, $\bar{U}/t = 1.3$, *and* $\Delta_0/t = 0.25$. ω_R *is the resonance frequency.*

Because of the form of the band structure selected, the states which are related by a momentum transfer of $\mathbf{Q}$ are located close to the Brillouin zone axis (see Fig. 8.3). These are approximately also the regions in $\mathbf{k}$ space where the d-wave superconducting gap is maximal, as represented by light background colors in Fig. 8.3. The spin response is therefore expected to be very sensitive to the magnitude of the superconducting energy gap.

Although a bilayer model is used here, strong magnetic interactions between closely spaced CuO_2 layers are not required for the formation of the resonant mode, as proved by the observation of the neutron scattering resonance in the single-layer cuprate $Tl_2Ba_2CuO_{6+\delta}$ [46]. The results of the Raman calculation are not qualitatively changed when a monolayer structure is considered.

In Fig. 8.4 is shown the spin susceptibility as given by Eq. (8.1). For the plot the superconducting gap maximum is chosen as $\Delta_0/t = 0.25$ and the effective interaction as $\bar{U}/t = 1.3$. The temperature is fixed at $T/t = 0.08$. Then, $t \simeq 100$ meV corresponds to $\omega_R \simeq 41$ meV.

The evolution of the resonant spin excitation energy ω_R with doping poses serious constraints for the theoretical modeling. From neutron scattering experiments, the energy of the magnetic resonant mode is found to scale with the transition temperature T_c in both the underdoped and the overdoped regimes [140]. This is well reproduced by the model considered here. In fact, the resonance ω_R scales linearly

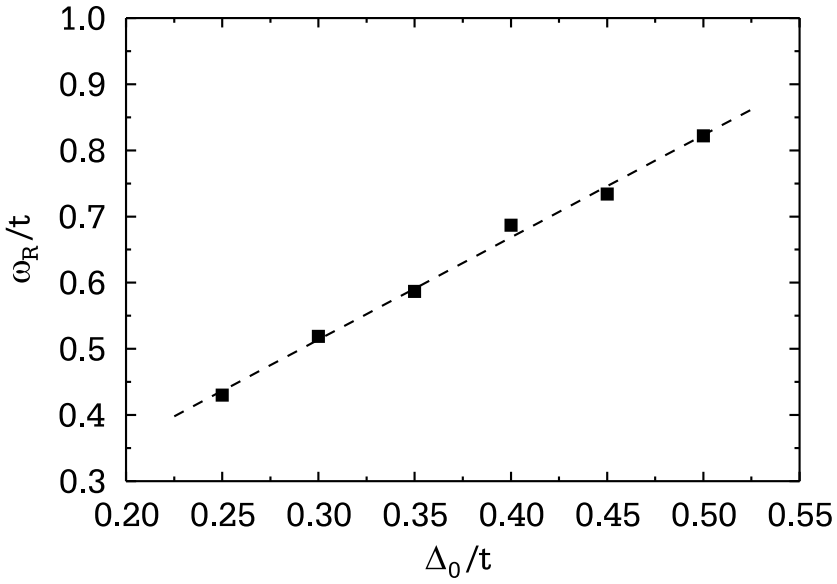

Figure 8.5: *Dependence of the resonance on the d-wave gap maximum. The parameters used for the plot are* $\langle n \rangle = 0.85$, $t'/t = 0.45$, $t_\perp/t = 0.1$, *and* $\bar{U}/t = 1.3$. *The dashed line is a linear fit to the data.*

with the d-wave superconducting gap maximum Δ_0 as shown in Fig. 8.5 and Δ_0 scales linearly with T_c [121].

Other forms for the spin susceptibility can be straightforwardly used for the calculation of the Raman contribution. However, the results are mainly determined by the collective mode at $\mathbf{Q}$. Therefore we take the bilayer susceptibility for a representative calculation.

Raman vertices

As described in Sect. 3.6.1, the Raman vertex is often expressed through an expansion in Brillouin zone or Fermi surface harmonics. However, for the limiting case of vanishingly small scattered (ω_S) and incident (ω_I) photon energies, it can be represented in the effective-mass approximation as

$$\gamma_{\mathbf{k}} = \sum_{\mu,\nu} e^I_\mu \frac{\partial^2 \varepsilon_{\mathbf{k}}}{\partial k_\mu \partial k_\nu} e^S_\nu \tag{8.5}$$

where $\mathbf{e}^I$ and $\mathbf{e}^S$ are the unit vectors representing the polarizations of the incoming and the scattered light, respectively, with $\mu, \nu \in \{x, y\}$. The convention used for the orientation of the axes is that of Fig. 3.7, so that B_{2g} symmetry, for example, is obtained with $\mathbf{e}^I = \hat{x} = (1, 0)$ and $\mathbf{e}^S = \hat{y} = (0, 1)$.

Using Eq. (8.5) and the bilayer tight-binding dispersion (Eq. (8.4)) the Raman

vertex in the various symmetries becomes

$$\begin{aligned}
\gamma_{\mathbf{k}}^{A_{1g}} &= 2a^2 t\gamma_{\mathbf{k}}^{s} - 2a^2 t_\perp \cos(k_z c)[\cos(2k_x a) + \cos(2k_y a)] \\
&\quad -4a^2 \cos(k_x a)\cos(k_y a)[t' + 2t_\perp \cos(k_z c)] \qquad (8.6)\\
\gamma_{\mathbf{k}}^{B_{1g}} &= 2a^2 t\gamma_{\mathbf{k}}^{d}\left(1 + \frac{4t_\perp}{t}\cos(k_z c)[\cos(k_x a) + \cos(k_y a)]\right) \qquad (8.7)\\
\gamma_{\mathbf{k}}^{B_{2g}} &= 4a^2[t' + t_\perp \cos(k_z c)]\sin(k_x a)\sin(k_y a) \qquad (8.8)
\end{aligned}$$

where $\gamma_{\mathbf{k}}^{d,s} = (\cos(k_x) \mp \cos(k_y))/2$. Since the incoming photons have an energy $\hbar\omega_I \simeq 2.5$ eV, which is of the order of the bandwidth and of the inter-band excitations according to local density calculations [36], the validity of the effective-mass approximation is questionable in cuprates [146, 147]. Indeed, a strong dependence of the response in A_{1g} symmetry on the detailed form of the bare Raman vertex [117] was found earlier. Here, other forms for the vertices, which obey the proper symmetry transformations, are considered as well,

$$\gamma_{\mathbf{k}}^{A_{1g}} = \cos(k_x a) + \cos(k_y a) \qquad (8.9)$$

and

$$\gamma_{\mathbf{k}}^{A_{1g}} = \cos(k_x a)\cos(k_y a)\ . \qquad (8.10)$$

These basis functions assign weight to different regions of the Brillouin zone. Hence the A_{1g} response resulted particularly sensitive to the specific choice of $\gamma_{\mathbf{k}}^{A_{1g}}$ in previous calculations.

Raman response function

The spin fluctuations lead to an additional contribution to the Raman response via a two-magnon-like process and the resulting total response is represented diagrammatically in Fig. 8.6 [144]. The Raman response function $\chi_{\gamma\gamma}(\mathbf{q}, i\omega)$ at finite

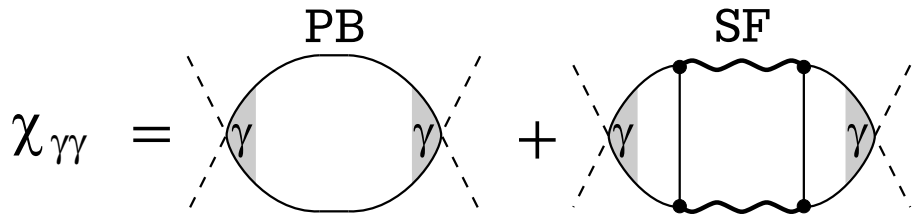

Figure 8.6: *Feynman diagrams for the Raman response function which includes the polarization-bubble (PB) and the two-magnon process (SF). Dashed, wiggly, and solid lines represent photons, spin fluctuations, and fermionic propagators. γ denotes the bare Raman vertex of a specific symmetry.*

temperature is therefore written as the sum of a polarization-bubble (PB), discussed

in Sect. 3.3, and a spin fluctuation (SF) contribution

$$\chi_{\gamma\gamma}(\mathbf{q}, i\omega) = \chi^{PB}_{\gamma\gamma}(\mathbf{q}, i\omega) + \chi^{SF}_{\gamma\gamma}(\mathbf{q}, i\omega) \tag{8.11}$$

with the index γ specifying the scattering geometry in the Raman vertex function.

In Fig. 8.7 the Feynman diagram for the spin fluctuation contribution is explicitly plotted. The spin fluctuation propagator is incorporated in its RPA form for the bilayer by the ladder diagram series with an effective on-site Hubbard interaction $\bar{U}$ [148].

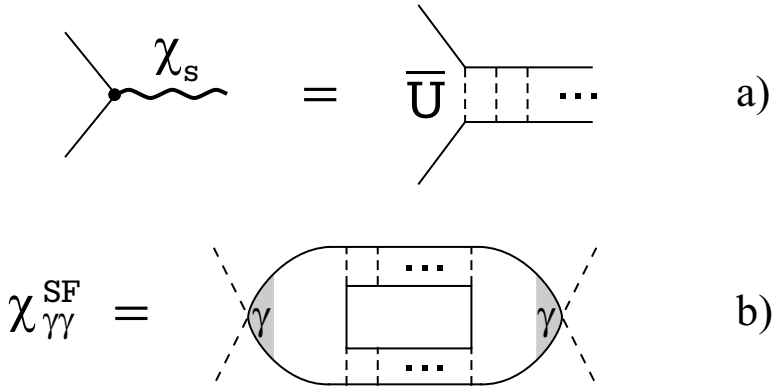

Figure 8.7: *Feynman diagrams for the spin fluctuation contribution. a) Ladder series for the spin fluctuation propagator χ_s. b) Explicit diagram for the spin fluctuation contribution. Dashed, wiggly, and solid lines represent photons, spin fluctuations, and fermionic propagators. γ denotes the bare Raman vertex in a selected scattering geometry.*

In the limit of vanishing momentum transfer $\mathbf{q} \to \mathbf{0}$ (Sect. 3.2) the diagram for the spin fluctuation contribution translates into

$$\begin{aligned} \chi^{SF}_{\gamma\gamma}(i\omega) &= \frac{1}{\beta} \sum_{\mathbf{q}', i\omega'} V^{\gamma}(\mathbf{q}', i\omega, i\omega') \chi_s(-\mathbf{q}', -i\omega') \\ &\quad \chi_s(\mathbf{q}', i\omega + i\omega') V^{\gamma}(\mathbf{q}', -i\omega, -i\omega') \end{aligned} \tag{8.12}$$

where $i\omega$, $i\omega'$ denote bosonic Matsubara frequencies. The vertex function $V^{\gamma}(\mathbf{q}', i\omega, i\omega')$ includes the bare Raman vertex $\gamma_{\mathbf{k}}$ and is evaluated as

$$\begin{aligned} V^{\gamma}(\mathbf{q}', i\omega, i\omega') = \frac{1}{\beta} \, \mathrm{Tr} \sum_{\mathbf{k}, i\omega''} \hat{\gamma}_{\mathbf{k}} \hat{G}(\mathbf{k}, i\omega'' + i\omega) \hat{\tau}_0 \bar{U} \\ \hat{G}(\mathbf{k} + \mathbf{q}', i\omega'' + i\omega + i\omega') \hat{\tau}_0 \bar{U} \hat{G}(\mathbf{k}, i\omega'') \; . \end{aligned} \tag{8.13}$$

$i\omega''$ are fermionic Matsubara frequencies, $\hat{\tau}_i$ with $i = 1, 2, 3$ are the 2×2 Pauli matrices and $\hat{\tau}_0 = \hat{1}$. The calculation of the analytical expression for the vertex function is described in Appendix B.

$\chi^{PB}_{\gamma\gamma}$ is evaluated as described in Sect. 3.3.2

$$\chi^{PB}_{\gamma\gamma}(i\omega) = \frac{1}{\beta}\,\mathrm{Tr}\sum_{\mathbf{k},i\omega'} \hat{\gamma}(\mathbf{k})\hat{G}(\mathbf{k},i\omega')\hat{\gamma}(\mathbf{k})\hat{G}(\mathbf{k},i\omega'-i\omega). \tag{8.14}$$

The total Raman response is calculated in the gauge invariant form of Eq. (3.12)

$$\chi(i\omega) = \chi_{\gamma\gamma}(i\omega) - \frac{\chi^2_{\gamma 1}(i\omega)}{\chi_{11}(i\omega)} \tag{8.15}$$

where $\chi_{\gamma 1}$ and χ_{11} are obtained by the replacement $\gamma_{\mathbf{k}} \to 1$ in one or both bare Raman vertices in the vertex function Eq. (8.13). The analytical continuation to the real axis is performed numerically using Padé approximants [149].

The two-magnon contribution to the A_{1g} channel given by $\chi^{SF}_{\gamma\gamma}$ alone, is plotted in Fig. 8.8. The parameters used for the plot are $\bar{U}/t = 1.3$, $T/t = 0.08$, and $\Delta_0/t = 0.25$. $\chi^{SF}_{\gamma\gamma}$ is the convolution of two spin susceptibilities (see Eq. (8.12)) and therefore has a maximum near twice the magnetic resonance frequencies of the imaginary part of the $\chi_s(\mathbf{q},\omega)$ at $\mathbf{q} = \mathbf{Q}$ and $\mathbf{q} = \mathbf{Q}' = (\pi/a, \pi/a, 0)$. For the chosen parameters, $\mathrm{Im}\chi_s$ has a strong peak for $\mathbf{q} = \mathbf{Q}$ near $\omega_R \simeq 0.4$ and a weaker peak for $\mathbf{q} = \mathbf{Q}'$ at a slightly higher frequency.

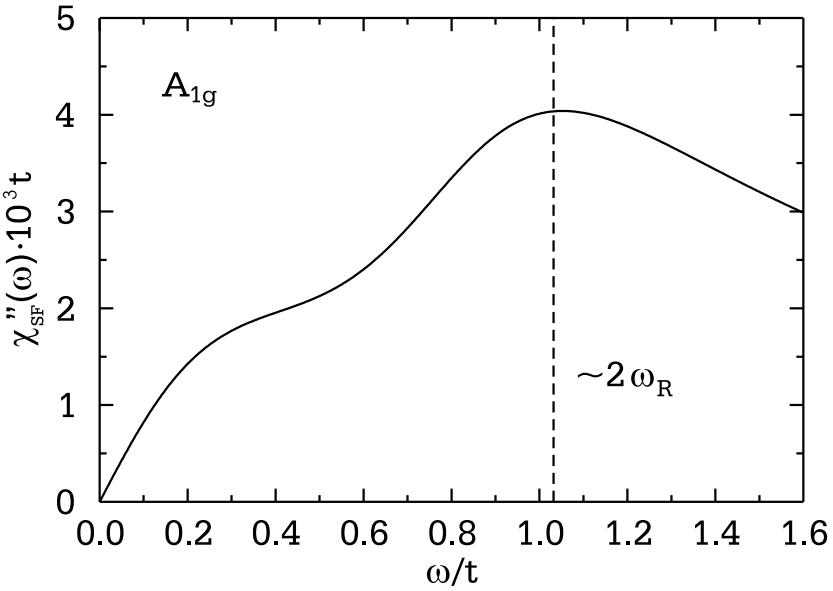

Figure 8.8: *Spin fluctuation contribution to the Raman response $\chi^{SF}_{\gamma\gamma}$ in A_{1g} symmetry. The parameters used are $t'/t = 0.45$, $t = 130$ meV, $\Delta_0/t = 0.25$, $\bar{U}/t = 1.3$ and $\langle n\rangle = 0.85$.*

A first fundamental result of this calculation is that in the B_{1g} and B_{2g} geometries the spin fluctuation term introduces vanishingly small corrections to the total

response. The presence of the spin fluctuation term is therefore important only in the A_{1g} geometry. This is due to the symmetry properties of the vertex function V^{γ}, explicitly written in Eq. (8.13). For spin fluctuations with momentum $\mathbf{Q}$, V^{γ} is the result of the sum over the Brillouin zone of the bare Raman vertex $\gamma_{\mathbf{k}}$ times a function which possesses A_{1g} symmetry. For $\gamma_{\mathbf{k}}$ of B_{1g} or B_{2g} symmetry such a sum vanishes identically. On the other hand, the contribution of spin fluctuations with momentum different from $\mathbf{Q}$ is negligible because of the sharpness of the resonance peak in momentum space. Therfore, for the B_{1g} and the B_{2g} channels the response is given by the polarization-bubble term alone.

The dependence of the total response (Eq. (8.15)) in A_{1g} symmetry on the effective interaction $\bar{U}$ is shown in Fig. 8.9. The parameters used are the same as for Fig. 8.8. For $\bar{U} = 0$ the response corresponds to polarization-bubble contribution alone. The shape of the Raman response is modified by varying $\bar{U}/t$ and in particular the position of the peak is shifted towards higher energies for increasing $\bar{U}$. With the inclusion of the spin fluctuation term the A_{1g} peak position in the superconducting spectra is at frequencies slightly above Δ_0 consistent with the experimental observations in YBCO and BSCCO (for a review see [66]).

A comment is in order on the relative magnitude of the spin fluctuation and the polarization-bubble term. A comparison of Figs. 8.8 and 8.9 makes it clear that the spin fluctuation term is much smaller than the polarization-bubble term.

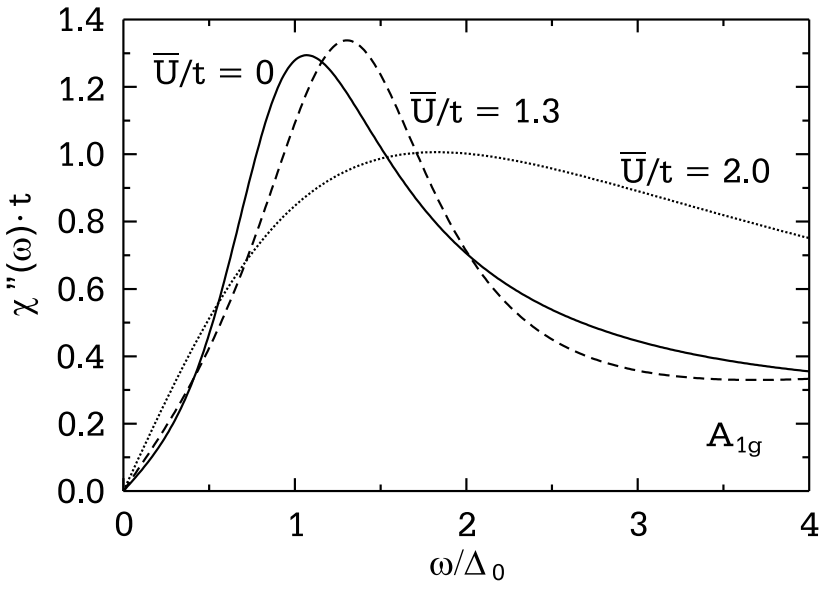

Figure 8.9: *Raman response in A_{1g} symmetry. Solid, dashed and dotted lines correspond to $\bar{U}/t = 0$, $\bar{U}/t = 1.3$ and $\bar{U}/t = 2.0$, respectively. The parameters used are $t'/t = 0.45$, $t = 130$ meV, $\Delta_0/t = 0.25$, $\bar{U}/t = 1.3$ and $\langle n \rangle = 0.85$.*

The effect of this new term is nevertheless visible since the backflow (the second term in Eq. (8.15)) mixes the two contributions in a nontrivial way. Since the spin fluctuation term varies as $\bar{U}^4$ in this model it starts to dominate for larger $\bar{U}$, leading to a shift in spectral weight out toward higher frequencies.

Previous studies [117] have shown that the calculations for the A_{1g} screened response are unstable to the inclusion of higher-order Brillouin zone harmonics for either the energy gap, the band structure or the Raman vertex. Thus, theories based on $d_{x^2-y^2}$ model fail to reproduce the rather universal character of the A_{1g} peak, present in different cuprates even with only one single CuO_2 sheet [150, 151].

This inconsistence is solved when the spin fluctuations term is included in the response. This is shown in Fig. 8.10 where the Raman response is calculated for the three different forms for the vertex given by Eq. (8.8), (8.9) and (8.10). All curves are normalized to their peak height to allow for an easier comparison. Clearly, the strong sensitivity to changes of the bare Raman vertex (Fig. 8.10 (a)) is much reduced when the spin fluctuation term is added (Fig. 8.10 (b)). Within this model it has been verified that this reduced sensitivity is not altered by different model parameter choices and different broadening of the response [148].

8.2.2 Comparison with experimental results

The comparison between theoretical and experimental results is shown in Fig. 8.11. Data for an optimally doped BSCCO sample are taken from [152]. For the Raman vertex the expression derived from the tight-binding dispersion is used. The parameters are $t = 130$ meV, $\Delta_0/t = 0.25$ and $T/t = 0.08$. The effective interaction $\bar{U}$ and the hopping integral t are used as the only two fitting parameters.

Adding the spin fluctuation contribution leads to a shift of the peak position from near Δ_0 for $\bar{U} = 0$ to higher frequencies, and thus to a better agreement with the experimentally observed relative peak positions in A_{1g} and B_{1g} geometries. For the fit, t is adjusted to achieve a good agreement with the B_{1g} channel, and then $\bar{U}$ is used to match the A_{1g} peak position.

The value of t obtained from the fit is $t = 130$ meV. This value has to be compared with $t \simeq 105$ meV, which results from the condition $\omega_R \simeq 40$ meV. This slight discrepancy is most probably related to our simple modeling of the propagators which neglects strong renormalization due to interactions as well as impurities. The value of $\bar{U}$ obtained from the fit is $\bar{U} = 1.3$ consistent with previous results ([136] and references therein). The excess experimental intensity in the A_{1g} channel above the theoretical curve in Fig. 8.11 is somewhat sample dependent and is possibly related to disorder-induced phonons.

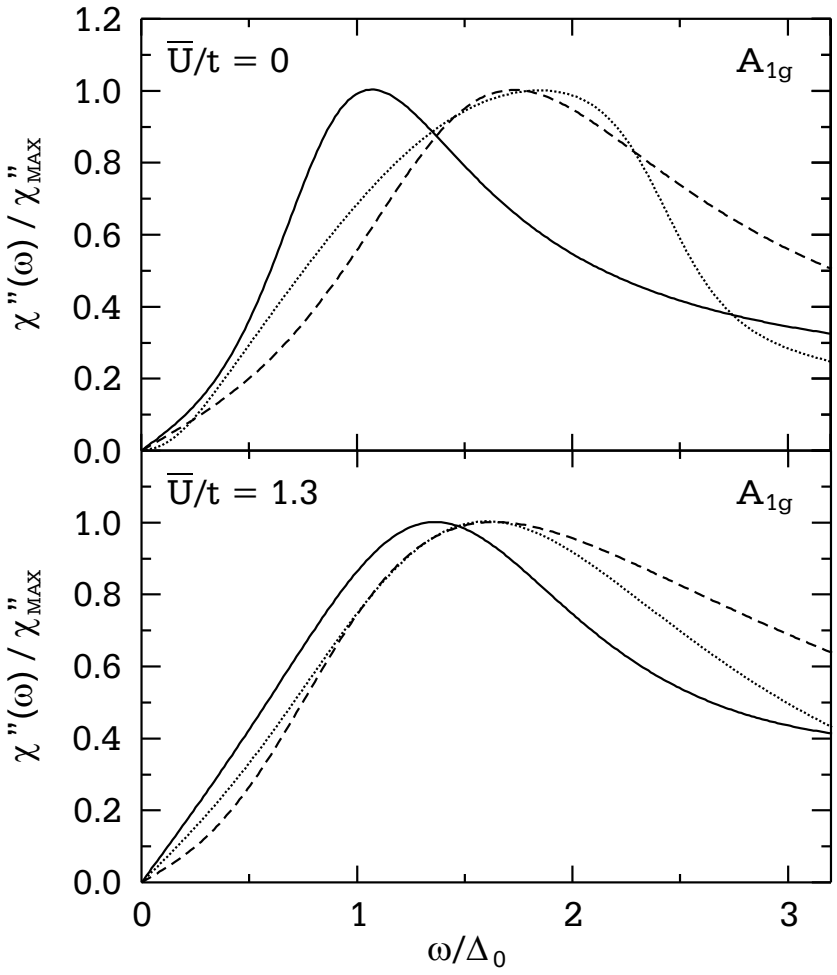

Figure 8.10: *Raman response in A_{1g} symmetry for different vertices: $\gamma_{\mathbf{k}}^{A_{1g}}$ obtained from effective mass approximation (solid line),* $\cos(k_x) + \cos(k_y)$ *(dashed line),* $\cos(k_x)\cos(k_y)$ *(dotted line). In the upper panel the Raman response is plotted for $\bar{U}/t = 0$, in the lower panel for $\bar{U}/t = 1.3$.*

The conclusion of this calculation is therefore that the scattering from the collective spin fluctuation mode plays an important role in the superconducting state. In fact, the inclusion of this contribution in the Raman response solves the previously unexplained sensitivity of the A_{1g} response to small changes in the Raman vertex. In addition, within the described model it is now possible to obtain the correct relative peak positions of the A_{1g} and the B_{1g} scattering geometry. Thus, the two-magnon-like contribution controls the A_{1g} peak and is ineffective in the B_{1g} and B_{2g} symmetries, which are mainly determined by the polarization-bubble term described in Sect. 3.3.

The interplay between the magnetic resonance and the Raman response has been investigated by experiments on Ni-substituted YBCO [153]. Ni is believed to replace

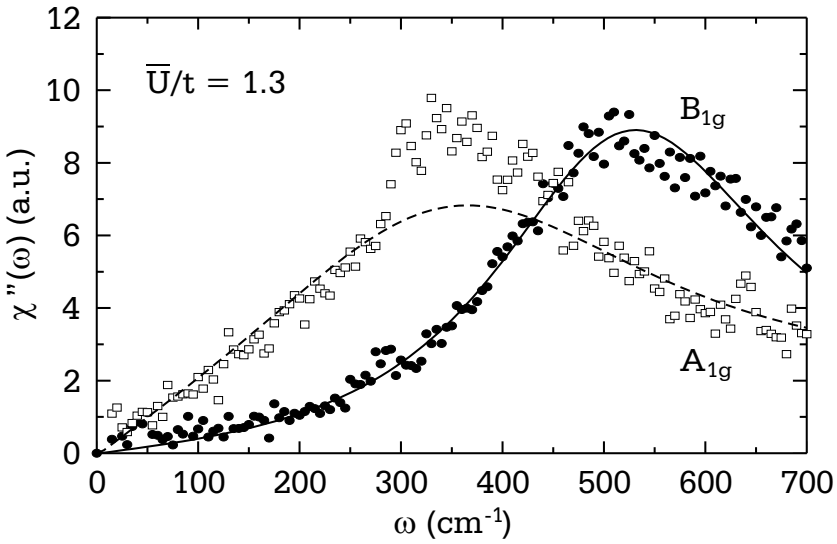

Figure 8.11: *Comparison of the calculated A_{1g} and B_{1g} response with the spectra of optimally doped BSCCO from [152]. The parameters used are $t'/t = 0.45$, $t = 130$ meV, $\Delta_0/t = 0.25$, $\bar{U}/t = 1.3$ and $\langle n \rangle = 0.85$.*

Cu in the CuO_2 planes [154] with the effect of reducing T_c without changing the carrier concentration. As a result the experimental peak positions of the superconducting spectra in A_{1g} symmetry are found to scale as ω_R when T_c is reduced and to remain constant in B_{1g} symmetry. Also, the temperature dependence of the peak intensity is found to follow the intensity evolution of the magnetic resonance only in A_{1g} symmetry. These results provide experimental evidence for the relevance of the scattering from spin fluctuations in the superconducting state for the A_{1g} response.

8.3 Chiral excitations and unconventional density waves

As shown in the two previous sections, spin fluctuations play a fundamental role in the phenomenology of cuprates. Here an additional contribution to the scattering from the spin degrees of freedom is considered.

In a Mott insulator, in which the insulating behaviour arises from electron-electron interactions, a charge excitation produces a distortion of the magnetic state. As a consequence, the phase of the excitation wave function may depend not only on its position, but also on the path which the hole followed to arrive at the site [155]. Therefore, a hole doped into a Mott insulator may acquire a phase while moving along a closed path. In this case the excitation is said to be chiral, and

the total solid angle formed by three adjacent spins given by the expectation value in the ground state of the chirality operator $\sum \mathbf{S}_i(\mathbf{S}_j \times \mathbf{S}_k)$ is different from zero. In the Raman response, the scattering from chiral excitations produces a finite A_{2g} symmetry component [155, 156]. Such a contribution has indeed been observed up to large energy shifts in insulating compounds [157, 158].

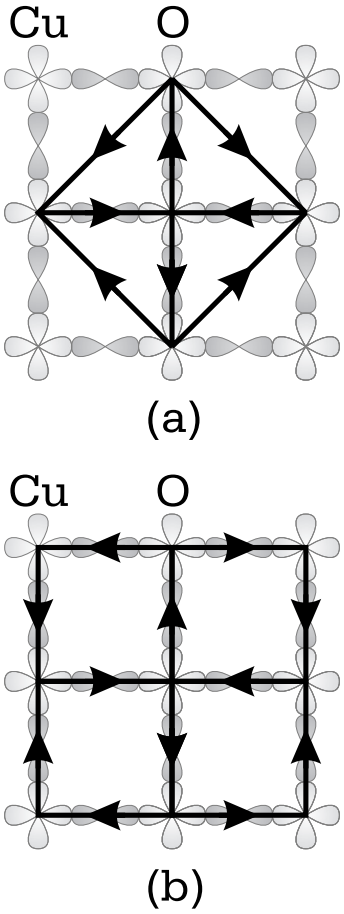

Figure 8.12: *Possible current patterns in the Cu-O planes proposed by [159] (a) and [67] (b).*

Recently the proposal of the existence of orbital currents circulating in the Cu-O planes [67, 159] has attracted great interest. Such currents break time-reversal symmetry and give rise to an unconventional charge density wave with d-wave symmetry (d-density wave or DDW in short) which competes with the superconducting order parameter producing the complex phenomenology of cuprates [67, 125, 160]. Indeed, experimental support for this scenario comes from photoemission spectroscopy. Using circularly polarized light a spontaneous breaking of time-reversal symmetry is observed at doping levels and temperatures corresponding to the "pseudogap" phase [161].

Raman scattering is another direct tool to investigate chiral excitations because excitations breaking time-reversal symmetry can be detected as a contribution in A_{2g} symmetry.

8.3.1 Complete symmetry analysis of the Raman spectra

As introduced in Sect. 3.6.2, both linear and circular polarizations are necessary to extract the pure symmetry components. The method developed to adjust and measure circular polarizations is described in Sect. 4.4.

With reference to Fig. 3.7 for the linear polarizations and Fig. 3.8 for the circular polarizations, the combination of the measured spectra used to extract the symmetry components is tabulated in Tab. 8.1. A linear combination involving all six spectra is always used to average over small changes in the experimental conditions during the experiment. To avoid the deposition of layers on the sample surface which would dramatically alter the spectra especially at high frequencies it is crucial to acquire the spectra in rapid sequence. Therefore, all six spectra at a given temperature are

Symmetry	Linear Combination
A_{1g}	(xx+x'x'+LL-(xy+x'y'+LR)/2)/3
A_{2g}	(xy+x'y'+LL-(xx+x'x'+LR)/2)/3
B_{1g}	(x'y'+xx+LR-(x'x'+xy+LL)/2)/3
B_{2g}	(xy+x'x'+LR-(xx+x'y'+LL)/2)/3

Table 8.1: *Linear combination of the measured spectra used to extract the pure polarizations.*

measured within a few hours.

A quantitative check of the consistency of the measurements can be performed by summing each two measured spectra with the same polarization state of the incident light. With reference to Figs. 3.7 and 3.8, the result is the sum of all four symmetry components

$$\left.\begin{array}{l} \text{xx + xy} \\ \text{x'x' + x'y'} \\ \text{LL+LR} \end{array}\right\} = A_{1g} + A_{2g} + B_{1g} + B_{2g} \ . \tag{8.16}$$

An example of such a consistency check is shown in Fig. 8.13 for optimally doped BSCCO (Opt95) at 30 K. The curves represent the sums given in Eq. (8.16) and are plotted without any adjustment. The discrepancies are of the order of 5%.

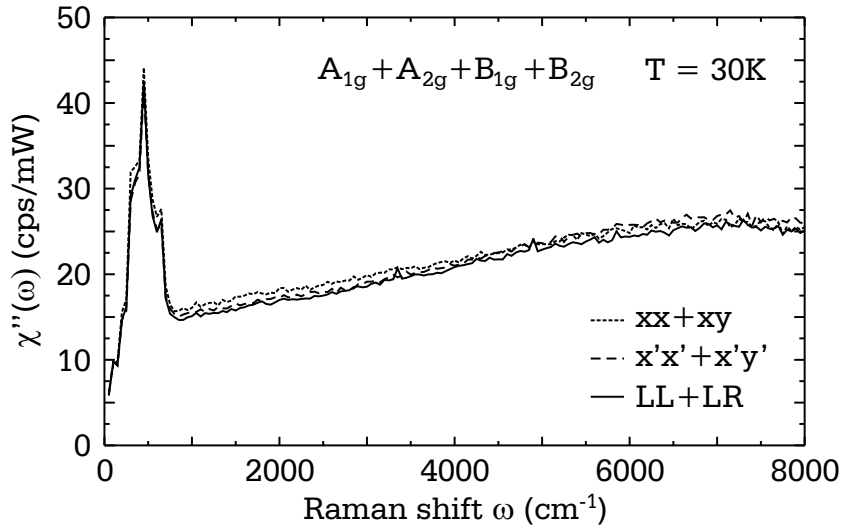

Figure 8.13: *Consistency check for the optimally doped BSCCO sample Opt95 at 30 K. Each curve is the sum of two experimentally measured spectra with the same incoming polarization state.*

8.3.2 Experimental evidence of A_{2g} component

The pure symmetry components of the optimally doped BSCCO Opt95 at 30 K are shown in Fig. 8.14. The sharp features at frequencies below 800 cm^{-1} are due to

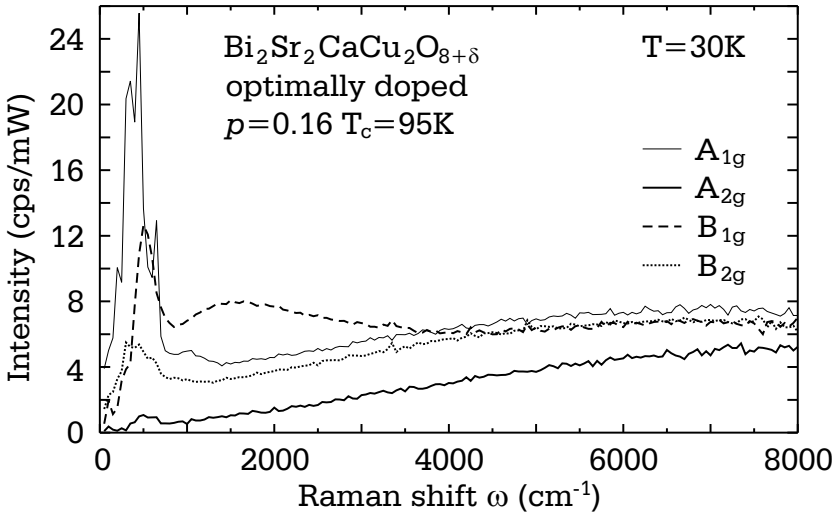

Figure 8.14: *Raman response of the optimally doped BSCCO sample Opt95 at 30 K in the four symmetries.*

lattice vibrations. At approximately 500 cm^{-1} the superconductivity-induced peak is visible in A_{1g}, B_{1g} and B_{2g} symmetries. As a result of the complete polarization analysis an A_{2g} symmetry component is clearly resolved. This component is negligible below 1000 cm^{-1} but becomes comparable in intensity to the other symmetry components at high frequencies. The two-magnon peak (Sect. 8.1) is clearly visible in B_{1g} symmetry.

For comparison, the pure symmetries in the overdoped OD65 sample (Tab. 4.3) at 157 K are plotted in Fig. 8.15. In the overdoped regime, too, the A_{2g} component is significant only for frequencies above 1000 cm^{-1}. The B_{1g} component does not show an indication of the two-magnon peak and is practically constant above 2000 cm^{-1}.

The result of the complete symmetry analysis in antiferromagnetic YBCO (Tab. 4.2) at 210 K is shown in Fig. 8.16. The electronic continuum at low frequency is strongly suppressed in all symmetries. A few sharp structures due to lattice vibrations are clearly visible in the A_{1g} and B_{1g} symmetries. The two-magnon peak in B_{1g} is the most prominent feature as expected for an antiferromagnetically ordered sample. Some intensity appears also in A_{1g} and B_{2g} symmetries, because of spin-flip processes involving next-nearest-neighbor sites [137]. The sharp peak at approximately 1300 cm^{-1} in the A_{1g} spectra is possibly related to two-phonon scattering [90].

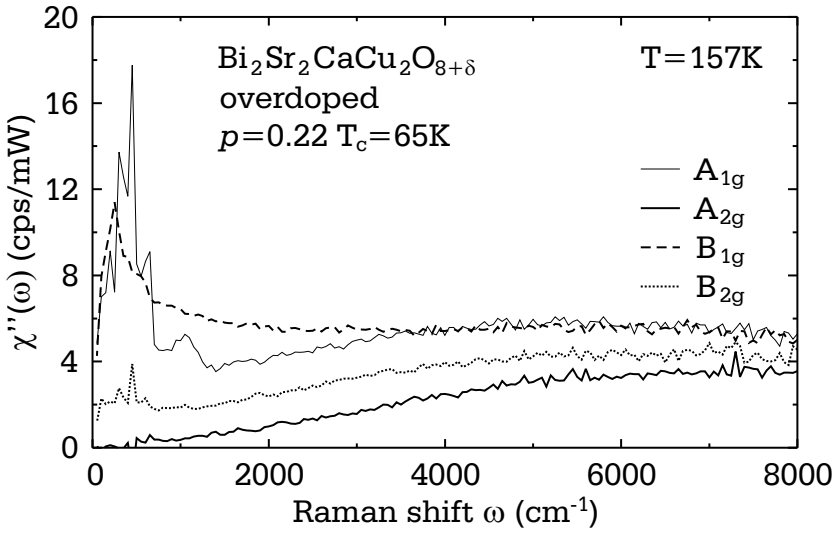

Figure 8.15: *Raman response of the overdoped BSCCO sample OD65 at 157 K in the four symmetries.*

8.3.3 Temperature and doping dependence of the A_{2g} component

The temperature dependence of the A_{2g} symmetry component in the optimally doped BSCCO sample Opt95 is shown in Fig. 8.17. Above 2000 cm^{-1} the spectra measured at the different temperatures are not distinguishable. Below 2000 cm^{-1} a weak temperature dependence is observed. Due to the weakness of the signal

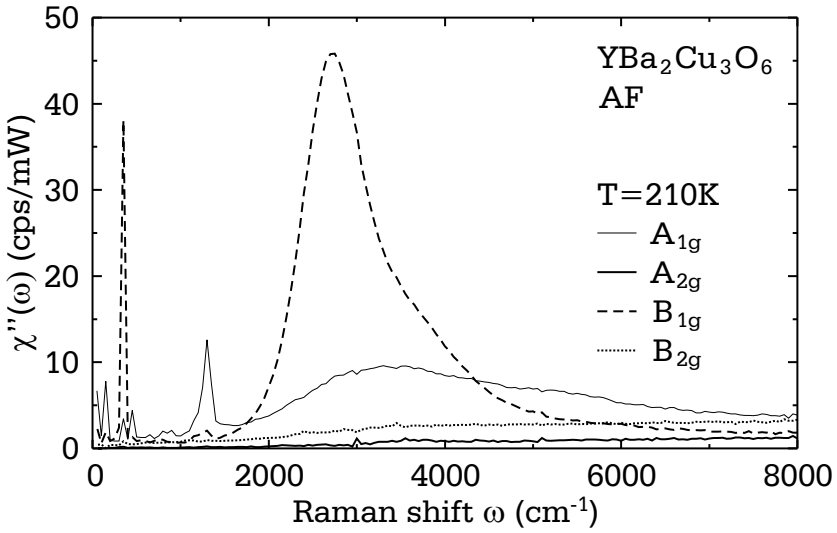

Figure 8.16: *Raman response of the antiferromagnetic YBCO sample at 210 K in the four symmetries.*

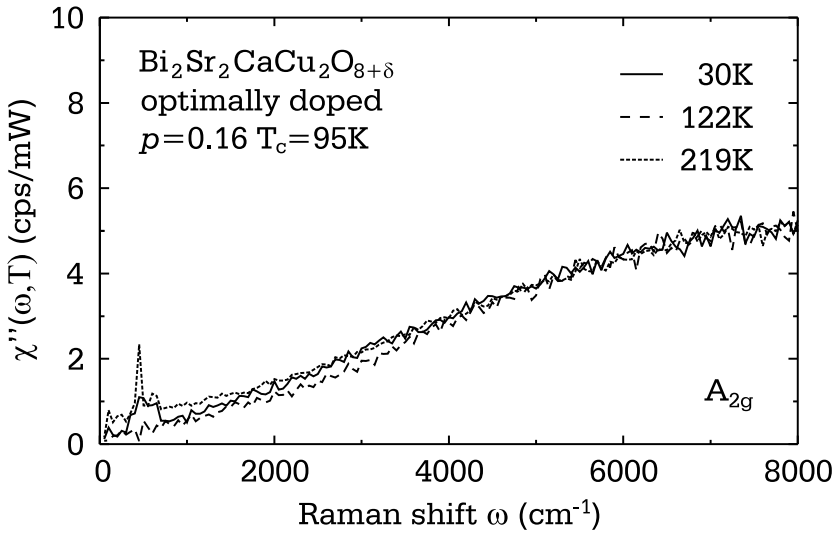

Figure 8.17: *Raman response in A_{2g} symmetry at different temperatures in the optimally doped BSCCO sample Opt95.*

(below one count per second) more precise measurements are required to rule out artifacts arising from improper subtraction of the different spectra. The sharp peak at 450 cm^{-1} in the spectrum at 220 K is a residue of a strong A_{1g} phonon (displacement in the c-direction of the apex oxygens in the Sr-O planes [162]) whose contribution is not properly canceled. Also in YBCO and LSCO samples there is no clear indication of temperature dependence up to high frequencies.

The doping dependence of the A_{2g} symmetry component is shown in Fig. 8.18

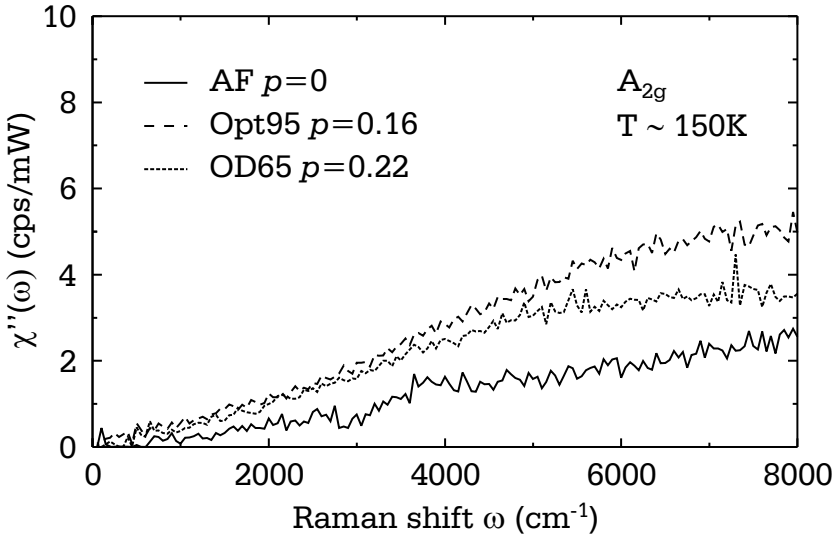

Figure 8.18: *Raman response in A_{2g} symmetry in the normal state of antiferromagnetic (AF), optimally (Opt95) and overdoped (OD65) BSCCO samples.*

where normal state spectra are plotted for the antiferromagnetic (AF), the optimally (Opt95) and overdoped (OD65) samples.

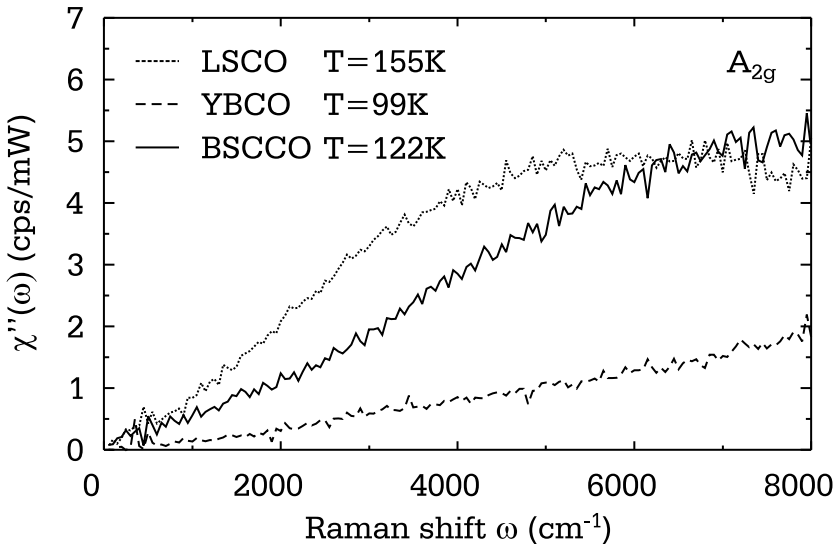

Figure 8.19: *Raman response in A_{2g} symmetry in the normal state of different cuprates: optimally doped LSCO, YBCO and BSCCO (Opt95) crystals. The temperatures of the measurements are indicated.*

The A_{2g} signal is maximal in the optimally doped sample where an almost linear frequency dependence is observed up to 7000 cm^{-1}. For higher frequencies it remains approximately constant. In the overdoped sample a similar frequency dependence is observed. However, above 5000 cm^{-1} the signal saturates to a constant value. The A_{2g} signal is smallest in the antiferromagnetic sample where it remains almost negligible (below 1 count per second) up to 3000 cm^{-1}.

Finally, in Fig. 8.19 the A_{2g} Raman response of the normal state is compared for different cuprates at optimal doping, LSCO, YBCO and BSCCO. In YBCO the A_{2g} signal is minimal with a linear increase with frequency in the entire range studied. In LSCO the strongest frequency dependence is observed up to 4000 cm^{-1}. The response reaches its maximum at approximately 6000 cm^{-1} and seems to saturate or slightly decrease for higher frequencies.

In Fig. 8.20 are summarized the temperatures and doping levels at which A_{2g} symmetry component has been investigated in the different compounds.

In conclusion, as a result of the complete symmetry analysis an A_{2g} component has been detected in all samples studied. The intensity of this signal is comparable to that of the other symmetries at high frequency, and negligible below 1000 cm^{-1}. The origin of such a component is, however, not yet clarified. It is not simply related to magnetic fluctuations because then its intensity would be maximal in

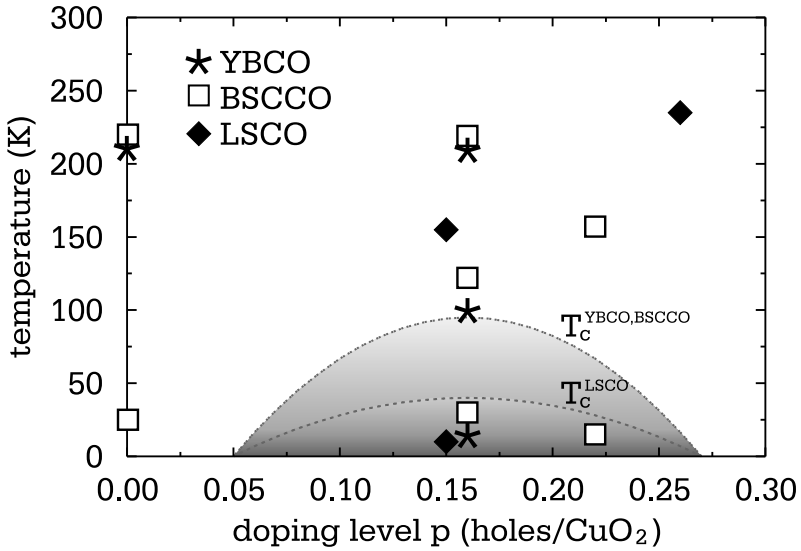

Figure 8.20: *Phase diagram investigated investigated to study the A_{2g} symmetry component. The critical temperatures of YBCO, BSCCO ($T_c^{YBCO,BSCCO}$) and LSCO (T_c^{LSCO}) are calculated from Eq. (4.1).*

the antiferromagnetic sample, similarly to what is observed for the two-magnon peak in B_{1g} symmetry (compare Fig. 8.2 and Fig. 8.14). On the other hand, it is not characteristic of superconducting samples either because it is present, although with different intensities, in antiferromagnetic and overdoped metallic samples. In particular, no influence of the metal-insulator transition at $p_c = 0.22$ could be found. The lack of a temperature dependence in the range of temperature and doping studied implies that no crossover is observed for the excitations probed. This result does not allow a straightforward interpretation in terms of orbital currents appearing in the pseudogap phase. In addition, the signal is clearly visible in the overdoped sample with $p = 0.22$ and at $T = 157$ K where no pseudogap is observed. Since the effect of such currents found by photoemission is at most 4% [161], it is well possible that such a contribution is not detectable with the present experimental setup. A better insight could be obtained by investigating the dependence of the A_{2g} component on the wavelength of the exciting light.

As mentioned, scattering from chiral spin fluctuations is not the only process that can give rise to an A_{2g} contribution. If the laser light can excite inter-band transitions, the selection rules for the Raman process are altered and such a component can appear [34].

It is, however, important to notice that the A_{2g} component is relevant for the analysis at larger energy transfers and cannot be neglected as done in previous studies. Once the pure symmetries are extracted, the Raman relaxation rate $\Gamma(\omega)$

and mass renormalization factor $1+\lambda(\omega)$ (see Sect. 3.4 for details) become consistent with infrared and photoemission results.

The dynamical relaxation rate calculated from the B_{2g} Raman response of optimally doped BSCCO (Opt95) at 200 K is shown in Fig. 8.21. $\Gamma(\omega)$ is shown

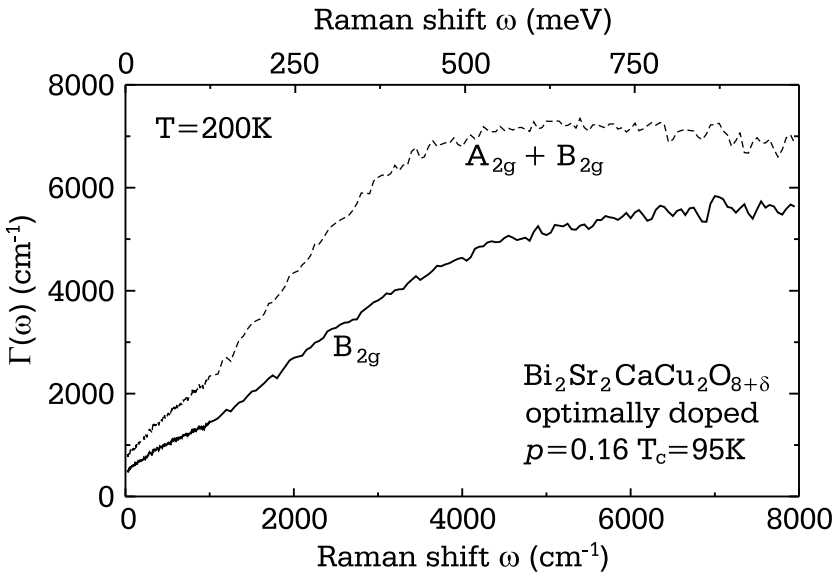

Figure 8.21: *Dynamical relaxation rate in B_{2g} symmetry of optimally doped BSCCO (Opt95) at 200 K.*

for the spectrum measured with $\hat{x}\hat{y}$ polarization orientations, corresponding to the $A_{2g} + B_{2g}$ symmetry components, and for pure B_{2g}. The relaxation rate in the B_{2g} symmetry spectrum has a frequency dependence consistent with the imaginary part of the self-energy derived from photoemission results (Fig. 5.10 and Fig. A.1). To facilitate the comparison a scale in meV has been added in Fig. 8.21.

The mass renormalization factor $1 + \lambda(\omega)$ calculated from the B_{2g} spectrum of optimally doped BSCCO (Opt95) at 200 K is shown in Fig. 8.22. As a result $1+\lambda(\omega)$ asymptotically approaches unity, differently from what was previously reported [30], indicating the validity of the quasiparticle description up to high energies. The linear fit in a logarithmic energy scale (dashed line) illustrates that $1 + \lambda(\omega)$ exhibits a logarithmic divergence over almost three decades. This result supports the marginal Fermi liquid scenario [88, 89, 163] introduced in Sect. 5.4.1 to evaluate the Raman response.

In conclusion, the B_{2g} spectrum obtained by a complete symmetry analysis is consistent with the carrier dynamics determined by other techniques, such as photoemission or infrared spectroscopies over a wide doping range.

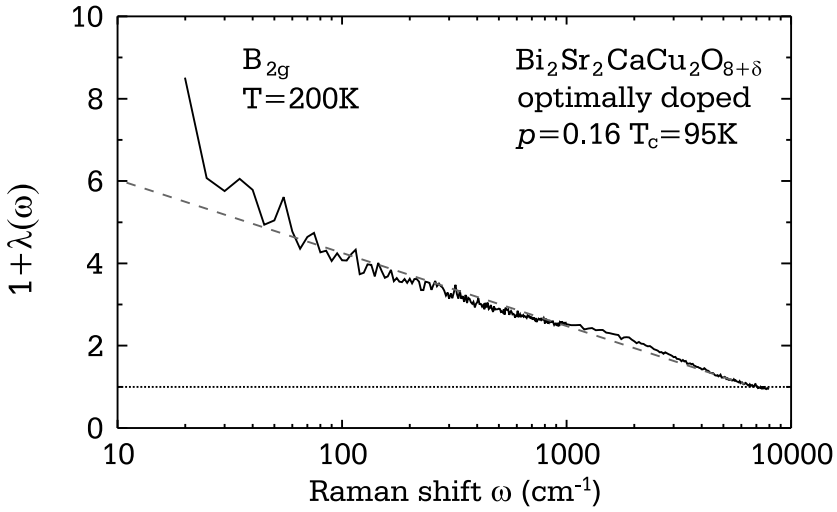

Figure 8.22: *Mass renormalization factor as calculated from the B_{2g} Raman response of optimally doped BSCCO (Opt95) at 200 K. The dashed line is a linear fit to the data in logarithmic scale.*

8.4 Experimental results in $La_{2-x}Sr_xCuO_4$: charge ordering and stripe formation

The effect of antiferromagnetic correlations is particularly strong in LSCO, where it is believed to produce spin-charge separation [17]. For this reason this compound has attracted particular attention in the last years. The early observation of an anomalous suppression of superconductivity in samples with a hole concentration of $x = 1/8$ [164] is probably related to the formation of a dynamical modulation of spin and charge.

In this chapter Raman spectra for differently doped samples are analyzed as a function of temperature and scattering geometry. In the underdoped region an anomalous response is observed which indicates a new type of electron dynamics. Infrared measurements on the same samples are also presented. The comparison between the two spectroscopies used to interpret the anomalous response observed leads to the conclusion that charge ordering is observed by Raman for the first time.

8.4.1 Stripes in $La_{2-x}Sr_xCuO_4$?

As introduced in Chapter 2, cuprate superconductors are obtained by doping the "parent" compounds, which are antiferromagnetic Mott-Hubbard insulators since their insulating behaviour is the result of strong electron-electron correlations. In Fig. 8.23 is depicted an example of the antiferromagnetic ground state. The arrows

indicate the spin orientations on the Cu sites. Even when doped with a sufficient number of holes to make the material superconducting, the local magnetic correlations persist up to the overdoped region.

A single hole in a two-dimensional antiferromagnet should have very low mobility because of the large magnetic energy required for the breaking of the spin bonds resulting from its motion. Since its motion inevitably frustrates the antiferromagnetic bonds, the hole will be strongly localized until the long-range antiferromagnetic order is destroyed.

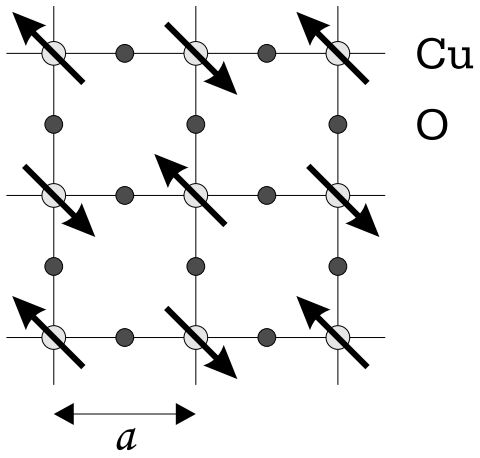

Figure 8.23: *Sketch of the CuO_2 plane. The arrows indicate possible alignment of the spins in the antiferromagnetic ground state. a is the lattice constant.*

However, recent resistivity measurements on LSCO [165] have shown that the doped holes in clean crystalline cuprates are surprisingly mobile in a wide range of temperatures, even in the antiferromagnetic phase. These results, together with the unexpected persistence of short-range antiferromagnetism in the superconducting phase, have been interpreted in terms of spin-charge ordering.

The basic idea is that the mobile carriers in the CuO_2 planes, the holes, are expelled from regions of well-formed local moments and confined to one-dimensional lines, which are therefore called charged "stripes". A proposed pattern for the spin-charge ordering is schematically represented in Fig. 8.24 [166], where only the Cu atoms are displayed. The arrows represent the local spins on the Cu site which are antiferromagnetically oriented within the domains. The charge stripes are the shaded areas. Since the number of holes per Cu is 1/2, one out of two Cu sites is occupied (filled circles). In inelastic neutron scattering experiments on $La_{1.6-x}Nd_{0.4}Sr_xCuO_4$ [17] it was observed that these structures are most pronounced for a hole concentration of 1/8 as represented by the magnetic unit cell shown in Fig. 8.24.

At the moment there is no agreement on what drives the separation of charge and spin and on what is the effect of stripes on superconductivity. Experimental evidence suggesting that stripes and superconductivity are related comes from neutron scattering measurements. In fact, a linear relation between the transition temperature T_c and the inverse modulation period of the spin-density wave was observed

up to optimal doping [167].

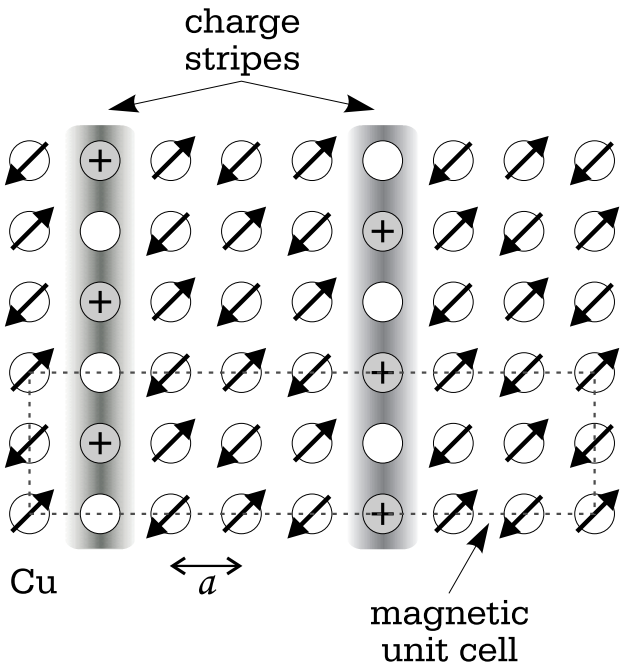

Figure 8.24: *Schematic representation of spin-charge separation in the CuO_2 planes with $x = 1/8$, according to the model of [166]. Only the Cu atoms are displayed; a is the lattice constant.*

Charge order is most easily detected when the stripes are static. For example, an anisotropic distortion of the crystal structure may be able to pin fluctuating stripes. Static stripes were first observed in $La_{1.6-x}Nd_{0.4}Sr_xCuO_4$ by neutron diffraction experiments [17] consistent with the pattern of Fig. 8.24. In fact, Nd changes the direction of the distortion of the crystal structure due to a rotation of the tilt of the CuO_6 octahedra from diagonal to parallel to CuO bonds. In this material it appears that stripes suppress superconductivity, as is most evident at the doping level $x = 1/8$ where the static stripes and a local minimum in the critical temperature T_c [164] are observed. In the absence of Nd it is believed that the stripes are still existing but strongly fluctuating, and are sometimes referred to as "dynamical" [168]. The experimental observations are still insufficient to clarify their existence or absence in LSCO. Therefore it is particularly important to investigate this compound by the Raman technique, since the **k**-resolution allows the detection of anisotropic conduction which cannot be observed by transport or magnetic measurements.

8.4.2 Raman and infrared conductivity experimental results

The measurements were performed on an underdoped and an optimally doped LSCO single crystals (UD and Opt in Tab. 4.1). The electronic Raman response $\chi''(\omega, T)$ of the underdoped crystal is shown in Fig. 8.25 for B_{1g} (panel (a)) and B_{2g} (panel (b)) symmetries. The contribution from vibrational excitations has been subtracted out for clarity. To facilitate the comparison between the spectra, their intensities have been adjusted by multiplicative factors (between 0.94 and 1.09) to make them coincide at high energies.

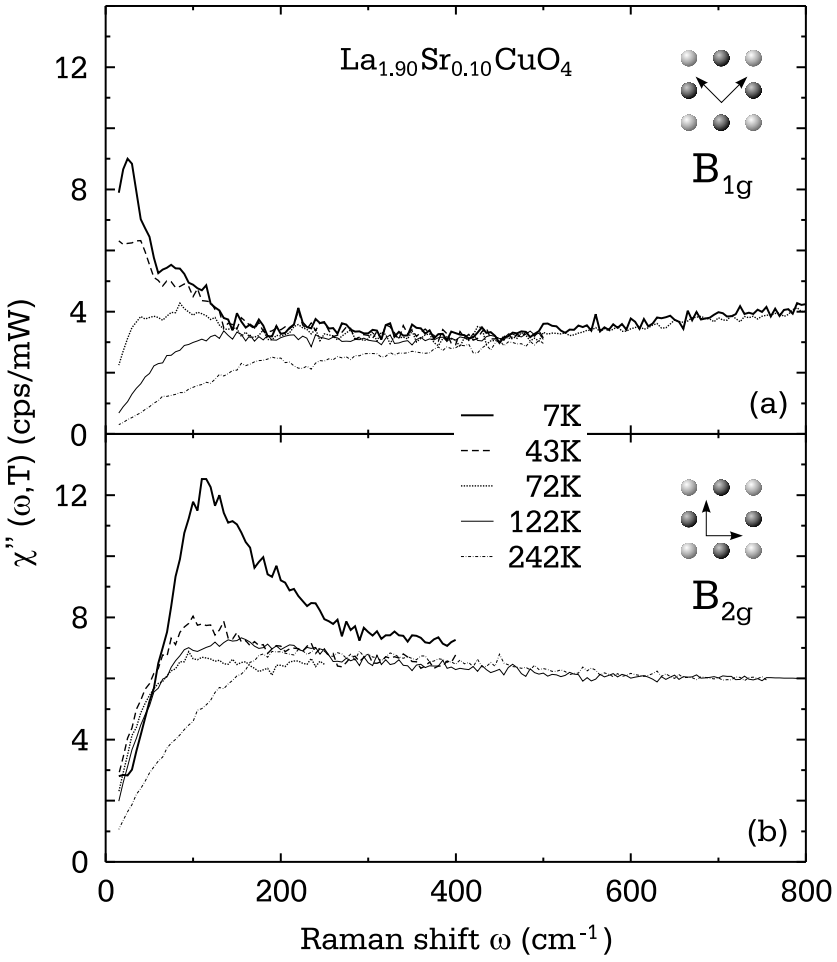

Figure 8.25: *Raman response $\chi''(\omega, T)$ of underdoped LSCO at different temperatures. In panels (a) and (b) are shown the B_{1g} and the B_{2g} configurations, respectively.*

At high frequencies, $\omega \geq 400$ cm^{-1}, the electronic spectra are featureless and consistent with earlier results in LSCO [112], YBCO and BSCCO [30, 114]. Up to approximately 1500 cm^{-1} the continuum is essentially constant in B_{2g} symmetry (panel (b)) and increases linearly in B_{1g} symmetry (panel (a)). In the range below 200 cm^{-1} the usual temperature dependence of the slope of the spectra is observed in B_{2g} symmetry (panel (b)): the increase of the spectral weight upon reducing the temperature leads to an increasing slope of the response in the dc limit (see for comparison Fig. 6.3 in BSCCO). Since $\partial\chi''(\omega \to 0, T)/\partial\omega$ is proportional to the static lifetime of the carriers (Sect. 6.2), this behaviour is compatible with the metallic decrease of the resistivity upon reducing the temperature. In the superconducting state (7 K) a clear redistribution of spectral weight at low frequencies is observed. This is an indication of the good quality of the sample, since a significant amount of

impurities would reduce the superconductivity-induced peak and eventually wash it out completely [31, 116].

In B_{1g} symmetry a similar metallic increase towards low temperature is observed between approximately 250 and 100 K. The spectra are more flat than in B_{2g} symmetry indicating a larger relaxation rate or a shorter lifetime as well as a weaker temperature dependence than. Below 200 K an anomalously strong increase of the low-energy response is observed. Although the spectra are measured down to 15 cm^{-1} the linear decrease toward zero energy, which is necessary to satisfy causality, cannot be resolved any more. Consequently, the lifetime must become very long and exceed the one observed at B_{2g} symmetry by far. In B_{1g} symmetry, despite the good sample quality, no superconducting peak can be observed. This is consistent with what was previously reported not only in LSCO [112] but also in underdoped BSCCO and YBCO [111].

The electronic Raman response $\chi''(\omega, T)$ of the optimally doped sample is shown in Fig. 8.26 (a) and (b) for B_{1g} the B_{2g} symmetries, respectively. Also in this case the contributions from the phonons have been subtracted out and the spectra have been adjusted by multiplicative factors (between 0.67 and 1.38) to make them match at high energies. Similarly as in the underdoped sample the B_{2g} spectrum at the lowest temperature (7 K) is characterized by a strong superconductivity -induced peak which is now visible also in the B_{1g} spectrum.

The high-energy spectra have generally similar behaviour to those of the underdoped sample in both symmetries. However, in the range between 300 cm^{-1} and 700 cm^{-1} the low-temperature spectra (7 K and 56 K) in B_{2g} symmetry display a loss of spectral weight. A similar depletion was previously observed in YBCO and BSCCO [111]. Also the low-energy response is consistent with YBCO and BSCCO results, since the anomalous increase in the B_{1g} normal-state spectra is absent and the evolution with temperature is similar to what is found in other cuprates [111].

In conclusion, below 100 K an unexpected long lifetime is observed in the underdoped sample in only one of the two symmetry components which is not visible at any of the temperatures measured ($T > 56$ K) in the optimally doped crystal. The fact that this behaviour is not observed in YBCO and BSCCO seems to indicate that a new type of electron dynamics is involved. For this reason it is interesting to analyze the infrared conductivity on the very same samples. Since the two spectroscopies are characterized by different selection rules but measure essentially the same quantity, they are complementary.

The infrared spectroscopy experiments were performed by the group of Prof. P. Calvani, at the University of Rome "La Sapienza", Italy. To compare directly

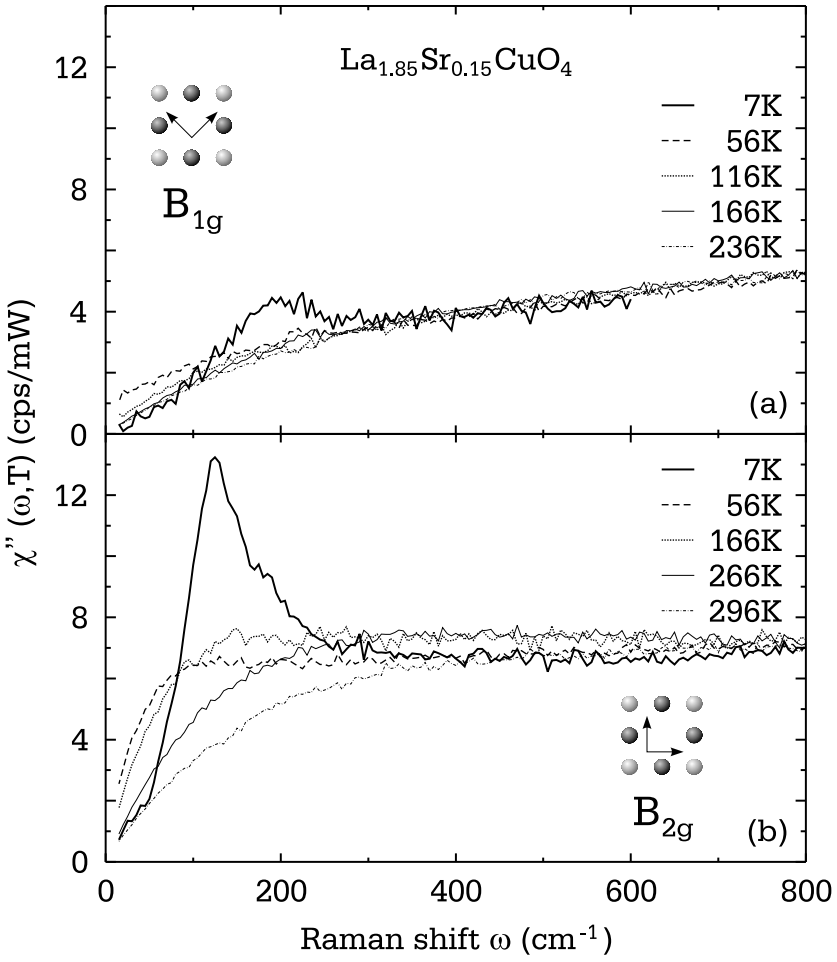

Figure 8.26: *Raman response $\chi''(\omega, T)$ of the optimally doped LSCO at different temperatures. In panels (a) and (b) are shown the B_{1g} and the B_{2g} configurations, respectively.*

the spectra obtained by the two spectroscopic methods, the measurements were performed on the very same surfaces of each sample.

In the infrared experiment the sample was mounted on the cold finger of a two stage closed-cycle cryostat, whose temperature was kept constant to within ± 2 K and could be varied from 20 to 295 K. The reflectivity $R(\omega, T)$ of the crystal was measured at quasi-normal incidence (8°) with the radiation field polarized in the CuO_2 $(a-b)$ planes. The reference was obtained by evaporating a gold layer onto the sample using a hot filament placed in front of the surface [169]. The spectra cover the range from 20 to 20,000 cm^{-1}. The real part of the optical conductivity $\sigma(\omega, T)$ was extracted from $R(\omega, T)$ by the usual Kramers-Krönig transformations. A Drude-Lorentz fit was used to extrapolate the reflectivity to $\omega = 0$. On the high-energy side, the data were extrapolated with the $R(\omega)$ reported in [170].

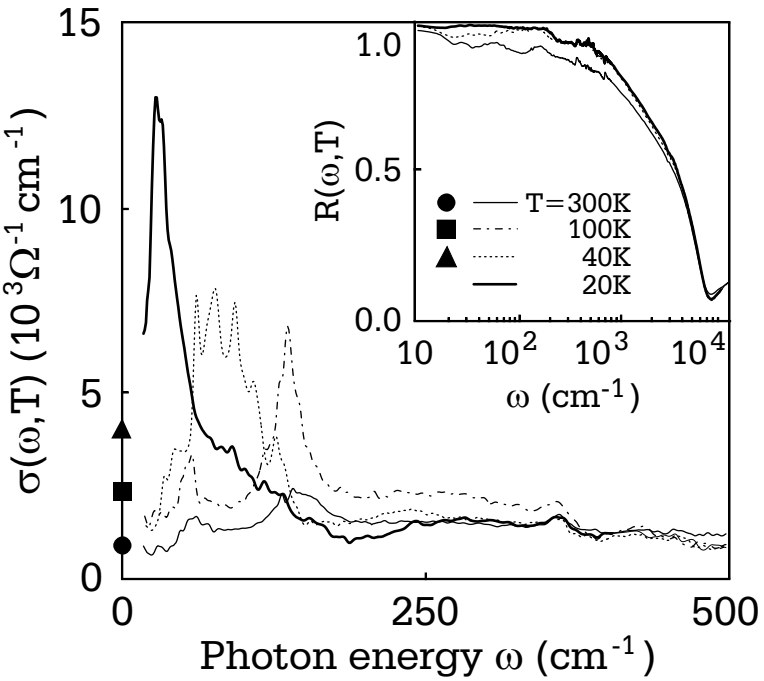

Figure 8.27: *In-plane optical conductivity $\sigma(\omega, T)$ of the underdoped LSCO sample. The corresponding reflectivity data are shown in the inset. The symbols at zero energy represent the dc conductivity values at the respective temperatures.*

The resulting real parts of the optical conductivity $\sigma(\omega, T)$ of the underdoped and of the optimally doped sample are shown in Fig. 8.27 and Fig. 8.28, respectively. The raw reflectivities $R(\omega, T)$ are shown in the inset of the figures.

In the underdoped sample strong spectral features well below 200 cm^{-1} are observed at all temperatures. These structures are not related to infrared-active lattice vibrations of LSCO in the $a-b$ plane, as a comparison with the weak phonon line at 360 cm^{-1} demonstrates immediately. They cannot be wings of a Drude contribution either because the dc conductivity at the respective temperatures (indicated by the solid symbols in Fig. 8.27) is much lower than the conductivity in the peak at finite energies. Below 100 K the spectral structures merge into a huge peak, and the conductivity reaches about 13,000 Ω^{-1} cm^{-1} at 40 cm^{-1} and 20 K. This softening goes along with a transfer of spectral weight which depletes the region between 100 and 200 cm^{-1}.

In the optimally doped sample a strong far-infrared structure is also clearly visible at $\omega \neq 0$ (Fig. 8.28). Although at this doping level the spectrum at the lowest temperature is not as sharp as in the underdoped sample, the various structures observed cannot easily be attributed to phonons alone for the high values of the conductivity and for the strong temperature dependence. In addition, a systematic

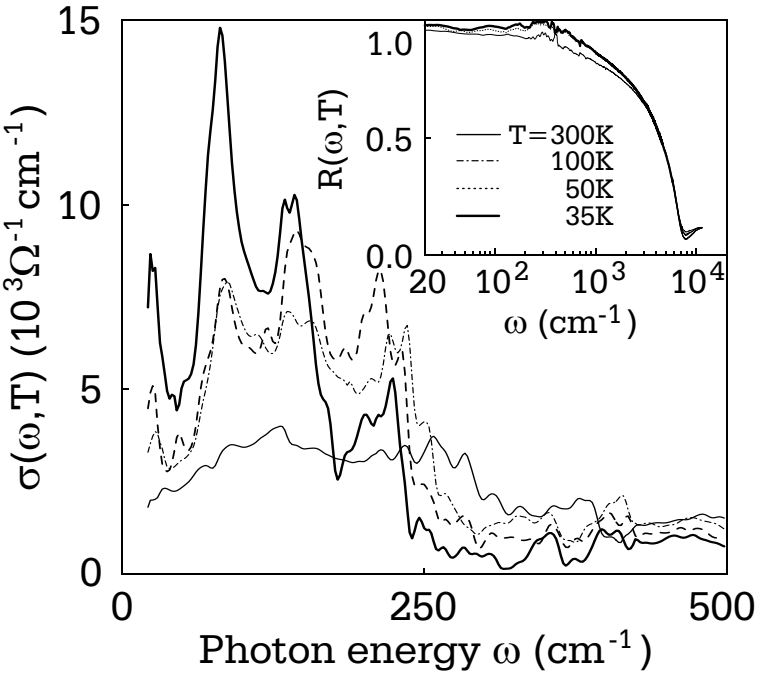

Figure 8.28: *In-plane optical conductivity $\sigma(\omega, T)$ of the optimally doped LSCO sample. The corresponding reflectivity data are shown in the inset.*

study of the infrared conductivity in differently doped LSCO samples has shown that the unconventional absorption is observed for a wide range of temperatures and doping [171].

8.4.3 Raman scattering versus infrared conductivity

To verify whether the increase in the lifetime of the quasiparticles observed by Raman is connected to the occurrence of the peak in the conductivity the temperature dependence of the spectral weight has been calculated. The first moment of the infrared spectrum between ω_1 and ω_2 is defined as

$$\langle\omega\rangle_{IR} = \frac{\int_{\omega_1}^{\omega_2} \omega\sigma(\omega)\, d\omega}{\int_{\omega_1}^{\omega_2} \sigma(\omega)\, d\omega} \,. \tag{8.17}$$

For small frequencies, if selection rules and vertex correction are neglected, the Raman response and the real part of the conductivity can be related as $\chi''(\omega, T) \sim \omega\sigma(\omega, T)$ [156]. It is therefore possible to define the first moments of the "Raman

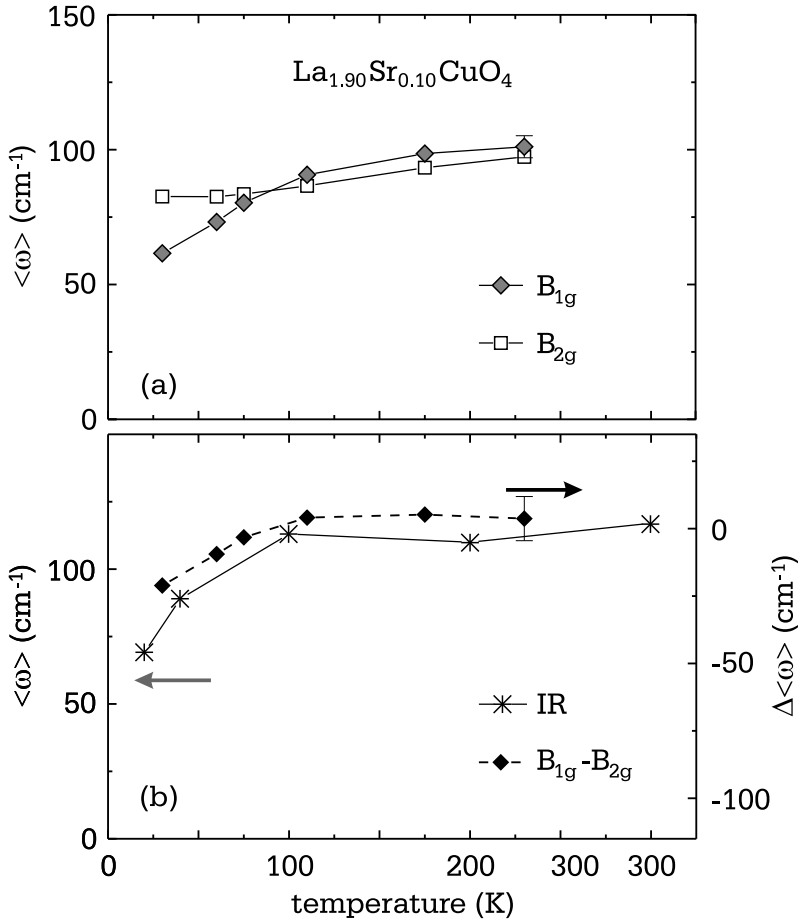

Figure 8.29: *(a) First moments of the Raman spectra in B_{1g} and B_{2g} symmetries for the underdoped sample. (b) First moments of the infrared spectra (left scale) and the difference between the B_{1g} and the B_{2g} moments $\Delta\langle\omega\rangle$ (right scale).*

conductivity" as

$$\langle\omega\rangle_\mu = \frac{\int_{\omega_1}^{\omega_2} d\omega \chi''_\mu(\omega,T)}{\int_{\omega_1}^{\omega_2} \frac{d\omega}{\omega} \chi''_\mu(\omega,T)} \tag{8.18}$$

with $\mu = B_{1g}, B_{2g}$.

The temperature dependence of the moments for the underdoped sample as calculated using Eq. (8.18) is shown in Fig. 8.29. In panel (a) the B_{1g} and B_{2g} moments calculated from the Raman spectra are plotted. In panel (b) the infrared moments and the difference between the B_{1g} and the B_{2g} moments $\Delta\langle\omega\rangle = \langle\omega\rangle_{B_{1g}} - \langle\omega\rangle_{B_{2g}}$ are shown. For the calculation the values of $\omega_1 = 20$ cm^{-1} and $\omega_2 = 200$ cm^{-1} have been used. The error on the data in indicated. The moments of the Raman response (panel (a)) are not temperature independent, since there is no sum rule.

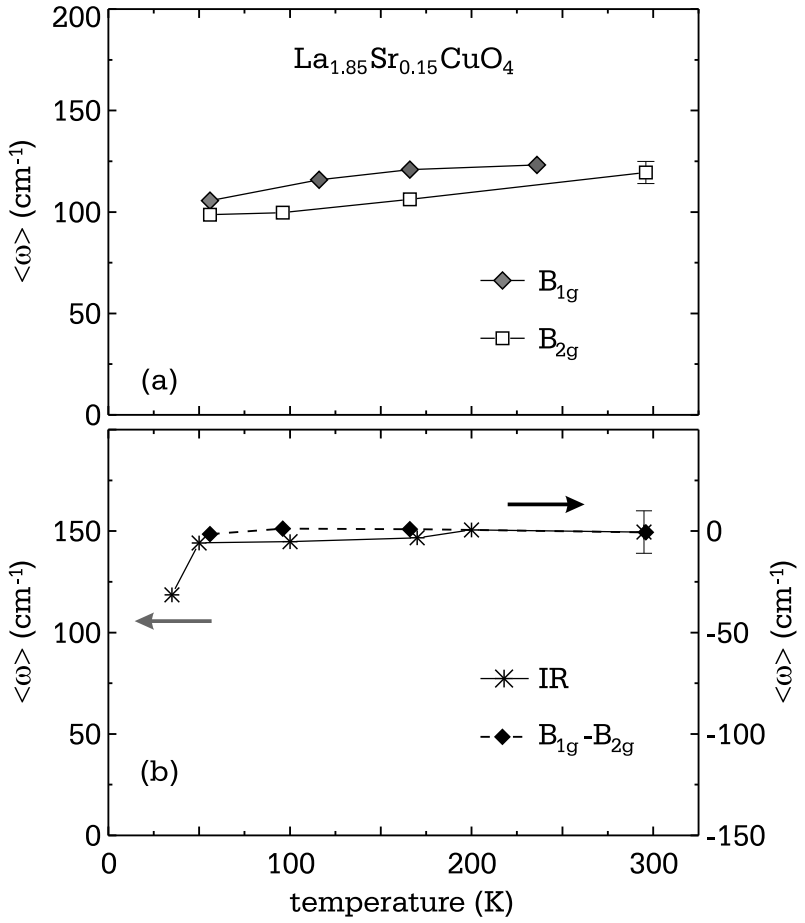

Figure 8.30: *(a) First moments of the Raman spectra in B_{1g} and B_{2g} symmetries for the optimally doped sample. (b) First moments of the infrared spectra (left scale) and the difference between the B_{1g} and the B_{2g} moments $\Delta\langle\omega\rangle$ (right scale).*

In B_{2g} symmetry an essentially linear decrease with temperature is observed, while in B_{1g} symmetry a crossover of two linear regimes with different slopes occurs. The moment derived from the conductivity (panel (b)) is temperature independent down to approximately 100 K and decreases by up to 40% for $T < 100$ K. The changes in B_{1g} symmetry are more clearly visualized by plotting the difference $\Delta\langle\omega\rangle$ in Fig. 8.29 (b). Apparently, $\Delta\langle\omega\rangle$ closely follows the behaviour of $\langle\omega\rangle_{IR}$. Both quantities are nearly constant at high T and exhibit a kink at around 100 K. Of course, the relative changes cannot be expected to be equal since different quantities are being measured. However, the comparison demonstrates that the enhanced conductivity at finite energy observed in the infrared spectra and the exceptionally long quasiparticle lifetime derived from the Raman response are apparently two aspects of a common underlying change in the electronic properties.

The same analysis has been carried out also in the optimally doped sample, and the first moments are shown in Fig. 8.30. In this sample, consistent with the lack of an anomalous Raman conductivity at low frequencies, no substantial difference between the B_{1g} and B_{2g} moments is detected (panel (a)). Therefore, the difference $\Delta\langle\omega\rangle$ (panel (b)) shows no temperature dependence in the range studied. The infrared moments reflect a similar constancy down to temperatures of approximately 50 K. Then a small but rapid decrease is observed.

8.4.4 Evidence of one-dimensional order in the underdoped region

For the similarity of the infrared response in LSCO and one-dimensional ladder compounds [172] charge ordering is a possible scenario for the explanation of the unexpected features both in the Raman and the infrared spectra. The different spectral shapes are possibly due to the selection rules and the coherence factors involved. In crystals or subunits such as the CuO_2 planes with a center of inversion the mutual exclusion principle holds, and infrared-active (odd or polar) excitations cannot be observed in the Raman spectrum (even excitations) and vice versa [173]. In addition, due to the coherence factors collective phenomena such as superconductivity or density waves, which are a possible way to look at charge ordering, lead to different spectra in the Raman response and in the conductivity.

The observation of the increased lifetime of the carriers in B_{1g} symmetry only would be consistent with the orientation of the stripes at this doping level. As schematically represented in Fig. 8.31 the stripe order changes orientation with the

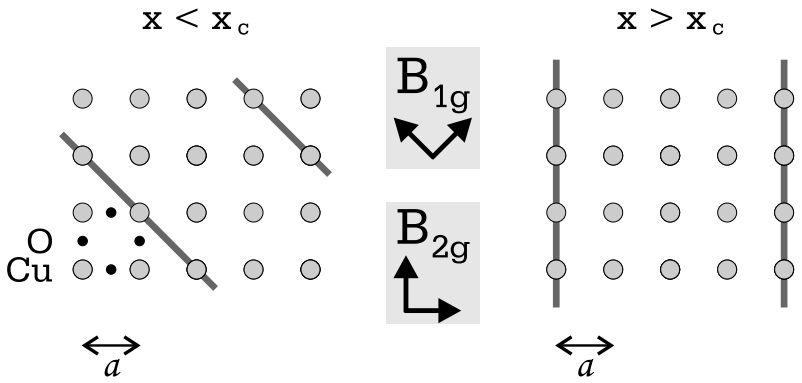

Figure 8.31: *Scheme of charged stripes orientation below and above the critical doping $x_c = 0.055$. The arrows represent the polarization vectors of the incident and scattered light used used in the Raman experiments to detect B_{1g} and B_{2g} symmetries. For clarity only four oxygen atoms are displayed.*

doping level being at 45° for $x < x_c$ and along the copper-oxygen bonds for $x > x_c$ [174]. $x_c = 0.055$ is the concentration at which the insulator to superconductor transition is observed. In Fig. 8.31 are also shown the polarization vectors of the incident and scattered light used in the Raman experiments and the corresponding symmetry components (see Sect. 3.6.2). In underdoped LSCO with $x \simeq 0.1$ the stripes are oriented parallel to the CuO bonds. In B_{1g} symmetry the polarizations of the incoming and outgoing photons are perpendicular to each other and along the diagonals of the CuO_2 unit cell having therefore a finite projection on the direction of the one-dimensional structures. This orientation of the stripes is then compatible with the observed symmetry dependence, i.e. the long lifetime seen in B_{1g} symmetry. In B_{2g} symmetry, instead, both polarization vectors are along the Cu-O bonds, and either the incoming or the outgoing light is perpendicular to the one-dimensional

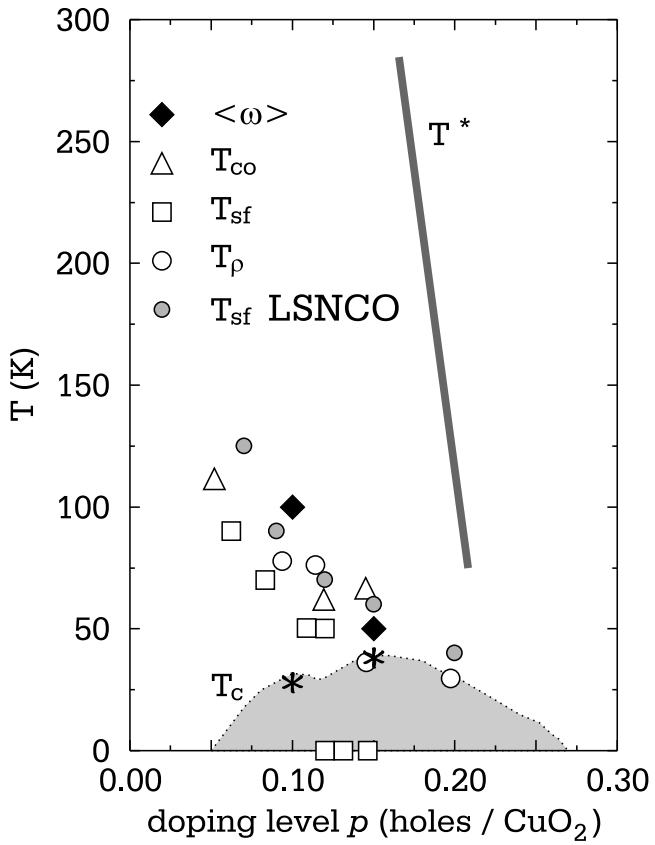

Figure 8.32: *Relevant temperature scales in the LSCO phase diagram. T_{co} is the charge-ordering temperature from x-ray absorption spectroscopy [175]; T_{sf} is spin freezing temperature determined from the wipeout effects in nuclear quadrupole resonance [176]; T_ρ is the upturn temperature in resistivity measurements [177]; T_{sf} in LNSCO is also shown [178]. The grey area is the superconducting phase. Asterisks mark the T_c of the samples studied here.*

structures, which therefore cannot be detected.

The onset temperature for one-dimensionality from the analysis of the first moments is consistent with the charge-ordering temperature observed by different experimental techniques (Fig. 8.32) [102]. Although the temperature for the first formation of charge inhomogeneities is generally identified with the temperature T^* where a pseudogap [16] opens, which is as high as 400 K in LSCO with $x \sim 0.10$, the modification of the Raman spectra, starting already at high temperatures, becomes visible only at lower temperatures. This is consistent with the present infrared observations showing a well-defined excitation peak already at room temperature.

Significant changes of the physical properties can be expected when one-dimensional structures become longer than the distance between the stripes and comparable to the electron mean free path. Indications of an enhanced dc conductivity along the stripe direction have indeed been found recently by longitudinal transport [179] close to temperatures at which the moments start to decrease (Fig. 8.29). Similarly, the transverse (Hall) conductivity decreases below approximately 80 K when the stripes are being completely pinned in Nd-doped LSCO [18]. Finally, recent results of inelastic neutron scattering on $La_{1.93}Sr_{0.07}CuO_4$ show [180] a strong increase in the stripe fluctuations below 100 K for energies between 2 and 8 meV (16 and 64 cm^{-1}, respectively).

Chapter 9

Summary

In this work the study of electronic properties of copper-oxide superconductors is described. Various compounds have been investigated by inelastic light (Raman) scattering as a function of temperature, carrier concentration, photon energy, and polarization. For the data analysis new models have been developed which allow a more general and consistent description of the results of Raman, photoemission, and infrared spectroscopies.

To access a wide range of the phase diagram a new setup was built for annealing and characterizing the samples. With a contactless inductive method the superconducting transition temperature T_c can be measured and possible inhomogeneities of the samples can be probed.

To extract all symmetry components from the measured spectra, experiments with linearly and circularly polarized light are necessary. For this purpose a new method for the precise determination and adjustment of the desired polarization state was developed.

In the normal state, the results from angle-resolved photoemission spectroscopy (ARPES) as a single-particle probe and Raman spectroscopy as a two-particle probe have been directly compared. From the analysis of the ARPES data of overdoped $Bi_2Sr_2CaCu_2O_{8+\delta}$ (BSCCO) electronic properties such as the Fermi velocity or the self energy were extracted and used to calculate the Raman response. Good agreement between the two spectroscopic techniques is obtained for both the low and the high-energy part of the spectra in B_{1g} and B_{2g} symmetries. Hence, the Raman spectra can be understood entirely in terms of single-particle properties in this region of the phase diagram.

When the carrier concentration is reduced, Raman and ARPES seem to reveal different properties of the carrier dynamics. In fact, while the single-particle self energy does not display substantial variations with doping, the Raman spec-

tra undergo dramatic modifications. An evolution of the spectra with temperature and doping indicates the presence of an unconventional metal-insulator transition at a critical doping $p_c \simeq 0.22$ where antinodal quasiparticles with momenta along the Brillouin zone axis become insulating while nodal quasiparticles with momenta along the Brillouin zone diagonals remain metallic. A phenomenological model has been developed which allows a quantitative understanding of the Raman results and provides a scenario which links single- and many-particle properties.

The transition observed in BSCCO is also found in $YBa_2Cu_3O_{6+x}$ but not in $La_{2-x}Sr_xCuO_4$ (LSCO). Instead, a new type of electronic state develops below approximately 100 K which is characterized by a very long lifetime of the electrons moving along the Cu-O bonds. By comparison with infrared spectroscopy measurements these results are interpreted as a signature of an enhanced 1D transport within a charge-density-wave (CDW) scenario where low-energy stripe fluctuations with a correlation length of several lattice constants develop at low temperatures. These effects are believed to be related to the strong coupling of spin, charge and lattice degrees of freedom in underdoped LSCO.

The observation of a metal-insulator transition at $p_c = 0.22$ in the normal state raises the question of whether there is a corresponding anomaly below T_c. A complete analysis of the response has been carried out in the superconducting state for various doping levels. The spectra in B_{2g} symmetry (nodal quasiparticles) are consistent with a $d_{x^2-y^2}$ energy gap with the maximum Δ_0 scaling with T_c. In B_{1g} symmetry (antinodal quasiparticles) the evolution of the spectral shape and the intensity is incompatible with $d_{x^2-y^2}$ pairing. At $p = p_c$ no anomaly is found. However, the new energy scale proportional to $1 - p$ may play a key role in the understanding the nature of the pairing state.

To pinpoint the origin of the metal-insulator transition the role of antiferromagnetic fluctuations has been explored both experimentally and theoretically. In the superconducting state, scattering of electrons by spin excitations is found to be particularly important. In general, magnetic correlations are found to be present for $p \leqslant p_c$ and seem to influence the normal state properties as well. The existence of an A_{2g} symmetry component, which can originate from chiral spin waves for instance, is clearly established for the first time in metallic cuprates. The intensity of this component is comparable to that of the other symmetries at high frequency and negligible below 1000 cm^{-1}. Although its spectral weight seems to scale approximately with T_c conclusions as to the origin and importance are premature.

Zusammenfassung

In der vorliegenden Arbeit wird eine Untersuchung der elektronischen Eigenschaften von Kupferoxidsupraleitern beschrieben. An verschiedenen Verbindungsklassen wurden Lichtstreuexperimente (Raman-Effekt) als Funktion der Temperatur, der Dotierung, der Photonenenergie und der Polarisation durchgeführt. Zur Beschreibung der Daten wurden zum Teil neue theoretische Modelle entwickelt, die es erlauben, einen breiteren Kontext herzustellen und die Ergebnisse von Raman-, Photoelektronen- und Infrarot-Spektroskopie konsistent zu erklären.

Um die Abdeckung eines weiten Dotierungsbereichs zu ermöglichen, wurden Apparaturen zum Tempern und zur Charakterisierung der Proben entwickelt. Über eine kontaktlos arbeitende, induktive Methode können sowohl die Sprungtemperatur bestimmt, als auch Probeninhomogenitäten erkannt werden.

Die Ableitung der reinen Symmetriekomponenten aus den gemessenen Spektren erfordert Messungen sowohl mit linear als auch mit zirkular polarisiertem Licht. Dafür wurde eine neue Methode zur präzisen Bestimmung und Einstellung der erforderlichen Polarisationszustände entwickelt.

Ein Ziel der Arbeit war die Untersuchung der Beziehung zwischen Ein- und Zweiteilchen-Response im Normalzustand. Dazu wurden die Ergebnisse von winkelaufgelöster Photoeelektronen- (ARPES) und Raman-Spektroskopie gegenüber gestellt. Aus den durch die Analyse der ARPES-Daten von überdotiertem $Bi_2Sr_2CaCu_2O_{8+\delta}$ (BSCCO) gewonnenen elektronischen Eigenschaften wie Fermi-Geschwindigkeit oder Relaxationszeit wurde der Raman-Response berechnet und mit den experimentellen Resultaten verglichen. In B_{1g} und B_{2g} Symmetrie findet man sowohl für den nieder-, als auch für hochfrequenten Spektralbereich gute Übereinstimmung. Das bedeutet, dass im überdotierten Bereich des Phasendiagramms die Raman-Spektren vollständig im Rahmen eines Einteilchen-Bildes beschrieben werden können.

Wird die Ladungsträgerkonzentration reduziert, scheinen ARPES und Raman-Spektroskopie verschiedene Eigenschaften der Ladungsträgerdynamik widerzuspiegeln. Während die Einteilcheneigenschaften nicht wesentlich von der Dotierung

abhängen, verändern sich die Raman-Spektren dramatisch. Die Entwicklung der Spektren als Funktion von Temperatur und Dotierung weist auf einen unkonventionellen Metall-Isolator-Übergang bei einer kritischen Dotierung $p_c = 0,22$ Ladungsträger/CuO_2 hin, bei dem "anti-nodale" Quasiteilchen mit Impulsen längs der Cu-O Bindungen keinen Strom mehr tragen, während "nodale" mit Impulsen längs der Flächendiagonalen metallisch bleiben. Um die Raman-Ergebnisse quantitativ zu interpretieren, wurde ein phänomenologisches Modell entwickelt, das Ein- und Mehrteilchen-Eigenschaften miteinander verknüpft.

Der in BSCCO gefundene Effekt wird auch in $YBa_2Cu_3O_{6+x}$, nicht aber in $La_{2-x}Sr_xCuO_4$ (LSCO) beobachtet. Stattdessen entwickelt sich hier unterhalb von etwa 100 K ein Zustand, der durch eine sehr lange Lebensdauer der sich längs der Cu-O Bindungen bewegenden Elektronen charakterisiert ist und den Einfluss des Metall-Isolatorübergangs überkompensiert. Raman- und parallel durchgeführte Infrarot-Messungen können im Rahmen eines Szenarios von fluktuierenden Ladungsdichtewellen mit einer Korrelationslänge von mehreren Gitterkonstanten qualitativ verstanden werden. Die Resultate legen eine starke Kopplung von Spin-, Ladungs- und Gitterfreiheitsgraden in LSCO nahe.

Der im Normalzustand bei $p_c = 0,22$ beobachtete Metall-Isolator-Übergang wirft die Frage nach einer zugeordneten Anomalie im Suprazustand auf. Daher wurde unterhalb von T_c eine ähnlich systematische Analyse wie oberhalb durchgeführt. Das B_{2g}-Spektrum ist konsistent mit einer Energielücke mit $d_{x^2-y^2}$-Symmetrie, deren Größe mit T_c skaliert. In B_{1g}-Symmetrie wird dagegen eine mit $d_{x^2-y^2}$-Paarung inkompatible Dotierungsabhängigkeit des spektralen Verlaufs und der Intensität beobachtet. Bei $p = p_c$ wird jedoch keinerlei Anomalie gefunden. Die neu entdeckte zu $1 - p$ proportionale Energieskala könnte aber eine Schlüsselrolle im Verständnis der Natur des Paarungszustandes spielen.

Um die Ursache des Übergangs einzugrenzen, wurde die Rolle antiferromagnetischer Fluktuationen experimentell und theoretisch untersucht. Im Suprazustand stellt sich die Streuung von Elektronen an Spinanregungen als besonders wichtig heraus. Experimentell können magnetische Korrelationen für $p \leq p_c$ nachgewiesen werden, was tatsächlich einen Einfluss auf die Normalzustandseigenschaften nahelegt. Die Existenz einer A_{2g}-Symmetriekomponente, die zum Beispiel von chiralen Spinwellen kommen kann, wurde zum ersten Mal in metallischen Kupraten nachgewiesen. Die Intensität dieser Komponente ist bei hohen Frequenzen vergleichbar mit der in anderen Symmetrien und vernachlässigbar unterhalb von 1000 cm^{-1}. Obwohl das spektrale Gewicht dieser Komponente etwa dem Verlauf von T_c folgt, sind Schlussfolgerungen über deren Ursprung und Bedeutung verfrüht.

Appendix A

Details of the single particle self energy

In Chapter 5 the imaginary part of the self energy determined from photoemission measurements can be represented, with $\hbar = 1$ and $k_B = 1$,

$$\Sigma''(\phi, \omega, T) = -\left[C(\phi) + \sqrt{(\alpha\omega)^2 + (\beta T)^2}\right] \ . \tag{A.1}$$

The term $C(\phi) = C_0 + C_1(\phi)$ (Eq. (5.12)) includes the zero-temperature contribution (C_0) and the angular modulation ($C_1(\phi)$) given by Eq. (5.10). To prevent the imaginary part of the self energy from diverging at high frequencies, Σ'' is multiplied by a Lorentzian $\omega_0^2/(\omega_0^2 + \omega^2)$ and is set constant at high frequencies by defining it as

$$\Sigma''(\phi, \omega, T) = \begin{cases} -\left[C(\phi) + \sqrt{(\alpha\omega)^2 + (\beta T)^2}\right] \dfrac{\omega_0^2}{\omega_0^2 + \omega^2} & \omega \leqslant \omega_M \\ -C(\phi)\dfrac{\omega_0^2}{\omega_0^2 + \omega^2} - \dfrac{\alpha^2\omega_0^2}{2} \dfrac{1}{\sqrt{(\alpha\omega_0)^2 + (\beta T)^2}} & \omega > \omega_M \end{cases} \tag{A.2}$$

with $\omega_M = \sqrt{\omega_0^2 - 2\left(\dfrac{\beta T}{\alpha}\right)^2} \simeq \omega_0$ for $\alpha = 1.1$, $\beta = 2$ and $T \leqslant 300$ K.

The resulting $\Sigma''(\phi, \omega, T)$ is plotted in Fig. A.1 for $\phi = 0°$, $\alpha = 1.1$, $\beta = 2$, $C_0 = 9$ meV and $\omega_0 = 1000$ meV.

Note that the temperature dependence is relevant only for frequencies below $\simeq 2k_BT$.

The real part of the self energy is calculated by Kramers-Krönig transformation of the imaginary part (Eq. (A.2)) to satisfy causality. The resulting expression is given in Eq. (A.3), where for simplicity the quantity $A = \beta T/\alpha$ has been introduced. The real part of the self energy $\Sigma'(\phi, \omega, T)$ is plotted in Fig. A.2 for $\phi = 0°$, $\alpha = 1.1$, $\beta = 2$, $C_0 = 9$ meV and $\omega_0 = 1000$ meV.

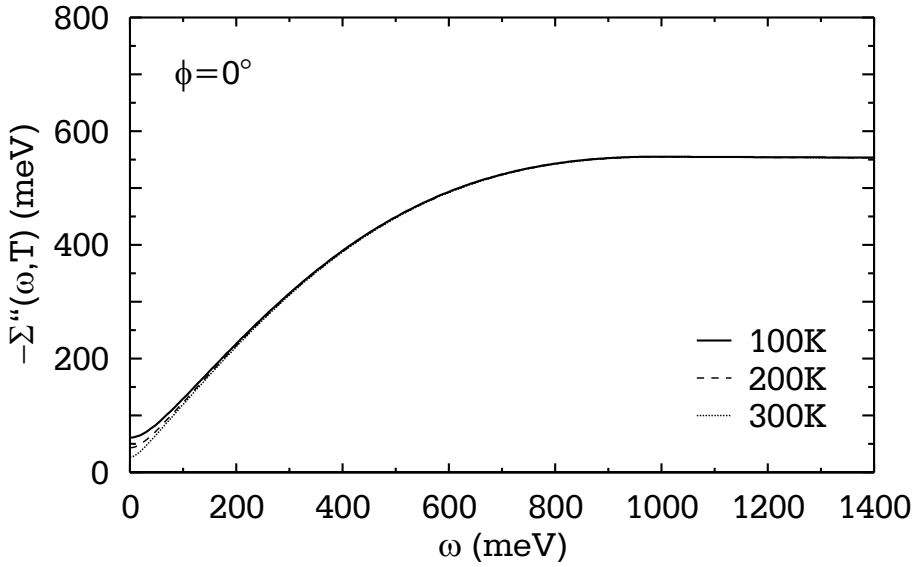

Figure A.1: *Frequency dependence of the imaginary part of the self energy at three temperatures at the antinodal ($\phi = 0°$) direction. The parameters used for the plot are $\phi = 0°$, $\alpha = 1.1$, $\beta = 2$, $C_0 = 9$ meV and $\omega_0 = 1000$ meV.*

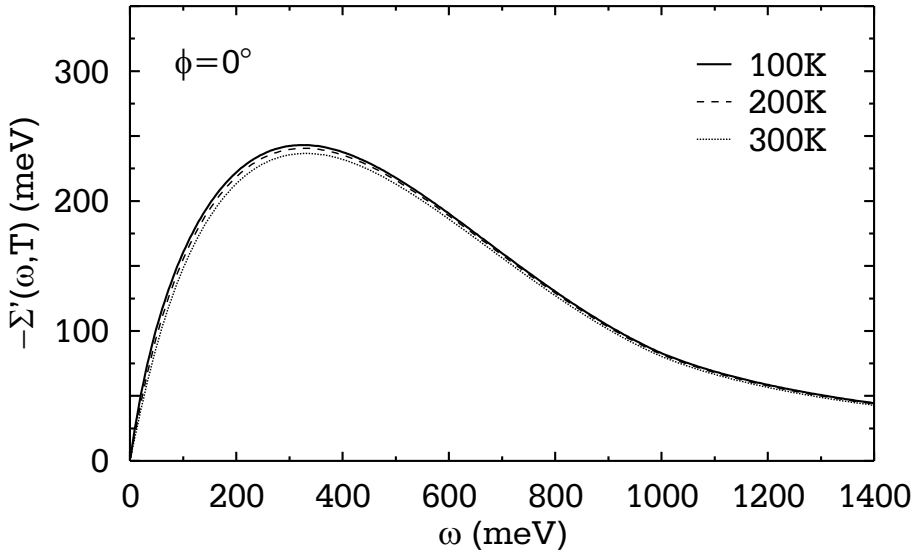

Figure A.2: *Frequency dependence of the real part of the self energy at three temperatures at the antinodal ($\phi = 0°$) direction. The parameters used for the plot are $\phi = 0°$, $\alpha = 1.1$, $\beta = 2$, $C_0 = 9$ meV and $\omega_0 = 1000$ meV.*

$$
\begin{aligned}
\Sigma'(\phi,\omega,T) \;=\; & -\frac{\omega_0\;\omega}{\omega_0^2+\omega^2}\;C(\phi)\;- \\
& \frac{\alpha\omega_0^2}{\pi}\left\{\frac{1}{2\sqrt{\omega_0^2-A^2}}\ln\left|\frac{\sqrt{\omega_0^2-2A^2}+\omega}{\sqrt{\omega_0^2-2A^2}-\omega}\right|+\right. \\
& -\frac{\omega^2+A^2}{\omega_0^2+\omega^2}\ln\left|\frac{\sqrt{\omega_0^2-2A^2}+\omega}{\sqrt{\omega_0^2-2A^2}-\omega}\right|+ \\
& -\frac{\omega^2+A^2}{\omega_0^2+\omega^2}\ln\left|\frac{\sqrt{\omega^2+A^2}\sqrt{\omega_0^2-A^2}+A^2+\omega\sqrt{\omega_0^2-2A^2}}{\sqrt{\omega^2+A^2}\sqrt{\omega_0^{2-2}}+A^2-\omega\sqrt{\omega_0^2-2A^2}}\right|+ \\
& \left.\frac{\omega}{\omega_0}\frac{\sqrt{\omega_0^2-A^2}}{\omega_0^2+\omega^2}\ln\left|\frac{\omega_0+\sqrt{\omega_0^2-2A^2}}{\omega_0-\sqrt{\omega_0^2-2A^2}}\right|\right\}\;.
\end{aligned}
\tag{A.3}
$$

Appendix B

Spin fluctuation vertex function

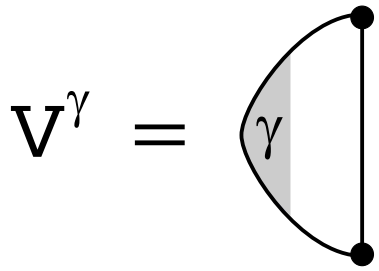

Figure B.1: *Vertex function used in the calculation of the spin fluctuation contribution.*

The vertex function $V^{\gamma}(\mathbf{q}', i\omega, i\omega')$ involved in the calculation of the spin fluctuation contribution (Sect. 8.2.1) to the Raman scattering (see Fig. B.1) is given by

$$V^{\gamma}(\mathbf{q}', i\omega, i\omega') = \frac{1}{\beta}\,\mathrm{Tr}\sum_{\mathbf{k},i\omega''}\hat{\gamma}\mathbf{k}\hat{G}(\mathbf{k}, i\omega + i\omega'')\hat{\tau}_0\bar{U}$$
$$\hat{G}(\mathbf{k}+\mathbf{q}', i\omega' + i\omega + i\omega'')\hat{\tau}_0\bar{U}\hat{G}(\mathbf{k}, i\omega'')\ . \tag{B.1}$$

where $i\omega$, $i\omega'$ denote bosonic and $i\omega''$ fermionic Matsubara frequencies [40]; $\hat{\tau}_i$ with $i = 1, 2, 3$ are the 2×2 Pauli matrices and $\hat{\tau}_0 = \hat{1}$.

After summing over the Matsubara frequencies $i\omega''$, V^{γ} reads

$$V^{\gamma}(\mathbf{q}', i\omega, i\omega') = \sum_{\mathbf{k}}\gamma_{\mathbf{k}}\iiint dy_1 dy_2 dy_3 \mathcal{A}(y_1, y_2, y_3)$$
$$\mathrm{Tr}\left\{\hat{\tau}_3\hat{G}_0''(\mathbf{k}, y_1)\hat{\tau}_0\hat{G}_0''(\mathbf{k}+\mathbf{q}', y_2)\hat{\tau}_0\hat{G}_0''(\mathbf{k}, y_3)\right\} \tag{B.2}$$

where the imaginary part of the bare matrix Green function $\hat{G}_0(\mathbf{k}, y)$ (Eq. (3.17))

is given by

$$\hat{G}_0''(\mathbf{k}, y) = \frac{1}{2E_{\mathbf{k}}}(y\hat{\tau}_0 + \xi_{\mathbf{k}}\hat{\tau}_3 + \Delta_{\mathbf{k}}\hat{\tau}_1)\left[\delta(y - E_{\mathbf{k}}) - \delta(y + E_{\mathbf{k}})\right] \tag{B.3}$$

and the scalar function $\mathcal{A}(y_1, y_2, y_3)$ is

$$\begin{aligned}\mathcal{A}(y_1, y_2, y_3) \;=\; & \left\{ \frac{n_F(y_3)}{(y_3 - y_1 + i\omega)(y_2 - y_3 + i\omega')} + \frac{n_F(y_1)}{(y_1 - y_3 - i\omega)(y_2 - y_1 + i\omega + i\omega')} \right. \\ & \left. \frac{n_F(y_2)}{(y_3 - y_2 - i\omega)(y_2 - y_1 + i\omega' + i\omega)} \right\} .\end{aligned} \tag{B.4}$$

Substituting Eq. (B.3) in Eq. (B.2), the vertex function is

$$\begin{aligned} & V(\mathbf{q}', i\omega, i\omega') = \sum_{\mathbf{k}} \gamma_{\mathbf{k}} \iiint dy_1 dy_2 dy_3 \mathcal{A}(y_1, y_2, y_3) \\ & \frac{1}{8E_{\mathbf{k}}^2 E_{\mathbf{k}+\mathbf{q}'}} \left[\delta(y_1 - E_{\mathbf{k}}) - \delta(y_1 + E_{\mathbf{k}})\right] \\ & \left[\delta(y_2 - E_{\mathbf{k}+\mathbf{q}'}) - \delta(y_2 + E_{\mathbf{k}+\mathbf{q}'})\right] \\ & \left[\delta(y_3 - E_{\mathbf{k}}) - \delta(y_3 + E_{\mathbf{k}})\right] \mathrm{Tr}\left\{\hat{\tau}_3(y_1\hat{\tau}_0 + \xi_{\mathbf{k}}\hat{\tau}_3 + \Delta_{\mathbf{k}}\hat{\tau}_1)\right. \\ & \left.(y_2\hat{\tau}_0 + \xi_{\mathbf{k}+\mathbf{q}'}\hat{\tau}_3 + \Delta_{\mathbf{k}}\hat{\tau}_1)(y_3\hat{\tau}_0 + \xi_{\mathbf{k}}\hat{\tau}_3 + \Delta_{\mathbf{k}}\hat{\tau}_1)\right\} . \end{aligned} \tag{B.5}$$

It is convenient to decompose the matrix term in Eq. (B.5), which will be labeled as $\hat{T}$, into the Pauli matrices $\hat{\tau}_i$ with $i = 1, 2, 3$ and the unity matrix $\hat{\tau}_0$. Using the properties of the Pauli matrices the result is

$$\begin{aligned} \hat{T}(y_1, y_2, y_3) \;\equiv\; & \{\hat{\tau}_3(y_1\hat{\tau}_0 + \xi_{\mathbf{k}}\hat{\tau}_3 + \Delta_{\mathbf{k}}\hat{\tau}_1) \\ & (y_2\hat{\tau}_0 + \xi_{\mathbf{k}+\mathbf{q}'}\hat{\tau}_3 + \Delta_{\mathbf{k}}\hat{\tau}_1) \\ & (y_3\hat{\tau}_0 + \xi_{\mathbf{k}}\hat{\tau}_3 + \Delta_{\mathbf{k}}\hat{\tau}_1)\} = \\ =\; & \hat{\tau}_3(T_0\hat{\tau}_0 + T_1\hat{\tau}_1 + T_2\hat{\tau}_2 + T_3\hat{\tau}_3) = \\ =\; & T_0\hat{\tau}_3 - iT_1\hat{\tau}_2 - iT_2\hat{\tau}_1 + T_3\hat{\tau}_0) \end{aligned} \tag{B.6}$$

where

$$\begin{aligned} T_0 &= \Delta_{\mathbf{k}}^2 y_2 + \xi_{\mathbf{k}}^2 y_2 + y_1 y_2 y_3 + \Delta_{\mathbf{k}}\Delta_{\mathbf{k}+\mathbf{q}'}(y_1+y_3) \\ &\quad +\xi_{\mathbf{k}}\xi_{\mathbf{k}+\mathbf{q}'}(y_1+y_3) \\ T_1 &= \Delta_{\mathbf{k}}^2\Delta_{\mathbf{k}+\mathbf{q}'} + \Delta_{\mathbf{k}+\mathbf{q}'}(-\xi_{\mathbf{k}}^2 + y_1 y_3) + \Delta_{\mathbf{k}}(2\xi_{\mathbf{k}}\xi_{\mathbf{k}+\mathbf{q}'}+ \\ &\quad y_2(y_1+y_3)) \\ T_2 &= -i(\Delta_{\mathbf{k}+\mathbf{q}'}\xi_{\mathbf{k}} - \Delta_{\mathbf{k}}\xi_{\mathbf{k}+\mathbf{q}'})(y_1-y_3) \\ T_3 &= 2\Delta_{\mathbf{k}}\Delta_{\mathbf{k}+\mathbf{q}'}\xi_{\mathbf{k}} - \Delta_{\mathbf{k}}^2\xi_{\mathbf{k}+\mathbf{q}'} + \xi_{\mathbf{k}}^2\xi_{\mathbf{k}+\mathbf{q}'} + \xi_{\mathbf{k}+\mathbf{q}'}y_1 y_3 + \\ &\quad \xi_{\mathbf{k}} y_2(y_1+y_3)\ . \end{aligned} \tag{B.7}$$

Finally the trace of the matrix $\hat{T}(y_1, y_2, y_3)$ is required to evaluate V^γ. Since Tr $\hat{\tau}_2$ = Tr $\hat{\tau}_1$ = Tr $\hat{\tau}_3 = 0$, only the 0th component of $\hat{T}$ contributes to the trace. Therefore,

$$\mathrm{Tr}\hat{T}(y_1, y_2, y_3) = 2T_3 \tag{B.8}$$

or explicitly

$$\begin{aligned} \mathrm{Tr}\hat{T}(y_1, y_2, y_3) &= 4\Delta_{\mathbf{k}}\Delta_{\mathbf{k}+\mathbf{q}'}\xi_{\mathbf{k}} - 2\Delta_{\mathbf{k}}^2\xi_{\mathbf{k}+\mathbf{q}'} + 2\xi_{\mathbf{k}}^2\xi_{\mathbf{k}+\mathbf{q}'} \\ &\quad +2\xi_{\mathbf{k}+\mathbf{q}'}y_1 y_3 + 2\xi_{\mathbf{k}} y_1 y_2 + 2\xi_{\mathbf{k}} y_2 y_3\ . \end{aligned} \tag{B.9}$$

The selection of the energies determined by the δ-functions can be more compactly written as

$$\begin{aligned} &[\delta(y_1 - E_{\mathbf{k}}) - \delta(y_1 + E_{\mathbf{k}})] \\ &\left[\delta(y_2 - E_{\mathbf{k}+\mathbf{q}'}) - \delta(y_2 + E_{\mathbf{k}+\mathbf{q}'})\right] \\ &[\delta(y_3 - E_{\mathbf{k}}) - \delta(y_3 + E_{\mathbf{k}})] = \\ &\sum_{s_1,s_2,s_3=\pm 1} s_1 s_2 s_3 \delta(y_1 - s_1 E_{\mathbf{k}})\delta(y_2 - s_2 E_{\mathbf{k}+\mathbf{q}'})\delta(y_3 - s_3 E_{\mathbf{k}}) \end{aligned} \tag{B.10}$$

where $s_1, s_2, s_3 = \pm 1$. In conclusion, applying the δ-functions the vertex function V^γ results as

$$\begin{aligned} V(\mathbf{q}', i\omega, i\omega') &= \sum_{\mathbf{k},s_1,s_2,s_3=\pm 1} \gamma_{\mathbf{k}}\mathcal{A}(s_1 E_{\mathbf{k}}, s_2 E_{\mathbf{k}+\mathbf{q}'}, s_3 E_{\mathbf{k}}) \\ &\quad s_1 s_2 s_3 \frac{1}{8E_{\mathbf{k}}^2 E_{\mathbf{k}+\mathbf{q}'}} \mathrm{Tr}\hat{T}(s_1 E_{\mathbf{k}}, s_2 E_{\mathbf{k}+\mathbf{q}'}, s_3 E_{\mathbf{k}})\ . \end{aligned} \tag{B.11}$$

Bibliography

[1] G. Bednorz and A. Müller, *Z. Phys. B* **64**, 189 (1986).

[2] E. Dagotto, *Rev. Mod. Phys.* **66**, 763 (1994).

[3] R.W. Hill, C. Proust, L. Taillefer, P. Fournier, and R.L. Greene, *Nature* **417**, 711 (2001).

[4] C. Castellani, C. Di Castro, and M. Grilli, *Z. Phys. B* **103**, 137 (1997).

[5] S. Sachdev, *Science* **288**, 475 (2000).

[6] P.W. Anderson, *cond-mat/0201431* (2002).

[7] H. Alloul, T. Ohno, and P. Mendels, *Phys. Rev. Lett.* **63**, 1700 (1989).

[8] G.S. Boebinger, Y. Ando, A. Passaner, T. Kimura, M. Okura, J. Shimoyama, K. Kishio, K. Tamasaku, N. Ichikawa, and S. Uchida, *Phys. Rev. Lett.* **77**, 5417 (1996).

[9] S. Andergassen, S. Caprara, C. Di Castro, and M. Grilli, *Phys. Rev. Lett.* **87**, 56401 (2001).

[10] M.K. Wu, J.R. Ashburn, C.J. Torng, P.H. Hor, R.L. Meng, L. Gao, Z.J. Huang, Y.Q. Wang, and C.W. Chu, *Phys. Rev. Lett.* **58**, 908 (1987).

[11] Z.Z. Sheng and A.M. Hermann, *Nature* **332**, 55 (1988).

[12] J. Bardeen, L.N Cooper, and J.R. Schrieffer, *Phys. Rev.* **108**, 1175 (1957).

[13] M. Cryot and D. Pavuna, *Introduction to Superconductivity and High-T_c Materials*, World Scientific, London, Singapore, New Jersey (1992).

[14] H. Ding, M.R. Norman, T. Yokoya, T. Takeuchi, M. Randeria, J.C. Campuzano, T. Takahashi, T. Mochiku, and K. Kadowaki, *Phys. Rev. B* **78**, 2628 (1997).

[15] A.A. Kordyuk, S.V. Borisenko, M.S. Golden, S. Legner, K.A. Nenkov, M. Knupfer, J. Fink, H. Berger, L. Forró, and R. Follath, *Phys. Rev. B* **66**, 014502 (2002).

[16] T. Timusk and B. Statt, *Rep. Prog. Phys.* **62**, 61 (1999).

[17] J.M. Tranquada, B.J. Sternlieb, J.D. Axe, Y. Nakamura, and S. Uchida, *Nature* **375**, 561 (1995).

[18] T. Noda, H. Eisaki, S. Uchida, *Science* **286**, 265 (1999).

[19] H. Takagi, B. Batlogg, H.L. Kao, J. Kwo, R.J. Cava, J.J. Krajewski, and W.F. Peck Jr., *Phys. Rev. Lett.* **69**, 2975 (1992).

[20] Z.-X. Shen and J.R. Schrieffer, *Phys. Rev. Lett.* **78**, 1771 (1997).

[21] J.C. Davis, *Cover of Physics Today, March* (2000).

[22] C.E. Gough, M.S. Colclough, E.M. Forgan, R.G. Jordan, M. Keene, C.M. Muirhead, A.I.M. Rae, N. Thomas, J. Abell, and S. Sutton, *Nature* **326**, 855 (1987).

[23] J.F. Annett, N. Goldenfeld and A.J. Leggett, edited by D.M. Ginzberg, *in Physical Properties of High-Temperature Superconductors V*, World Scientific, Singapore (1996).

[24] S.H. Pan, E.W. Hudson, K.M. Lang, H. Eisaki, S. Uchida, and J.C. Davis, *Nature* **403**, 746 (2000).

[25] G. Deutscher, *Nature* **397**, 410 (1999).

[26] C.P. Slichter edited by K.S. Bedell *et al.*, *in Strongly Correlated Electron Systems*, Addison-Weasley, Reding, MA (1994).

[27] A.J. Millis, H. Monien and D. Pines, *Phys. Rev. B* **42**, 167 (1990).

[28] J. Schmalian, D. Pines and B.P. Stojković, *Phys. Rev. B* **60**, 667 (1999).

[29] R. Hubina and T.M. Rice, *Phys. Rev. B* **51**, 9253 (1995).

[30] M. Opel, R. Nemetschek, C. Hoffmann, R. Philipp, P.F. Müller, R. Hackl, I. Tüttő, A. Erb, B. Revaz, E. Walker, H. Berger, and L. Forró, *Phys. Rev. B* **61**, 9752 (2000).

[31] T.P. Devereaux, *Phys. Rev. B* **45**, 12965 (1992).

[32] T.P. Devereaux and D Einzel, *Phys. Rev. B* **51**, 16336 (1995).

[33] F.A. Blum, *Phys. Rev. B* **1**, 1125 (1970).

[34] W. Hayes R. Loudon, *Scattering of Light by Crystals*, John Wiley ans Sons, New York (1978).

[35] A.A. Abrikosov and V.M. Genkin, *Zh. Eksp. Teor. Fiz.* **65**, 842 (1973).

[36] O.K. Andersen, O. Jepsen, A.I. Liechtenstein, and I.I. Mazin, *Phys. Rev. B* **49**, 4145 (1994).

[37] P. Allen, *Phys. Rev. B* **13**, 1416 (1976).

[38] A.C. Durst and P.A. Lee, *Phys. Rev. B* **62**, 1270 (2000).

[39] A.C. Durst and P.A. Lee, *Phys. Rev. B* **65**, 094501 (2002).

[40] G.D. Mahan, *Many-Particle Physics*, Plenum Press, New York (1993).

[41] M. Gurvitch and A.T. Fiory, *Phys. Rev. Lett.* **59**, 1337 (1987).

[42] B. Puchkov, D.N. Basov, and T. Timusk, *J. Phys.Condens. Mater.* **8**, 10049 (1996).

[43] J.R. Schrieffer, *Theory of Superconductivity*, W.A. Benjamin, Inc. Publishers, New York (1964).

[44] H.A. Mook, M. Yethiraj, G. Aeppli, T.E. Mason, and T. Armstrong, *Phys. Rev. Lett.* **70**, 3490 (1993).

[45] H.F. Fong, P. Bourges, Y. Sidis, L.P. Regnault, A. Ivanov, G.D. Gu, N. Koshizuka, and B. Keimer, *Nature* **398**, 588 (1999).

[46] H. He, P. Bourges, Y. Sidis, C. Ulrich, L.P. Regnault, S. Pailhès, N.S. Berzigiarova, N.N. Kolesnikov and B. Keimer, *Science* **295**, 1045 (2002).

[47] W. Götze and P. Wölfle, *Phys. Rev. B* **6**, 1226 (1972).

[48] A. Kaminski, J. Mesot, H.M. Fretwell, J.C. Campuzano, M.R. Norman, M. Randeria, H. Ding, T. Sato, T. Takahashi, T. Mochiku, K. Kadowaki, and H. Hoechst, *Phys. Rev. Lett.* **84**, 1788 (2000).

[49] J. Yu and A.J. Freeman, *J. Phys. Chem. Solids* **52**, 1351 (1991).

[50] H. Takagi, T. Ido, S. Ishibashi, M. Uota, S. Uchida, and Y. Tokura , *Phys. Rev. B* **40**, 2254 (1989).

[51] B. Keimer, N. Belk, R.J. Birgeneau, A. Cassanho, C.Y. Chen, M. Greven, M.A. Kastner, A. Aharony, Y. Endoh, R.W. Erwin, and G. Shirane, *Phys. Rev. B* **46**, 14034 (1992).

[52] W.E. Pickett, *Rev. Mod. Phys.* **61**, 433 (1989).

[53] A. Santoro, *in High Temperature Superconductivity, ed. J.W. Lynn*, Springer-Verlag, New York, NY (1990).

[54] C. Niedermayer, C. Bernhard, T. Blasius, A. Golnik, A. Moodenbaugh, and J.I. Budnick, *Phys. Rev. Lett.* **80**, 3843 (1998).

[55] A. Erb, *The impact of crystal growth, oxygenation and microstructure on the physics of the rare earth (123) superconductors*, Thèse d'habilitation, University of Geneva (1999).

[56] J.M. Tranquada, A.H. Moudden, A.I. Goldman, P.Zolliker, D.E. Cox, G. Shirane, S.K. Sinha, D. Vaknin, D.C. Johnston, M.S. Alvarez, A.J. Jacobson, J.T. Lewandowski, and J.M. Newsam, *Phys. Rev. B* **38**, 2477 (1988).

[57] A. Erb, E. Walker, and R. Flükiger, *Physica C* **258**, 9 (1996).

[58] J.L. Tallon, C. Bernhard, H. Shaked, R.L. Hitterman and J.D. Jorgensen, *Phys. Rev. B* **51**, 12911 (1995).

[59] J.W. Chen and F.-A. Yang, *Physica C* **176**, 257 (1991).

[60] G. Triscone, J.Y. Genoud, T. Graf, A. Junod, and J. Muller, *Physica C* **176**, 247 (1991).

[61] J.H. Claassen, M.E. Reeves, and R.J. Soulen Jr., *Rev. Sci. Instrum.* **62**, 996 (1991).

[62] C.P. Bean, *Phys. Rev. Lett.* **8**, 250 (1962).

[63] S. Shatz, A. Shaulov, and Y. Yeshurun, *Phys. Rev. B* **48**, 13871 (1993).

[64] L. Ji, R.H. Sohn, G.C. Spalding, C.J. Lobb, and M. Tinkham, *Phys. Rev. B* **40**, 10936 (1989).

[65] R. Hackl, *Inelastische Lichtstreuung an A15-Verbindungen*, Dissertation TU Muenchen, Hieronymus München (1987).

[66] R. Hackl, *in The Gap Symmetry and Fluctuations in High-T_c Superconductors*, Plenum Press, New York, NY (1998).

[67] S. Chakravarty, R.B. Laughlin, D.K. Morr and C. Nayak, *Phys. Rev. B* **63**, 094503 (2001).

[68] M.E. Simon and C.M. Varma, *Phys. Rev. Lett.* **89**, 247003 (2002).

[69] M. Born and E. Wolf, *Principles of Optics*, Pergamon Press, Oxford, UK (1980).

[70] A. Zawadowski and M. Cardona, *Phys. Rev. B* **42**, 10732 (1990).

[71] A. Virosztek and J. Ruvalds, *Phys. Rev. B* **45**, 347 (1992).

[72] T.P. Devereaux and A.P. Kampf, *Phys. Rev. B* **59**, 6411 (1996).

[73] J.C. Campuzano, M. Randeria, M.N. Norman, and H. Ding, *in The Gap Symmetry and Fluctuations in High-T_c Superconductors*, Plenum Press, New York, NY (1998).

[74] S.V. Borisenko, A.A. Kordyuk, S. Legner, C. Dürr, M. Knupfer, M.S. Golden, J. Fink, K.A. Nenkov, D. Eckert, G. Yang, S. Abell, H. Berger, and L. Forró, *Phys. Rev. B* **64**, 094513 (2001).

[75] A. Bansil and M. Lindroos, *Phys. Rev. Lett.* **83**, 5154 (1999).

[76] M. Lindroos, S. Sahrakorpi, and A. Bansil, *Phys. Rev. B* **65**, 054514 (2002).

[77] M.R. Norman, H. Ding, H.M. Fretwell, M. Randeria, and J.C. Campuzano, *Phys. Rev. B* **60**, 7585 (1999).

[78] T. Valla, A.V. Fedorov, P.D. Johnson, Q. Li, G.D. Gu, and N. Koshizuka, *Phys. Rev. Lett.* **85**, 828 (2000).

[79] H. Shaked, P.M. Keane, J.C. Rodriguez, F.F. Owen, R.L. Hitterman, and J.D. Jorgensen, *Crystal Structures of the High-T_c Superconducting Copper-Oxides*, Elsevier Science B.V., Amsterdam (1994).

[80] J.C. Campuzano, G. Jennings, M. Faiz, L. Beaulaigue, B.W. Veal, J.Z. Liu, A.P. Paulikas, H. Claus, R.S. List, A.J. Arko, and R.J. Bartlett, *Phys. Rev. Lett.* **64**, 2308 (1990).

[81] J. Mesot, M. Randeria, M.R. Norman, A. Kaminsky, H.M. Fretwell, J.C. Campuzano, H. Ding, T. Takeuchi, T. Sato, T. Yokoya, T. Takahashi, I. Chong, T. Terashima, M. Takano, T. Mochiku, and K. Kadowaki, *Phys. Rev. B* **63**, 224516 (2001).

[82] S.V. Borisenko, M.S. Golden, S. Legner, T. Pichler, C. Dürr, M. Knupfer, J. Fink, G. Yang, S. Abell, and H. Berger, *Phys. Rev. Lett.* **84**, 4453 (2000).

[83] P.V. Bogdanov, A. Lanzara, X.J. Zhou, S.A. Kellar, D.L. Feng, E.D. Liu, H. Eisaki, J.-I. Shimoyama, K. Kishio, Z. Hussain, and Z.X. Shen, *Phys. Rev. B* **64**, 180505 (2001).

[84] D.L. Feng, N.P. Armitage, D.H. Lu, A. Damascelli, J.P. Hu, P.V. Bogdanov, A. Lanzara, F. Ronning, K.M. Shen, H. Eisaki, C. Kim, Z.X. Shen, J.-I. Shimoyama, and K. Kishio, *Phys. Rev. Lett.* **86**, 5550 (2001).

[85] Y.-D. Chuang, A.D. Gromko, A.V. Fedorov, Y. Aiura, K. Oka, Y. Ando, D.S. Dessau, *cond-mat/0107002* (2001).

[86] A. Kaminski, M. Randeria, J.C. Campuzano, M.N. Norman, H.M. Fretwell, J. Mesot, T. Sato, T. Takahashi, and T. Kadowaki, *Phys. Rev. Lett.* **86**, 1070 (2001).

[87] T. Valla, A.V. Fedorov, P.D. Johnson, B.O. Wells, S.L. Hulbert, Q. Li, G.D. Gu, and N. Koshizuka, *Science* **285**, 2110 (1999).

[88] C.M. Varma, P.B. Littlewood, and S. Schmitt-Rink, *Phys. Rev. Lett.* **63**, 1996 (1989).

[89] C.M. Varma, P.B. Littlewood, and S. Schmitt-Rink, *Phys. Rev. Lett.* **64**, 497 (1990).

[90] M. Opel, *Eigenschaften des Elektronensystems und seiner Wechselwirkungen in antiferromagnetischen und supraleitenden Kupraten: Eine Raman-Studie*, Dissertation TU München, Shaker Verlag, Aachen (2000).

[91] D.B. Tanner and T. Timusk, edited by D.M. Ginzberg, *in Properties of High-Temperature Superconductors III*, World Scientific, Singapore (1992).

[92] F. Venturini, M. Opel, R. Hackl, H. Berger, L. Forró, and B. Revaz, *J. Phys. Chem. Solids* **63**, 2345 (2002).

[93] N. Mott, *in Conduction in Non-Crystalline Materials*, Clarendon Press, Oxford (1987).

[94] N. Furukawa, T.M. Rice, and M. Salmhofer, *Phys. Rev. Lett.* **81**, 3195 (1998).

[95] J.K. Freericks and T.P. Devereaux, *Phys. Rev. B* **64**, 125110 (2001).

[96] J.K. Freericks, T.P. Devereaux, and R. Bulla, *Phys. Rev. B* **64**, 233114 (2001).

[97] M.R. Norman, M. Randeria, H. Ding, and J.C. Campuzano, *Phys. Rev. B* **57** (1998).

[98] F. Venturini, M. Opel, T.P. Devereaux, J.K. Freericks, I. Tüttő, B. Revaz, E. Walker, H. Berger, L. Forró, and R. Hackl, *Phys. Rev. Lett.* **89**, 107003 (2002).

[99] S. Ono, Y. Ando, T. Murayama, F.F. Balakirev, J.B. Bettes, and G.S. Boebinger, *Phys. Rev. Lett.* **85**, 638 (2000).

[100] P. Fournier, P. Mohanty, E. Maiser, S. Darzens, T. Venkatesan, C.J. Lobb, G. Czjzek, R.A. Webb, and R.L. Greene, *Phys. Rev. Lett.* **81**, 4720 (1998).

[101] J.L. Tallon and J.W. Loram, *Physica C* **349**, 53 (2001).

[102] M. Gutmann, E.S. Bŏzin, and S.J.L. Billinge, *cond-mat/0009141* (2000).

[103] J.H. Kim, H.S. Somal, M.T Czyzyk, D. van der Marel, A. Wittlin, A.M. Gerrits, V.H.M. Duijn, N.T. Hien, and A.A. Menovsky, *Physica C* **247**, 297 (1995).

[104] F. Venturini, Q.-M. Zhang, R. Hackl, A. Lucarelli, M. Ortolani, P. Calvani, N. Kikugawa, and T. Fuijita, *Phys. Rev. B* **66**, 060502 (2002).

[105] M. Oda, K. Hoya, R. Kubota, C. Manabe, N. Momono, T. Nakano and M. Ido, *Physica C* **281**, 135 (1997).

[106] K. Ishida, K. Yoshida, T. Mito, Y. Tokounaga, Y. Kitaoka, K. Asayama, Y. Nakayama, J. Shimoyama, and K. Kishio, *Phys. Rev. B* **58** (1998).

[107] C. Castellani, C. Di Castro, and M. Grilli, *J. Phys. Chem. Solids* **59**, 1694 (1998).

[108] B.P. Stojković and D. Pines, *Phys. Rev. B* **55**, 8576 (1997).

[109] T.P. Devereaux, D. Einzel, B. Stadlober, R. Hackl, D.H. Leach, and J.J. Neumeier, *Phys. Rev. Lett.* **72**, 396 (1994).

[110] C. Kendziora and A. Rosenberg, *Phys. Rev. B* **52**, 9867 (1995).

[111] M. Opel, R. Nemetscek, F. Venturini, R. Hackl, A. Erb, E. Walker, H. Berger, and L. Forró, *Phys. Stat. Sol. (b)* **215**, 471 (1999).

[112] J.G. Naeini, X.K. Chen, J.C. Irwin, M. Okuya, T. Kimura, and K. Kishio, *Phys. Rev. B* **59**, 9642 (1999).

[113] M. Opel, F. Venturini, R. Hackl, B. Revaz, H. Berger, and L. Forró, *Physica B* **284**, 669 (2000).

[114] X.K. Chen, E. Altendorf, J.C. Irwin, R. Liang, and W.N. Hardy, *Phys. Rev. B* **48**, 10530 (1993).

[115] A. Ino, C. Kim, N. Nakamura, T. Yoshida, T. Mozokawa, A. Fujimori, Z.X. Shen, T. Kakeshita, H. Eisaki, and S. Uchida, *Phys. Rev. B* **65**, 094504 (2002).

[116] T.P. Devereaux, *Phys. Rev. Lett.* **74**, 4313 (1995).

[117] T.P. Devereaux, A. Virosztek, and and A. Zawadowski, *Phys. Rev. B* **54**, 12523 (1996).

[118] G. Blumberg and M.V. Klein, *Physica B* **280**, 180 (2000).

[119] C. Panagopoulos, J.R. Cooper and T. Xiang, *Phys. Rev. B* **57**, 13422 (1998).

[120] C. Renner, B. Revaz, J.-Y. Genoud, K. Kadowaki, and Ø. Fischer, *Phys. Rev. Lett.* **80**, 149 (1998).

[121] C. Panagopoulos and T. Xiang, *Phys. Rev. Lett.* **81**, 2336 (1998).

[122] N. Miyakawa, P. Guptasarma,J.F. Zasadzinski, D.G. Hinks, and K.E. Gray, *Phys. Rev. Lett.* **80**, 157 (1998).

[123] J. Mesot, M.R. Norman, H. Ding, M. Randeria, J.C. Campuzano, A. Paramekanti, H.M. Fretwell, A. Kaminsky, T. Takeuchi, T. Yokoya, T. Sato, T. Takeuchi, T. Mochiku and K. Kadowaki, *Phys. Rev. Lett.* **83**, 840 (1999).

[124] A. Perali, C. Castellani, C. Di Castro, M. Grilli, E. Piegari, and A.A. Varlamov, *Phys. Rev. B* **62**, 9296 (2000).

[125] R. Zeyher and A. Greco, *Phys. Rev. Lett.* **89**, 177004 (2002).

[126] G. Blumberg, M. Kang, M.V. Klein, K. Kadowaki, and C. Kendziora, *Science* **278**, 1427 (1997).

[127] T. Staufer, R. Nemetschek, R. Hackl, P. Müller, and H. Veith, *Phys. Rev. Lett.* **68**, 1069 (1992).

[128] M. Rübhausen, O.A. Hammerstein, A. Bock, U. Merkt, C.T. Rieck, P. Guptasarma, D.G. HInks, and M.V. Klein, *Phys. Rev. Lett.* **82**, 5349 (1999).

[129] R. Hackl, *unpublished results.*

[130] G. Blumberg, A. Koitzsch, A. Gozar, B.S. Dennis, C. Kendziora, P. Fournier, and R.L. Greene, *Phys. Rev. Lett.* **88**, 107002 (2002).

[131] V.G. Hadjiev, X. Zhou, T. Strohm, M. Cardona, Q.M. Lin and C.W. Chu, *Phys. Rev. B* **58**, 1043 (1998).

[132] E.Ya. Sherman, C. Ambrosch-Draxl, and O.V Misochko, *Phys. Rev. B* **65**, 140510 (2002).

[133] J.R. Kirtley, C.C. Tsuei, J.Z. Sun, C.C. Chi, L.S. Yu-Jahnes, A. Gupta, M. Rupp, and M.B. Ketchen, *Nature* **373**, 225 (1995).

[134] V.J. Emery S.A. Kivelson, *Nature* **374**, 434 (1995).

[135] P.A. Fleury and R. Loudon, *Phys. Rev.* **166**, 514 (1968).

[136] A.P. Kampf, *Phys. Rep.* **249**, 219 (1994).

[137] D.K. Morr and A.V. Chubukov, *Phys. Rev. B* **56**, 9134 (1997).

[138] J.M. Rossat-Mignod, L.P. Regnault, C. Vettier, P. Bourges, P. Burlet, J. Bossy, J.Y. Henry, and G. Laperot, *Physica C* **185**, 86 (1991).

[139] H.F. Fong, B. Keimer, P.W. Anderson, D. Reznik, F. Dogan, and I.A. Aksay, *Phys. Rev. Lett.* **75**, 316 (1995).

[140] H. He, Y. Sidis, P. Bourges, G.D. Gu, A. Ivanov, N. Koshizuka, B. Liang, C.T. Lin, L.P. Regnault, E. Schoenherr, and B. Keimer, *Phys. Rev. Lett.* **86**, 1610 (2001).

[141] J.P. Carbotte, E. Schachinger, and D.N. Basov, *Nature* **401**, 354 (1999).

[142] M. Eschrig and M.R. Norman, *Phys. Rev. Lett.* **85**, 3261 (2000).

[143] N. Bulut and D.J. Scalapino, *Phys. Rev. B* **53**, 5149 (1996).

[144] A.P. Kampf and W. Brenig, *Z. Phys. B- Condensed Matter* **89**, 313 (1992).

[145] F. Venturini, U. Michelucci, A.P. Kampf and T.P. Devereaux, *Physica C* **341**, 2265 (2000).

[146] F. Wenger and M. Käll, *Phys. Rev. B* **55**, 97 (1997).

[147] T. Strohm and M. Cardona, *Phys. Rev. B* **55**, 12725 (1997).

[148] F. Venturini, U. Michelucci, A.P. Kampf and T.P. Devereaux, *Phys. Rev. B* **62**, 15204 (2000).

[149] H.J. Vidberg and J.W. Serene, *J. Low Temp. Phys.* **29**, 179 (1977).

[150] R. Nemetschek, O.V. Misochko, B. Stadlober, and R. Hackl, *Phys. Rev. B* **47**, 3450 (1993).

[151] C. Kendziora, D. Pelloquin, A. Daignere, P. Fournier, Z.Y. Li, R.L. Greene, A.F. Goncharov, V.V. Struzhkin, R.J. Hemley, and H.K. Mao, *Physica C* **341**, 2189 (2000).

[152] T.P. Devereaux, D. Einzel, B. Stadlober, and R. Hackl, *Phys. Rev. Lett.* **72**, 3291 (1994).

[153] Y. Gallais, A. Sacuto, P. Bourges, Y. Sidis, A. Forget, and D. Colson, *Phys. Rev. Lett.* **88**, 177401 (2002).

[154] S.A. Hoffman, M.A. Castro, G.C. Follis, and S.M. Durbin, *Phys. Rev. B* **49**, 12170 (1994).

[155] D.V. Khveshchenko and P.B. Wiegmann, *Phys. Rev. Lett.* **73**, 500 (1994).

[156] B.S. Shastry and B.I. Shraiman, *Phys. Rev. Lett.* **65**, 1068 (1990).

[157] P.E. Sulewski, P.A. Fleury, K.B. Lyons, and S.-W. Cheong, *Phys. Rev. Lett.* **67**, 3864 (1991).

[158] R. Liu, D. Salamon, M.V. Klein, S.L. Cooper, C.W. Lee, S.-W. Cheong, and D.M. Ginzberg, *Phys. Rev. Lett.* **71**, 3709 (1993).

[159] C.M. Varma, *Phys. Rev. B* **61** (2000).

[160] L. Benfatto, S. Caprara, and C. Di Castro, *Eur. Phys. J. B* **17**, 95 (2000).

[161] A. Kaminski, S. Rosenkranz, H.M. Fretwell, J.C. Campuzano, Z. Li, H. Raffy, W.G. Cullen, H. You, C.G. Olson, C.M. Varma, and H. Höchst, *Nature* **416**, 610 (2002).

[162] C. Thomsen, *in Light Scattering in Solids VI*, Springer-Verlagd, Berlin Heidelberg (1991).

[163] E. Abrahams and C.M. Varma, *Proc. Natl. Acad. Sci.* **97**, 5714 (2000).

[164] A.R. Moodenbaugh, *Phys. Rev. B* **38**, 4596 (1988).

[165] Y. Ando, *cond-mat/0206332* (2002).

[166] X.J. Zhou, P.V. Bogdanov, S.A. Kellar, T. Noda, H. Eisaki, S. Uchida, Z. Hussain, and Z.X. Shen, *Science* **286**, 268 (1999).

[167] K. Yamada, C.H. Lee, K. Kurahashi, J. Wada, S. Wakimoto, S. Ueki, H. Kimura, Y. Endoh, S. Hosoya, G. Shirane, R.J. Birgeneau, M. Greven, M.A. Kastner, and Y.J. Kim, *Phys. Rev. B* **57**, 6165 (1998).

[168] V.J. Emery, S.A. Kivelson, and J.M. Tranquada, *Proc. Natl. Acad. Sci.* **96**, 8814 (1999).

[169] C.C. Homes, M. Reedyk, D.A. Cradles, T. Timusk, *Appl. Opt.* **32**, 2976 (1993).

[170] S. Tajima, H. Ishii, T. Nakahashi, H. Takagi, S. Uchida, M. Seki, S. Suga, Y. Hidaka, M. Suzuki, T. Murakami, K. Oka, and H. Unoki, *J. Opt. Soc. Am. B* **6**, 475 (1989).

[171] A. Lucarelli, S. Lupi, M. Ortolani, P. Calvani, P. Maselli, M. Capizzi, P. Giura, H. Eisaki, N.Kikugawa, T. Fujita, and K. Yamada, *Phys. Rev. Lett.* **90**, 037002 (2003).

[172] T. Osafune, M. Motoyama, H. Eisaki, S. Uchida, and S. Tajima, *Phys. Rev. Lett.* **82**, 1313 (1999).

[173] M. Tinkham, *Group Theory and Quantum Mechanics*, McGraw-Hill, New York, NY (1964).

[174] M. Shastry, K. Yamada, H. Hiraka, P.M. Gehring, S.H. Lee, S. Wakimoto, and G. Shirane, *Phys. Rev. B* **65**, 064505 (2002).

[175] A. Lanzara, G.-M. Zhao, N.L. Saini, A. Bianconi, K. Conder, H. Keller, and K.A. Müller, *J. Phys.: Condens. Matter* **11** (1999).

[176] A.W. Hunt, P.M. Singer, K.R. Thurber, and T. Imai, *Phys. Rev. Lett.* **82**, 4300 (1999).

[177] N. Ichikawa, S. Uchida, J.M. Tranquada, T. Niemöller, P.M. Gehring, S.-H. Lee, and J.R.Schneider, *Phys. Rev. Lett.* **85**, 1738 (2000).

[178] P.M. Singer, A.W. Hunt, A.F. Cederström, and T. Imai, *Phys. Rev. B* **60**, 15345 (1999).

[179] Y. Ando, K. Segawa, S. Komiya, and A.N. Lavarov, *Phys. Rev. Lett.* **88**, 137005 (2002).

[180] X. Hiraka, Y. Endoh, M. Fujita, Y.S. Lee, J. Kulda, A. Ivanov, R.J. Birgeneau, *J. Phys. Soc. Japan* **70**, 853 (2001).

Acknowledgments

I am deeply grateful to Prof. Dr. R. Gross for giving me the opportunity to do this work and for his continuous encouragement.

I would like also to thank Prof. Dr. G. Abstreiter for the support in the initial part of my stay.

This work would not have been possible without the continuous support and encouragement of Rudi. I greatly benefited from his vast experimental experience and from his various knowledge. His helpfulness made the research and the lab work always pleasant. I really enjoyed the lively discussions and the brainstorming we had together. His spontaneous help in any direction made my stay in German very enjoyable.

I am truly grateful to Matthias who with his talk in 1997 in Washington introduced me to the research done here at the Institute. I am indebted to him for his patience in answering all my many questions on the laboratory, on computers and on the German bureaucracy.

I owe to Tom Deveraux my very interest in Raman scattering. It was him with a "win-win" project that introduced me to the complexity of many-body calculation. I very much enjoyed the exciting discussions and shared his enthusiasm for physics. A special thank also for the hospitality during my stay in Waterloo.

I am indebted to Prof. Dr. A.P. Kampf for inviting me in Augsburg during the first months of my stay in Germany. I greatly profited from his rigorous approach to physics and from the many instructive discussions.

I was lucky to meet Prof. Dr. B.S. Chandrasekhar and to share the office with him. I am very thankful to him for the many stimulating discussions, continuous encouragement and the careful reading of this manuscript. I very much enjoyed the music concerts and thanks to him I am now fond of Indian food.

I am very thankful to Dr. Dietrich Einzel for his theoretical support and for reading the manuscript. The spontaneous discussions and the jokes made any interaction very pleasant.

I would like to thank Istvan Tüttő, Fred Zawadowski, Attila Virosztek, and

Kati Kamaràs for the kind hospitality in Budapest. I particularly benefited from the many clarifying discussions with Tüttő, whom I thank also for reading the manuscript.

I am very grateful to Prof. Paolo Calvani, Prof. Carlo Di Castro, and the colleagues in Rome, Alessandro, Andrea, Michele, Stefano, for the stimulating discussions, the pleasant hospitality and for answering all my questions on infrared spectroscopy.

I would like to thank Dr. Sergey Borisenko and Dr. Mark Golden for sharing their photoemission data.

I am also grateful to Q.-M. Zhang for the support during the year he spent in Germany.

I am indebted to Andreas Erb, B. Revaz, E. Walker, H. Berger, L. Forró, N. Kikugawa and T. Fujita for providing excellent samples.

Last but not least I am grateful to all the diploma and doctoral students, to the scientific and technical staff of the WMI for the spontaneous support and friendly atmosphere.

This work would not have been possible without the financial support of the Gottlieb Daimler and Karl Benz foundation.

Ringrazio la mamma e Chiara per l'affetto e la fiducia mostratami in questi anni trascorsi lontano da casa.

Infine ringrazio Umberto senza il cui sostegno questo lavoro non sarebbe stato possibile. Grazie per il continuo aiuto, incoraggiamento e affetto, per la pazienza nel sopportare e rispondere a tutte le mie numerose domande di fisica, per la compagnia nelle lunghe serate in laboratorio e per la lettura e rilettura del manoscritto.